

An Evaluation of an Airborne Remote Sensing System used to Determine Ice Thickness and Geometry of a First Year Sea Ice Ridge Located in the Beaufort Sea

by

Robert G. Bowen
B.Sc., Trent University, 1988

Thesis Submitted in Partial Fulfilment of the
Requirements for the Degree of

ACCEPTED

FACULTY OF GRADUATE STUDIES

MASTER OF SCIENCE

in the Department of Geography

DEAN

28 Apr 13

We accept this thesis as conforming
to the required standard.

Dr. Olaf Niemann, Supervisor (Department of Geography)

Dr. Stanton Tuller, Department Member (Department of Geography)

Dr. David Topham, Outside Member (Institute of Ocean Sciences)

Dr. Peter Stephenson, External Examiner (Department of Anthropology)

©ROBERT G. BOWEN, 1993

University of Victoria

All rights reserved. Thesis may not be reproduced in whole or in part, by mimeograph or other means, without the permission of the author.

G70.4
B6

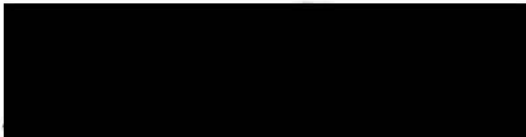
1970.4
B6

Abstract

Supervisor: Dr. Olaf Niemann

One dimensional and two dimensional interpretation techniques have been applied to the electromagnetic (EM) anomalies obtained from a state of the art airborne remote sensing system field tested over a first year ice ridge. This airborne system combines the technology of a laser altimeter, an impulse radar and an electromagnetic induction sounding system in an attempt to accurately measure irregular ice geometry. This paper focuses on the evaluation of the EM component of the airborne system based on a volumetric comparison of the airborne EM interpreted data with extensive ground truth data obtained from submersible sonar surveys and surface theodolite surveys. The overall form of the ridge geometry at the study site was obtained by generating digital terrain models from the ground truth data. Two interpolation routines were used in this process, both yielding similar form and volumetric results. Comparison of the ground truth data with the EM interpreted data indicate that the interpretation techniques poorly resolve ice feature definition. Raw EM anomalies records overlaid onto appropriate cross sections of the ridge suggest that the resolution of the system is far better than the interpreted data would suggest. It is, therefore, recommended that further development of EM interpretation techniques over ice keels be made.

Examiners:



Dr. Olaf Niemann, Supervisor (Department of Geography)



Dr. Stanton Tuller, Department Member (Department of Geography)



Dr. David Topham, Outside Member (Institute of Ocean Sciences)



Dr. Peter Stephenson, External Examiner (Department of Anthropology)

Acknowledgements

The author would like to acknowledge the following contributors for their involvement in the 1991 field program. The field project and subsequent analysis was funded by PERD as part of their Task 6.2 mandate for Arctic Research. Processed 1-D interpreted EM data was supplied by Dr. Scott Holladay of Aerodat Limited who also provided knowledgeable comments on equipment and EM results. The Arctic Group of the Institute of Ocean Sciences, led by Dr. David Topham, performed many hours of TARS data collection, providing the ground truth keel data necessary for the airborne system. The author would like to thank both the Institute of Oceans Sciences Arctic Group and Dr. Olaf Niemann of the University of Victoria for providing this opportunity to be involved in this interesting field study.

In addition, a number of individuals were helpful in key areas of the thesis analysis and writing. These include:

Gary Anderson of Anderson and Associates for his help in generating digital terrain models using the software EMXS;

Dr. Melvyn Best of the Pacific Geoscience Centre for his helpful comments on geophysics and EM theory;

Steve Chatwin and Darren Ham of the B.C. Ministry of Forest, Research Branch for the use of their Stereo Analyzer (AP190);

Dr. Harry Dosso of the University of Victoria for helpful comments on EM data analysis;

David Riedel of the Institute of Ocean Sciences for his help with the computer analysis of the TARS data;

Stanton Tuller of the University of Victoria for his helpful editorial comments on writing this thesis.

Finally, the author would like to thank Suzanne Bowen for her continual support during the Masters program.

CONTENTS

Abstract	ii
Acknowledgements	iii
Contents	iv
List of Figures	vi
List of Tables	viii
1.0 Introduction	1
2.0 Research Objectives	4
2.1 Overview	4
2.2 Contribution to Knowledge	6
3.0 Background	8
3.1 Physical Attributes of Ice Ridging	8
3.11 Sea Ice Structure and Rheology	9
3.12 Pack Ice Driving Forces	12
3.13 Ridge Geometry	14
3.14 Electrical Conductivity of Snow, Sea Ice and Sea Water	21
3.2 Airborne Remote Sensing of Ice Thickness	24
4.0 Geophysical Electromagnetic Induction	30
4.1 General EMI Theory	30
5.0 Project Instrumentation	46
5.1 Airborne Survey Instrumentation	46
5.11 Laser Altimeter	50
5.12 Impulse Radar	50
5.13 Airborne EMI	50
5.2 Ground Truth Instrumentation	52
5.21 Sail Instrumentation	52
5.22 Keel Instrumentation	53
6.0 Methodology	57
7.0 Data Acquisition	58

8.0 Analysis	60
8.1 Topside survey	60
8.2 Keel survey	62
8.21 ATS Analysis	64
8.22 Mesotech Analysis	66
8.23 TARS Analysis	67
8.3 Combining Keel Data	69
8.31 Resolving for Pitch and Roll	70
8.4 Digital Terrain Modelling	74
8.41 Sail Data Coverage	75
8.42 Keel Data Coverage	76
8.43 Modelling Software	77
8.431 DTMs Generated from Stochastic Processes	77
8.432 DTMs Generated from Triangulation	88
8.5 Airborne Survey	96
8.51 EM Raw Data	100
8.52 1-D Inversion of EM Data	103
8.53 2-D Model Interpretation of EM Data	108
9.0 Discussion	115
9.1 Evaluation of Airborne EM Thickness Sensor	115
9.3 Ridge Geometry Attributes	120
10.0 Conclusions and Recommendations	124
REFERENCES	127
APPENDICES	
A Field Log	133
B Multi-Line Header (MLH) Format	135
C Computer Programs Developed for Thesis Analysis	138
D Calibration Curve of Pressure Transducer	177
E Resolving Pitch and Roll Transformations for TARS	178
F Neural Networks	184
G Ice Ridge Cross Sections	186

List of Figures

Figure 1: Approximate Location of Study Site	3
Figure 2: Schematic Diagram Showing Major Ice Structure and Crystal Texture . .	10
Figure 3: Thin Section of an Undeformed Ice Sample	11
Figure 4: Pack Ice Driving Forces. (a) Forces, (b) Free floating flow velocity	13
Figure 5: Ridge Formation. (a) Compression, (b) Shear, (c) & (d) Rafting	15
Figure 6: Aspect Ratios of Sail Height to Keel Depth	16
Figure 7: Ridge Geometry. (a) First Year Ridge, (b) Multiyear Ridge.	17
Figure 8: Consolidation Curve of Rubble Ice	20
Figure 9: Brine Migration	23
Figure 10: Comparison of Airborne Ice Thickness Measuring Techniques	28
Figure 11: Electric Field Lines	31
Figure 12: Magnetic Field Lines	32
Figure 13: Faraday's Law of Induction	33
Figure 14: Magnetic fields generated from electric current	34
Figure 15: Electromagnetic Ray Diagram	36
Figure 16: Geophysical Electromagnetic Induction	37
Figure 17: Primary and Secondary Phase Lag Relationships	39
Figure 18: Vector Diagram of EM Fields	40
Figure 19: Coil Configurations	42
Figure 20: Surficial Electric Currents of EM Footprint	43
Figure 21: Co-axial and Coplanar Footprint Areas	44
Figure 22: Skin Depth Penetration of EM Waves	45
Figure 23: Photograph of Airborne Remote Sensing System	46
Figure 24: Physical Dimensions of Airborne Remote Sensing Bird	48
Figure 25: Remote Sensing System illustrating the Key Conductive Interfaces . . .	49
Figure 26: Photograph of TARS showing the Umbilical Cable	53
Figure 27: Diagram of TARS	56
Figure 28: Photograph of sail block structure	61
Figure 29: Photograph of sail block structure	61

Figure 30: Flow Chart of Submersible Data Analysis	63
Figure 31: ATS Time Sampling Interval	65
Figure 32: Compass Heading Malfunction	71
Figure 33: Point Data for Sail Geometry	75
Figure 34: Resolved Point Data for Keel Geometry	76
Figure 35: Search Algorithms for Interpolation of Raw Data	78
Figure 36: Sail DTM	80
Figure 37: Overlay of DTM Contour Map onto Air Photograph of Study Site	82
Figure 38: Keel DTM	85
Figure 39: Overlay of Sail Contour Map onto Keel Contour Map	87
Figure 40: Plan View of Triangular Network Constructed for Sail DTM	91
Figure 41: 3-D Grid of Sail DTM	92
Figure 42: Plan View of Triangular Network for Keel DTM	94
Figure 43: 3-D Grid of Keel DTM	95
Figure 44: Locations of Airborne Survey Overflights	97
Figure 45: Frame Grabbed Image of Airborne System flying over Study Site	98
Figure 46: Ground Truth DTM in the Vicinity of the EM overflight	99
Figure 47: Raw Data Strip Chart Recordings (data supplied by AERODAT)	101
Figure 48: Raw Data Strip Chart Recordings of Evaluation Overflight	102
Figure 49: One Dimensional Model of Ice/Water Layers	103
Figure 50: 1-D Interpretation of EM Anomalies	106
Figure 51: Assumed 3-D Model of Ice Keel based on 1-D Interpreted Data	107
Figure 52: 2-D Laboratory Model of Ice Keel	110
Figure 53: Comparison of 2-D Lab Results with 2-D Numerical Solutions	111
Figure 54: Nomogram Look-Up Table	112
Figure 55: Gaussian Curve of Keel based on 2-D Analysis	114
Figure 56: Ground Truth Grid Cross-Sections of EM Swath	117
Figure 57: Comparison of EM Anomalies with Grid Cross-Sections	118
Figure 58: Underwater Video Image of Enveloped Keel Rubble	122

List of Tables

Table	Title	
Table 1	Satellite Sensing of Ice	25
Table 2	Airborne Remote Sensing Specifications	52
Table 3	ATS Raw Data Array	64
Table 4	TARS Raw Data Array	68
Table 5	Gridding Parameters for Sail DTM	81
Table 6	Gridding Parameters for Keel DTM	83
Table 7	Skin Depth Calculations	109
Table 8	Percent of Ice Contained within the Sail and Keel of the Ridge . .	120

1.0 Introduction

The Arctic Ocean is largely covered by a canopy of moving sea ice that is continually being stretched and compressed by climatic factors, currents, internal ice pressures and tides. The resultant sea ice surface consists of open leads, uniform ice, and nonuniform features such as rubble fields, pile-ups and ridges. Flato and Hibler (1991) concluded that between 10 and 40% of the central arctic ice mass is ridged with pockets of heavily ridged ice as high as 100% in active shear zones. These shear zones are common near shorelines where moving pack ice interacts with fixed landfast ice. Ice ridges vary in shape and size and pose significant hazards to arctic vessel traffic and offshore structures. Pressures exerted by large moving ridges can result in structural damage and overtopping of offshore structures, ice scour of marine cables, and overloading of ship bow and hull designs. As a result of this powerful damage potential, design load philosophies have been developed that consider:

- (1) ice-loading conditions
- (2) maximum loading events
- (3) probabilistic ice-load generation
- (4) risk of structural failure

(Sanderson, 1988).

These logical considerations quantify risk potential; however, the input required in the various stages of calculations is limited by our knowledge of ice/ice and ice/structure interactions. In addition, ice thickness, which is a fundamental component necessary for determining force and momentum, is at best poorly understood for irregular features such as pressure ridges.

Common to all geophysical studies involving sea ice is the determination of ice thickness. This becomes especially difficult in ridged ice where consolidated and unconsolidated rubble extend well below the adjacent level ice thickness. Unfortunately, at present, there are no spaceborne remote sensing techniques capable of measuring ice thickness directly (Shuchman and Onstott, 1990).

Airborne remote sensing systems such as impulse radar (Rossiter and Lalumiere, 1988) and electromagnetic induction (Kovacs and Holladay, 1989) have been used on level ice with success; however, these instruments have consistently underestimated ridge thickness and geometry. Measurement of the exposed topside or sail of ridges is straightforward and has been carried out by stereo air photo interpretation and theodolite surveys; however, the measurement of keel geometry has been limited to fixed upward looking sonar systems, submarine tracks and more recently, sonar equipped submersibles. All of these techniques are time consuming, costly and require large amounts of post processing time.

An effort has been made to develop a state of the art airborne remote sensing system capable of real time ice thickness measurements of irregular features. This system, operated by Aerodat Limited with radar equipment from Canpolar Limited, integrates an electromagnetic induction sounding system, an impulse radar and a laser altimeter in an attempt to measure surface and subsurface geometry of first year ice ridges. The development of this new system is part of an ongoing research program designed to investigate the dynamics of pack ice driving forces, ice/ice and ice/structure interactions. This broader research program was developed and funded by the Panel on Energy Research and Development (PERD) which has coordinated the efforts of government research institutes, private industry and university researchers.

This paper examines the findings of the April 1991 field testing program carried out on a first year ice ridge located approximately 60 km north of Tuktoyaktuk (Figure 1). In order to evaluate the performance of the airborne system, it was necessary to carry out extensive ground truthing which involved both sail and keel surveys. Ridge geometry surveys were carried out by a research team from the Arctic Group of the Institute of Ocean Sciences (IOS), Sidney, British Columbia. In addition, snow thickness, salinity and level ice thicknesses were measured near the ridge by Dr. Simon Prinsenbergh of Bedford Institute of Oceanography, Dartmouth, Nova Scotia. Only the IOS survey data will be presented and compared to the analysis of the data

obtained from the electromagnetic component of the airborne system.

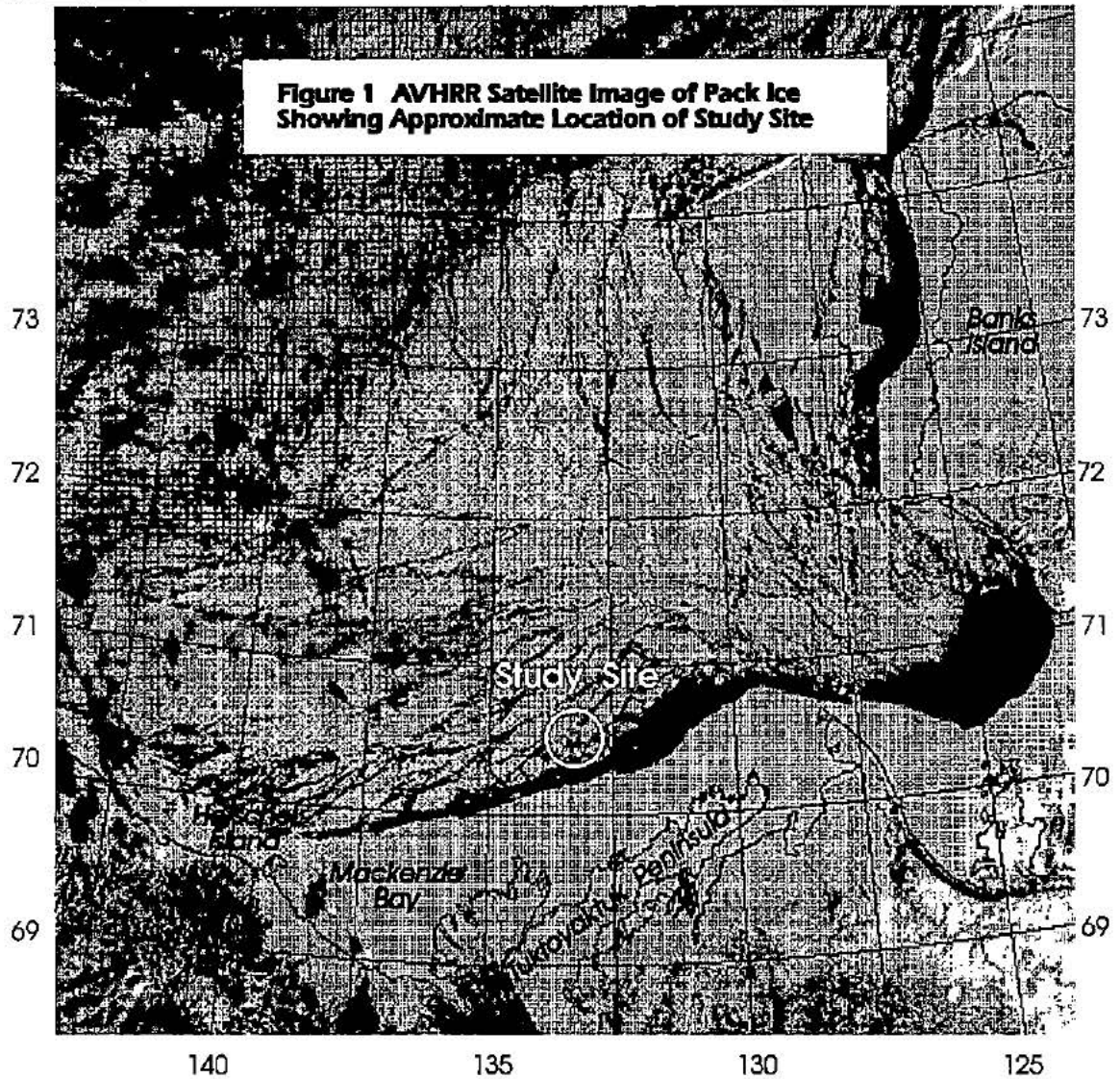


Figure 1: Approximate Location of Study Site (Image taken April 17, 1991).
(AVHRR refers to an Advanced Very High Resolution Radiometer)

2.0 Research Objectives

The objectives of this study are two-fold. The primary objective will be to evaluate the electromagnetic component of Aerodat's newly designed integrated airborne remote sensing system on the detection of the complex geometry of a first year ice ridge. This will be carried out by comparing ridge volumetric calculations obtained from ground truth surveys with ridge volumetric calculations obtained from the remote sensing system. The second objective will be to provide detailed ridge geometry of surface and subsurface features to add to the limited knowledge that exists on ridge geometry. The second objective will be a by-product of the fulfilment of the primary objective.

2.1 Overview

In order to fulfil the objectives of this study, it was necessary to use a number of methods to obtain the required data. Five research groups were involved in this field project in various capacities. Each group contributed to the instrumentation and interpretation of the data obtained. These groups and their contributions are as follows:

- (1) Institute of Ocean Sciences
Sonar equipped submersible, Global Positioning System (GPS), Theodolite and Electronic Distance Measuring device (EDM), analysis of keel and sail data.
- (2) Aerodat Limited
Electromagnetic Induction Sounding System, Kevlar Bird, GPS, Pitch and Roll Sensors to monitor bird attitude, Laser Altimeter, 1-D interpretation of results.
- (3) Canpolar Inc.
Impulse Radar and interpretation of data.
- (4) Bedford Institute of Oceanography
Ground truthing of snow and ice thickness on level ice adjacent to

pressure ridge. Laboratory analysis of ice samples.

- (5) National Research Council
Stereo air-photography of study site.

Once a site was selected, the field study consisted of three phases. Phase one involved the deployment of a submersible in order to obtain keel data of the pressure ridge. Phase two was to perform a theodolite survey of the sail geometry at the site. Phase three was to carry out an aerial survey using the airborne remote sensing system. The entire field program was carried out in approximately ten days.

The intention of this thesis is to present an evaluation of the airborne remote sensing system's ability to measure ice ridge thickness and geometry. A brief background on ice structure, ridging and the driving forces responsible for ridge formation is included in order to provide the necessary details relevant for the evaluation of the remote sensing system. Some very general theory is presented identifying basic concepts used by the airborne instrumentation. Testing procedures are described identifying the methods used during the field program. The collected data is then analyzed in order to generate digital terrain models of the sail and keel surfaces. Volumetric calculations of these surfaces are compared to the electromagnetic induction system swath over the ridge using both 1-D and 2-D interpretive techniques. The raw remotely sensed electromagnetic induction data were proprietary and were, therefore, not released. As a result, both 1 and 2-D interpretation of the data were performed by AERODAT. Some of this interpreted data were released and are presented graphically. The interpretation techniques used by AERODAT are briefly described. Conclusions are formulated based on the comparison of this data to the ground truth data. Significant findings, limitations and further research and development steps necessary to improve the airborne system and its data interpretation techniques are presented.

2.2 Contribution to Knowledge

The ability to accurately map ice thickness of regular and irregular ice features in real time has long been a goal in ice research. Ice thickness influences the amount of light penetration and biological productivity, the upper ocean salt balance, ocean-ice-air heat exchanges, ice pressures due to ice and thermal action, and the trafficability on, through and under an ice cover (Rothrock, 1986). In addition to thickness, snow cover and surface irregularities modify these phenomena to varying degrees. The development and validation of an airborne remote sensing system that actively measures ice thickness, snow cover and surface geometry would have significant value for determining any one of the above phenomena either in a site specific area or over larger regions of interest.

One significant benefit of such a design recognized by the Canadian Coast Guard would be to equip ice breakers and ice capable ships with operational airborne ice sensors. Such airborne systems could be quickly deployed from ship helicopters in order to chart safe passage through difficult ice conditions either for the host ship or a vessel requiring assistance (Prinsenberget al., 1992).

An additional benefit of an effective ice thickness sensor would be its ability to supply measurements of ice subsurface geometry. Sea ice pressure ridges provide excellent study sites to examine pack ice driving forces and associated ridge building processes. Pressure ridges display the magnitude of the energy within an ice field. The geometry of pressure ridges gives a static account of a series of dynamic processes that occurred during the ridge building event(s). Ridge geometry, obtained from a working airborne system could provide valuable clues as to the magnitude of the driving forces responsible for ridge formation and, therefore, aid in the design criteria for structures. Sayed and Frederking (1989), in an attempt to better understand large scale ice movement and the forces that produce pressure ridges, carried out an extensive field study of ridge sails located in the southern Beaufort Sea. In their

concluding remarks they identified ice ridging to be a complex phenomenon that remains poorly understood. Also, they stated: "No theory thus far can adequately predict ridge geometry and ridging forces in the ice cover." This issue of force/geometry relationships is of current interest to the ice community and is often referred to as ice tectonics. The airborne system examined in this paper may provide a method for measuring ridge geometry and aid the pursuit to discover such relationships.

The development of the airborne sensor may have other research applications. Fine tuning of the electromagnetic fields set up by the airborne system may reveal information about the keel structure and porosity. These attributes of keel morphology are presently difficult to obtain. Such attributes are significant design considerations for structure loading thresholds (i.e. a structure encountering a highly porous ridge would experience less loading than a structure encountering a similar ridge with low porosity).

3.0 Background

Ultimately, the complexity of ridge geometry affects the response of the remote sensing system. The size and distribution of ice blocks coupled with the voids between blocks create a nonuniform porous rubble that presents significant challenges to the remote sensing of ice thickness. The horizontal deformation fields responsible for creating ridge and rafting events play a fundamental role in ice thickness attributes and distribution. Remote sensing of these complex features requires an understanding of the ice parameters that influence the ability of the remote sensing instrumentation to resolve accurate ice thicknesses. For this reason, this chapter has been divided into two segments. The first segment, containing a number of sections, addresses relevant background information on ridge formation, morphology and electrical conductivity. The second segment reviews previous field studies which utilized airborne remote sensing systems. In this second segment, the techniques of the various airborne instrumentation will briefly be addressed setting the context for the following chapter on electromagnetic theory.

3.1 Physical Attributes of Ice Ridging

The processes involved in the formation of pressure ridges requires an understanding of the essential elements involved in atmosphere-sea-ice-dynamics. These interactive processes are characterized by the following components:

- (1) Pack ice driving forces including wind and current shear stresses, Coriolis effect, internal ice stresses and inertial forces.
- (2) Rheological behaviour of sea ice relating driving forces to ice strength, deformation, failure modes and ridge geometry.
- (3) Ice characteristics influencing both driving forces and ice rheology. These characteristics include ice type, temperature and salinity, ice surface and subsurface roughness, floe size and thickness.

- (4) Climatic factors controlling air and water temperatures and amount and forms of precipitation (Hibler, 1989).

3.11 Sea Ice Structure and Rheology

The single most influential component that governs the dynamics of ice/ice interactions is the behaviour of ice itself. The behaviour of ice is not only important during ridge building events but it also governs the static deformation processes that occur after ridge building is complete.

Ice, typically, is within a few degrees (rarely more than 40°C) of its melting point. It is, therefore, considered to be at a "high temperature state" (Gold, 1981). Under these conditions the properties of ice can vary drastically (Kerr, 1975). Lavrov (1969) points out that as the temperature of ice approaches its melting point, liquid water can act as a lubricant, resulting in the reduction of the internal strengths of the ice. Since ice typically has a large thermal gradient, that is, cold at the air/ice interface and relatively warm at the ice/water interface, the mechanical and electrical properties of ice vary with depth even within a given ice sheet.

The crystal structure and orientation of the ice also influence the behaviour of ice/ice interactions. Ice has a nonuniform, polycrystalline structure that exhibits anisotropic behaviour (Sinha, 1978; Vaudrey and Katona, 1977). As ice grows, the thermal conditions vary at the advancing ice/melt interface. Growth rates tend to decrease with depth as a function of the thermal gradient (Weeks and Assur, 1967). This results in ice crystals of varying shapes and sizes. Michel and Ramseier (1971) classified different ice types according to crystal size, shape and orientation. Incorporated into this classification system are the environmental factors responsible for the formation of these different ice types. According to this system there are three distinct classifications for ice types. They are P type (primary ice), S type (secondary ice), and T type (superimposed ice). Ice plates experiencing a series of environmental

changes or ice action events may contain one or more of these types of ice. Examination of ice cores extracted from level or ridged ice reveals a tremendous amount of historical detail about ice type, environmental conditions and possibly ice interaction events which may have occurred to produce its structure (Lange and Eicken, 1991). Figure 2 and 3 illustrates some of the variety of ice types.

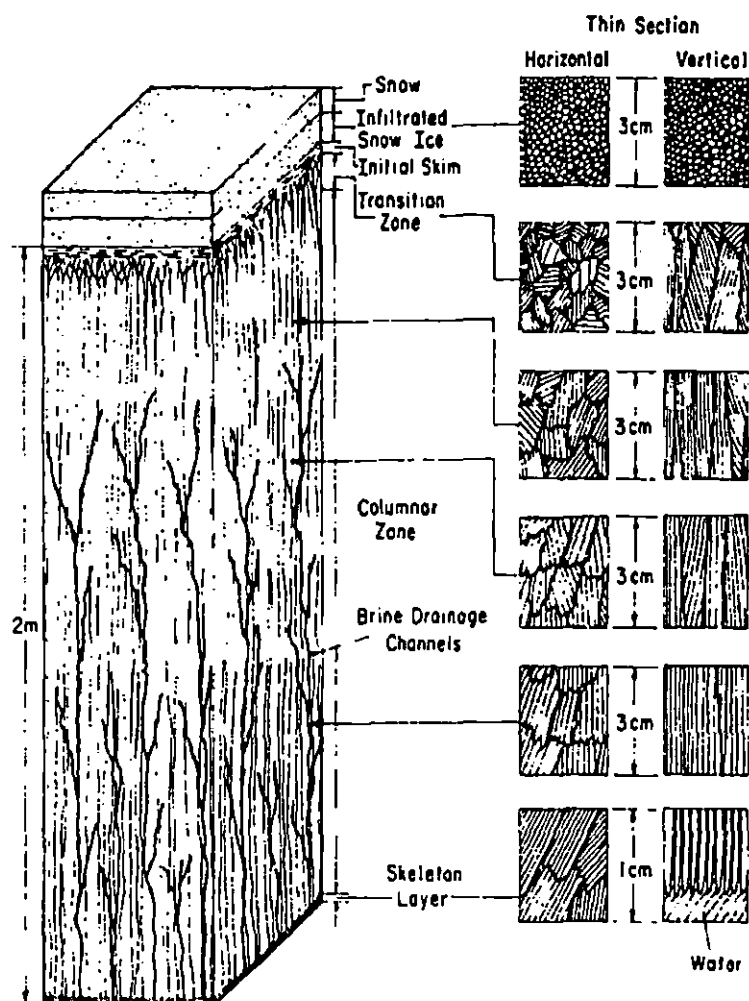


Figure 2: Schematic Diagram Showing Major Ice Structure and Crystal Texture.
(Gow and Tucker, 1990)

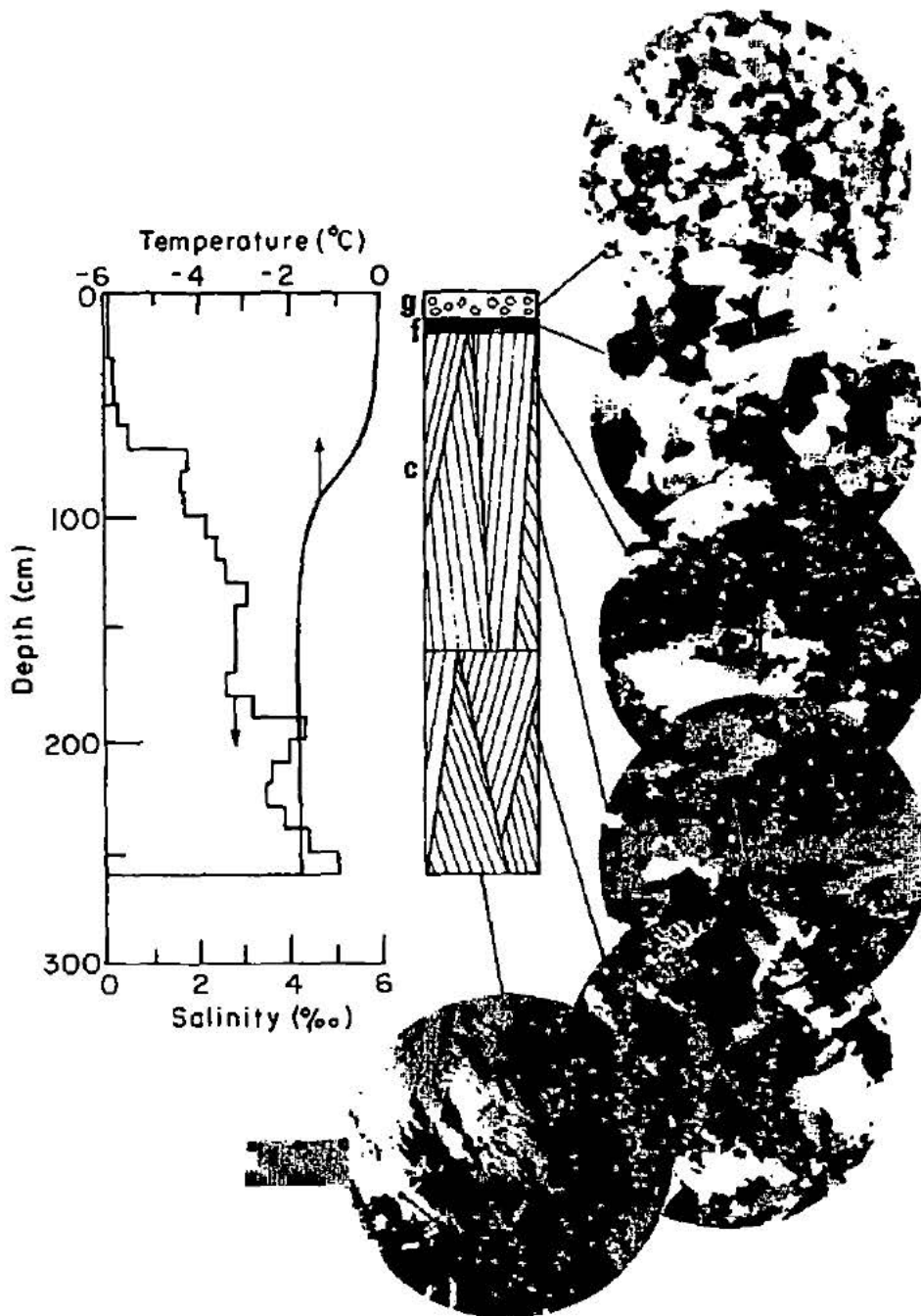


Figure 3: Thin Section of an Undeformed Ice Sample. The Symbols g, f and c represent granular (T-type), freshwater pond ice (T-type) and columnar (S-type) ice respectively (Gow and Tucker, 1990).

The dynamics of ice/ice interaction are also determined by the rate in which

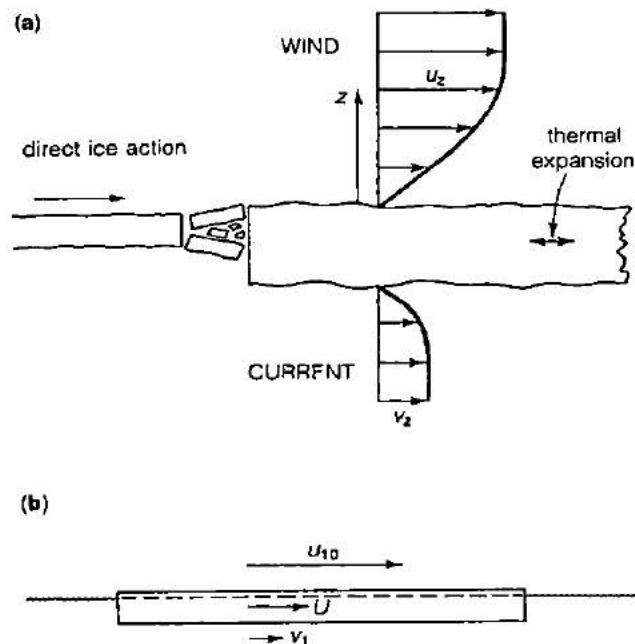
horizontal driving forces are applied. This is of extreme importance for the deformation of ice is rate dependent. Many of the papers reviewed consider ice to behave as a viscoelastic material (Nevel, 1976; Pounder, 1965; Michel and Gagnon, 1978; Sinha et al., 1987). This term is merely an attempt to classify ice in all of its stress-strain conditions. The rheological attributes (stress/strain relationships) of ice largely determine the type and extent of deformation, failure modes and ice block size. The behaviour of ice experiencing stress can be divided into a time independent linear elastic strain which results in no net deformation as well as a time dependent viscous strain which results in permanent deformation. The complex ridge geometry of an observed ridge is but a snapshot in time of a series of previous combinations of these strain responses which influence ice mechanical properties and failure modes. The induced stresses largely responsible for these strain responses and resulting ice failure is the result of dynamic action of moving ice.

3.12 Pack Ice Driving Forces

The magnitude of the environmental driving forces that create ice ridging events indicate the available energy within the ice field and therefore aid in the design of structures and navigational routing. These forces shape the structure and size of the ridge feature.

The movement of free floating ice floes is caused by a number of pack ice driving forces. These forces can be broken up into four different components: wind, current, thermal expansion, and direct ice action. The first two forces are the dominating driving forces. Wind and current driving forces develop from frictional drag as air and water flow over top and bottom surface features. Figure 4 illustrates a simplified model of two uniform flow patterns moving adjacent to an ice cover. The roughness of the top and bottom sides of the ice influence the flow velocity gradients U (air velocity) and V (current velocity).

Figure 4: Pack Ice Driving Forces. (a) Forces, (b) Free floating flow velocity.



(Sanderson, 1988)

When two or more ice floes collide, a complex process of ice failure and ridge building begins. The initial stages of the interaction involves the dissipation of kinetic energy as the floes decelerate (Croasdale and Marcellus, 1981). Two general methods have been used to predict and describe ridge-building forces. The first method estimates the total energy expended during the ridge building process and considers energy dissipation and storage from frictional losses, energy to fracture the ice floe, and gravitational potentials. The second method examines the complex failure processes of bending, buckling and crushing. If the failure modes are determined and ice strength in these modes is understood, then forces required to build the ridge can be calculated (Vivatrat and Kreider, 1981). At best, however, both these approaches are but generalizations of the complex relationships that exist between ice forces and geometry.

A number of influential factors that result in the formation of ridge geometry

have been identified. Numerous field studies have examined the jumbled blocks that shape ice ridges and some attempts have been made to quantify total ice thickness by using remote sensing systems. Both field studies of ridge geometry and airborne remote sensing of ice thickness will briefly be reviewed.

3.13 Ridge Geometry

First-year ridge formations are accumulations of ice blocks which protrude both above and below abutting ice floes (Kovacs, 1972). They are generally formed by the collision of two or more floes where collision forces exceed the failure strengths at the ice/ice contact zone or by internal ice pressures that concentrate stress. The type of forces exerted and the resultant ridge feature have been divided into two distinct classifications as illustrated in Figure 5 (Sanderson, 1988).

Compression Ridge

Compression ridging takes place when direct collisions occur between ice floes and/or internal ice forces exceed the ultimate strength of an ice plate. Compression, as the name implies, is the result of horizontal driving forces that press ice floes together resulting in crushing, buckling, flexural or mix mode failures of floe leading edges. Ridges, formed by these processes, tend to be highly irregular in longitudinal variation and in vertical height (Sanderson, 1988).

Shear Ridge

The less frequent shear ridge is created by the lateral shearing motion of adjacent ice floes. The frictional grinding of ice against ice produces near vertical walls of finely pulverized ice (Sanderson, 1988).

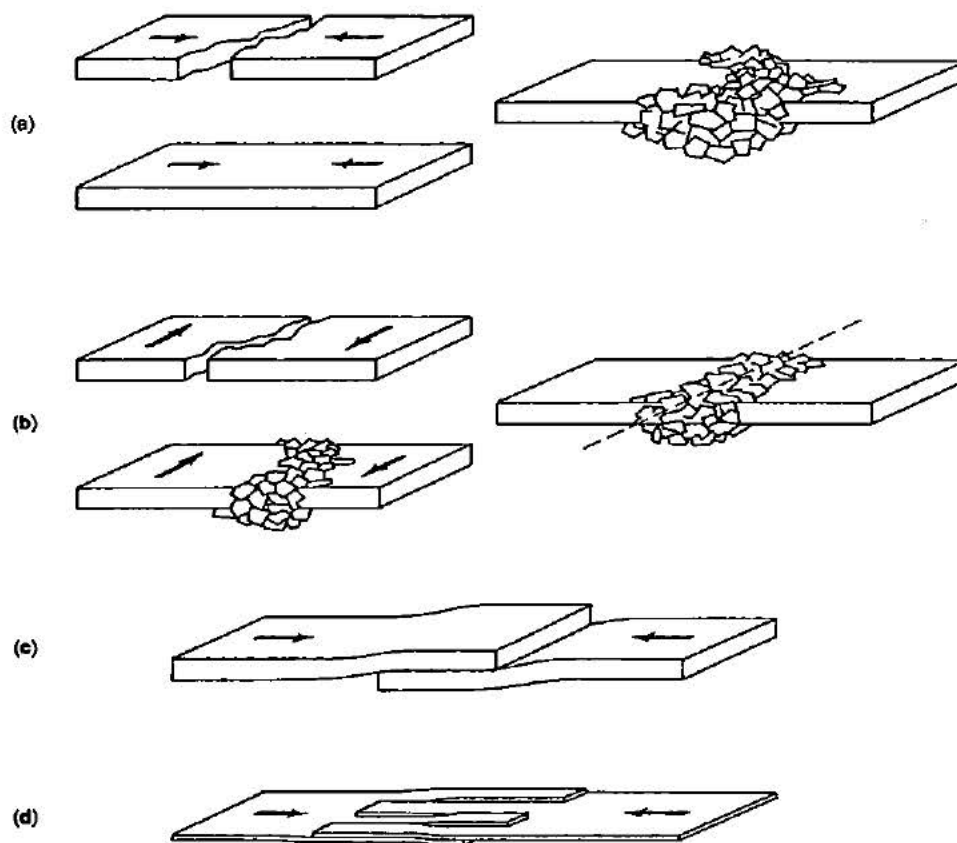


Figure 5: Ridge Formation. (a)Compression, (b)Shear, (c)&(d) Rafting.
(Sanderson, 1988)

Kovacs (1972) aerial photographed a shear ridge which clearly delineated the boundary between shorefast ice and moving pack ice. Such ridge features may be in the order of several kilometres long and are easily identified by their striking linearity. Only a limited amount of qualitative information is available on shear ridges and since the ridge being studied is a compression ridge, shear ridges will be dropped from this discussion.

Ice Ridge Morphology

A number of studies have been carried out to study ice ridge morphology (Wright and McGonigal, 1980; Tucker and Govoni, 1981; Kovacs, 1972). Surveys have been performed on near shore shear zones (Wadhams, 1976; Weeks et al., 1971; Tucker et al., 1979; Sayed and Frederking, 1991) and offshore ridge characteristics (Sayed and Frederking, 1989; Hibler et al., 1974; Tucker and Westhall, 1973) providing information on ridge geometry. The measurement of surface ridge geometry has been performed by theodolite surveys, air photo interpretation using stereo-pair analyzers, and laser profilometers (Sayed and Frederking, 1991; Kovacs and Holladay, 1989). Measurement of the lower ridge surface or keel has been measured by submarine surveys, lowered upward looking sonar systems or more recently by remote control underwater vehicles with upward looking sonar (Wadhams and Lowry, 1977; Wadhams, 1981; Melling et al., 1993).

A compilation of fifteen surveyed multiyear ridges (ridges surviving at least one summer melt) revealed a mean aspect ratio of sail height to keel depth of 1:3.19 with a standard deviation of 0.36 (Wright et al., 1978). A more recent review of sail to keel aspect ratios found similar results (Figure 6).

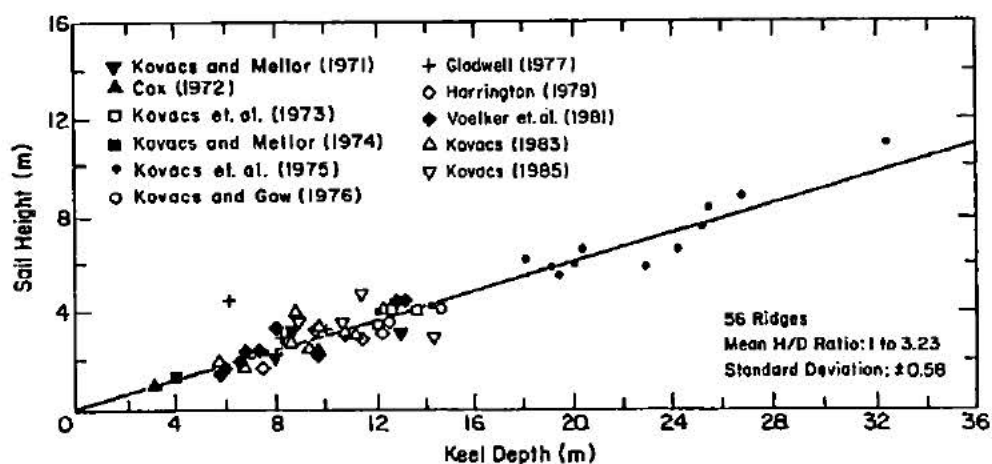


Figure 6: Aspect Ratios of Sail Height to Keel Depth (Kovacs and Holladay, 1990).

It should be noted that not all field studies obtained such consistent values for aspect ratios. Wright and McGonigal (1980) found aspect ratios of sail height to keel depth to be highly variable ranging from 1:4.5 to as high as 1:7 for younger first year ridges.

Field observations of compressive ridges show a strong tendency of triangular geometry for both sail and keel profiles (Kovacs, 1972; Weeks et al., 1971). Newly formed ridges, referred to as first year ridges (having an age of less than one year), had averaged measured slope angles of 28° for sails and 36° for keels. Multiyear ridges were observed to be much more rounded due to summer melt and characteristically had slope angles of 20° and 30° for sails and keels respectively (Figure 7).

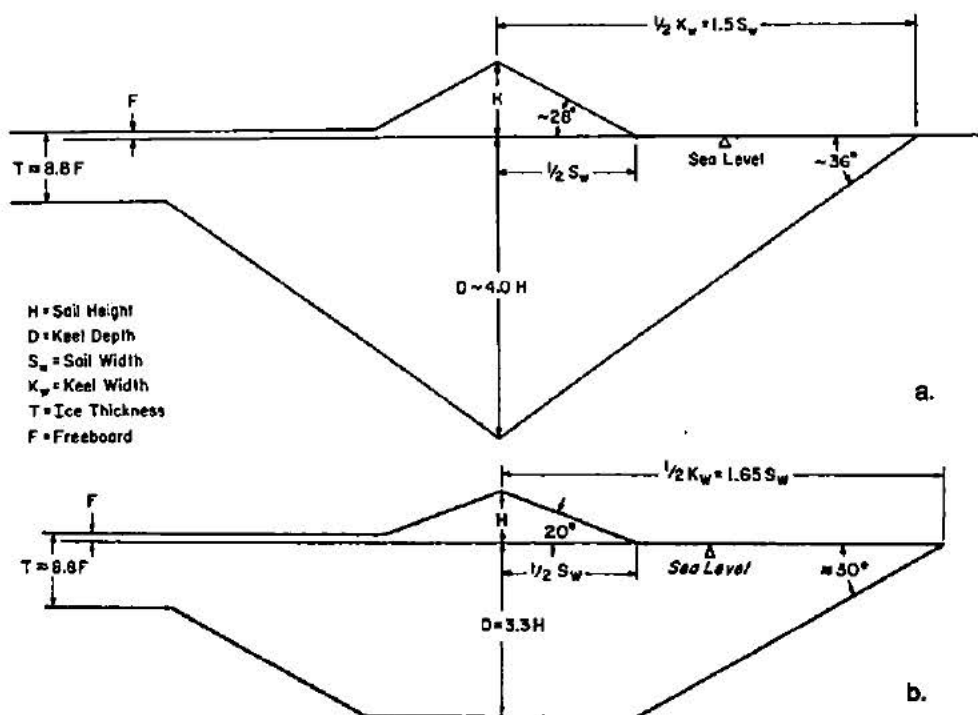


Figure 7: Ridge Geometry. (a) First Year Ridge, (b) Multiyear Ridge.

(Kovacs and Holladay, 1990)

An extensive field study performed by Sayed and Frederking (1989) surveyed a total

of nineteen first year compression ridges. From these sites, 76 cross-sectional profiles were measured and dimensions were taken for 165 representative ice blocks. The average characteristic values of height and width of each ridge were calculated and a regression of the average values gave the following relationship:

$$h = 0.91 + 0.18w$$

where: h and w represent sail height and width respectively. (The correlation coefficient for this relationship was 0.85).

In addition, statistical analyses have been performed to determine spatial distributions of ridges and general longitudinal ridge dimensions (Hibler et al., 1972; Kreider and Thro, 1981; Wadhams and Davy, 1986; Brooks, 1983). These studies revealed information about ridge shape, size, spatial and temporal variability.

Rubble Consolidation

Initially when an ice ridge forms, it consists of a large pile of unconsolidated rubble. Thermal sintering (freeze-bonding) of ice blocks as well as freezing of water filled voids consolidate the surface and to some degree subsurface regions of the ridge. The extent to which this consolidated/unconsolidated interface migrates downwards is poorly understood. Kry (1977) suggested that the solidification process is influenced by initial pore volume, ice temperature, sail height, average air temperature and the surface wind speed. In addition to these attributes, snow, transported from the surface during the ridge building event, as well as crushed ice may initially be incorporated into the water filled voids. These additions result in the reduction of void temperature and salinity thereby accelerating the freezing process (Weeks, 1976).

Intuitively, the thermal regime within a newly formed ridge takes some time to adjust. Relatively cold ice blocks displaced from the air/ice interface are plunged below sea level and held together by gravitational overburden, friction and buoyant forces (Cammaert and Muggeridge, 1988). The considerable weight of the sail,

counterbalanced by the buoyant forces of the keel, result in a compressive interface at the waterline. This zone of compaction tends to consolidate at a much higher rate than rubble below (Kry, 1977).

The porosity of an ice ridge, consisting of varying ice block sizes and containing many voids hydrostatically filled with sea water, is difficult to measure and has, therefore, not been well documented. Some temperature and salinity profiles have been extracted from rubble fields adjacent to offshore structures with only qualitative descriptions of ice drilling resistance to suggest porosity (Sayed, 1988). Extensive coring of a large pressure ridge carried out as part of the Arctic Ice Dynamics Joint Experiment (AIDJEX 1976) obtained subjective data of porosities ranging from 10 to 30% (Rigby and Hanson, 1976). Using this range of porosities, Kry (1977) generated a consolidation curve based on porosity and temperature (Figure 8). This curve is based on the relationship:

$$\gamma = (1-\gamma_i)(C\Delta T/L) \quad (1)$$

Where:

γ_i initial rubble porosity (dimensionless percentage)

C is the specific heat of ice (J/g°C)

L is the latent heat of ice (J/g)

T is mean ice temperature °C.

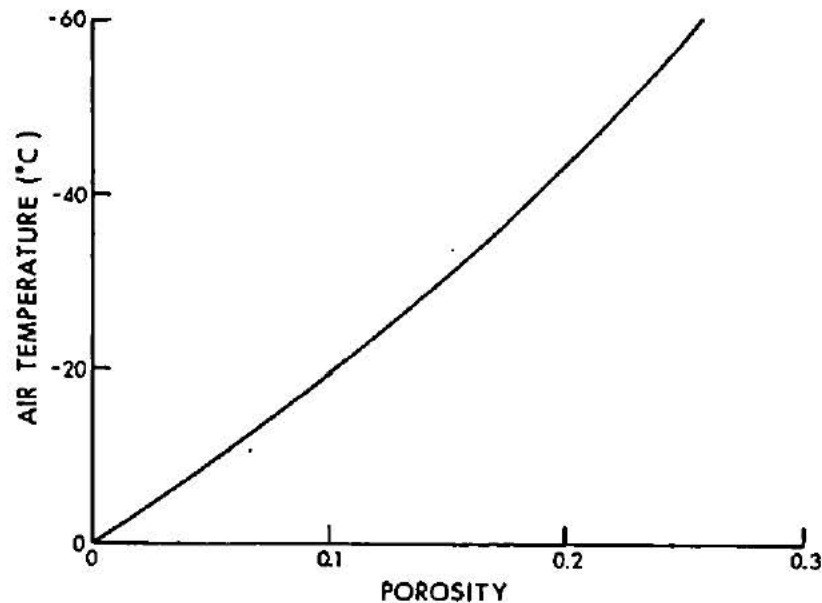


Figure 8: Consolidation Curve of Rubble Ice (Kry, 1977).

Once the initial consolidation at the water level has occurred, the solidification process continues but at a much slower rate. It is thought that the mechanism for the advancing consolidation boundary is the transfer of heat from the keel through the sail to the air (Kry, 1977). The sail, therefore, has a significant role in that the exposed surface area increases the removal of heat from the keel. Strong surface winds increase this rate even further. Laboratory studies carried out on rubble ice indicate that the freezing rate of rubble is as much as twice that of adjacent level ice (Timco and Goodrich, 1988). These tests were performed without the influence of snow. The sail may, however, act as a snow fence creating an insulation effect that would ultimately decrease the heat transfer process. An additional modifier of the heat transfer process is the relatively warm surrounding waters which locally warms the deep exterior portions of the keel (Allyn and Wasilewski, 1979). It has been concluded that complete consolidation is highly unlikely since the thermal sink of the ice fragments is significantly less than the thermal reserve of the underlying sea water connected with water filled voids within the keel (Roth and Marcellus, 1986).

Vaudrey (1983) concluded that within the geographical reaches of the Beaufort Sea, the consolidation layer of first year ridges is limited to between 2.5m to 4m. This generalization is based on sparse data suggesting a need for further research.

3.14 Electrical Conductivity of Snow, Sea Ice and Sea Water

Consolidated and unconsolidated ice within ridges sometimes present fuzzy boundaries of varying conductive properties. The electrical conductivity of ice, snow and sea water influence the electromagnetic fields that are induced by active airborne remote sensing systems.

The electrical conductivity of sea ice is influenced by :

- (1) Salinity
- (2) Temperature
- (3) Ice type
- (4) Structure
- (5) Age.

The most significant of these attributes is salinity. During the formation of sea ice, numerous salts contained within sea water become entrapped within the ice structure. Generally, the forming ice consists only of hexagonal lattices of hydrogen and oxygen atoms. All other constituents of sea water are rejected from the forming lattice by the process known as defusion. The continued downward growth results in a concentration of the rejected salts at the advancing solid-liquid interface. These salts become entrapped between the vertically growing platelets as periodic bridging between adjacent platelets dams salts into small inclusions known as brine cells. These cells contain a relatively high concentration of salts to that of the bulk sea water solution. It is the spatial arrangement of these brine cells that largely controls the conductivity of the ice. Ice formed under rapid growth conditions tends to be more conductive than the more efficiently defused ice structure grown under less extreme conditions.

These brine cells are by no means immobile and are greatly affected by air and ice temperature. During the winter months, temperature gradients within the ice govern the direction and rate of migration of the brine. Typically the air/ice interface is much colder than the ice/water interface creating a vertical thermal gradient. The brine content, in an attempt to maintain its phase equilibrium, migrates vertically in the direction of the higher temperature (Pounder, 1965). To understand this statement it is important to obtain some background about the behaviour of brine entrapped within ice. Generally, the salinity of brine cells is always in phase equilibrium with the surrounding thermal conditions of the ice. That is, the brine solution is always at its freezing point (Kovacs et al. 1987). A simplified expression has been used to describe the relationship that exists between brine, temperature and ice salinity.

$$v_b = 0.001S \left(0.53 - \frac{49.2}{\theta} \right) \quad (2)$$

where: v_b is brine volume (expressed as a percentage--dimensionless)
 θ is temperature ($^{\circ}\text{C}$)
 S is salinity (ppt) (equation from Sanderson, 1988).

It is clear from this relationship that if the temperature of the brine solution increases, the salinity of the brine must decrease. Given that a thermal gradient exists within ice, the mechanism for brine migration can be represented by a vertical cylinder as depicted in Figure 9. The thermal gradient within brine cells establishes a brine concentration gradient in order to maintain phase equilibrium.

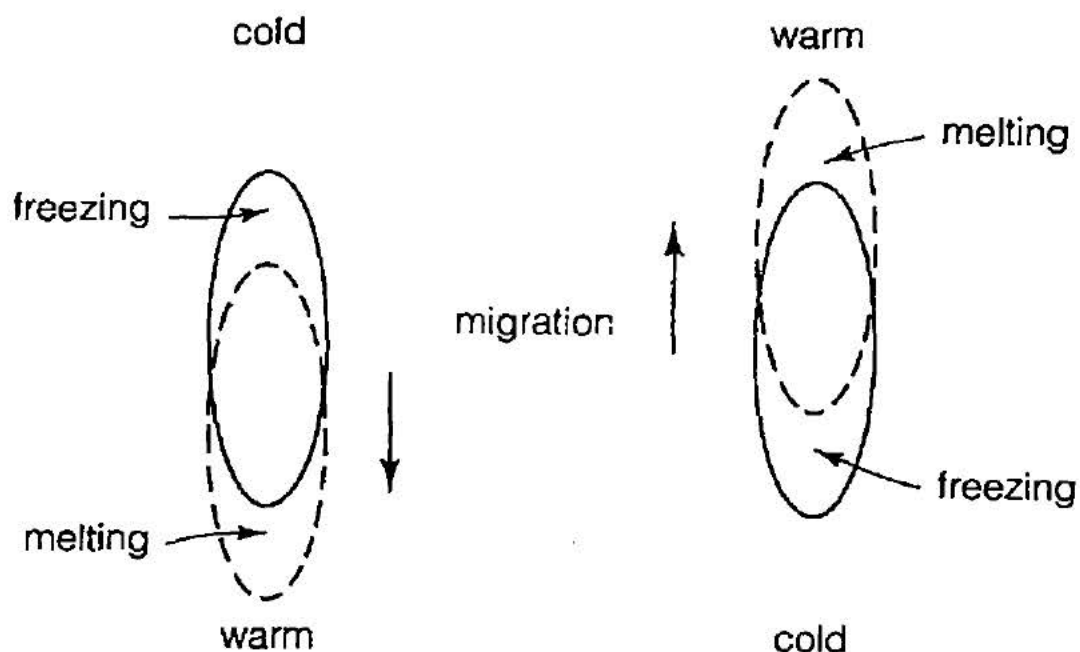


Figure 9: Brine Migration (Sanderson, 1988).

The warmer bottom end of the cell exposes the brine to a slightly higher temperature resulting in a local shift in the phase relationship. In order to maintain equilibrium, the contacting ice is dissolved until the concentration is reduced to the corresponding phase equilibrium. In contrast, the top end of the cylinder is slightly cooler resulting in the freezing of water enriching the concentration of the brine solution. Over time these cells become larger as they travel through progressively warmer ice. They may in the course of migration encounter other brine cells resulting in the formation of interconnecting channels which accelerate brine drainage. Through this process, brine is slowly expelled from the ice thereby reducing the gross salinity of the ice. Typically, this reduction of entrapped brine decreases the salinity of first year ice by approximately 0.5 ppt per month (Nakawo and Sinha, 1981).

This process of vertical migration of brine results in a salinity distribution that

is generally low above the sea surface and relatively high at the base of the ice plate (Morey et al., 1984). A conductivity study performed by McNeill and Hoekstra (1973) reveals similar findings. In their field program, they discovered that first year ice conductivity ranges from 0.016 S/m (Siemens per metre--a measure of conductivity which is equal to the inverse of resistivity --ohms) at the near topside surface to 0.2 S/m at the ice/water interface. In contrast, sea water is at least an order of magnitude higher than the highest value for ice conductivity. Kovacs et al. (1987) determined that the conductivity of sea water at a typical temperature of -1.8 C with salinity of 32 is approximately 2.5 S/m. The conductivity of snow has also been measured. Its range varies between.... As will be seen later, the conductivity contrast between snow, ice and sea water provide valuable conductivity interfaces that can be detected from actively emitted electromagnetic fields.

3.2 Airborne Remote Sensing of Ice Thickness

Numerous spaceborne remote sensing systems are being used to measure sea ice characteristics including ice motion, extent, concentration, and type. Shuchman and Onstott (1990) compiled a table listing specific details on satellite systems designed to collect data on sea ice characteristics (Table 1). A thorough treatment of these and other satellite systems is presented in the recently published book entitled Satellite Remote Sensing of Polar Regions (Massom, 1991). Of all the satellite sensors described, none of these systems are capable of direct ice thickness measurements. The recent launch (July 1991) of the European Remote Sensing Satellite (ERS-1), with its Radar Altimeter (ALT) may, however, be used to indirectly estimate ice thickness distribution. These estimates are based on a derived ice freeboard assuming the ice to be at hydrostatic equilibrium within an assumed sea level geoid. Accepted aspect ratio values of freeboard to ice draft (approximately 1:9) are then used to resolve total ice thickness. The estimated ice thickness is an average thickness over a footprint diameter of 16-20 km (Massom, 1991) (height

Satellite	Sensor	Type	Swath (km)	Resolution	Revisit time/day	Sea ice and ocean parameters measured	Advantage	Disadvantage	Status
Landsat	Multispectral Scanner (MSS)	Passive visible and infrared	186 X 186	30 m	0	Ice edge, ice concentration, floe size distribution, ice motion, chlorophyll concentration, suspended sediment, location of ocean fronts	High-resolution information is easily extracted	Clouds, coverage limited to 81°	Operational
Spot	Multispectral Scanner (MSS)	Passive visible and infrared	60 X 60	10 m	0-2	Ice edge, ice concentration, floe size distribution, ice motion, chlorophyll concentration, suspended sediment, location of ocean fronts	High-resolution information is easily extracted	Clouds, coverage limited to 81°	Operational
DMSP	Optical line Scanner (OLS)	Passive visible and infrared	2900	0.6-3 km	2-12	Meteorology, ice motion, ice edge location, eddy structure, sea surface temperature, ice kinematics	Large swath	Clouds	Operational
DMSP	Special Scanning Microwave Imager (SSM/I)	Passive microwave	750	50-60 km	0-2	Ice type, ice extent, ice concentration, eddy structure, water vapor, and ocean surface winds, sea surface temperature	Penetrates clouds	Resolution, melt and freeze period	Operational
NOAA 9/10	Advanced Very High Resolution Radiometer (AVHRR)	Passive visible and infrared	2500	1-4 km	2-12	See DMSP, OLS	Large swath	Clouds	Operational
GEO-SAT	Radar Altimeter	Active microwave	Nadir profile 7-10	Height 10 cm, spot size 7-10 km	0	Ice edge, ice roughness, gravity wave detection, ice concentration, ocean height topography, geostrophic currents	All weather, minimum data processing	Limited polar coverage, profile only, large spot size	Operational
Japanese MOS-1	Multispectral Electronic Self-Scanning Radiometer (MESSR)	Passive visible and infrared	200	50 m	0	See Landsat, MSS	High-resolution information is easily extracted	Clouds	Operational
Japanese MOS-1	Visible and Thermal Infrared Radiometer (VTIR)	Passive visible and infrared	1500	1-3 km	2-12	See DMSP, OLS	Large swath	Clouds	Operational
Japanese MOS-1	Microwave scanning Radiometer (MSR)	Passive microwave	300	30-40 km	0-1	See DMSP, SSM/I	Penetrates clouds	Resolution, melt and freeze period	Operational
ESA ERS-1	Radar Altimeter	Active microwave	Nadir profile 7-10	Height 10 cm, spot size 7-10 km	0	Ice edge, ice roughness, gravity wave detection, ice concentration, ocean height topography, geostrophic currents	All weather, minimum data processing	Profile only large spot size	Proposed launch late 1990
ESA ERS-1	Synthetic-Aperture Radar (SAR)	Active microwave (C band)	80-100	30 m	0	Ice edge location, eddy and ocean front structure, ice type, floe size distribution, ice kinematics, gravity wave propagation, Internal wave measurements, ice concentration, surface wind speed, detection of leads, mapping of icebergs	All weather, high resolution	Coverage, data processing	Proposed launch late 1990

Table 1: Satellite Systems used to Measure Ice Attributes (Shuchman & Onstott, 1990).

resolution of 10 cm) and is, therefore, general in nature and completely absent of feature definition. This type of data may be useful for large scale ice studies; however, greater resolution is required to provide tactical ice information for icebreaker operations as well as a host of small scale ice issues including force/geometry relationships within pressure ridges.

In order to obtain the necessary details for local ice conditions, airborne platforms have been developed, deployed and evaluated. Two techniques have been employed for this task. These are the impulse radar (Rossiter, 1979; Butt and Gamberg, 1979) and the electromagnetic induction system (Kovacs et al., 1987; Kovacs and Holladay, 1989; Prinsenberg et al., 1992). To date these systems have been field tested over level ice in both the Canadian and American Beaufort Seas. Evaluation of the test programs have been carried out and the results indicate reasonable agreement with ice thickness measurements carried out in the overflight areas (Rossiter and Lalumiere, 1988).

Each of these systems utilize different techniques to obtain thickness information. In the case of the impulse radar, ice thickness is determined by measuring the delay time between the echo reflected off the top surface of the ice and the echo reflected off the bottom surface. Simply put, ice thickness is given by:

$$d = \frac{vt}{2} \quad (3)$$

where: *d* is ice thickness (m)
 t is the time delay (s)
 v is the propagation velocity in ice (ms⁻¹)

and

$$v = \frac{C}{\sqrt{\epsilon}} \quad (4)$$

where: C is the speed of light (ms^{-1})
 ϵ is the effective dielectric constant of ice
 (equations: Butt and Gamberg, 1979).

The dielectric constant of equation 4 is defined as a measure of the response of a material to an applied electric field--dimensionless (Hall and Martinec, 1985).

Impulse radar systems transmit pulses at VHF frequencies that are in the order of 100 MHz. Such frequencies are capable of penetrating cold undeformed ice; however, field testing has revealed certain limitations inherent with this technology. It has been discovered that deformed and/or relatively conductive ice cannot be effectively penetrated by impulse radar. Pressure ridging, rafting and rubble fields are virtually opaque to this type of sensor (Rossiter and Lalumiere, 1988). Since pack ice is generally a composite of level and deformed ice of various ice types, this technique would, therefore, have limited use.

The second and preferred technique (Rossiter and LaLumiere, 1988) is that of the electromagnetic induction sensor. This sensor, which consists of a transmitter and receiver, detects the relatively high conductivity of the underlying sea water. This is achieved by transmitting an electromagnetic field in frequencies ranging from 500-500,000 Hz (Rossiter and Lalumiere, 1988). These frequencies pass through the snow and ice layers virtually unaffected until contact is made with the ice/water interface. At this interface, secondary electromagnetic fields are created and radiate back through the ice and snow to a receiver. Interpretation of the received data yields information about the distance the ice/water interface is from the instrument. A laser altimeter is used to measure the instrument to snow surface and, therefore, the total thickness of the snow and ice layer can be calculated (Kovacs and Holladay, 1989). Both transmitter and receiver are housed within a cylindrical tube called a bird.

These birds are towed beneath helicopters and vary in sizes ranging from over 4 metres to approximately 9 metres. This technique and the interpretation of its data will be expanded upon in the following chapters.

The electromagnetic induction system is considered to be much more versatile than the impulse radar. Figure 10 illustrates a comparison between these two systems. A Synthetic Aperture Radar (SAR) is also included showing its relatively poor capabilities as an ice thickness sensor.

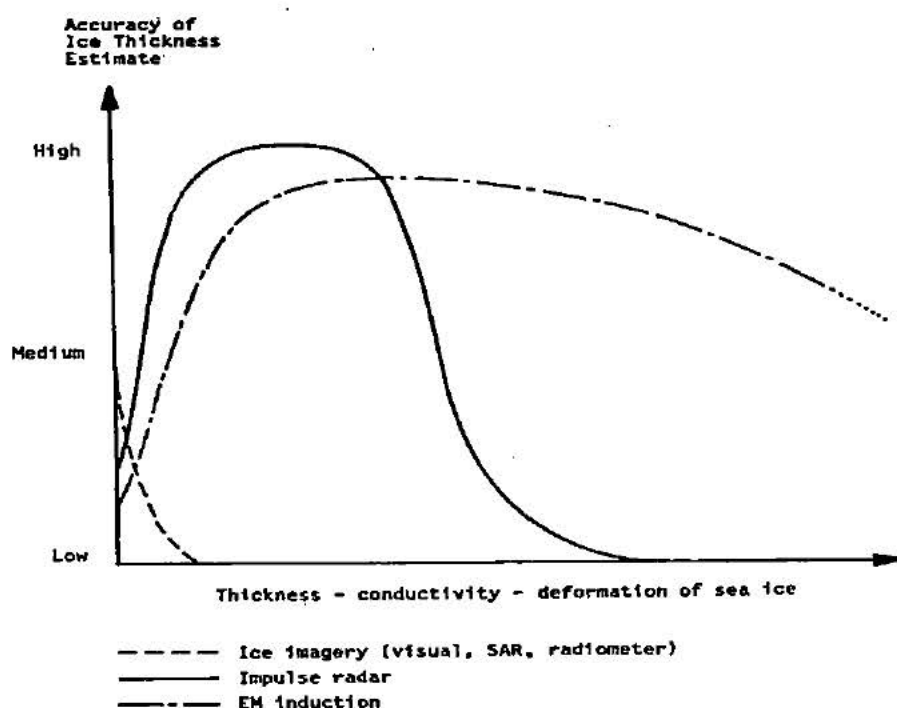


Figure 10: Comparison of Airborne Ice Thickness Measuring Techniques (Rossiter and Lalumiere, 1988).

As can be seen from Figure 10, ice thickness for very thin ice can be effectively estimated using the SAR sensor; however, in thicker more complex ice conditions, the ice penetrating impulse radar and electromagnetic sensors become more effective.

With increased thickness, conductivity and deformation, the ability of the impulse radar to determine ice thickness quickly drops off. It has been recommended that further efforts towards the designing of an ice thickness sensor be based on electromagnetic induction technology which performs well under the greatest range of ice conditions (Rossiter and Lalumiere, 1988).

Since the time of this recommendation, electromagnetic induction systems have proven to be an effective method for determining level ice thickness. Holladay et al. (1990; p. 309) concluded:

A practical technique for the measurement of sea ice thickness from an airborne platform, based on electromagnetic (EM) induction, is now reaching the end of its validation stage.

Further in this paper the issue of ice ridging was addressed as the next phase of development for airborne EM induction systems.

Almost all the quantitative airborne remote sensing work has been done on level ice where ice thickness remains relatively constant. The challenge to measuring ice ridge thickness is the irregularity of ice thicknesses, porosity and salinity over a relatively small area. This not only demands high sampling rates but also sophisticated algorithms to determine ice irregularities within footprint swaths. The early attempts of using EM induction systems over first year ice ridges yielded results that constantly underestimated ice thickness (Kovacs and Holladay, 1989). The literature in this area indicates a need for adjustment and modification to existing systems in order to better detect the complexities of ridged ice.

4.0 Geophysical Electromagnetic Induction

Electromagnetic induction methods were initially developed for the geological exploration industry in the early 1930s. At that time, electromagnetic induction was used to map the conductivity of rock types. During this period of early development, EM ground units and airborne systems were developed and used primarily in Canada and Sweden to locate volcanogenic massive sulphides within the Precambrian Shield. Since that time, many new improvements have been implemented expanding EM technologies to a host of new geophysical applications.

4.1 General EMI Theory

Fundamental to the geophysical applications of electromagnetic induction are James Clerk Maxwell's equations on the behaviour of electric and magnetic fields. Using the building blocks provided by Gauss, Faraday and Ampere, Maxwell predicted the existence of electromagnetic waves that propagate through free space at the speed of light. These electromagnetic waves, verified experimentally by Heinrich Hertz just eight years after Maxwell's death, were and are governed by the following equations which collectively are known as Maxwell's equations. The detail in which Maxwell mathematically describes electromagnetism is far beyond the scope of this paper. Only the basic concepts are presented here.

Gauss' Law:

The total electric flux through any closed surface equals the net charge inside that surface divided by ϵ_0 .

$$\oint \mathbf{E} \cdot d\mathbf{A} = \frac{Q}{\epsilon_0} \quad (5)$$

Where: **E** is the electric field (Newtons/Coulombs)
A is the plane area perpendicular to the electric field (m^2)
Q is the total electric charge (Coulombs)
 ϵ_0 is the permittivity of free space
 (definition: quantity measuring substance's ability to store electrical energy in electric fields ($\text{C}^2/\text{N}\cdot\text{m}^2$)) (C = Coulomb (Amp/s) (equation from Serway, 1990).

Fundamental to Gauss' Law of electric fields is the concept of electric charge distribution. Michael Faraday in his work determined that electric fields originate on positive charges and terminate on negative charges (Figure 11).

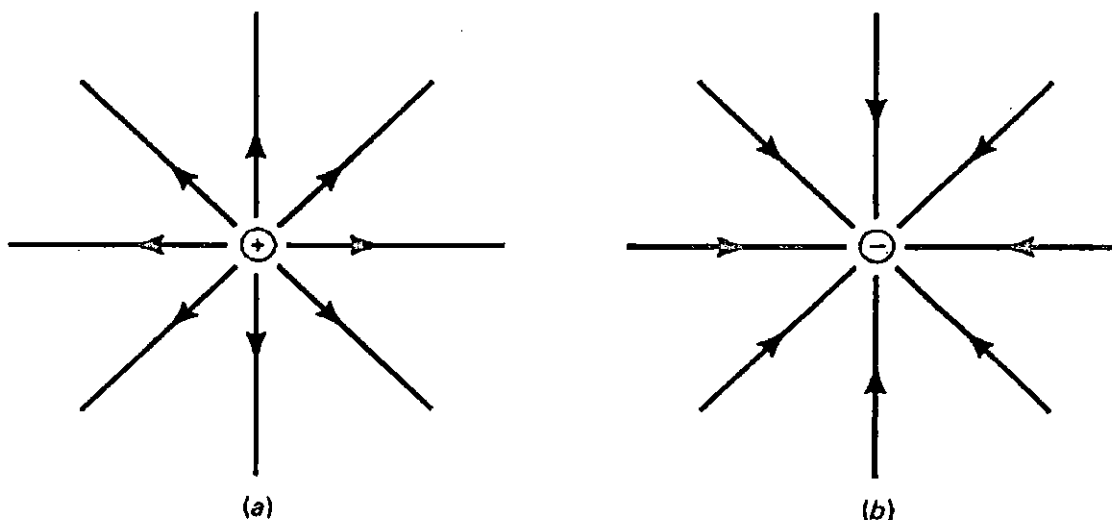


Figure 11: Electric Field Lines (Blatt, 1983).

Gauss' Law of Magnetism:

The net magnetic flux through any closed surface is always zero. That is, the number of magnetic field lines that enter a closed volume must equal the number that leave that volume.

$$\oint \mathbf{B} \cdot d\mathbf{A} = 0 \quad (6)$$

Where: \mathbf{B} is the magnetic flux density (webers/m²)
(weber=volt/s)(equation from Serway, 1990)

This law implies that magnetic field lines are continuous having no beginning or ending sites and are illustrated in Figure 12.

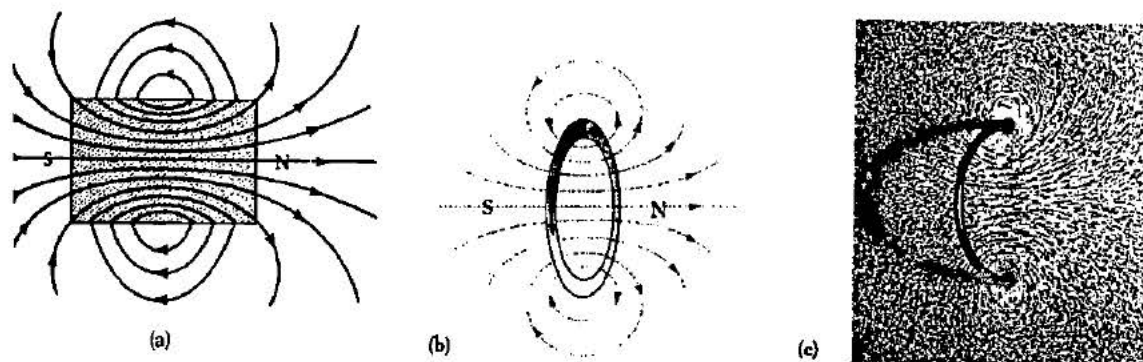


Figure 12: Magnetic Field Lines (Serway, 1990).

Faraday's Law:

The line integral of the electric field around any closed path equals the rate of change of the magnetic flux through any surface area bounded by that path.

$$\oint \mathbf{E} \cdot d\mathbf{S} = -\frac{d\Phi_m}{dt} \quad (7)$$

Where: S is the displacement in metres
 Φ_m is the magnetic flux in webers
 t is time in seconds (equation from Serway, 1990)

The significance of this law is that an electric field can be induced by an electromotive force created by a changing magnetic flux as illustrated in Figure 13.

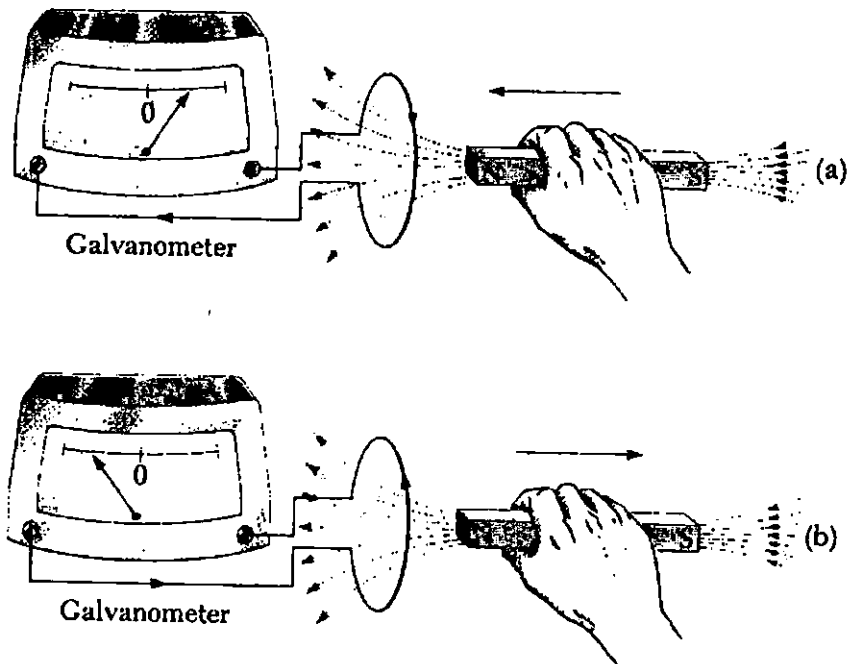


Figure 13: Faraday's Law of Induction (Serway, 1990).

Ampere-Maxwell's Law:

The line integral of the magnetic field around any closed path is determined by the sum of the net conduction current through that path and the rate of change of electric flux through any surface bounded by that path.

$$\oint \mathbf{B} \cdot d\mathbf{S} = \mu_0 I + \epsilon_0 \mu_0 \frac{d\Phi_e}{dt} \quad (8)$$

Where:

- μ_0 is the permeability of free space (weber/A·m)
- I is current in amperes (A in this equation = amperes)
- Φ_e is electric flux (N·m²/C) (equation from Serway, 1990)

The Ampere-Maxwell's law describes how a magnetic field can be produced by changing an electric field or by conduction currents.

This law, together with Faraday's law of electromagnetic induction, show the inter-dependence of electric and magnetic fields. Just as a time-varying magnetic field can produce an electric field (Faraday's Law-Figure 13) so too can a time-varying electric field produce a magnetic field as can be seen in the case of a solenoid (Figure 14).

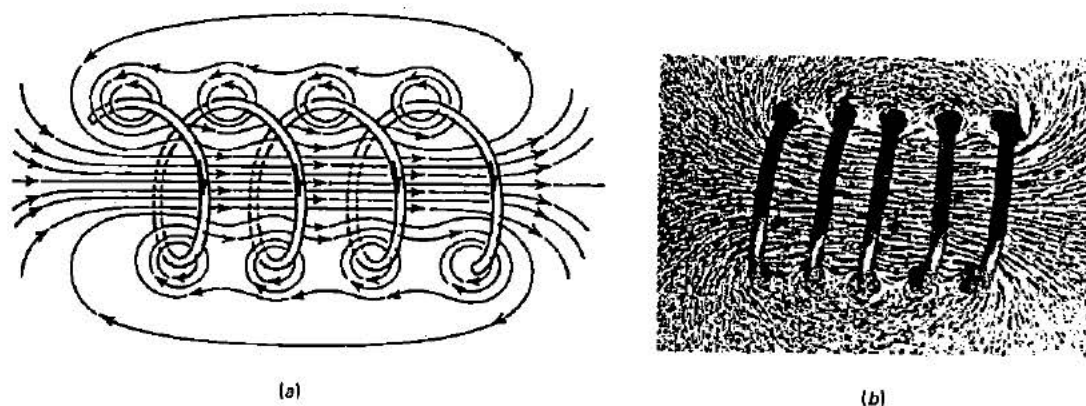


Figure 14: Magnetic fields generated from electric current (Blatt,1983).

If this solenoid were to be energized by an alternating current, then the current would initially move through the coil in one direction producing corresponding lines of magnetic fields. As the current peaks and alternates its direction, the magnetic fields would also change direction and its magnitude would be proportional to the electric current. Given the nature of magnetic and electric fields, it becomes apparent that electrical and magnetic forces act at right angles to each other.

Maxwell, using eloquent mathematics, took equations 7 and 8 to derive equations for the electric (Equation 9) and magnetic (Equation 10) components of electromagnetic waves in free space. These equations (Serway, 1990) are expressed as follows:

$$\frac{\partial^2 E}{\partial X^2} = \mu_0 \epsilon_0 \frac{\partial^2 E}{\partial t^2} \quad (9)$$

$$\frac{\partial^2 B}{\partial X^2} = \mu_0 \epsilon_0 \frac{\partial^2 B}{\partial t^2} \quad (10)$$

During his development of these equations he discovered mathematically that these waves travel at 2.99792×10^8 m/s which is precisely the calculated speed of light. Maxwell, therefore, deduced that light is an electromagnetic wave - a concept that is generally accepted in modern physics.

Using Maxwell's equations and assuming that electromagnetic waves travel in one direction, a time-varying sinusoidal voltage used to energize a solenoid would create electromagnetic waves that would propagate outwards through free space. It is these waves (Figure 15), containing both electrical and magnetic forces that are used in geophysical research to induce both magnetic and electrical responses from conductive bodies.

Figure 15 illustrates a ray diagram slicing through the electromagnetic fields radiating out from an energized transducer coil. E and H vectors, representing the electrical and magnetic components are indicated by the labelled arrows. The two vectors are at right angles and are in the same phase. The second part of the figure, part b, is a diagram representing the intensity of both the electrical and magnetic fields moving along the ray path. The electric fields are represented by the vertical lines (arrows show the field direction) and the corresponding magnetic fields are represented by a series of dots and xs; dots coming out of the page and xs going into the page.

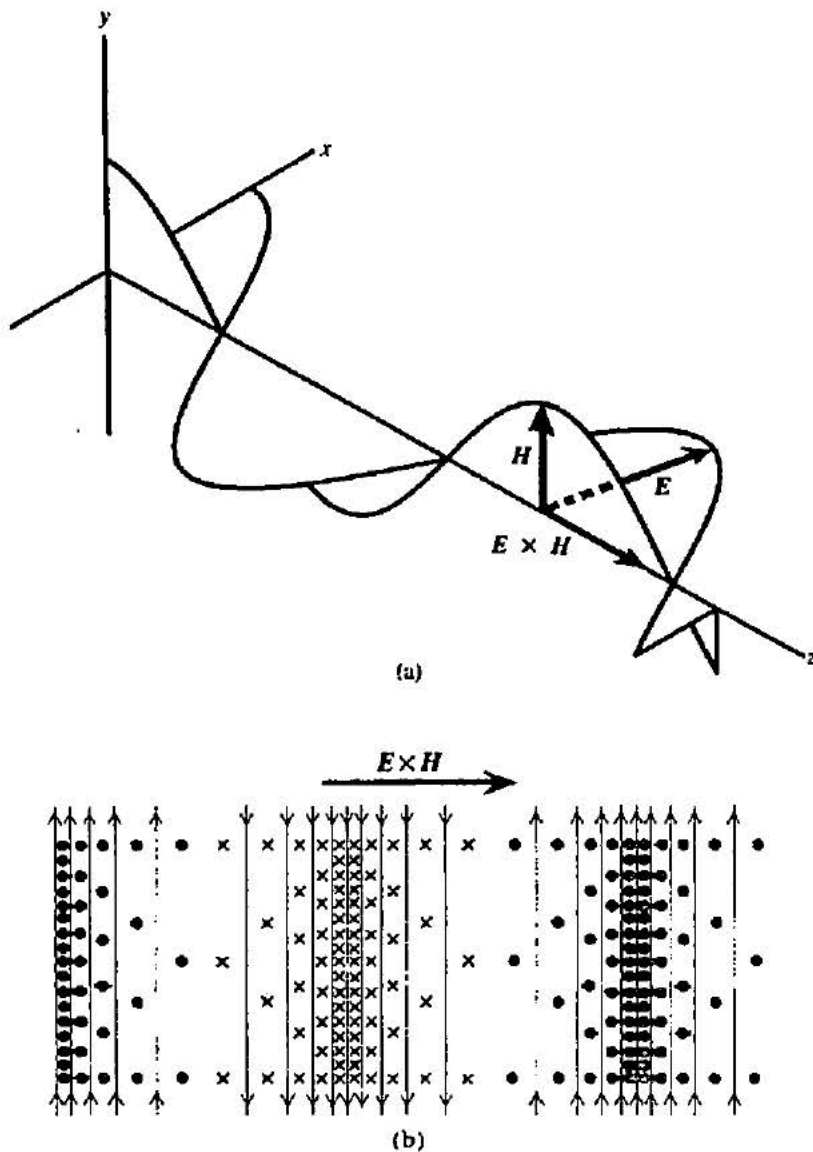


Figure 15: Electromagnetic Ray Diagram. (a) In-phase E (electrical) and H (magnetic) components of EM Wave. (b) Field Intensity: electrical fields (vertical lines), magnetic fields (dots out of the page, Xs into the page) (Lorrain et al., 1989).

The basic principles used in geophysical electromagnetic induction are illustrated in Figure 16.

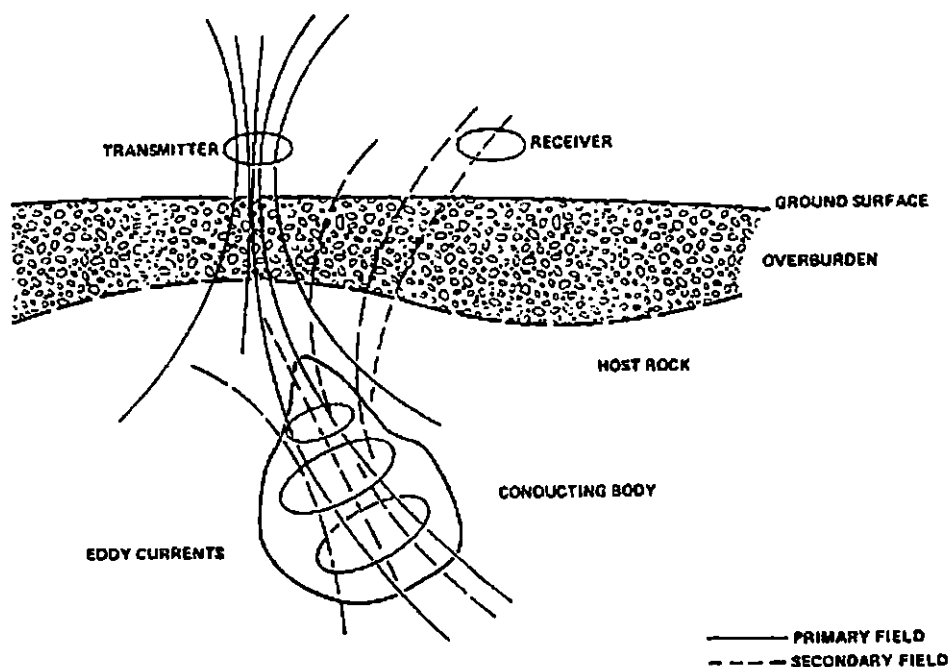


Figure 16: Geophysical Electromagnetic Induction (Best and Boniwell, 1989).

The majority of EMI systems consist of one or more transmitter/receiver coil pairs. Typically, transmitter coils are electrically energized with alternating electric currents. These currents produce dipole alternating magnetic induction fields which interact with adjacent conductive bodies. As the magnetic induction field moves through the conductive body, eddy currents are induced. These eddy currents in turn produce secondary magnetic fields which are detected by the receiver coil. The electrical current induced in the receiver is measured and interpreted in order to deduce attributes of the conductive body.

Figure 17 illustrates the relationships between the primary and secondary fields utilized by electromagnetic induction techniques (Parasnis, 1975). The interaction between the primary alternating magnetic field and the conductive body results in an induced electromotive force that sets up a voltage of the same frequency as the primary field. This induced voltage, however, lags behind the primary field by a quarter of a period ($\pi/2$ or 90°)(Figure 17 (2)). This lag is true of any sinusoidal applied voltage inducing current within a conductive body (Serway, 1986). Since the conductor is not perfect, the voltage experiences a resistance. Self inductance also occurs; that is, as the current within the conductive body changes in response to the applied external voltage, the current within the conductive body generates its own magnetic flux. This flux in turn induces an electromotive force that opposes the change of the external current resulting in a gradual (not instant) increase in the conductive body's current. This creates an additional lag behind the primary field (Figure 17 (3)). The addition of (1) and (3) of Figure 17 yield the resultant field that would be detected by an EM receiver (Figure 17 (4)). The phase lag between the primary field and the secondary field is an indicator of conductivity. A good conductor has a phase lag of a half period and a poor conductor has a phase lag of a quarter period (Parasnis, 1975).

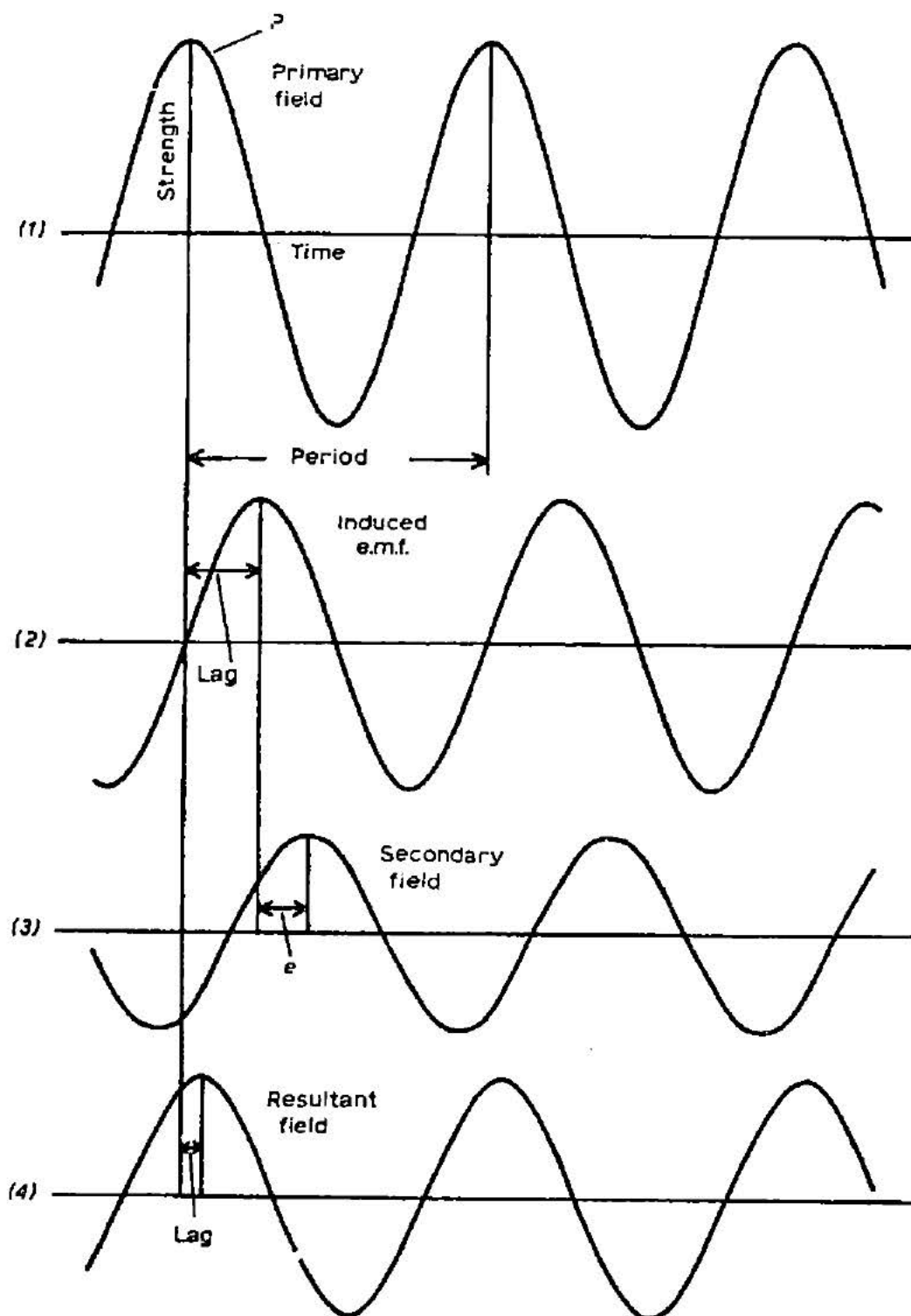


Figure 17: Primary and Secondary Phase Lag Relationships (Parasnis, 1975).

To further clarify this phase lag, consider the vector diagram illustrated in Figure 18.

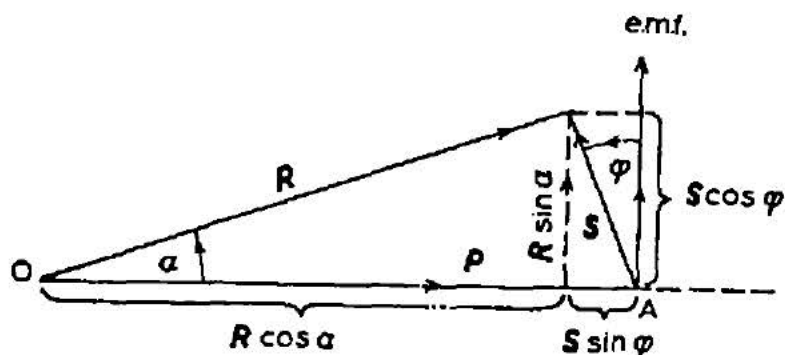


Figure 18: Vector Diagram of EM Fields (Parasnis, 1975).

Let the period defined in Figure 17 represent an angle of 360° . Let P (line segment OA of Figure 18) represent the amplitude of the primary field. For the purpose of this example, set the convention that a vector making an anticlockwise angle with respect to the sense of P is understood to be lagging behind P . As the primary field encounters a conductive body, an induced electromagnetic force (e.m.f.) is experienced in that body which resists change and, therefore, lags behind the primary field by 90° ($1/4$ period). This e.m.f. is represented on the diagram as a vector radiating outward along the y axis from point A . The e.m.f. induces a secondary field S which lags even further behind differing from the e.m.f. lag by an additional fraction of a period. The length of S represents the amplitude of the secondary field. Finally, the resultant field R is the vector sum of both the primary and secondary fields. As above, the length of the line segment R indicates the amplitude of the resultant field.

The extent to which the secondary field lags behind the e.m.f. can be used to determine whether the conductive body is a good or poor conductor. If the lag angle is great (i.e. almost 90°), then the conductive body is considered to be a good conductor. If, however, the lag angle is small (i.e. almost 0°), then the conductive body is considered to be a poor conductor.

The concept of in-phase (real) and quadrature (imaginary) can also be gleaned from this vector diagram. By projecting \mathbf{R} onto the x-axis which in this case is the primary field line segment, the in-phase component of the EM field can be mapped out. Likewise, if \mathbf{R} is projected onto the y-axis which is 90° out of phase from the primary field, then this component of the EM field is called the out-of-phase, imaginary or quadrature EM response.

Transmitter/receiver coil orientation, size, separation and height over conductive bodies all play an important role in the electromagnetic fields generated and detected. Many coil configurations have been designed, some more successful than others. The geometries of coil orientation typically used are:

- (1) Coplanar
- (2) Co-axial
- (3) Null coupled coils.

These orientations are illustrated in Figure 19. The selection of coil orientation largely depends on the type of feature being prospected. For instance, the coplanar coil orientation has significantly different foot print attributes than a co-axial coil pair. Figure 20 illustrates surficial electric currents of both co-axial and coplanar dipole transmitters flown over seawater at a height of 30 metres. The current strength at any point on the seawater surface is proportional in magnitude and orthogonal to the horizontal magnetic field emitted from the transmitter (Liu and Becker, 1990). The extent of the footprint of these two systems is very different. Liu and Becker (1990) defined an airborne EM system footprint as being a square surface on the top of a conductive body directly below the transmitter coil. They defined the boundaries of the footprint as containing the area over which the primary magnetic field induced currents which account for 90% of the observed secondary magnetic field.

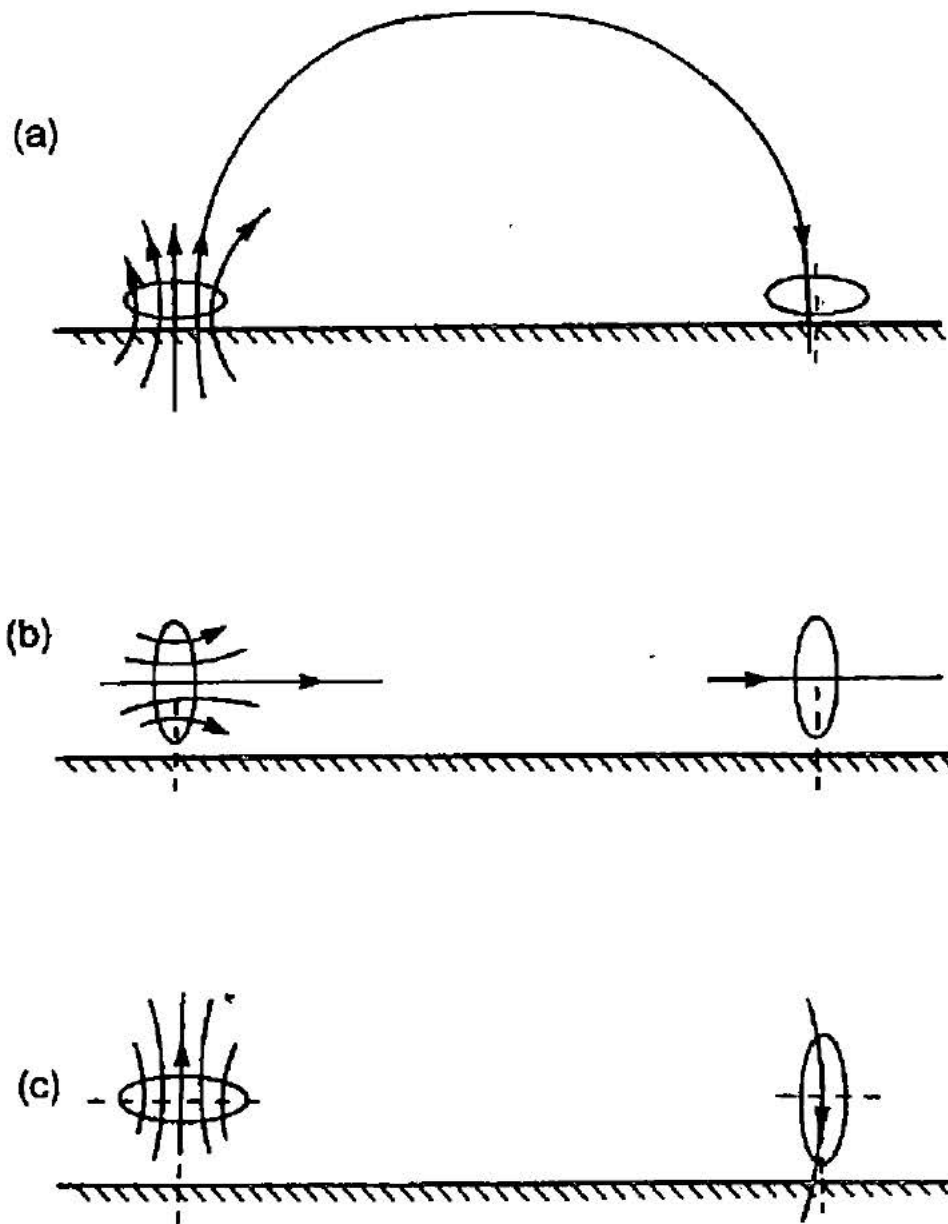
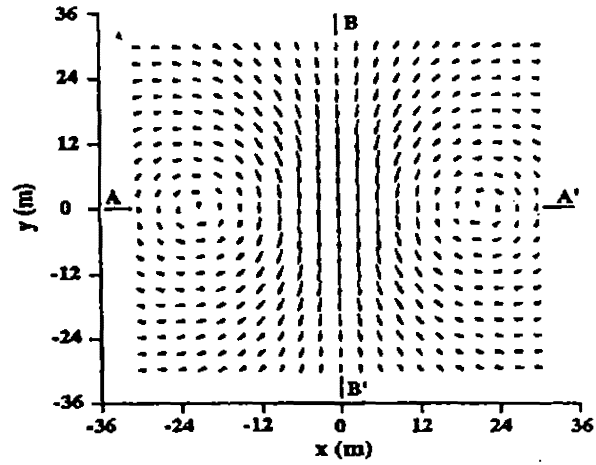
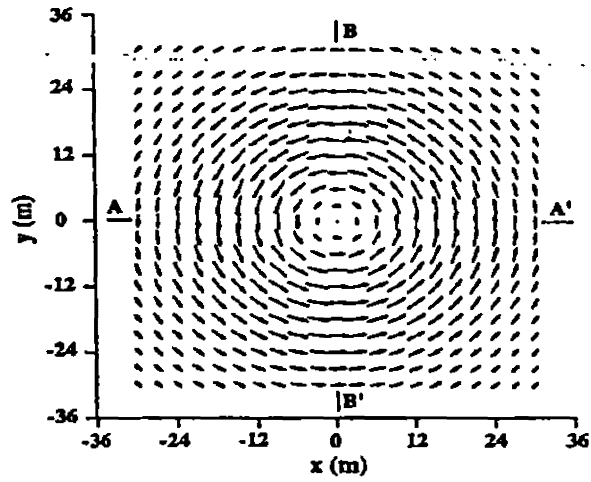


Figure 19: Coil Configurations. (a)Co-planar, (b)Co-axial, (c)Null Coupled coils.
(Milsom, 1989)



(a) Horizontal axis dipole transmitter - Co-axial loops



(b) Vertical axis dipole transmitter - Co-planar loops

Figure 20: Surficial Electric Currents of EM Footprint (Liu and Becker, 1990).

Figure 21 plots the contribution percentage of observed secondary magnetic field against the normalized square size. Note the dotted lines intersect the coplanar and co-axial curves at the respective footprints' sizes.

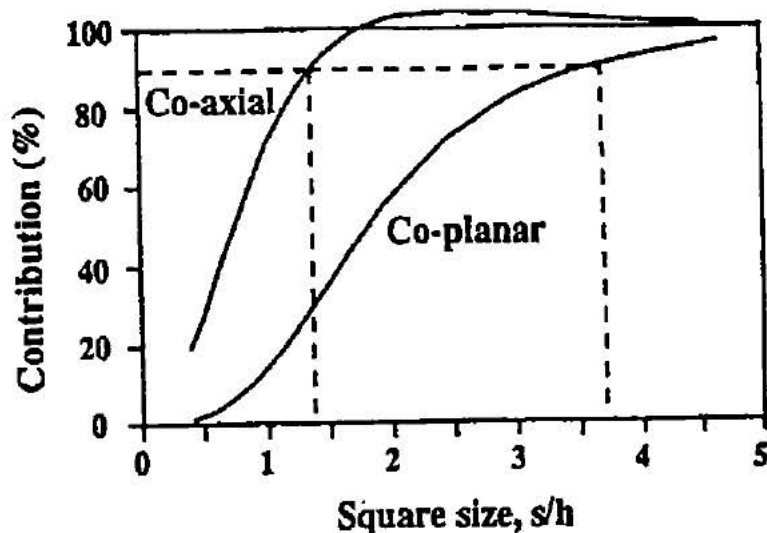


Figure 21: Co-axial and Coplanar Footprint Areas (Liu and Becker, 1990).

From Figure 21, the footprint for a co-axial coil is 1.35 times the coil height above the conductor. The coplanar in comparison has a much larger current distributions resulting in a footprint size of 3.73 times the coil height above the conductor. In the case where formations have horizontal orientations, the use of a coplanar coil configuration would be of greater value than the co-axial. Similarly, when trying to locate formations with vertical orientations such as dykes, the co-axial coil configuration would be most useful.

As the primary magnetic field begins to penetrate the conductive medium, eddy currents are generated. These eddy currents dissipate energy, resulting in the attenuation of the primary electromagnetic field. The effective depth of penetration is dependent upon the frequency of the electromagnetic field and the conductivity of the medium in which the field travels. The term skin depth is used to define the depth at

which the initial amplitude of the electromagnetic field attenuates to a value of $1/e$ (Best and Boniwell, 1989). It is expressed as:

$$\delta(m) = 503(\rho/f)^{\frac{1}{2}} \quad (11)$$

Where δ is skin depth (m)
 ρ is resistance of medium (ohms m)
 f is frequency of electromagnetic field (hz)

Figure 22 illustrates skin depth versus frequency.

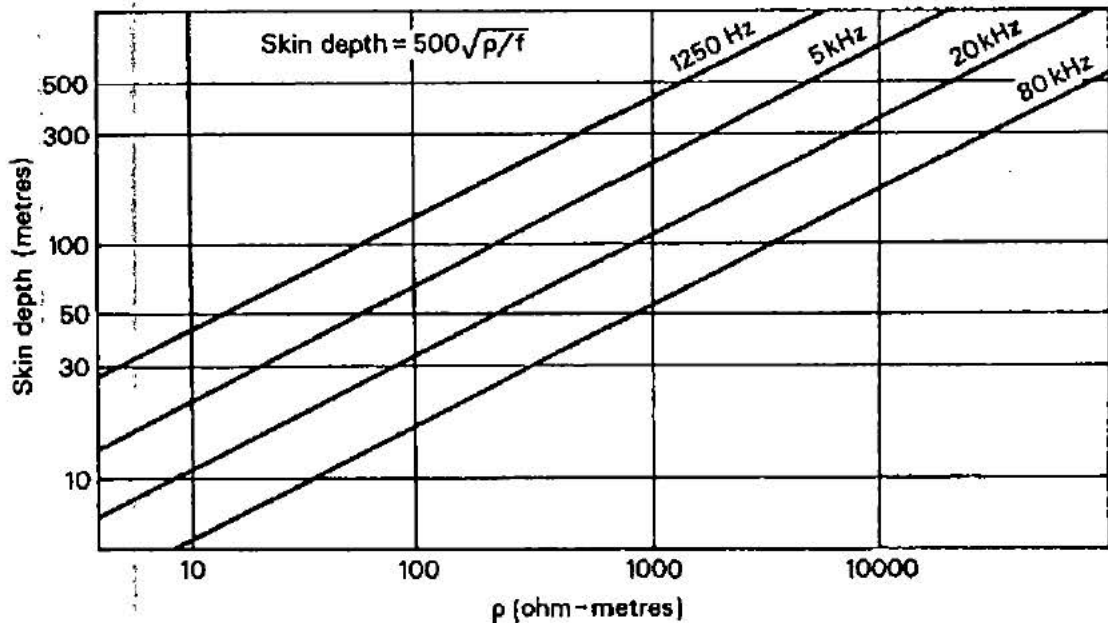


Figure 22: Skin Depth Penetration of EM Waves (Best and Boniwell, 1989).

Note that with an increased signal frequency, the skin depth decreases due to increased energy attenuation.

5.0 Project Instrumentation

5.1 Airborne Survey Instrumentation

The overall approach to the design of an airborne system capable of resolving ridge geometry was to select instrumentation that could accurately detect the air/snow, snow/ice and ice/water interfaces. The state of the art system used in this field study was the next step in a line of helicopter towed instrumented birds that have been used over ice (Figure 23).

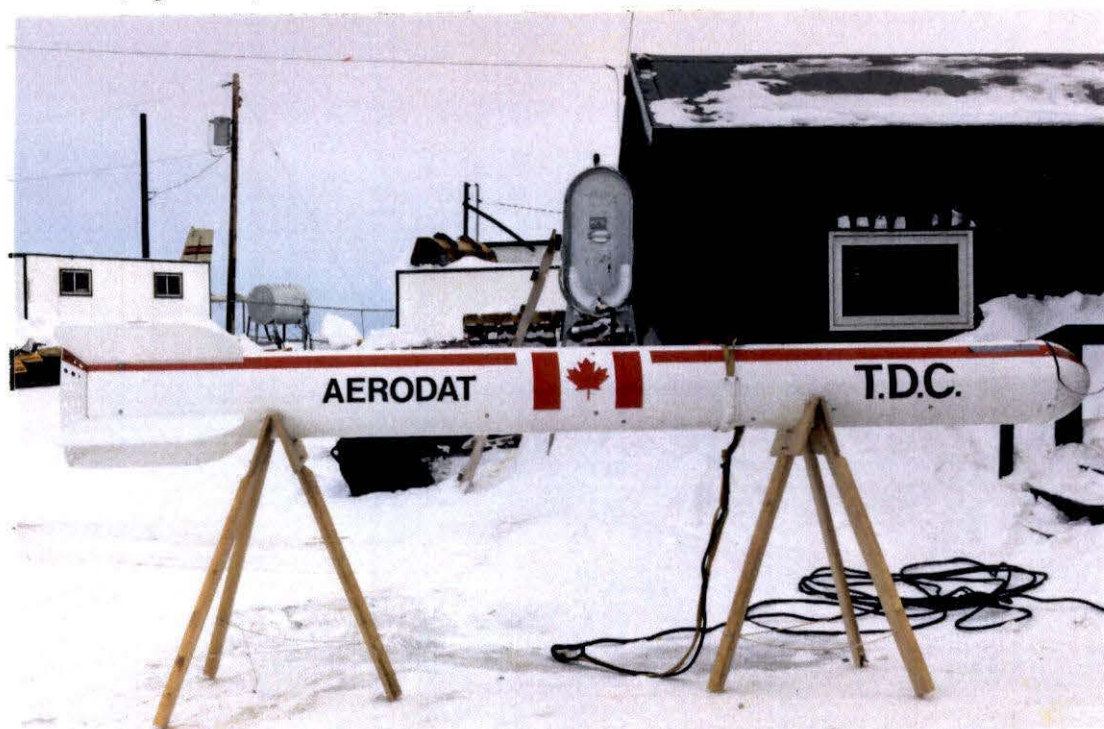


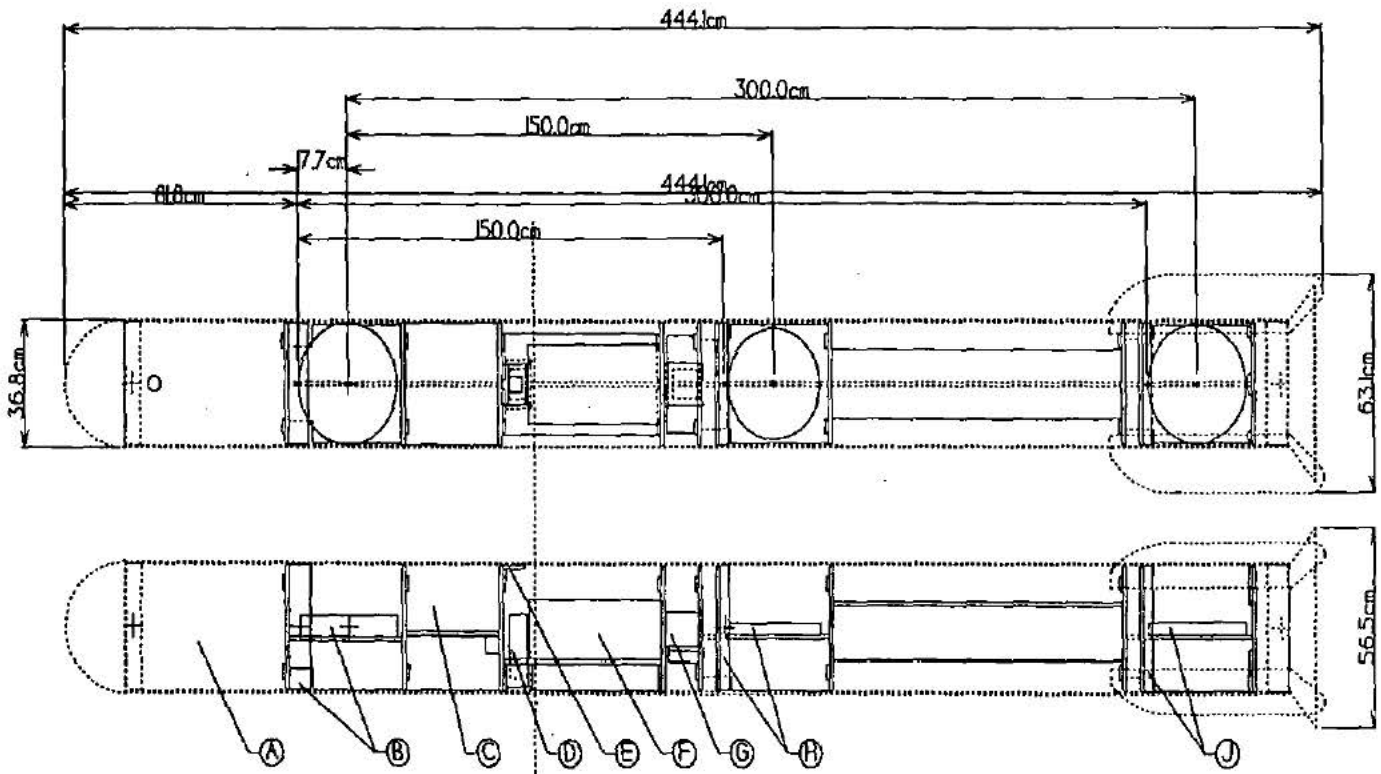
Figure 23: Photograph of Airborne Remote Sensing System.

Six issues were used as guideline in the design philosophy of this new airborne system (Holladay et al.,1992). These were:

- (1) The system must be able to be operated by non-specialist personnel;
- (2) Real-time ice thickness information should be available for most types of sea ice;
- (3) The system should be self-calibrating;

- (4) The system should be modular for ease of trouble shooting, maintenance, installation and upgrading;
- (5) The system should be easily installed ("bolt-on, bolt-off") in a variety of small helicopters operating from an icebreaker or other ship; and
- (6) The system should be robust in design and based on proven technology wherever possible.

Unlike previous surveys, this bird had a number of improvements and additions designed specifically to detect the irregular geometry of ice ridges. This new design incorporated a laser altimeter to measure bird to snow distance, an impulse radar to measure snow thickness and an electromagnetic (EM) induction sounding system to measure ice thickness. Although these systems have been used before, as discussed earlier, they have never been packaged together. Figure 24 illustrates the physical characteristics of the airborne system.



- A: Radar Unit Location
- B: Transmitter Coils
- C: Transmitter Electronics
- D: Laser Rangefinder
- E: Pop-Up Connector Bracket
- F: Receiver Electronics Box
- G: Preamp Box
- H: Bucking Coils
- J: Receiver Coils

C of G

Figure 24: Physical Dimensions of Airborne Remote Sensing Bird.
(Holladay et al., 1992)

Frequencies for the impulse radar and the EM system were selected to optimize their ability to detect boundary interfaces. Both of these instruments have significantly different frequency signals and, therefore, different attenuation rates through snow and ice. All three of these instruments were housed within a rigid 4.4 m Kevlar bird and towed below a Bell 206 helicopter. Data acquisition for the remote sensing system was controlled by a computer onboard the helicopter. During flight, each instrument was designed to measure one of the three interfaces as illustrated in Figure 25.

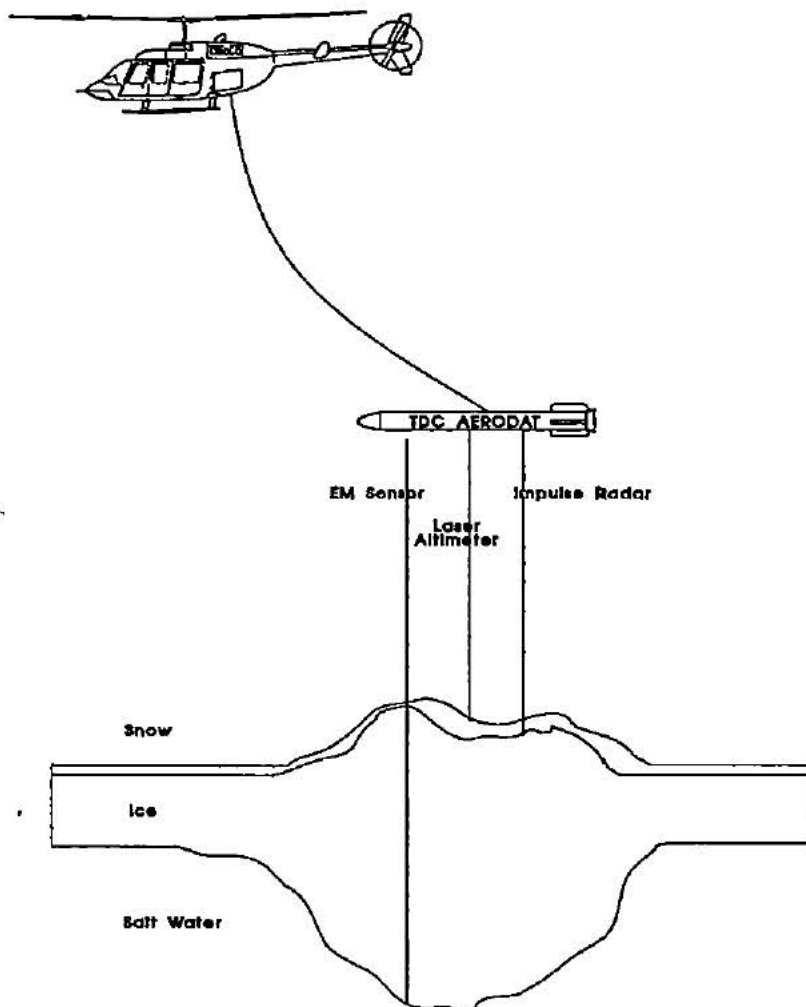


Figure 25: Remote Sensing System illustrating the Key Conductive Interfaces.

5.11 Laser Altimeter

An Optech Model G150 laser altimeter, which is essentially a laser range finder, targeted the air/snow interface. It was installed within the bird at the bottom centre and was directed downwards perpendicular to the plane of the bird. This instrument is capable of making 40 bird to surface measurements per second with a listed manufacturer's accuracy of approximately ± 5 cm (within the operational range of 10-40 metres). This was verified by AERODAT during laboratory calibrations. The sampling rate utilized for this test series was 10 Hz.

5.12 Impulse Radar

The impulse radar system supplied by Canpolar Limited was developed by Geophysical Survey Systems Inc. (GSSI), and includes an SIR System 7 timing control unit and a 3102DP 500 MHz transducer. The transducer was mounted at the aft of the bird. The system's high frequency pulse, transmitting at pulse durations of 3 ns, attenuates rapidly in sea ice. The design philosophy was that the pulse would travel relatively unimpeded through the top layer of snow and reflect off the snow/ice interface. By subtracting laser data of the air/snow interface from the impulse radar data of the snow/ice interface, an approximate snow thickness could be calculated for any given footprint radius. This is the first application of an airborne impulse radar for snow thickness measurements. The scan rate selected for this instrument was 12 Hz and the analog output was recorded on the HQ audio track of the flight path imagery videotape recorder during profiling operations at the ridge site. The illuminated footprint of the impulse radar is approximately equal to the flying height of the bird (Rossiter and Lalumiere, 1988).

5.13 Airborne EMI

The Aerodat Limited electromagnetic induction sounding system used for this project was designed for the Transport Development Centre of Transport Canada. This

survey was the first Arctic field test of the system. The principal components used in this system were two pairs of transmitter and receiver coils. The transmitter coils were mounted in the forward section of the bird and the receiver coils at the extreme aft. The transmitted electromagnetic fields were emitted from the forward coils producing strong primary fields which penetrated through the ice inducing eddy currents in the electrically conductive ice and water masses. These eddy currents generated secondary magnetic fields which were detected by the receiver coils (Kovacs and Holladay, 1990; Lintz and Simonett, 1976). The system could transmit at a frequency of 2.5 or 102 kHz. The two transmitter/receiver coil pairs had different coil orientations. The 2.5 kHz transmitter was in a coaxial orientation, whereas the higher frequency 102 kHz transmitted from a coplanar orientation. Secondary fields detected by the receiver coils were largely influenced by the electrical properties of ice and sea water. These properties for snow, ice and sea water differ with the greatest differential conductivity contrast being at the sea water/ice interface (Kovacs et al, 1987). As described earlier, sea water, due to its relatively high salt content, is several orders of magnitude more conductive than ice. The EM system was, therefore, designed to measure the distance between the sensor and this high contrast ice/water interface to a vertical resolution of about 10 cm.

Pitch and roll sensors were installed within the bird in order to correct for changes in the bird attitude. A Global Positioning System (GPS) was used to record the flight path during the airborne surveys. In addition, a downward looking video camera with on screen annotated fiducial marks was used to visually track the flight path. Both the GPS and the video recordings would aid in tying down the airborne survey with the ground truth data.

Table 2 summarizes the targeted specifications of the airborne remote sensing system as required by Canadian Coast Guard personnel (Holladay et al., 1992).

Table 2: Airborne Remote Sensing Target and Performance Specifications
(Holladay et al., 1992)

Parameter	Target Specification	Performance Obtained
Ice types	All level sea ice, most ridges	On target
Ice thickness range	.2 to 15 m	On target
Ice thickness accuracy	Greater of $\pm 5\%$ or 0.2 m	Greater of $\pm 5\%$ or 0.1 m
Minimum resolvable ice thickness change	0.1 m	0.05 m
Ice regime range	Warm F.Y., cold F.Y., M.Y.	On target (subject to test)
Ice regime accuracy	3 categories above	On target
Snow thickness range	0.3 - 5 m (dry snow)	New specification
Snow thickness accuracy	$\pm 10\%$ (dry snow)	New specification
Minimum resolvable snow thickness change	.05 m (dry snow)	New specification
Horizontal footprint	Approximately bird altitude	On target
Horizontal sampling rate	10 - 20 samples/second	20 samples/sec max.
Aircraft type	MBB BO105 (or larger)	Bell 206L, BO105 or larger
Flying conditions	< 40 knots wind speed	On target
Flying altitude (helicopter)	40 - 70 m	On target
Bird altitude	Helicopter altitude less 30 m	On target
Ice imagery	Downward-looking video	Downward-looking video with ice info, time added

5.2 Ground Truth Instrumentation

5.21 Sail Instrumentation

The sail geometry ground truthing instrumentation consisted of a WILD T2 theodolite, a WILD Distomat 120 Electronic Distance Measuring device (EDM) with prism reflectors and a WILD RC-10 air photo camera which was flown over the area to obtain good quality stereo pairs of the ridge site.

5.22 Keel Instrumentation

Keel geometry surveys required the use of a Tethered Arctic Reconnaissance Submersible (TARS)(Figure 26).



Figure 26: Photograph of TARS showing the Umbilical Cable.

This tethered underwater work vehicle could be manoeuvred under the ice keel from a sheltered control console. Commands from the console to the TARS could be down traffic telemetried through an umbilical cable. The maximum travel of the TARS from its entry hole was approximately 150 meters. Movement of the TARS was governed by a single joy-stick that activated four fully integrated .5 horsepower universal thrusters. Two of the four thrusters were mounted at the stern and were responsible for forward/reverse propulsion, the third thruster was located at the centre of the unit and was dedicated to vertical ascent/decent, and the forth thruster was

mounted near the bow and governs lateral yaw mobility. Both the TARS and the umbilical cable were ballasted to be neutrally buoyant thereby eliminating any need to compensate for buoyant forces during the course of the survey.

Two remote control VHS video cameras were mounted to the TARS to aid in obstacle avoidance as well as record information about ice block geometry and orientation. The forward camera had the ability to pan, tilt, and focus in the forward direction and was installed primarily to avoid collisions with irregular ice block features. It could also serve to guide the TARS to a sited target of known bearing. The second camera was mounted on top of the TARS in an upward looking attitude and was used for observing the underside features of the ice (Riedel, 1990).

The TARS, manufactured by International Submarine Engineering Limited of Vancouver, B.C., utilized the following instrumentation:

- (1) Acoustic Tracking System (ATS)
- (2) Mesotech Sonar
- (3) TARS pressure transducer.

The ATS was used to accurately track the position of the TARS as it moved under the ice. The system was designed by Nautronix and has been used extensively for numerous offshore applications such as underwater vehicle tracking, drill rig positioning and mine neutralisation tasks for the military. The specific model used for the TARS application was the Acoustic Position Indicator, model S04 (API-S04). This system is composed of the following components:

- (1) Master control unit
- (2) Responder interface unit
- (3) Hydrophone
- (4) Mini beacon.

Trigger commands are issued from the master control unit and relayed to the responder interface unit. This unit sends coded interrogation signals to the TARS mini beacon via the umbilical cable. The mini beacon responds with an acoustic train of

eight individual chirps each of which is a linear frequency sweep in the 15 to 18 kHz bands. This response pattern travels through the water and is received by a hydrophone located at the TARS entry hole. Contained within the hydrophone are six equi-spaced receiving transducers. As the eight chirps move across the hydrophone, phase differences and time intervals are measured which give accurate direction and range of the TARS. The resultant output from this system is in the form of X,Y coordinates. The Z component is also given as the mini beacon on the TARS houses a pressure transducer for determining the depth of the TARS (Nautronix ATS-S04 manual, 1989).

Surveys of the underside of ice ridges were performed by radiating survey paths from the entry holes. Depth of the TARS was continually monitored by a Gulton differential pressure transducer and the bearings of survey paths recorded by a Humphrey DG-04 directional gyro compass. Information from both systems was telemetried to the surface, and recorded digitally.

The Mesotech sonar is an upward looking sonar system mounted on the top of the TARS. Its pulse transmits at a 675 kHz frequency and produces a narrow conical beamwidth of 1.8 degrees. The beam footprint on the underside of the ice of the Mesotech transmitting at a depth of 20 metres below the ice would be approximately 0.5 metres in diameter. Underside ice features are measured by the delay time between the initial pulse and its acoustic reply. Depth of the TARS is continually monitored by a Gulton differential pressure transducer. Pressure data are transmitted through the umbilical cable to the surface at a rate of 1Hz. Figure 27 illustrates the TARS keel data acquiring system.

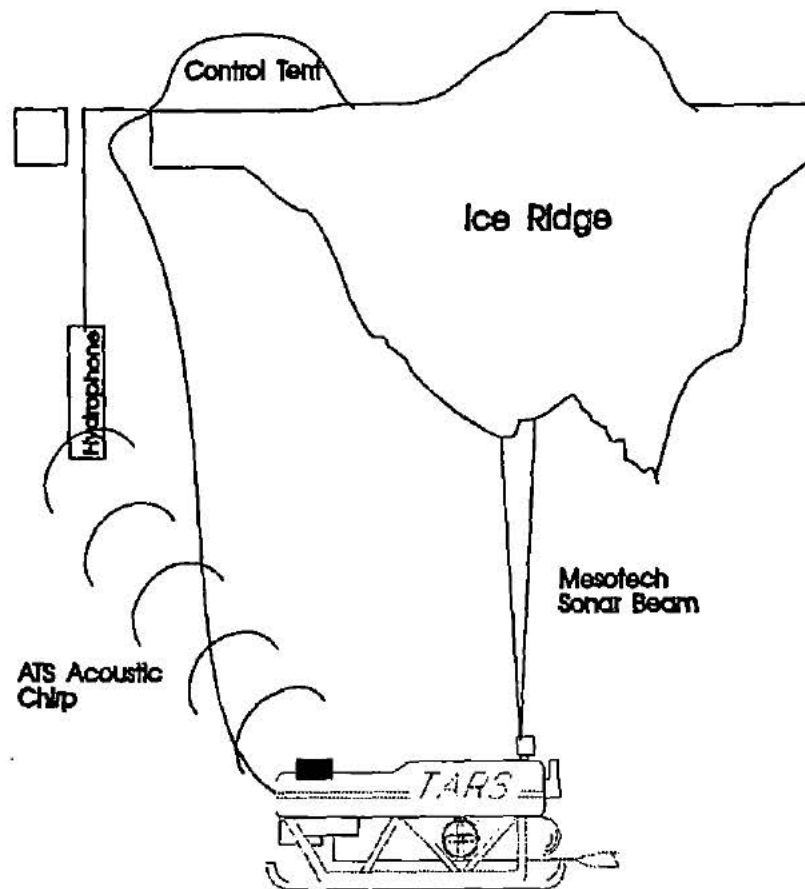


Figure 27: Diagram of TARS.

6.0 Methodology

The field testing program began April 11, 1991. A first year pressure ridge was selected from aerial reconnaissance and was located at the GPS measured coordinates of 70°28.574'N and 133°54.780'W. A D.H.Twin Otter was used to shuttle equipment from Tuktoyaktuk to the site and a makeshift runway was marked out. The ridge selected was in the order of 300 metres long and varied in width from 15 to 40 metres. The sail of the ridge was largely wind swept exposing the cardhouse stacking of ice blocks of various sizes, shapes and orientations. A baseline adjacent to the longest axis of the ridge was surveyed and a coordinate system established. There were 192 XYZ survey points collected using the theodolite and EDM in tandem. Survey points were carefully chosen to be representative of the somewhat irregular surface of the ridge. A number of large snow filled garbage bags visible from the air were placed on and beside the ridge and a fixed wing aircraft was flown over the area photographing the site. These garbage bags were surveyed into the topside data and acted as tie down points for post processing air photo interpretation. Two TARS entry holes were bored through the level ice adjacent to the ridge for keel surveys. Boring through the 2 metre thick ice was achieved by the use of a large ring hole melter. Hot water, injected into the melt ring gradually melted through the ice. Once melted through, the large ice plug was then pushed under the level ice plate out of the way of the submersible. Both of these entry holes were also surveyed into the topside data in order to align sail geometry to keel geometry. In addition, the gyro compass of the TARS was aligned with the topside coordinate system by lining up the TARS with a surveyed target hole in the ice. Sixteen survey tracks radiated out from the first hole and eighteen tracks from the second. The data acquisition system used for the submersible was a 386 laptop computer. This computer system was located within a heated control tent on the ice. In-house software was developed to time stamp all three incoming data streams (ATS, Mesotech and pressure transducer) in order to synchronize the data for post processing alignment. Underwater video recordings were made of each track.

Seven overflights were made using the airborne remote sensing system. Five of the survey lines traversed the short axis and two overflights ran along the crest of the ridge for the entire 300 metres. For three of the seven overflights both GPS and video recordings were made in order to tie down data to the ground survey coordinate system. The altitude of the bird over the ice varied somewhat ranging from 15 metres to well over 30 metres. The ground speed of the bird over the ridge segments was on the order of 60-80 km/hr as measured by the helicopter instruments.

7.0 Data Acquisition

The data acquired from the field topside surveys consisted of vertical azimuths, horizontal bearings and distances to targets. Six reflective prisms each mounted on top of 1.6 metre long metal rods were used as targets for both the theodolite and EDM instruments. The locations of these targets were logged by hand and any relevant descriptive details noted.

Acquiring bottomside geometry was much more involved. A data handling procedure entitled the Underwater Acquisition System (UAS) was designed to gather information from the various underwater instruments (written by Todd Warnes (IOS), 1991). The information received through this acquisition system included ATS, TARS and Mesotech data. Since these three sets of data were logged independently and at different time intervals, a trigger pulse, generated from the ATS system was used to create common time stamps encoded into each of the data sets. These timing stamps were necessary in order to align the data for post processing.

Once the UAS program had been initiated, all three instruments began sampling. During the first minute, trigger pulses were encoded onto each of the separate data files. Each instrument was treated separately. The first data set to receive timing information was the ATS navigational system. The serial buffer for the ATS was cleared until the first trigger pulse was received. Once a trigger pulse was

detected, data from the ATS was saved in a serial buffer but not read to file. A total of five trigger pulses containing timing information were encoded into the incoming ATS data. The interval between trigger pulses was approximately 3 seconds. After the ATS data had been assigned time information, the serial buffer continued to fill but was not read to file. Trigger pulses were then sent to the serial buffer for the Mesotech and the same time stamp sequence was carried out. Finally after the Mesotech received its time information, the same procedure was carried out for the incoming TARS data files. At the completion of the TARS last time stamp, all the accumulated data from the three filling buffers were dumped to file and the acquired data from this point onward was continuously recorded to file.

8.0 Analysis

8.1 Topside survey

There were 192 data points collected during the theodolite survey. Theodolite angles, EDM distances, instrument heights, backsight checks and point descriptions were keyed into a database for processing. CONCAP Program C70-TOPO REDUCTION was used to convert raw survey data into XYZ (plus point descriptor) data points. This program, a commercially available surveyor's software package is in common use for land surveys. Using these data points, a first attempt was made at generating a topographic map of the site. The density of points however, was too sparse to make an accurate representation of the sail geometry. In order to obtain more detail, air photos, supplied by NRC, were used to digitize an additional 4000 XYZ data points of the ridge. The air photos were taken from a fixed-wing aircraft at a height of 1000 feet (304.8 m) by a WILD RC-10 camera (25x25 cm negatives). Five frames were taken over the long axis of the ridges, each frame overlapping the previous by 60%. Digitization of these additional points was carried out on an AP190 analytical stereo plotter which was made available for this study by the BC Ministry of Forests Research Branch. The XYZ data points generated from the theodolite surveys were used as ground control points to tie down the air photos. Sixteen surveyed markers (including marker bags, flags, and the control tent), clearly visible on the photographs, were used to check the AP190's accuracy. In all cases, the AP190 measured value between markers was within 10 cm both horizontally and vertically of the known distance taken from the theodolite measurements. This instills confidence in both the stereo analyzer data output as well as the original theodolite surveys. A second check was performed using the Twin Otter's dimensions obtained from the aircraft manual. The AP190's measured distances of wing tip to wing tip and nose to wing tail were less than 5 cm off of the manufacture's specifications. All data collected from the AP190, as was the case with the theodolite survey, is referenced to a flat sea surface plane.

Figures 28 and 29 illustrate the block structure of the sail.



Figure 28: Photograph of sail block structure.



Figure 29: Photograph of sail block structure.

8.2 Keel survey

A significant portion of this study required detailed analysis of the data acquired from the submersible. In order to obtain keel geometry, all of the onboard TARS instrumentation had to be separately processed and then combined in order to produce keel XYZ coordinates.

Data processing of the ATS, Mesotech and TARS files was performed on the Institute of Ocean Sciences' VAX mainframe. This system runs within a VMS environment and all programs were written in FORTRAN 77, utilizing various NAG (Numerical Algorithms Group Inc.) routines from linked libraries. In order to work with the field data, each file was converted into an IOS standardized format. This format, referred to as the Multi Line Header (MLH) format, separates each file into a data and header component. Once in this format, the data are compatible with a host of inhouse softwares developed specifically for data processing. After running any inhouse software application, new data and header files are written. The header file is automatically updated with an information stamp documenting the processing step. As a result, the processing history of any data file is readily available by viewing its associated header file. Appendix B gives an example of the efficient documentation that occurs within the multiline header format.

The overall approach of the keel analysis is illustrated in Figure 30. All software developed for the analysis of the keel data can be found in Appendix C.

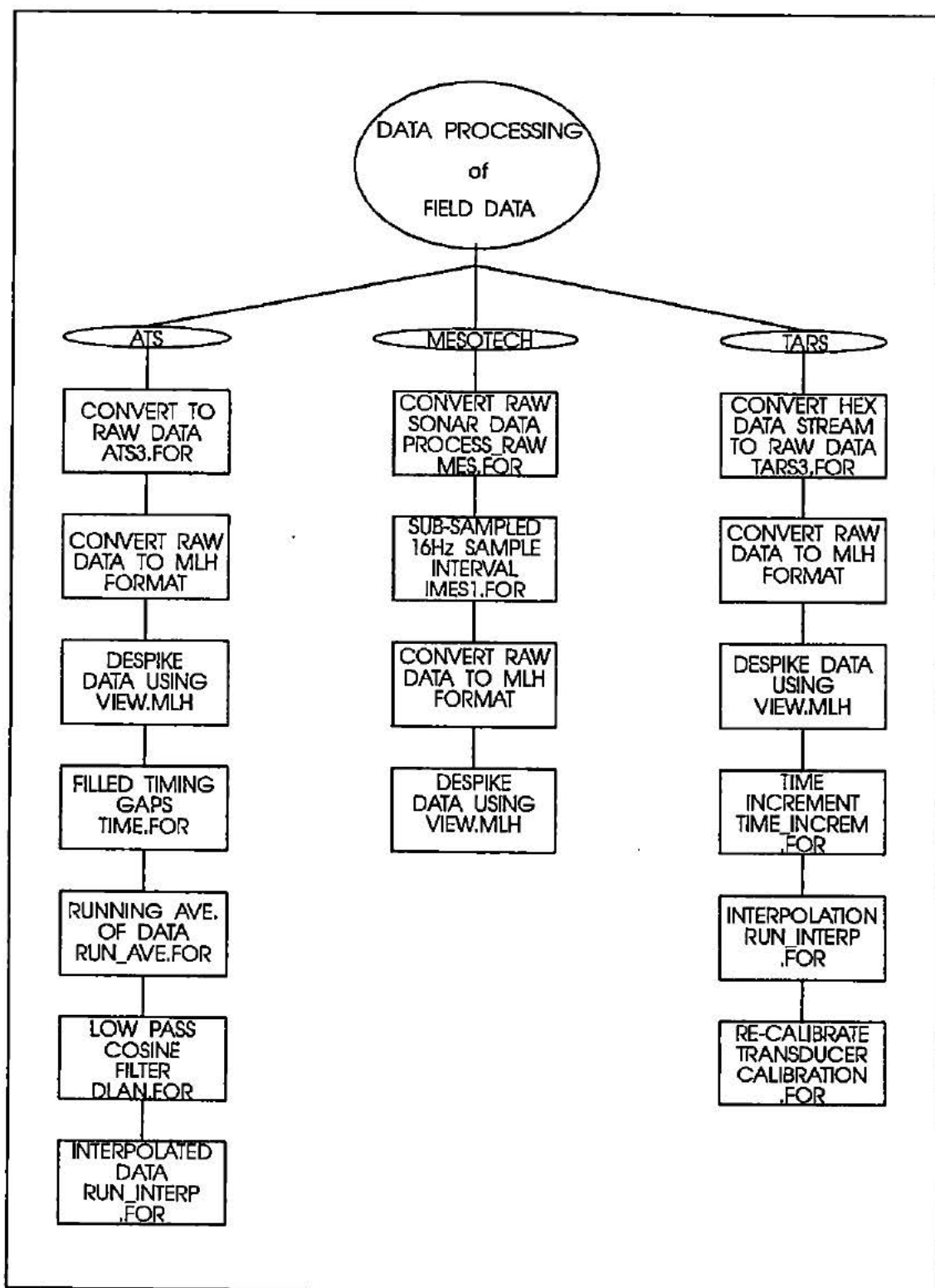


Figure 30: Flow Chart of Submersible Data Analysis.

8.21 ATS Analysis

ATS field data were converted into raw data by the program ATS3.FOR (Appendix C). The raw data files contained the acoustically determined X, Y and Z locations of the TARS as it travelled under the keel. Also contained within these files are orientation sensor data of the receiving hydrophone. The data were arranged into seven column real arrays in the following format (Table 3):

Table 3: ATS Raw Data Array

Column	Attribute
1	Time (seconds)
2	X coordinate (m)
3	Y Coordinate (m)
4	Z Coordinate (m)
5	Heading of hydrophone
6	Pitch of hydrophone
7	Roll of hydrophone

The raw data files were then converted into the multiline header format and then run through the manual despiking features of the IOS inhouse program VIEW_MLH. This program was useful for visually eliminating erroneous data such as large deviations in X, Y or Z coordinate values. These large deviations in positioning could be the result of acoustic multipathing off the irregular ice surface of the keel. Given that the TARS travels at a velocity of approximately 1 metre per second and no greater than 2 metres per second (accounting for any strong currents), any points in the coordinate data that exceeded a reasonable distance between sample intervals were deleted (i.e. an X coordinate excursion of 10 metres in 3 seconds would not be reasonable). A linear interpolation routine was applied automatically to fill any deleted data point(s).

Upon closer examination of the ATS data, there appeared to be a problem with the time interval between data records. Communications with AANDERAA Instruments, the suppliers of the Nautronix ATS, indicated that the time interval for

the interrogation of the ATS mini beacon was constant. The recorded time output of the field data was, however, in integer values of differing sizes as illustrated in the first 100 data records of Figure 31.

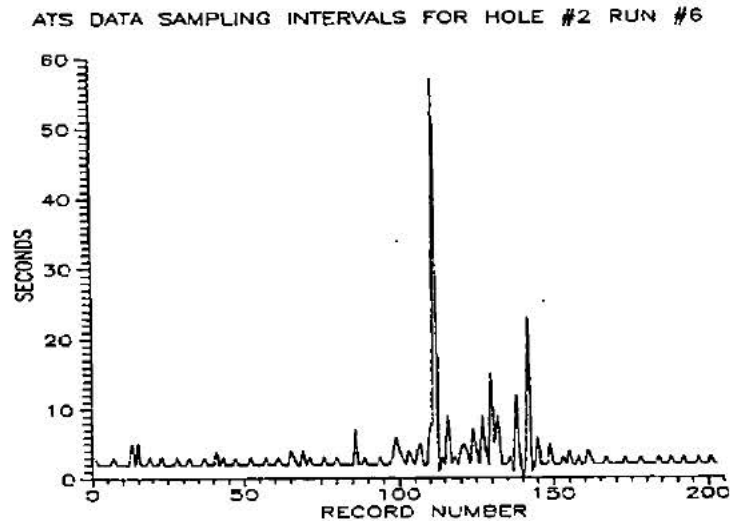


Figure 31: ATS Time Sampling Interval.

In fact, the sample interval was not fixed, but depended on the length of time to complete the position calculations. As a result it was uncertain as to when the data were actually received, the time required for location computations and the round off function applied to the output. There also appeared to be significant data gaps where time intervals were much larger than the 2-3 seconds intervals (typical of the data). It is thought that these data gaps, illustrated in the 100 to 150 record number of Figure 31, are a result of multipathing and/or regions of shadow zones where the TARS travelled beyond the maximum depth of the keel and out of sight of the receiving hydrophone. The program TIMCO.FOR (Appendix C) was written in order to assess the time intervals between regularly spaced sequential data and data containing skips. This program enabled the user to specify a time interval tolerance window in order to identify segments of non-interrupted data from irregularly skipped segments. By specifying a tolerance window of 1 to 3 seconds, sequential non-interrupted integer time intervals could be averaged in order to obtain more precise real time increment

values. In 32 of the 35 files (the first three files were somewhat erratic), a time increment for sequential data segments was approximately 2.20 seconds \pm 0.02.

The data gaps for each file were filled using the program TIME.FOR Appendix C). This program filled gaps with integer time intervals similar to the sequential data segments. Once the gaps were filled, a program called RUN_AV.FOR (Appendix C) was written which modified the data using a running average method. The running average program used a user specified averaging window which essentially smoothed the data. A specified averaging window of 11 data lines was used. This number of points was used based on the calculated time interval of 2.2 seconds.

The data at this point were interpolated to the desired 0.5 second interval by the IOS inhouse program INTERPOLATION.FOR. It was assumed since the TARS travelled through water that its motion was relatively free from abrupt direction changes. As a result, the final stage of the ATS data processing was to run the data files through an in-house low pass Cosine filter (DLAN.FOR:IOS inhouse program) in order to eliminate any high frequency displacements caused by position errors.

8.22 Mesotech Analysis

Analysis of the Mesotech data was straightforward due to the high quality of the data. The two-way response times of the echo soundings were converted to metre values representing the TARS distances from the keel surface. The Fortran program PROCESS_RAW_MES.FOR (Appendix C) which was written for previous Mesotech data was modified somewhat for the 1991 field data. TARS to keel distances were calculated by the following formula:

$$Distance = \frac{Mesotechdata * T * C_w}{2.0 * 10^6} \quad (12)$$

Where C_w is the speed of sound in water ($m s^{-1}$)

T is the time measure per Mesotech count (11.3932 micro-second).

(note: the denominator balances the units so that the Distance value is in metres)

The speed of sound used for this calculation was based on a local sea water temperature of $-1.74^{\circ}C$ and salinity of 31.85 practical salinity units. Using UNESCO and National Institute of Oceanography data bases, a speed of 1436.7 m/s was calculated and applied to the response times. The sample interval of 16 hz provided more data than were usable. All Mesotech data files processed through PROCESS_RAW_MES.FOR were then subsampled to time intervals of 0.5 seconds by the program IMES1.FOR (Appendix C). Data files were then converted to multiline header format in order to despike data using VIEW_MLH.FOR. Generally, there were very few spikes encountered in the Mesotech data.

8.23 TARS Analysis

The TARS field data containing 32 byte hexadecimal data blocks (data expressed in base 16) were processed by the program TARS3.FOR (Appendix C). Each of the attributes of the bundled TARS data were treated separately. The pressure transducer, recording an analog voltage proportional to PSI in a hexadecimal format, were converted to real numbers. Laboratory calibrations, carried out in January 1989 (over a pressure range from 0 to 200 PSI) were used to adjust the analog output in order to obtain corrected PSI values. Adjustment of the analog output was based on a least-squares fit of the calibration curve obtained from the laboratory pressure check. The adjustment equation used was as follows:

$$P.S.I._{adjusted} = \frac{ANALOG\ VOLT\ OUTPUT(HEXADECIMAL) + 0.854365389}{7.6740} \quad (13)$$

(the values: 0.854365389 is the offset from the least-squares fit (the precision of this value is kept for book keeping purposes) and 7.674 is the scaling factor used for transducer values in order to convert to P.S.I.).

PSI values were then converted to metres by using equation 14.

$$DEPTH_{metres} = \frac{P.S.I. * (6.895 Pa\ m/P.S.I.\ s^2)}{g} \quad (14)$$

where g is the gravitational constant equal to $9.81\ m/s^2$

($6.895\ Pa\ m/P.S.I.s^2$ is the conversion factor for P.S.I. to Pascals)

Hexadecimal data obtained for the sine and cosine of the TARS heading as well as hexadecimal data from the pitch and roll of the TARS were converted to real numbers. The output from the conversion of hexadecimal data to real decimal data was arranged in the following format (Table 4):

Table 4: TARS Raw Data Array.

Column	Attribute
1	Time (seconds)
2	Transducer pressure in P.S.I.
3	Depth of TARS in metres
4	Sine of TARS heading in radians
5	Cosine of TARS heading in radians
6	Pitch of TARS in degrees
7	Roll of TARS in degrees

These data were then converted into the multiline header format and then despiked using VIEW_MLH. Further processing of the TARS data was necessary during the combining of data files as well as the resolving of TARS pitch and roll.

8.3 Combining Keel Data

ATS, Mesotech and TARS data streams were combined by the Fortran program COMBINE.FOR (Appendix C). This program synchronized all three data arrays by aligning the initial computer time stamps found in each file. Computer time stamps were to the nearest 0.01 second while the analyzed data were resolved to 0.5 second intervals. Through a series of IF THEN statements the combined data were aligned to be within a potential offset no greater than 0.25 seconds. It was discovered during the combining of these data sets that the TARS data files were, in all cases, ending before the other two data sets. Upon closer examination, there appeared to be a consistent ratio of TARS file length to the other two data sets. By using the ATS running clock contained within the raw ATS files, the number of TARS records were compared to the total time taken during the TARS sampling period. It was determined that the sampling interval was not the assumed one second but rather 1.17 ± 0.05 seconds as averaged over 34 files. Although this was a fairly small correction, over 1000 seconds (the approximate length of an average run) this would create a timing error in the sonar data of approximately 170 seconds, or 170 metres in the submersible location. As a result of this discovery, it was necessary to backtrack somewhat to effect changes. Corrections were made to the timing channel of the TARS data and then re-interpolated to the common 0.5 second timing interval. During these corrections, the TARS data were also adjusted slightly for calibration errors based on a calibration curve for the pressure transducer (Appendix D calibration curve). Once the data were corrected, the program COMBINE.FOR was then run again, this time with success. These combined files were then downloaded from the VAX to the PC for further manipulation.

8.31 Resolving for Pitch and Roll

During the course of the TARS survey, the Mesotech beam was directed upwards towards the keel surface. The submersible generally offered a relatively stable platform for this transmission; however, ocean currents, obstacle avoidance, heading corrections and tethered cable tensions introduced yaw, pitch and roll transformations which affected the direction of the beam. It was not uncommon for the submersible to experience pitch and roll values exceeding 10° . Such transformations would yield sonar 2-way response times that would be of longer duration than if the beam were directed straight upwards. Use of these response times would result in incorrect ice thicknesses at the acoustically derived XY location of the submersible. An existing program (Riedel, 1991) was modified to correct the data for pitch, roll and yaw. This required transforming the location of the submersible in order to correct for the focused two-way sonar signal. In order to begin corrections, it was necessary to determine the heading of the submersible as it moved under the ice. Heading information of the submersible was given by the TARS gyro compass in two components: (1) Sine of heading and (2) Cosine of heading. As was the case with the 1989 submersible survey (Melling et al., 1993), the compass readings did not give accurate heading information. On screen heading information on the TARS control terminal appeared to be reasonable but the data file containing the heading information was not correct. A number of attempts were made to determine whether or not heading errors were the fault of signal interpretation or the result of a sudden event such as an abrupt pitch, roll or strike against the ice. After considering a number of possible problems, it was decided that resolving this problem would require a significant amount of time, some of which would involve a full diagnostic check of the gyro compass, the signal conditioning and the effect of pitch and roll on the gyro element. Since the submersible is in storage at Tuktoyaktuk, bench testing is not possible at this time. Communications with the manufacturers has not provided any information as yet as to the nature of this problem (personal communication with Dr. Topham).

Figure 32 illustrates the inconsistency of the submersible headings.

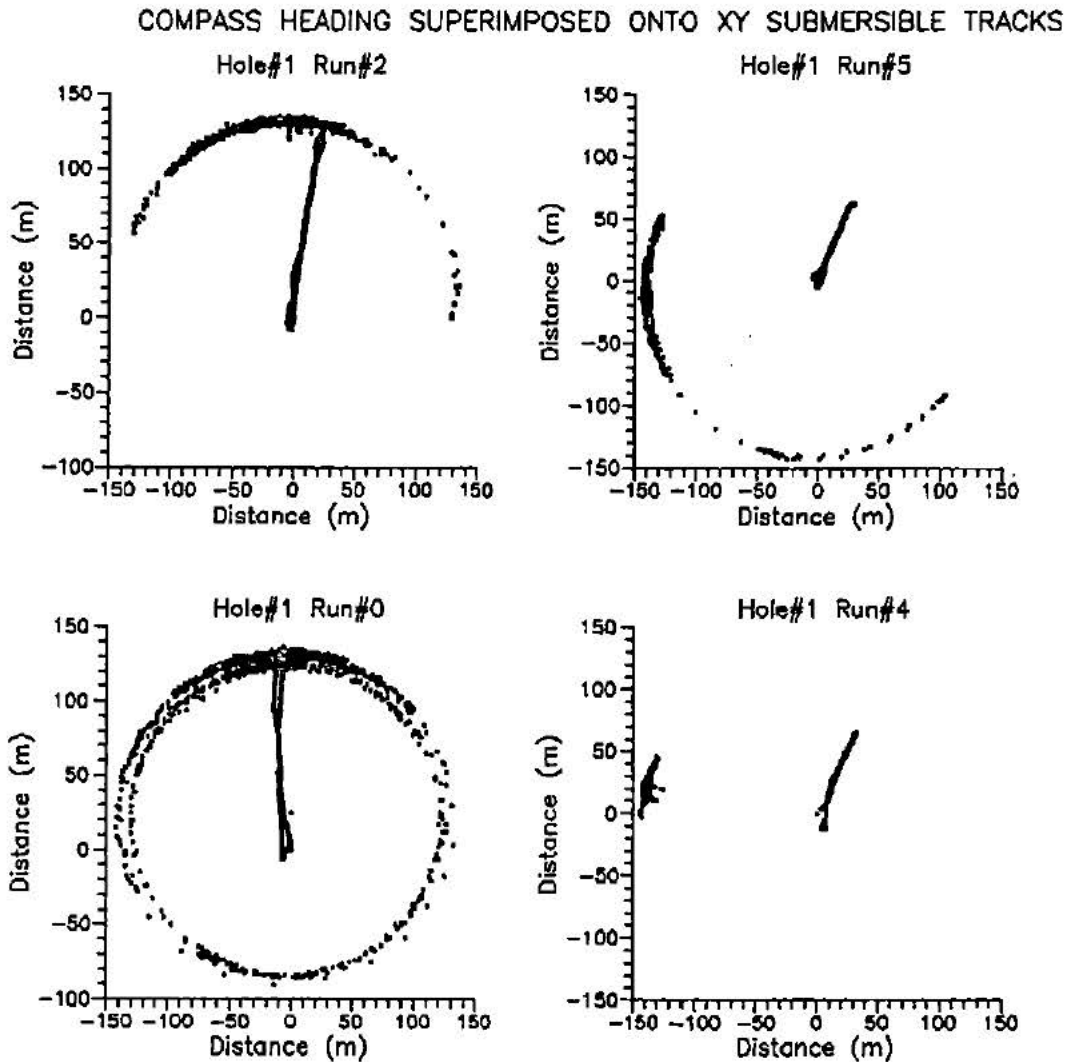


Figure 32: Compass Heading Malfunction.

Each of the four plots contain heading information (appearing as arcs) superimposed onto the corresponding XY tracks (solid lines). There did not appear to be a corresponding pattern between these two data attributes. Sometimes the heading would appear to be in the direction of the XY tracks and other times it would not.

As a result of these inconsistencies, an alternative method was used to obtain the needed heading information.

It was assumed that the submersible was heading in the direction it moved. This is a reasonable assumption as the thrusters on the vehicle powered and steered the submersible on outgoing tracks according to a fixed heading and, similarly, the vehicle returning to the entry hole was backhauled by pulling the umbilical cable affixed to the back of the submersible. Determination of the heading was achieved by plotting both the X and the Y coordinates with time. Each of these plots were fitted with polynomial curves using the software GRAPHER. Before accurate fitting could occur, the tracks needed to be split into outgoing and backhaul tracks. Segmenting of the tracks enabled better fitting of polynomial curves to the data--i.e. the shorter the data segment the easier it was to fit a polynomial function to it. Segmentation of files was a time consuming step using the spread sheet within GRAPHER. Once separated into respective segments, polynomials were fitted to:

(1) X versus Time (dx/dt)

(2) Y versus Time (dy/dt)

Polynomials were generally of order 6 (as high as 10 for meandering segments). The order of polynomial was based on the goodness of fit. Generally the goodness of fit, which is calculated by taking the square root of the residuals divided by the number of data points in the segment, was of the order of 1 metre and in all cases less than 2 metres. These polynomial fits, therefore, were reasonable representations of the actual data. The coefficients from the polynomial fits were entered as headers to each of the respective outgoing and backhaul tracks. The QuickBASIC program RESOLVE3.BAS utilizing geometric transformation derivations recorded by Dr. Topham (Appendix E) was modified for the 1991 data. The modified program FIT_RES.BAS (Appendix C) used the dx/dt and dy/dt coefficients to determine the change in Y with respect to the change in X (dy/dx). This gave the effective heading of the submersible and was used to adjust the X, Y and Z data for pitch and roll. For an explanation of the transformation geometry used to resolve for pitch and roll see Dr. Topham's notes

attached in Appendix E.

Once resolved for pitch and roll, the data were thinned in order to generate a digital terrain model of the keel surface. The total number of data points before thinning exceeded 35,000. This could not be handled by the software due to insufficient memory. As a result, the data were subsampled by the program THIN2_A.BAS (Appendix C). This program deleted any data where the TARS pressure transducer was 5 metres or less in depth (the area where the pressure transducer deviated from the calibration curve shown in Appendix D). The program also deleted data where the Z component was less than 1 metre (from thickness profiles reported by Prinsenberget al.,1992), the thinnest ice thickness near the ridge was 1 metre). Thinning the data was achieved by using a user specified minimum distance between points. In all cases the minimum distance specified was 30 cm. This program reduced the data set to a more reasonable size of approximately 14,000 data points.

8.4 Digital Terrain Modelling

In attempting to generate a representative surface of an ice ridge, two significant aspects of ice thickness were considered. The first aspect was the accuracy of the measuring techniques at a point (discussed in the data analysis section) and the second aspect was the density and distribution of the data coverage. As noted by Rothrock (1986), all methods of ice thickness measurements are seriously limited either by measurement errors or sampling errors or both. In many cases it is possible that the island of information supplied by sparse data may be surrounded by an ocean of ignorance (McCullagh, 1988). In order to reduce such errors, great care was taken during the ground truthing surveys in order to obtain a large sample of representative data. The sail survey was largely enhanced by the use of aerial photographs which yielded virtually unlimited data with X, Y and Z accuracies of 10 cm or less. Sampling of sail geometry was point specific and not averaged over a footprint diameter as was the case with both submersible data and airborne remotely sensed data. Further, generating a digital terrain model from sail geometry data had the distinct advantage of visible comparison as a means of determining how well the model represented the form of the ridge.

Keel surveys obtained large amounts of densely packed data from survey tracks radiating outwards at 15° increments from the entry holes. This meant that the data distribution of points per unit area diminished with distance from the entry holes. Near the entry holes the distribution of data points was in the order of 1 to 2 metres between tracks. At the far reaches of the submersible runs the closest adjacent tracks were approximately 20 metres or more away. These relatively sparse areas of coverage were generally on the other side of the keel and in level ice conditions. Sufficient overlap due to the two radiating rosettes of tracks about the relatively close entry holes resulted in reasonable coverage of the keel (tracks generally less than 10 metres apart for the keel feature); however, it is difficult to determine how representative this data coverage is without a visual view of the surface. As far as the

accuracy of the data, the ATS X and Y coordinates of the keel data have a horizontal accuracy of better than 0.25% (i.e. accurate to within 25 cm per 100 m). The Z component of the keel measurement had an accuracy of approximately 0.1m for the operational range.

8.41 Sail Data Coverage

The information extracted from the sail geometry was obtained from both field surveys and air photo stereo analysis. The total number of sail data points was 4131. Using the software GRAPHER (Golden Software), a 2-D map was generated which illustrates the data point distribution (Figure 33) which was later used to generate a 3-D surface of the sail.

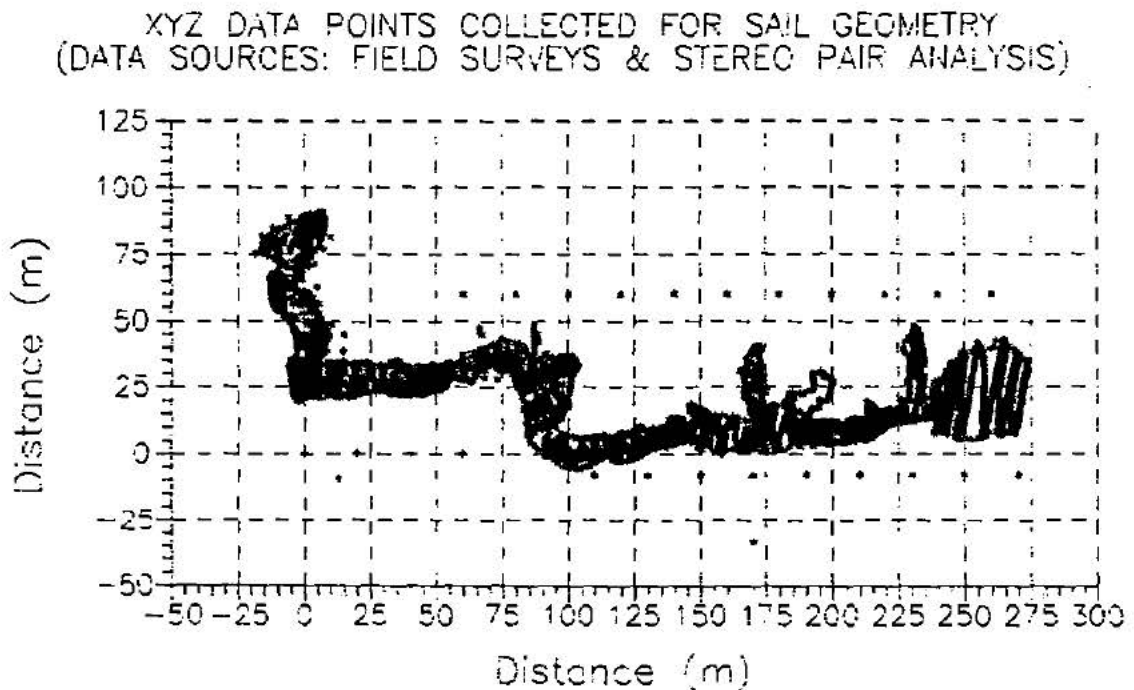


Figure 33: Point Data for Sail Geometry.

Unfortunately, during the theodolite survey very few survey shots were taken of the level ice on either side of the ridge. At the time, the ice appeared to be level on both sides; however, given the considerable size of the keel which extended beyond the perimeter of the sail (as will be described in the following section), buoyant forces under the undeformed ice probably resulted in a doming of the level ice adjacent to the sail. Stereo analysis of the sail was only performed on the exposed ice features as snow depths were not discernable from photographs. For this reason a number of constraining points were placed on either side of the sail in order to control the interpolation routines employed to grid the sail surface.

8.42 Keel Data Coverage

A total of 14,029 data points were obtained from the analysis of the submersible data. These data points are presented in Figure 34.

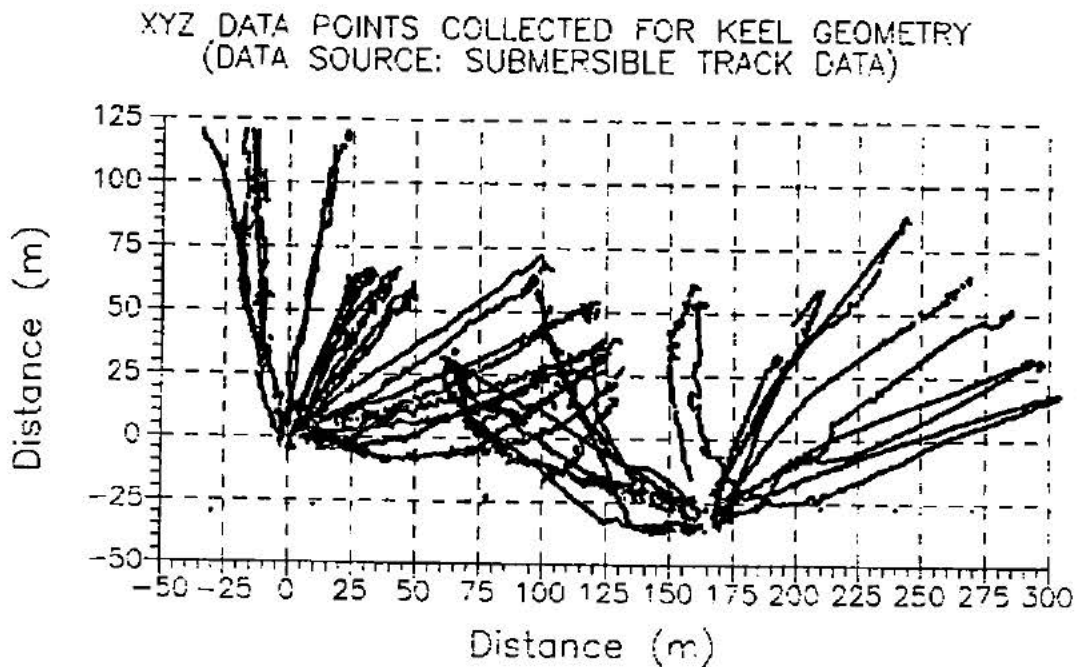


Figure 34: Resolved Point Data for Keel Geometry.

8.43 Modelling Software

Two software programs were used to grid the sail surface. These were SURFER (Golden Software) and EMXS (Sundance Software). Both programs are digital terrain modellers (DTM); but, each approximate surface geometry by very different techniques. SURFER, using a stochastic process of interpolation routines selected from one of three available (Inverse distance, Kriging or Minimum curvature), takes randomly spaced data and statistically generates a regularly spaced grid. The result is that input data are interpolated to generate approximate data at grid nodes. Once approximations are completed, the input data are discarded. EMXS approaches the DTM problem by using a triangulation algorithm which maintains the integrity of the input data. All the terrain data are joined by a network of triangles. From these triangles, linear interpolation between adjacent data points can be performed at any location within the data range. In order to make this discussion more generic, the techniques employed by the softwares will be addressed as (1) stochastic processes and (2) triangulation.

8.431 DTMs Generated from Stochastic Processes

A number of gridding parameters could be manipulated in order to generate a stochastic terrain model. These included:

- (1) Interpolation methods
- (2) Search algorithms
- (3) Grid spacings.

During the pursuit of obtaining a representative model, these parameters were altered many times. The final DTMs for both the sail and keel surfaces were arrived at by comparing the gridded surface with actual data obtained from the field work. Although attempts were made using inverse distance and minimum curvature interpolation methods, the kriging interpolation method proved to be the most effective. Both inverse distance and minimum curvature models yielded relatively

high residuals. Kriging was preferred as it was designed to cope with irregularly scattered data similar to that of the data gathered from the field. A thorough statistical treatment of the kriging technique can be found in Olea (1975) and Huijbergts and Matheron (1970).

The following search algorithms were experimented with:

- (1) Normal (Nearest Neighbour)
- (2) Quadrant
- (3) Octant

These are local-fit algorithms that are used for interpolating data to a regularly spaced grid. Both search radius (distance constraint used for the search pattern) and the number of nearest points are user specified. The first three algorithms are illustrated in Figure 35.

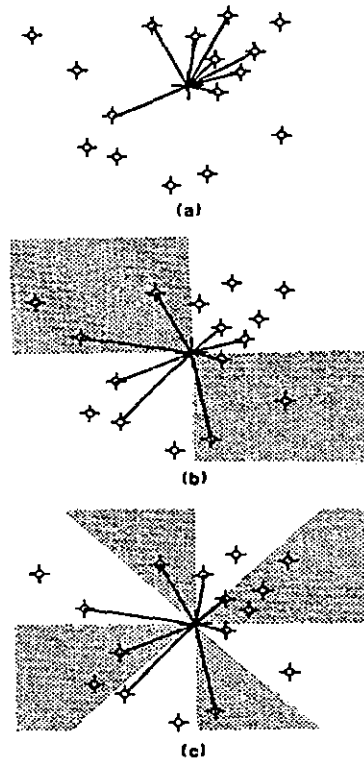


Figure 35: Search Algorithms for Interpolation of Raw Data.

(a) Nearest Neighbours, (b) Quadrant, (c) Octant.

<u>Nearest Neighbour</u>	searches for the nearest n user specified points closest to the grid node.
<u>Quadrant</u>	searches n nearest points in each of four quadrants to assure equal radial distribution of points around grid nodes.
<u>Octant</u>	searches n nearest points in each of eight octants to assure equal radial distribution of points around grid nodes.
<u>All</u>	uses all the data to generate grid nodes.

(SURFER version 4 Manual)

Finally, the grid spacing could be specified in both the X and Y axes. This gave the flexibility of selecting the distance between grid lines. The smaller the number of grid lines, the more crude the model as only a small number of grid nodes would be utilized to represent the surface. The selection of the number of grid lines is, therefore, dependent on the distribution of the data. If the data are sparse, then choosing a large number of grid lines would result in the generation of many approximated grid nodes in areas where very few real data points exist.

Selecting the appropriate combinations of the above parameters required a number of trial attempts. Assessment of each model was based on a comparison of the model with actual data posted onto the model. This comparison was both visual and statistical using the residual routine embedded within a SURFER utility. Calculation of residuals was based on the difference between real Z value data with interpolated Z values obtained at the same X,Y location on the gridded surface. Large mean and standard deviation values for Z indicated poor agreement of the model with the actual data.

Figure 36 illustrates the final DTM for the sail geometry.

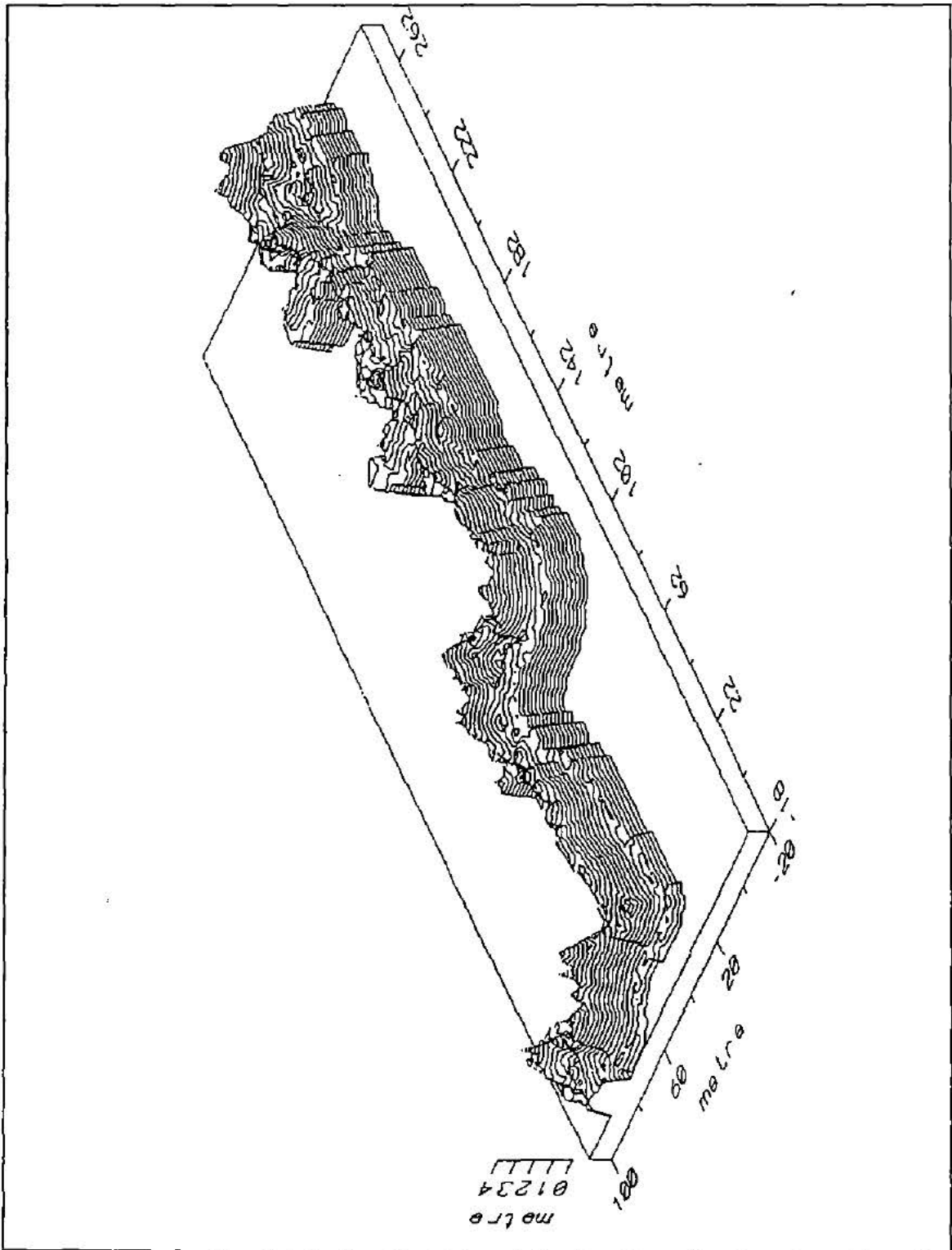


Figure 36: Sail DTM.

The parameters chosen to generate this model were (Table 5):

Table 5: Gridding Parameters used to create the Sail DTM

Interpolation Method:	Kriging
Search Algorithm:	Octant
Search Radius:	4 metres
Number of Points:	4 points
Grid Spacing X:	2 metres
Grid Spacing Y:	2 metres

Figure 36 displays the sail DTM using Z contours only. Each contour line represents 0.2 metres. The DTM highlights only the sail portion and not any surrounding elevation details. The model is orthographically projected and, therefore, parallel grid lines remain parallel making it easier to make measurements off the model. The displayed model has been rotated so that the minimum X and Y coordinates are at the closest corner to the observer. The model has also been tilted in order to appreciate the vertical relief by an angle of 35° (0°-- horizontal view, 90°-- plan view). Comparison of this model with the actual aerial photographs of the site (Figure 37) shows that the perimeter of both the model and the actual site line up very well. Figure 37 illustrates this point by overlaying a topographic map generated from the gridded data onto an aerial photograph of the site.

Gilbert
neu-tech

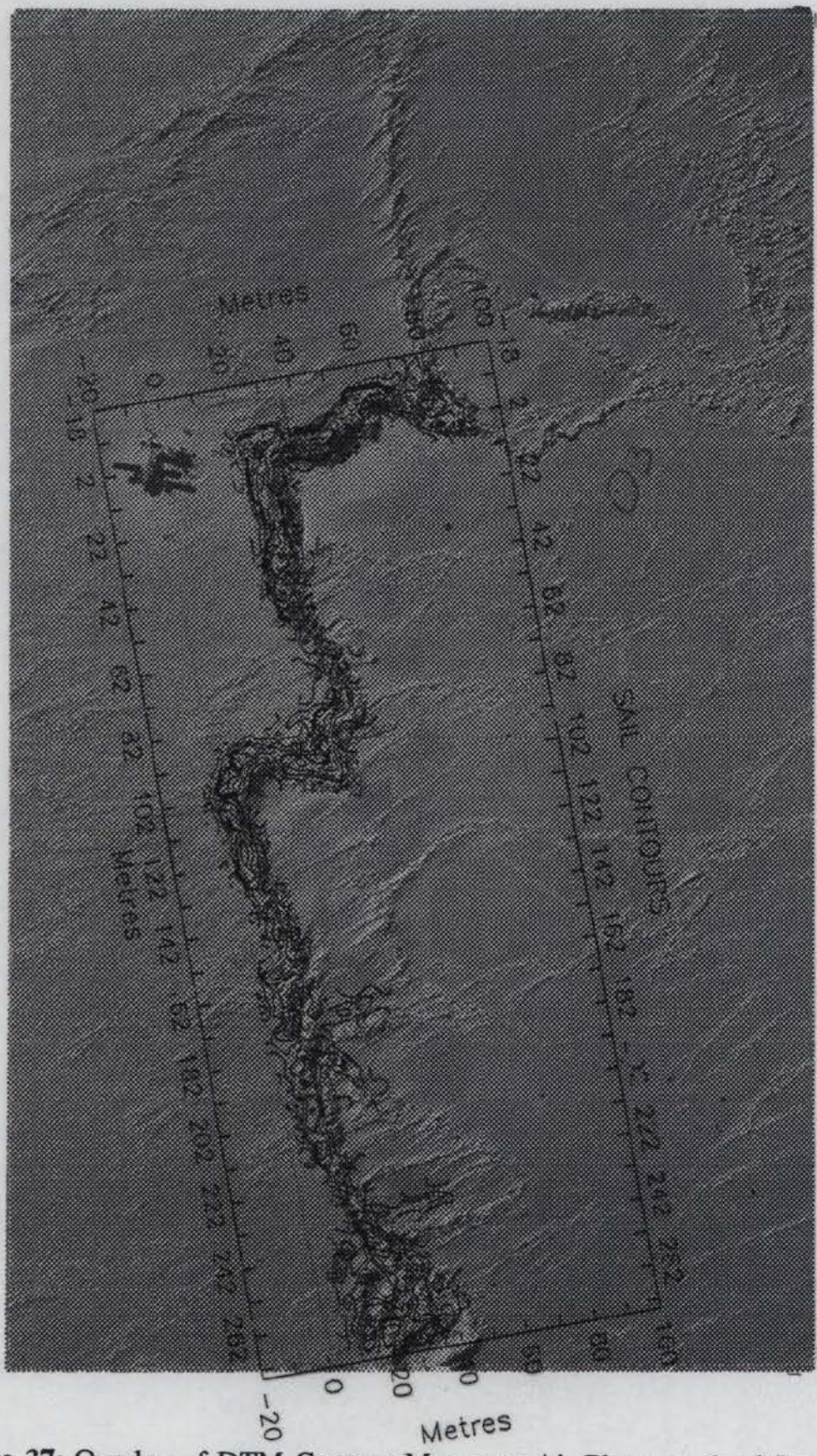


Figure 37: Overlay of DTM Contour Map onto Air Photograph of Study Site.

Residuals calculated for the sail model were as follows:

Residual Mean: 0.0053 metres

Residual Standard Deviation: 0.2817 metres

These values indicate that the gridding technique worked very well, retaining the integrity of the field data. The best results for residuals using the inverse distance algorithm were 0.2 and 1.6 metres for the mean and standard deviation of the mean of the residuals.

Gridding the keel surface required many more attempts given the nature of the data distribution. Fifteen different combinations of gridding parameters were compared to actual data. The chosen surface (Figure 38) had the following gridding parameters (Table 6):

Table 6: Gridding parameters used to create the keel DTM.

Interpolation Method:	Kriging
Search Algorithm:	Octant
Search Radius:	50 metres
Number of Points:	2 metres
Grid Spacing X:	2 metres
Grid Spacing Y:	2 metres

The residual calculations based on the keel model yielded the following results:

Residual Mean: 0.0328 metres

Residual Standard Deviation: 0.9667 metres

These values indicated reasonable agreement between interpolated values obtained from the kriging technique and the actual data (best residuals with inverse distance technique -0.5 ± 3.9 metres). This can only be said of areas where real data existed. A large portion of the surface generated is without any source of comparison; however, the general form of the keel is surprisingly similar to that of the sail. This

similarity suggests that at least the form of the keel is correct based on the isostatic balance of buoyant and gravitational forces.

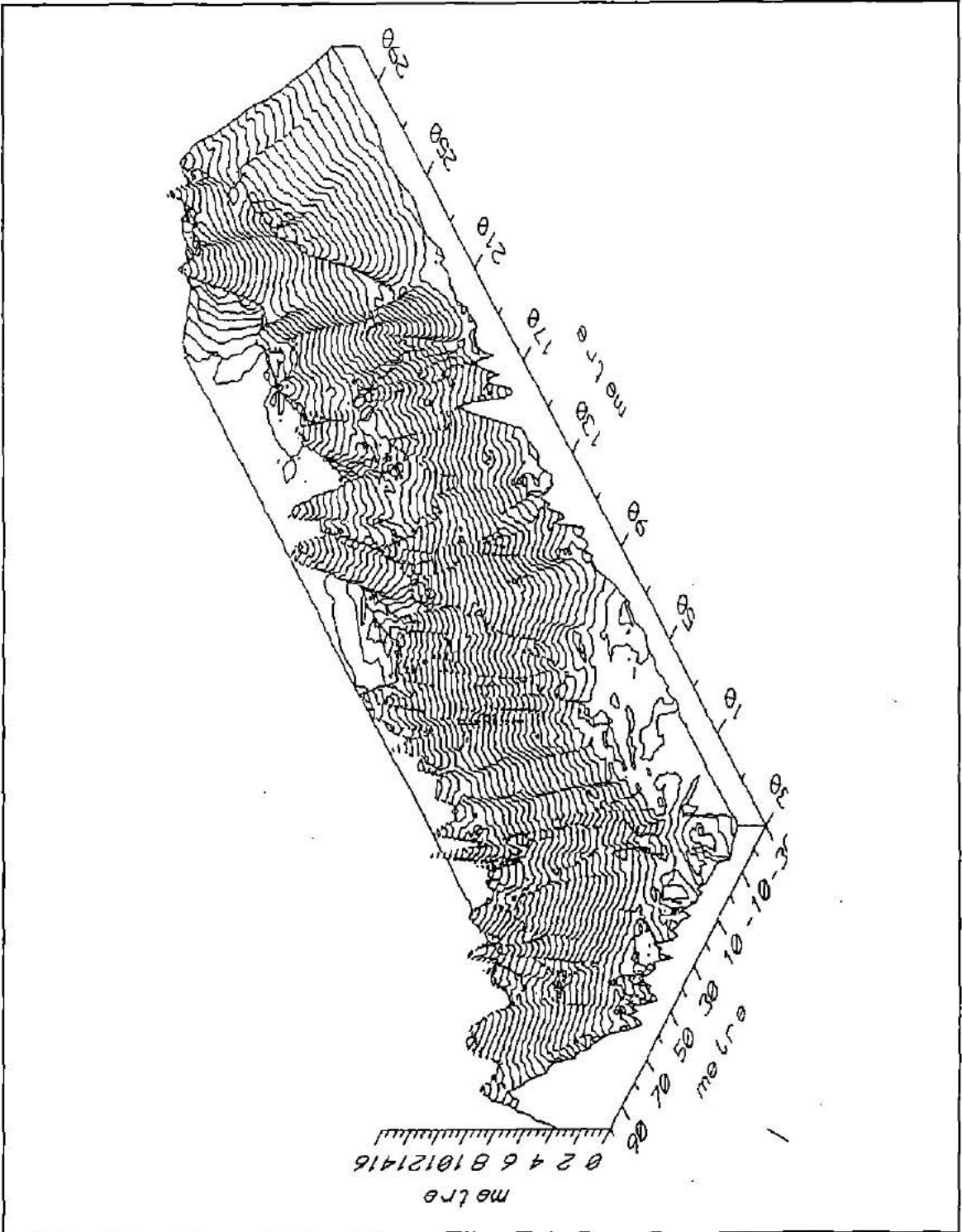


Figure 38: Keel DTM.

The keel model illustrated in Figure 38 has been inverted for ease of visualization and is displayed using the same viewing parameters as the sail DTM. As noted before, the X and Y coordinate system of the ridge are common for both keel and sail data and therefore these models can be directly overlaid for comparison. Overlapping of the two models in plan view (Figure 39) shows just how well the corresponding sail relief matches with the keel relief. There do, however, seem to be exceptions. These exceptions generally appear in the areas where the ridge takes an abrupt bend. In these areas or joints, the classical triangular geometry described in the literature review is apparently no longer valid. It is not clear as to why the ice accumulations are greater and in some cases offset than ice accumulated in areas where the ridge building event appeared to be simply compressive. Speculations as to why these anomalous areas exist are briefly considered later in section 9.3 on aspect ratios.

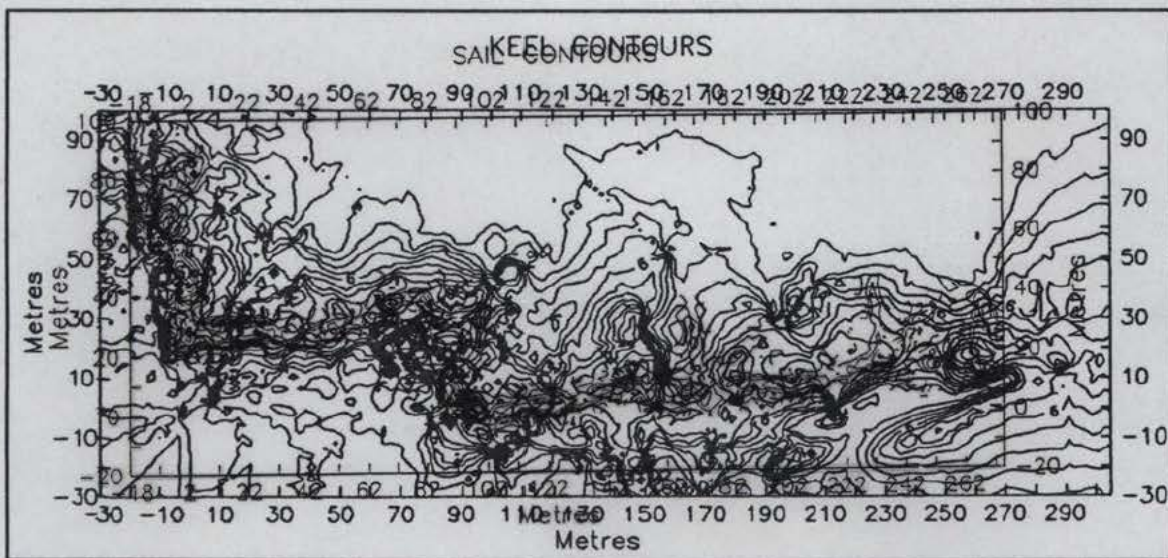


Figure 39: Overlay of Sail Contour Map onto Keel Contour Map.

Gilbert
 New-Tech
 25% COTTON

8.432 DTMs Generated from Triangulation

It was useful to model both the sail and keel portions of the ridge using a second interpolation approach. It was hoped that this would increase confidence in the generated models. Volumetric comparisons of the two modelling techniques were performed in order to check for redundancy. Generally the two techniques generated similar models. This comparison will be discussed in section 9.3 (Ridge Geometry Attributes).

Just as the stochastic technique had user specified parameters, the triangulation technique offered a range of interpolation constraints. Unlike the first technique, triangulation constructs its models by using input data to generate a network of irregular interconnecting triangles between points. Data are, therefore, not forced into a regularly spaced grid of approximated grid nodes. Triangulation techniques generally use a two step process in designing a visual representation of the terrain. The first step connects the data points to form a surface network of smallest possible triangles between points. The second step allows the user to overlay a wire mesh grid in order to visualize the surface. This grid is superimposed over the triangular network and elevation of the grid lines are calculated by linear interpolation as the grid lines intersect the connecting triangles.

The first DTM constraint prompt is: "*Maximum Length of a triangle side*". This allows the user to specify the longest length of a line segment to be used to connect data points. This is an important consideration especially in areas where data are sparse. Too large a length may create inaccuracies in the model by forcing the connection of two distant points that may be separated by unknown significant relief. An example of this would be two points that are jointed on a flat plain. If, for example, a river has been incised into the plain between the two points, this important feature would be overlooked. In a very loose sense, this may be viewed as a method of autocorrelating data (i.e. objects that are closer together are more similar than

objects farther apart).

The second DTM constraint prompt is "*Discontinuity Line Length*". Prior to generating a DTM, breaklines or discontinuity lines can be inserted into the data set. These lines are designed by the user and join data points where significant changes occur in slope. They are used to prevent the triangulation of data across these abrupt slope changes. Without these breaklines it is possible that narrow ridges or troughs may be lost as the triangulation algorithm is based on the shortest possible triangle between points. For example, in some cases, the distance between two trough edges may be less than the depth of the trough itself and, therefore, a triangle would be generated across the trough resulting in the loss of feature detail. Once discontinuity lines have been defined within the data set, this option of defining the discontinuity line length can be specified. By entering a length value, each of the line segments which are joined to make up the discontinuity line are compared to this user specified length. If the length of a discontinuity line segment is greater than the specified discontinuity line length, then a point is added at each user specified line length. For example, if a discontinuity line segment is 12 metres and a user specified discontinuity line length is 3 metres, then 3 points (3 metres apart) will be added to the line segment. Each of these additional point elevations will be linearly interpolated between the two real data end points. This procedure is done before the triangulation algorithm is applied and, therefore, the break in slope is densified (that is the number of points that represent the break in slope increases and the spacings between these points decreases). Densifying the discontinuity line increases definition in adjacent areas to the slope change as more triangles can be generated.

A final feature available in the triangulation software is the ability to perform on screen editing of the generated DTM. Triangles as well as data points can be added or subtracted as the user sees fit. This gives flexibility in terms of controlling the design of the model.

Due to the dense data coverage of the sail surface, generating a sail DTM did not require a large number of attempts. Since the modelling of the surface is based on the actual input data, calculating residuals was irrelevant. The irregular jumble of ice blocks made it difficult to define discontinuity lines and since the quality of data was high and spacings between data points were low, the discontinuity procedure was discarded (recommended by the designers of EMXS). The only parameter that was specified was therefore the "*Maximum Length of a Triangle Side*".

A maximum length of 5 metres was chosen in order to generate the sail DTM. Experimentation with larger length values resulted in the bridging of uncommon areas. Lower length values resulted in gaps in the ridge feature where data point spacings were greater than the maximum specified triangle length. Very little on screen editing was necessary using this maximum length. Figure 40 illustrates a plan view of the triangle network that composes the feature definition of the sail DTM.

A 3-D grid was generated from this DTM in order to visualize the sail geometry (Figure 41). A grid of 1 metre was used to represent the DTM. The displayed model may not be as eloquent as that of the model generated from the stochastic software but the surface texture visually compares well with the stereo photographs of the sail. Unfortunately, the triangulation software did not offer the hidden line capability that the stochastic modelling software did. As a result, viewing angles must be high in order to prevent overlapping of lines due to viewing perspective. For this reason, the model is displayed at an angle of 65° , with a vertical exaggeration of 5.

All of the figures generated from the triangulation software have the same scale. In each case the long axis is approximately 300 metres.

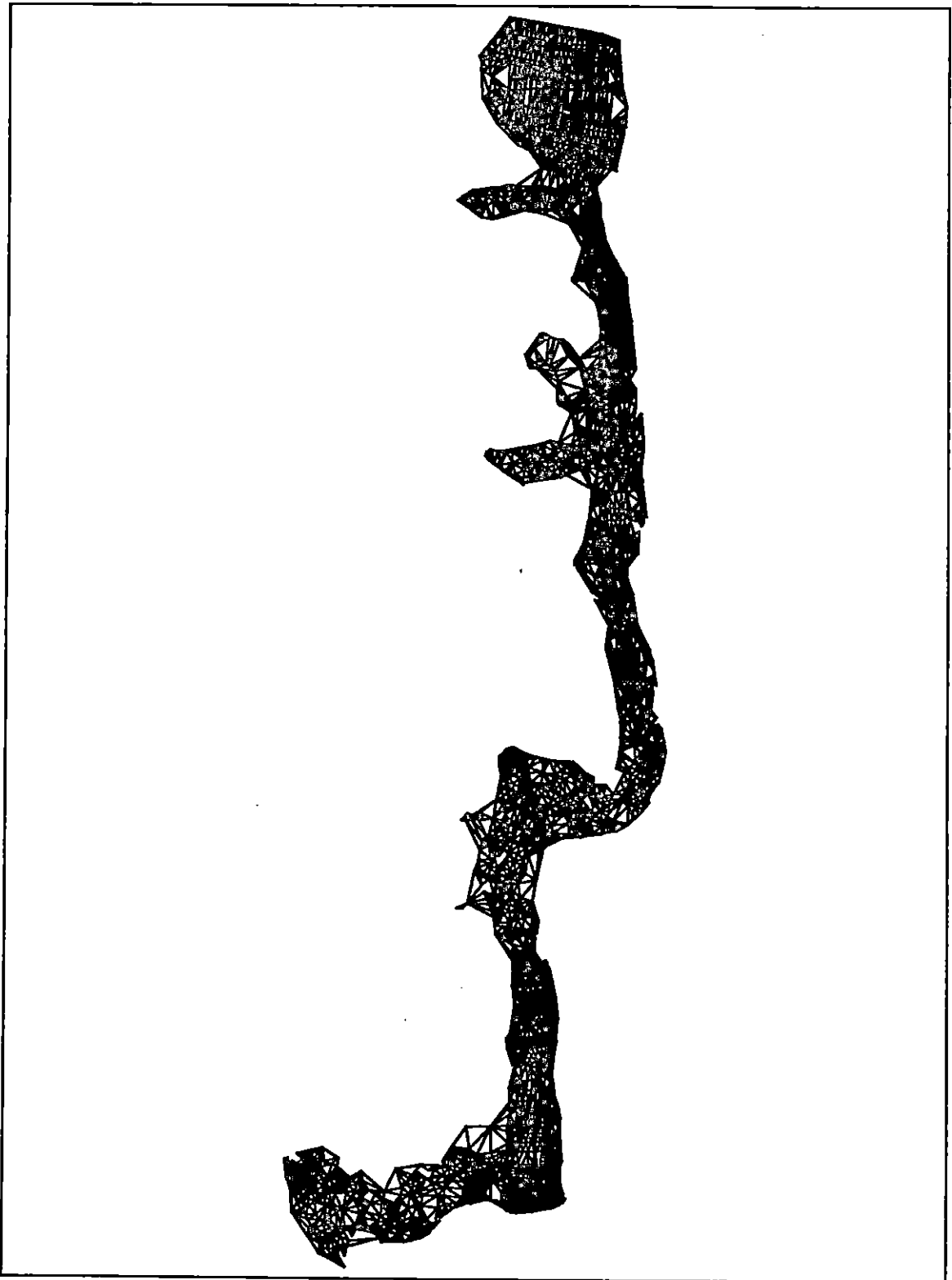


Figure 40: Plan View of Triangular Network Constructed for Sail DTM.

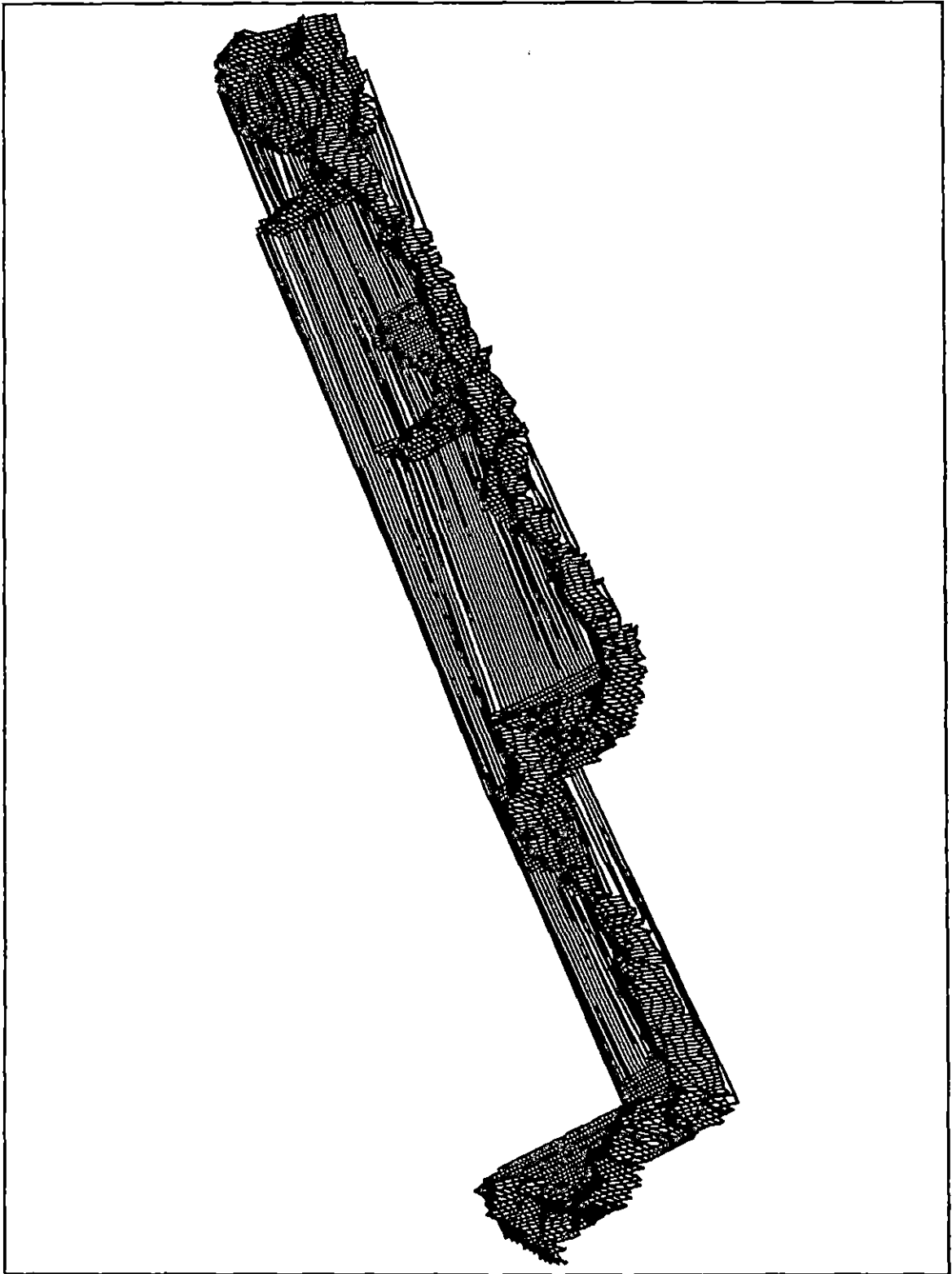


Figure 41: 3-D Grid of Sail DTM.

The maximum length of a triangle side used to generate the keel DTM was 35 metres. This value was also experimented with. Values larger than 35 metres bridged areas that filled in known troughs and values smaller than 35 metres did not connect related feature data. Unfortunately the size of the keel data file was beyond the memory capabilities of the software. It was therefore necessary to parcel the data into smaller files no greater than 5500 points. These parcels were modelled individually and combined to form the keel DTM. Figure 42 illustrates the triangular network constructed by triangulation to form the keel DTM. Figure 43 is a 3-D gridded representation of the keel surface.

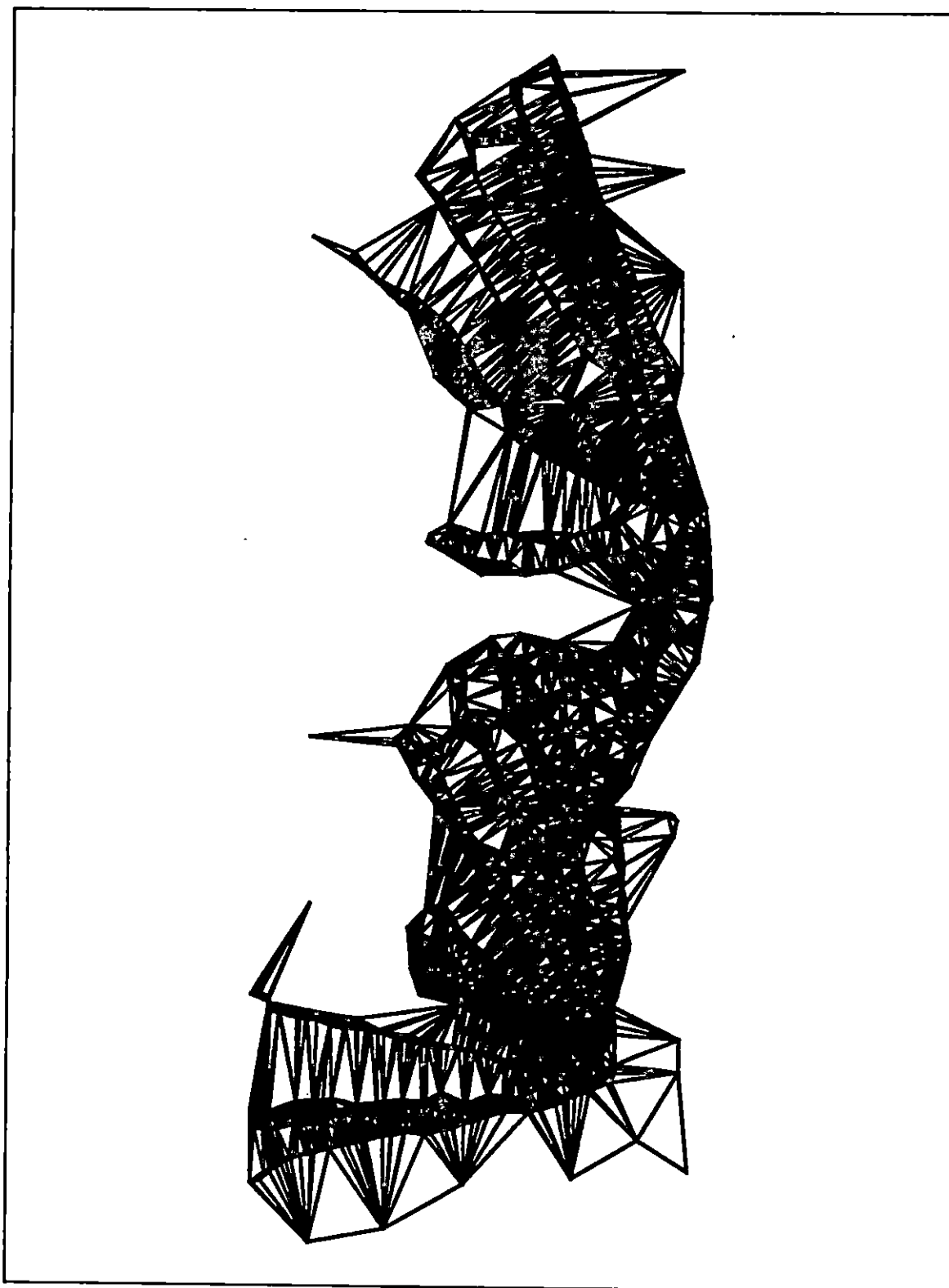


Figure 42: Plan View of Triangular Network for Keel DTM.

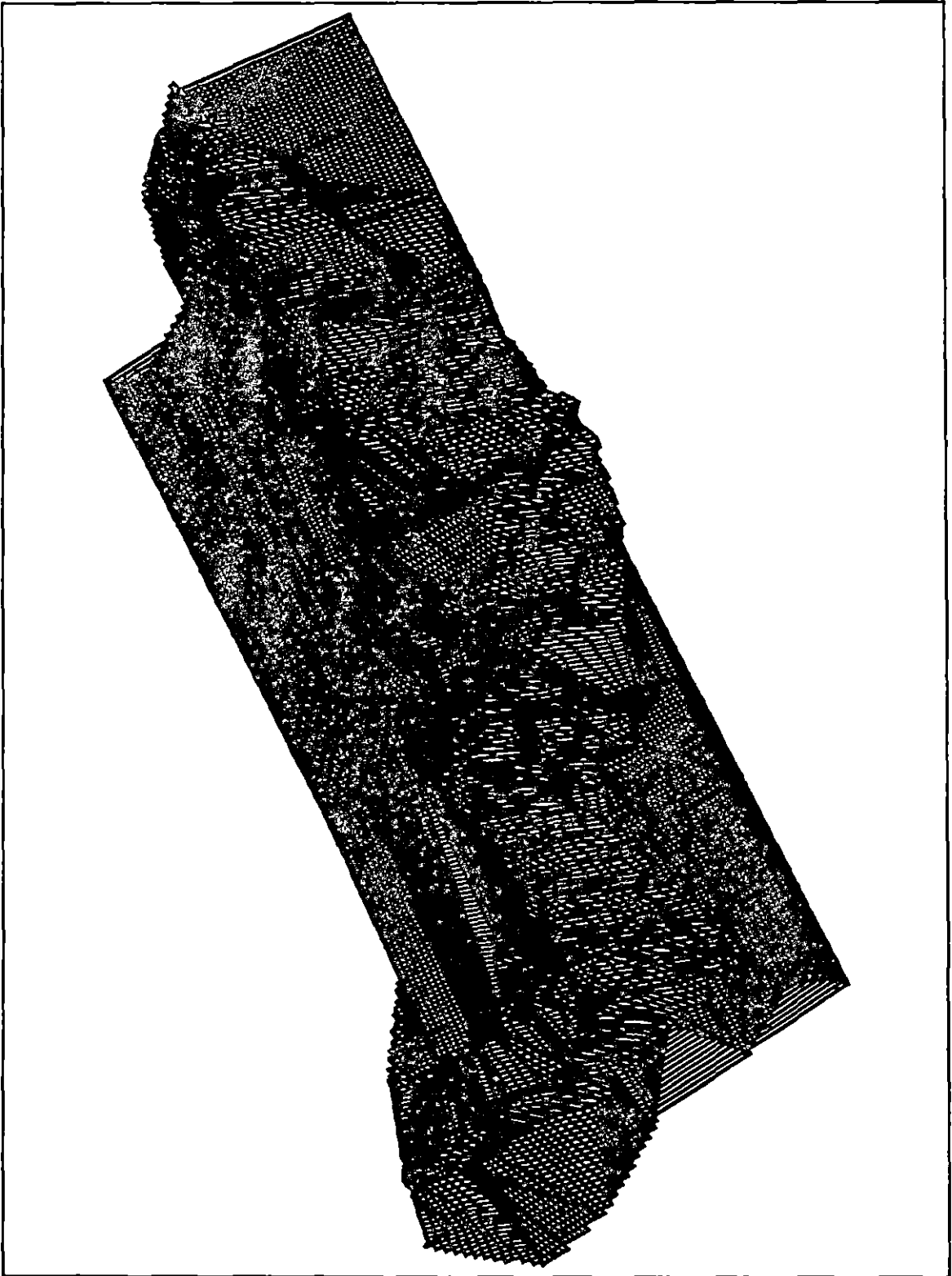


Figure 43: 3-D Grid of Keel DTM.

8.5 Airborne Survey

In order to assess the performance of the airborne EM system it was necessary to interpret the EM data. Analysis of selected segments of the EM data was carried out by Aerodat Limited using in-house algorithms. These processed segments were supplied by Aerodat and preliminary analysis was based on these supplied data. There were, however, some significant problems encountered with the data and its initial interpretation.

The first step in analyzing the EM data required the airborne GPS readings to be tied down to the GPS readings taken on the ice. Unfortunately, at the time of the airborne survey, the last on ice GPS reading had been taken many hours before. Previous on ice GPS readings taken over the course of a number of days indicated that the ice ridge and surrounding plates had significant net motion. Averaged ice plate velocities were as high as 15 cm/s. The absolute airborne GPS readings were, therefore, of little use; however, the relative spacings of the readings could be used to convert GPS coordinates to metres. A videotape of the overflights (also supplied by Aerodat) provided a method of tying down the airborne survey to the ground truth coordinate system. Only three of the seven overflights could be coordinated with the ground survey data as video coverage was unavailable for the first five flight lines. Accurate measurements of the bird flight path relative to the ice ridge were made using video frame grabbing software. The on screen fiducial marks annotated onto the video and encoded with the incoming EM data served to align the data to the XY coordinate system used for the ground truth data. Of the three usable overflights, the flight line over the 255 metre mark of the ridge was chosen for evaluation as the bird height was relatively low and bird flight stable. Figure 44 illustrates the locations of the airborne survey overflights.

Figure 44: Locations of Airborne Survey Overflights.

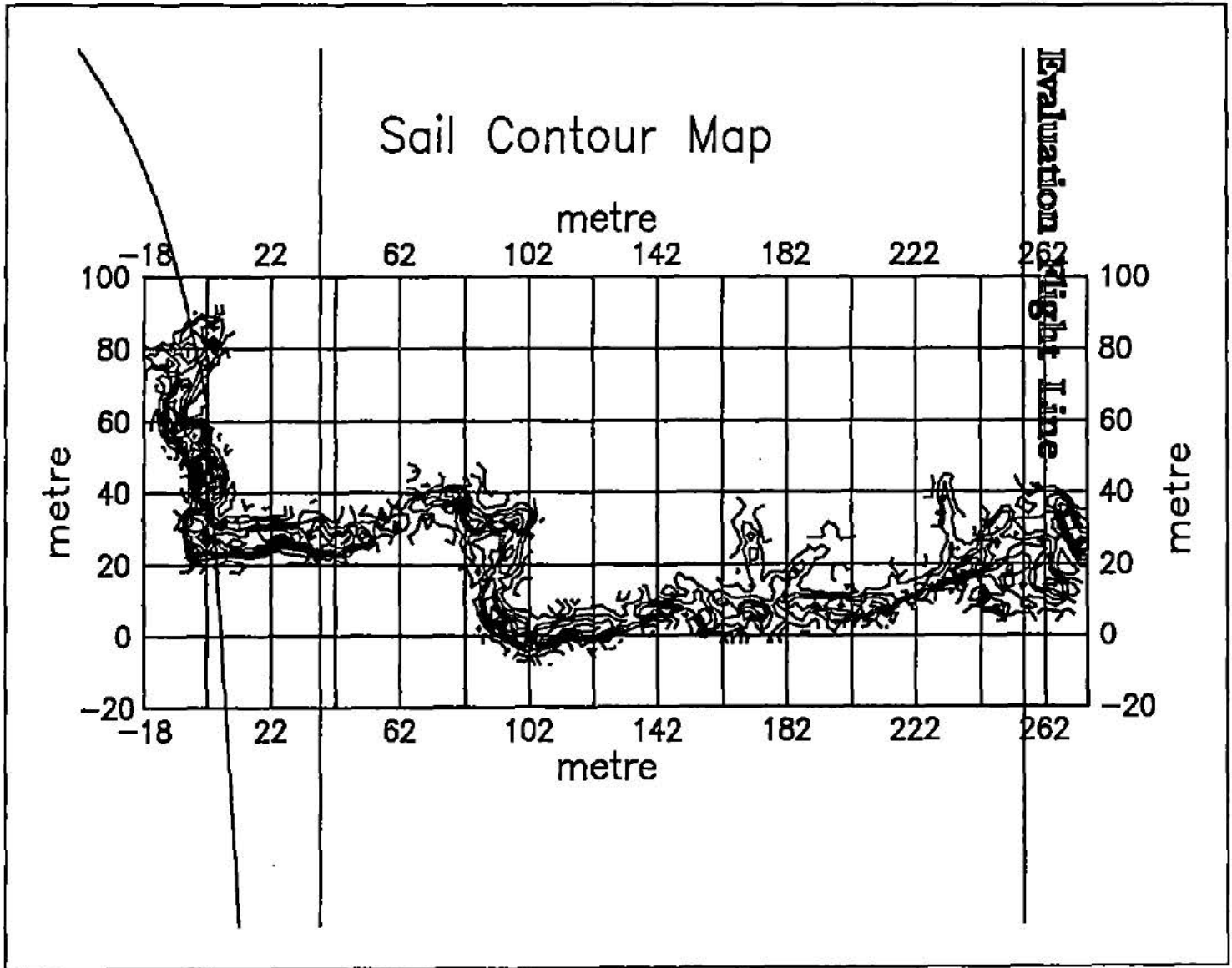


Figure 45 is an image obtained from the airborne video camera. It is this overflight that will be used for evaluation purposes.

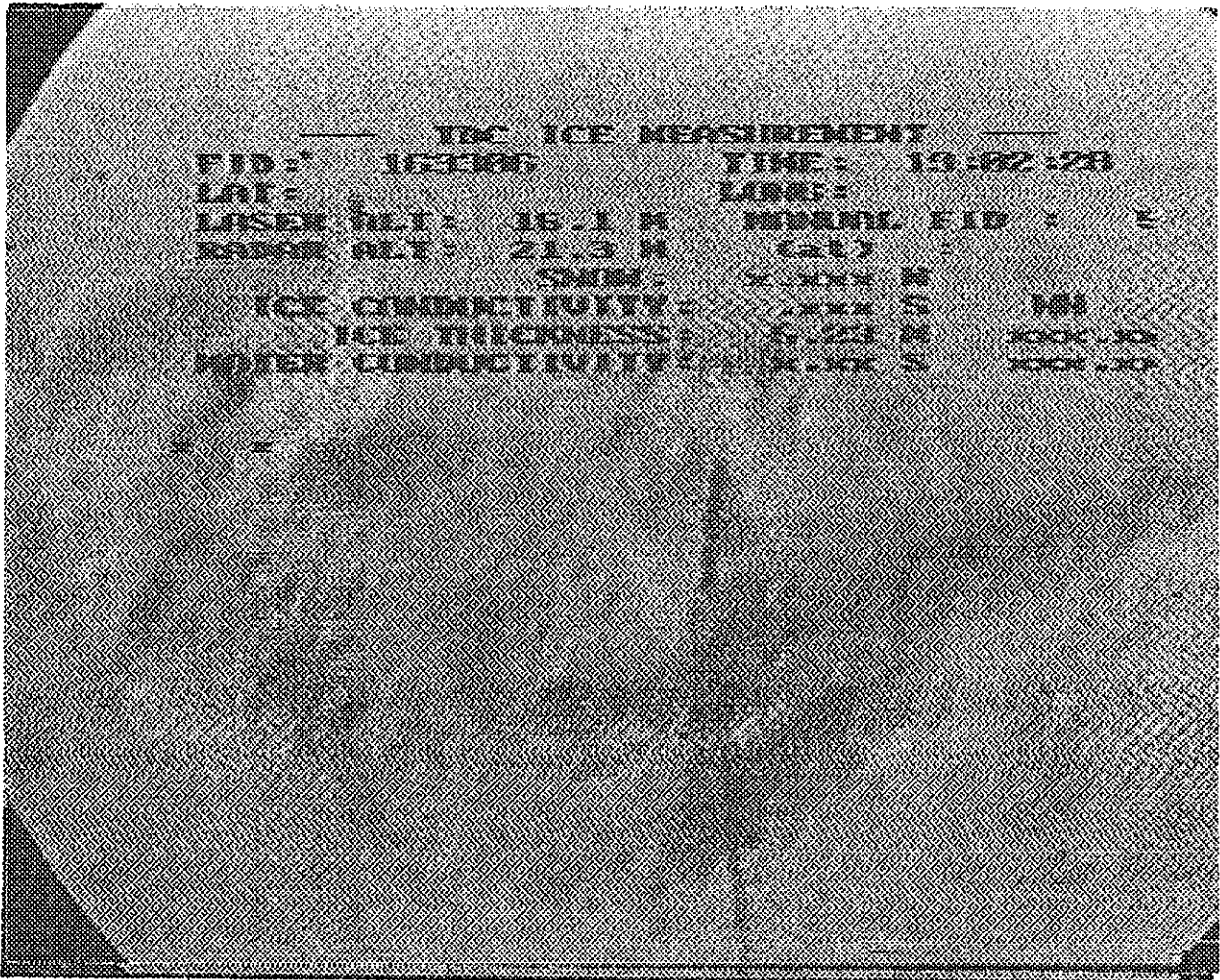


Figure 45: Frame Grabbed Image of Airborne System flying over Study Site.

The bird height over this swath was approximately 15 metres above the ice. According to AERODAT; the EM footprint, therefore, would be approximately 15 metres as well. Figure 46 illustrates the ground truth keel geometry for the area of the EM swath. The volume for this swath was calculated by using Simpson's, Simpson's 3/8 and the trapezoid rules found in a utility within SURFER. The total volume of the ground truth swath model was 6656 cubic metres. This value will be used to compare with 1 and 2-D models of the swath generated from the EM data.

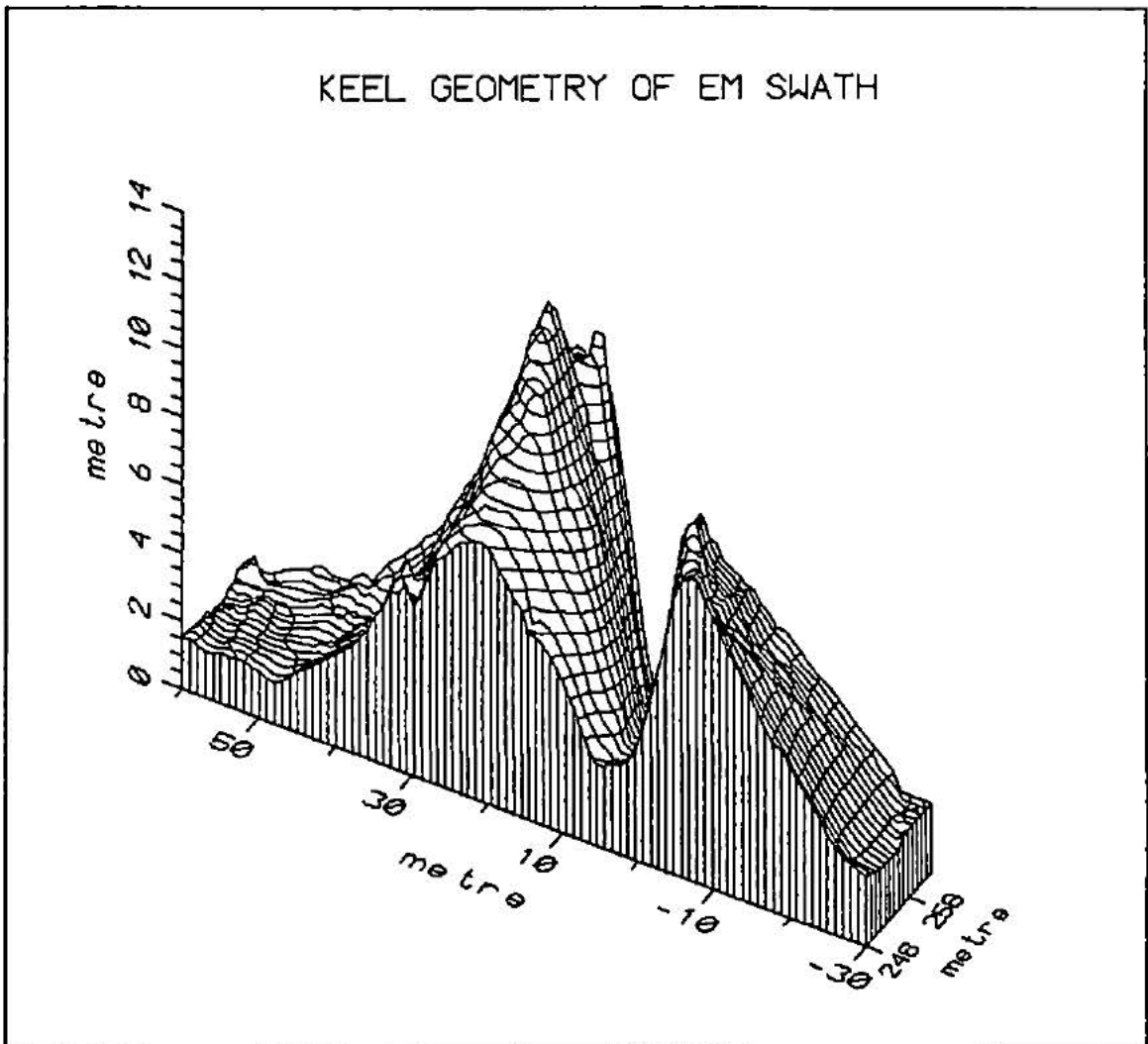


Figure 46: Ground Truth DTM in the Vicinity of the EM overflight.

8.51 EM Raw Data

A number of problems were encountered with the EM system during the field program. Scott Holladay of AERODAT reported these problems as follows:

. . . a number of hardware problems were encountered in "new technology" parts of the system, all of which have been corrected since the field work. These include excessive noise and drift, an error in the calibration, and a weak nonlinearity in the receiver preamplifiers. While the former three difficulties could be overcome in straightforward ways, the nonlinearity (an extremely rare problem in such EM equipment) required major efforts for each flight before the data could be adequately corrected for interpretation. The need for data recalibration meant that the results of the real-time ice thickness calculation, though available, were not usable. Even with the correction applied post-survey, the data are not sufficiently accurate for use in ice conductivity estimation. As a result, relatively few profiles of ice thickness, and none of ice conductivity, have been prepared from the survey results to date.

(Prinsenberget al., 1992)

Figures 48 and 49 illustrate the stripchart recordings of two raw data segments obtained from both the laser altimeter and EM signals during two ridge overflights. The figures have been labelled in order to avoid confusion of the line segments. Note also the fiducial marks are indicated at the top of the page on both chart recordings. The second stripchart is the selected evaluation overflight at the 255 metre mark of the ridge.

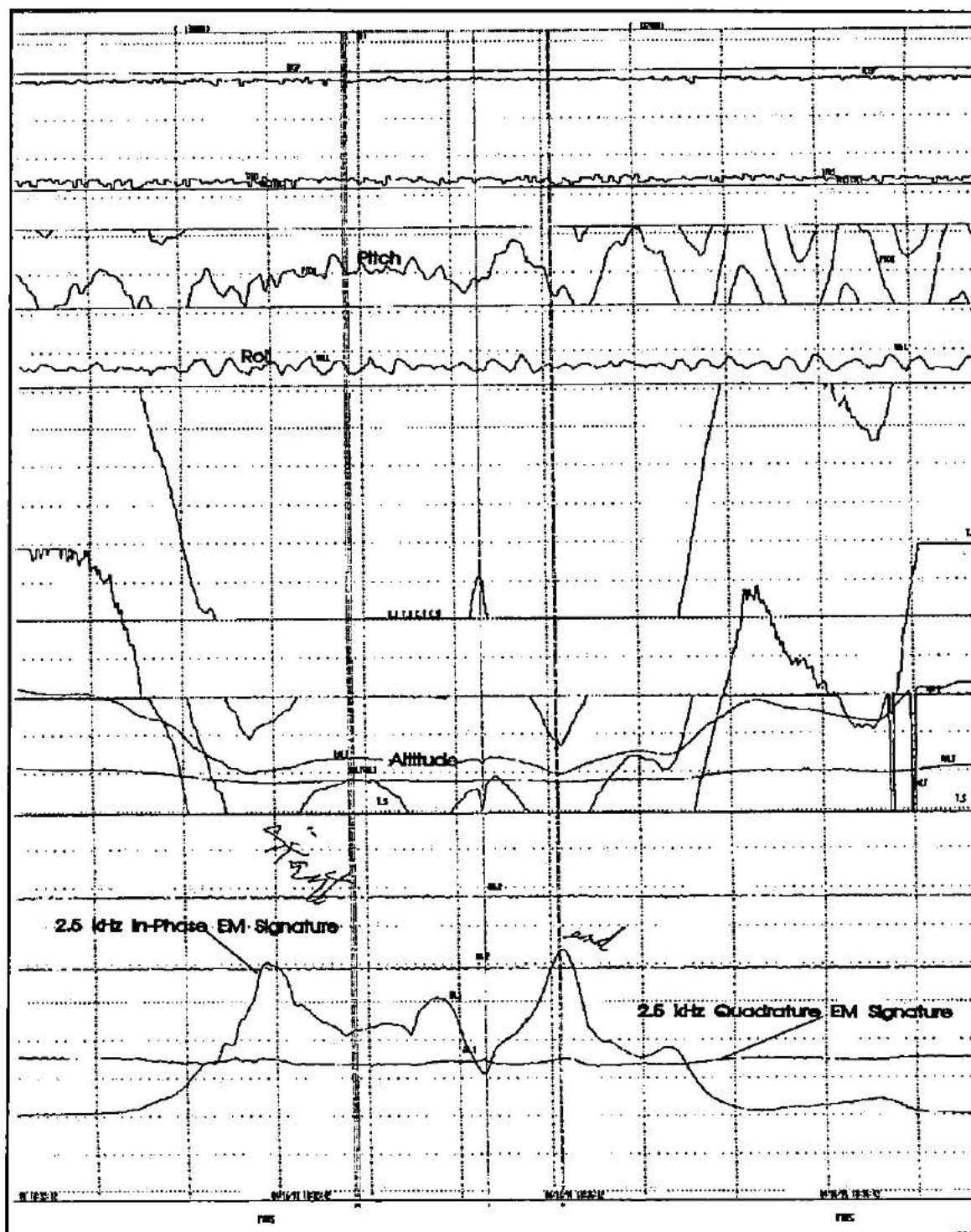


Figure 48: Raw Data Strip Chart Recordings (data supplied by AERODAT).

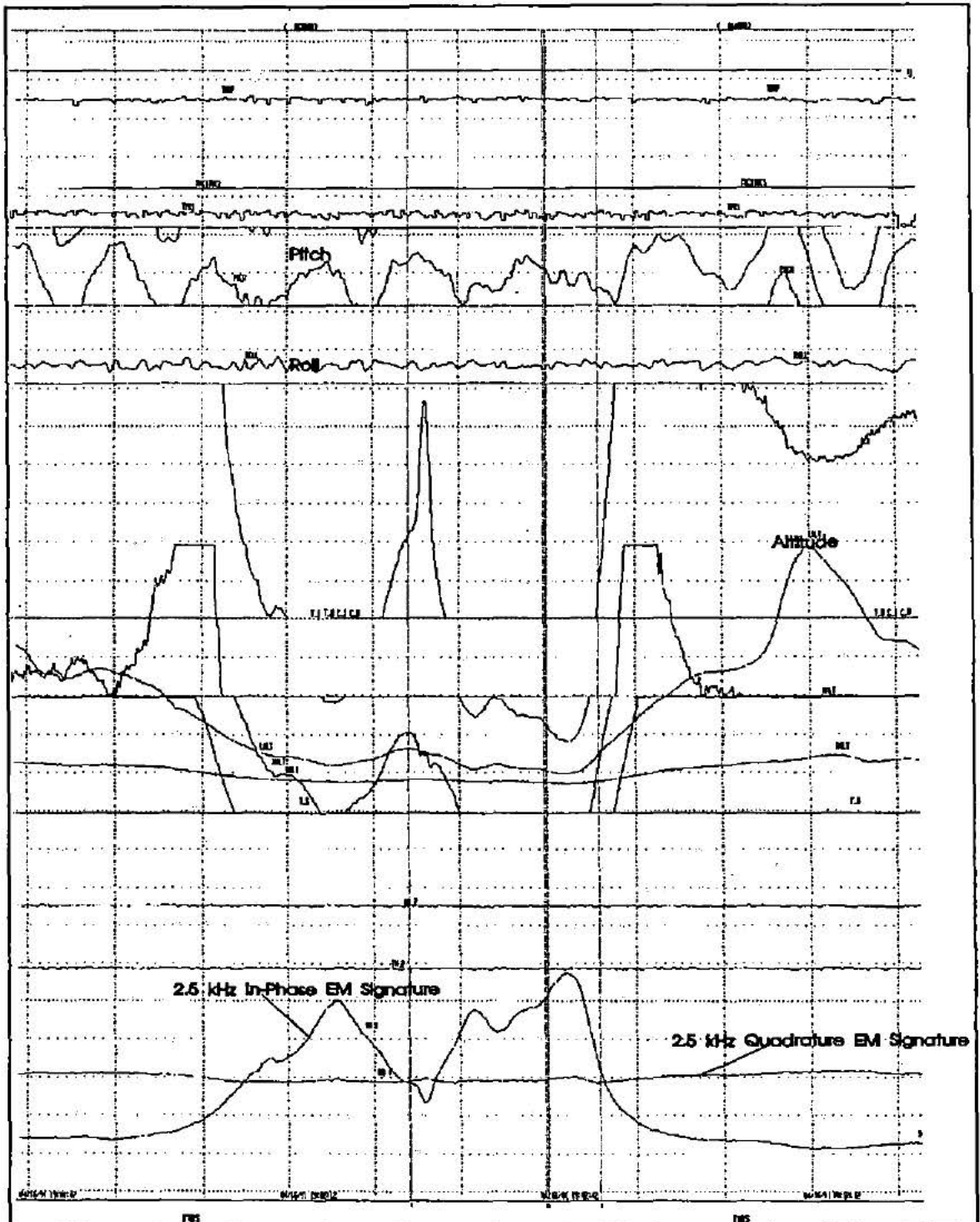


Figure 49: Raw Data Strip Chart Recordings of Evaluation Overflight (AERODAT).

8.52 1-D Inversion of EM Data

The raw EM data were interpreted by AERODAT using an in-house one dimensional (1-D) inversion process. Very little information about this technique was released. The 1-D interpretation technique used for sea ice applications is based on a model of layered conductivity structures of air, ice and sea water (Figure 49).

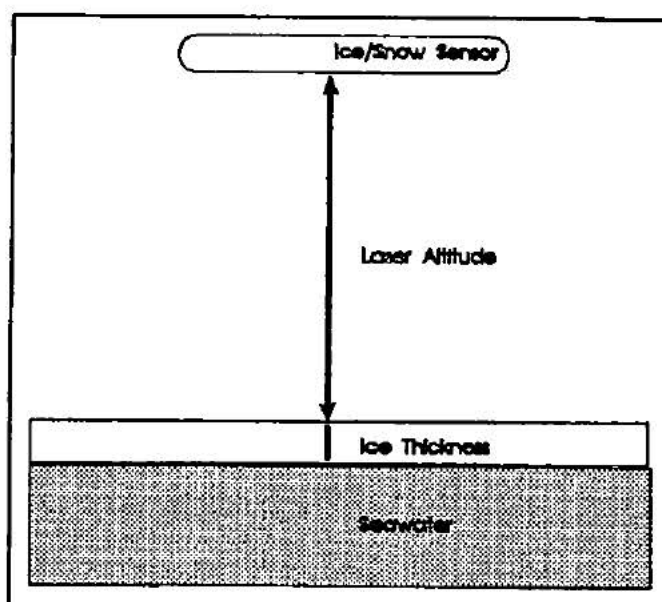


Figure 49: One Dimensional Model of Ice/Water Layers (Holladay et al., 1992).

This model varies only in the vertical dimension assuming that the footprint illuminates a flat plate (Holladay et al., 1992). This is adequate for regular level ice; however, this assumption breaks down when irregular steep-sided features are encountered. It has been noted in a number of papers that 1-D inversion techniques are too simplistic for irregular ice features such as ridges (Kovacs and Holladay, 1990; Holladay et al., 1990).

This is clearly evident in the concluding remarks of Kovacs and Holladay (1989):

It is clear that one-dimensional interpretation of sea ice thickness works well for relatively flat ice, but when major changes in ice thickness occur over lateral distances of less than about two bird elevations, errors will be introduced by the 1-D approximation due to footprint area effects. Thus, the measurement of sea ice thickness using AEM (Airborne Electromagnetic) techniques may no longer be limited by instrumentation problems, but rather by inadequate interpretation capability in the vicinity of complicated 2-D or 3-D ice structures.

(Kovacs and Holladay, 1989; pg 44)

Generally, inversion of geophysical data consists of a set of mathematical techniques operating directly on real data in order to generate a view of the structure which caused the real data (Vozoff and Jupp, 1975). Menke (1984), gives the simple example of temperature variations within the earth's crust to illustrate forward and inverse problem approaches used in inversion of geophysical data.

Let us assume that the temperature increases linearly with depth in the earth; that is, temperature T is related to depth Z by the rule $T(Z) = aZ + b$, where a and b are numerical constants. If one knows that $a = 0.1$ and $b = 25$, then one can solve the forward problem simply by evaluating the formula for any desired depth. The inverse problem would be to determine a and b on the basis of a suite of temperature measurements made at different depths in, say, a bore hole.

(Menke, 1984; pg 2)

The interpretative approach utilized by AERODAT involved two steps. The first step was to use a forward approach modelling routine. This routine calculated EM responses to a theoretically determined layered conductive model using specific parameters including:

- (1) bird altitude above the ice/water interface,
- (2) ice conductivity,
- (3) sea water conductivity.

The second step was to apply a nonlinear regression routine that iteratively attempted to obtain the best fit of the observed EM response to that of the calculated model. The assumed model obtained from the first step, was then used as the "starting model" to generate a first attempt at a model EM response. The difference between the model and observed EM responses was then calculated to determine a residual. This residual was used to estimate an appropriate modification to the model parameters which reduced the difference between the model and the observed EM response. The new parameters were then used to recalculate a new model EM response which was again compared to the observed response. This iterative process continued until the residual was within a specified tolerance or until the residual could not be reduced.

Before the interpretation of the EM data could be carried out, AERODAT performed a number of necessary steps to prepare the data.

- (1) All EM data were drift corrected. During each run, the bird was taken to a zeroing altitude of approximately 400 metres both before and after the ridge surveys. At this height, the system was not influenced by the conductive surfaces below and a baseline or zero level referencing of EM background could be measured. Drift encountered through the duration of the survey could then be accounted for by comparing the before and after background levels measured at the zeroing altitude.
- (2) EM data were then calibrated based on a ground truth correction factor (known EM response to a known ice thickness and conductivity).
- (3) Calibrated EM data, together with laser altimeter and bird pitch and roll measurements were then input into the inversion algorithm which estimated ice thickness (Scott Holladay, personal communications, 1992; Holladay et al., 1992).

Figure 50 shows the in-house AERODAT 1-D EM interpreted values for two

ridge overflights. Since the ice relief is averaged over a footprint (i.e. equivalent to the height of the instrumentation above the ice for a coaxial configuration), the interpreted data is a smoothed fit, generalizing the ice topography over the entire area of the footprint. This smoothing results in what amounts to a moving averaging filter (Kovacs and Holladay, 1990). One dimensional modelling takes this averaged footprint and equates this thickness to the ice thickness directly under the flight-line. The ice thicknesses illustrated in Figure 50 show the total ice plus snow thickness as well as the bird altitude above the snow surface. Note the X axis is in fiducial marks. These marks were used to associate data to the video tape recordings made during the survey. The dips in the records represent the ridge feature.

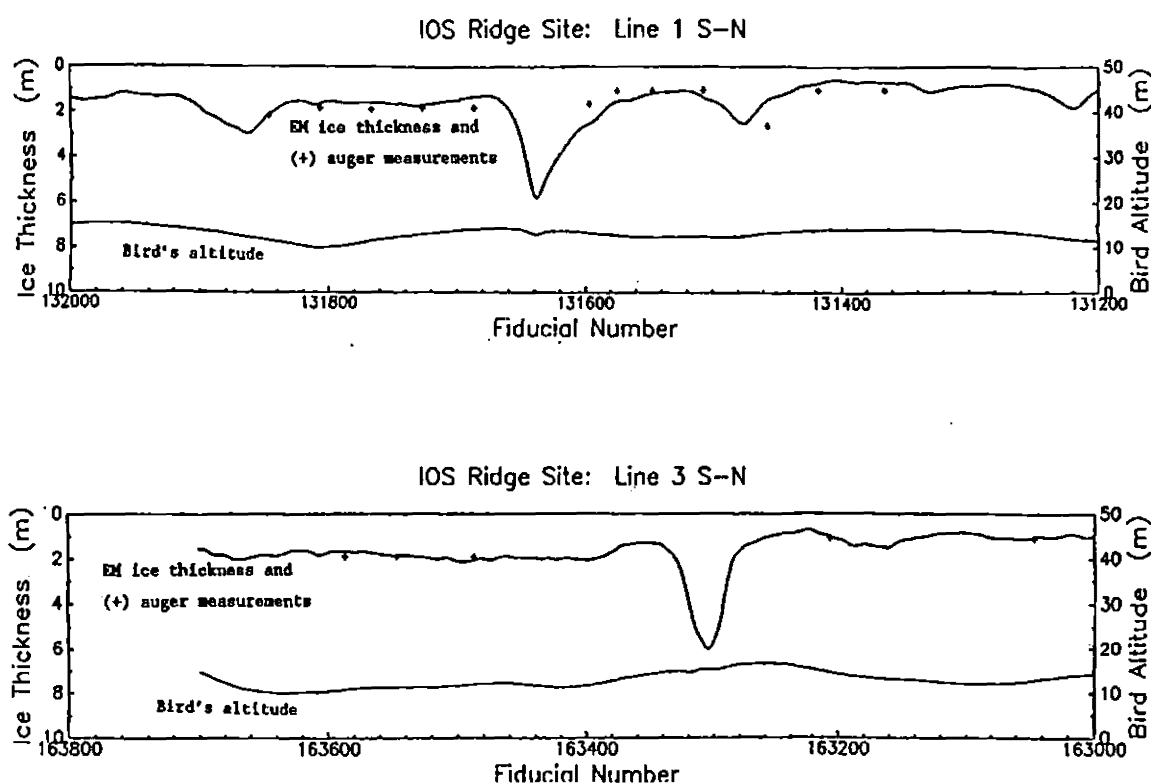


Figure 50: 1-D Interpretation of EM Anomalies (Holladay et al., 1992).

The second plot in Figure 50 illustrates the 1-D representation of the ice thickness at

the 255 metre mark of the ridge. Using the data supplied with this plot, a 3-D plot was generated assuming that the averaged footprint width extended halfway into the page and half way out of the page (i.e. infinite strike). This plot (Figure 51) was generated in order to compare volumetric calculations of the 1-D model with the actual ground truth survey data for the same swath. The 3-D plot should in no way be regarded as a topographic representation of the keel based on 1-D data. Only the centre line of the plot is resolved from the 1-D interpretation of the EM anomalies. The actual topography of the ice either side of the centre line may be higher or lower than the footprint average. The calculated volume of the 3-D model based on the 1-D interpretation was 3206 cubic metres of ice.

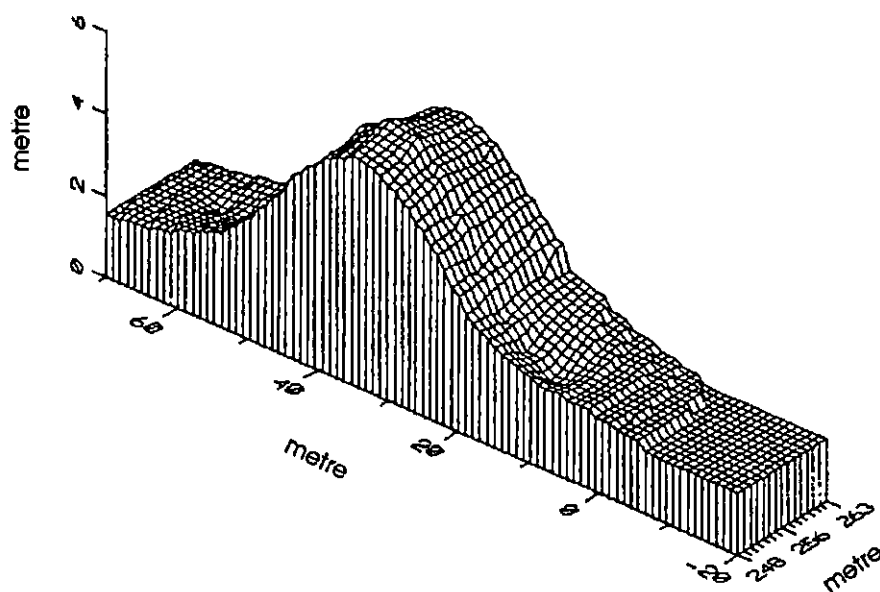


Figure 51: Assumed 3-D Model of Ice Keel based on 1-D Interpreted Data.

8.53 2-D Model Interpretation of EM Data

A 2-D interpretation method has been developed which is considered to be more appropriate for irregular sea ice ridges than the 1-D technique (Liu and Becker, 1990). For a complete explanation of the derived numerical solution of this technique see Liu and Becker (1990). The 2-D approach differs from the 1-D approach in that the conductivity structure of the ice is considered in the horizontal as well as the vertical planes. This technique uses a forward problem approach. That is, the technique utilizes a process of predicting data based on general principles (a model) and a set of specific conditions relevant to the problem (Menke, 1984).

A number of assumptions are required for this 2-D interpretive technique.

- These are:
- (1) It is assumed that the general shape of an ice keel is similar to a Gaussian curve.
 - (2) Sea ice is transparent to EM waves.
 - (3) Sea water is regarded as a perfect conductor.

As has been seen, keel geometry does not necessarily comply to the classical triangular structure that is generally reported in the literature. A Gaussian curve may be appropriate in linear portions of the keel, however, compression ridges are characterized by their frequent bends and adjacent rafted features. In these common nonlinear portions of the ridge, the geometric attributes would be far more complex than a Gaussian curve. Such is the case at the evaluation overflight area where there are two distinct lobes of ice. The assumption of conductivity of the two layers (ice and sea water) would appear to be reasonable based on the large conductivity contrast that occurs at the ice/water interface. In reality, this interface may not be so clear due to sea water voids between ice blocks. Skin depth penetrations for the 2.5 kHz and the 102 kHz transmitters were calculated using equation 11 in order to assess the EM wave attenuation through both ice and sea water (Table 7).

Table 7: Skin Depth Calculations for EM Transmitters.

Transmitter Frequency	Sea Ice Resistance Range		Sea Water Resistance
	62 (ohms)	5 (ohms)	0.4 (ohms)
2.5 kHz	79.21 m	22.49 m	6.36 m
104 kHz	12.4 m	3.52 m	1.0 m

Measured salinities of ice adjacent to the ridge indicated that the ice had relatively low bulk concentrations of salts (approximately 5-6 ppt--Prinsenburg et al., 1992). The conductivity of this ice would, therefore, be low and, as a result, the skin depth would be on the deeper end of the calculated range. This would apply to solid ice and not unconsolidated ice containing sea water voids. Sea water entrapped within the ice would probably reduce the skin depth to some degree. In contrast, the sea water skin depth calculated was much thinner (6.36 m and 1.0 m for the 2.5 and 102 kHz transmitter respectively). Attenuation of the EM wave would occur more rapidly in the relatively high conductive sea water body than in the low conductive ice layer. A sea water skin depth of 6.36 metres for the 2.5 kHz transmitter would suggest that the conductive boundary detected by the EM receiver would not be abrupt but rather over a region. Assumptions (2) and (3) are, therefore, not accurate but the conductive contrast between the ice and sea water interface could be simplified to comply with these general assumptions.

Lui and Becker (1990) used a scaled laboratory model to verify the numerical solution of the 2-D approach. This model is illustrated in Figure 52. In this model (and also the numerical solution) the keel relief is considered to follow a Gaussian curve governed by the following equation:

background level (labelled "B"). Characterization of the shape of the anomaly is defined by "d" which is the anomaly width at one half the anomaly amplitude.

The anomaly amplitude and width depend not only on the geometry of the ice keel but also on the bird height above the ice-water interface. In order to minimize the influence of factors other than keel geometry, we also use the normalized anomaly amplitude, which is the anomaly amplitude normalized by the background level (i.e., ratio C/B), and the normalized anomaly width, which is the anomaly width normalized by the average bird height above the sea water surface. (Liu and Becker, 1990)

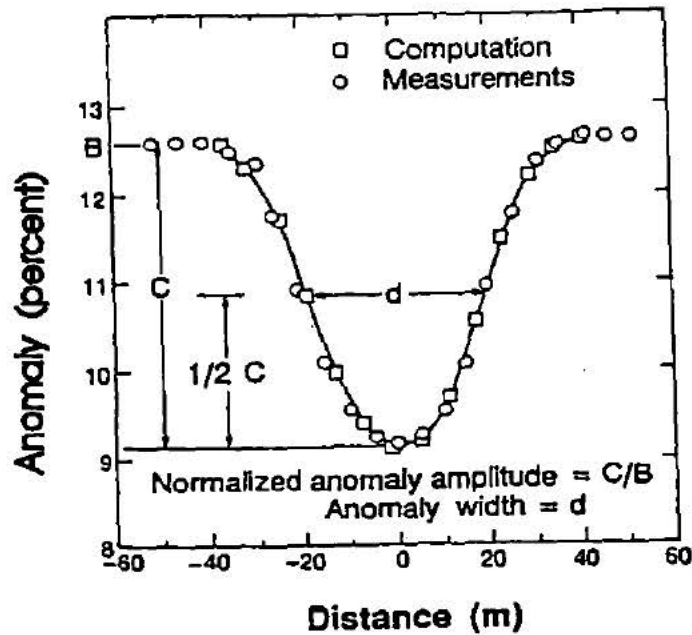


Figure 53: Comparison of 2-D Laboratory Results with 2-D Numerical Solutions (Liu and Becker, 1990).

In order to interpret EM field data anomalies, it is necessary to develop a strategy which relates the EM anomalies to the actual keel geometry. Using this 2-D technique, it is necessary to estimate the maximum keel draft (A) and the half width of the keel (W) from the observed EM anomalies. For this purpose, an interpretation nomogram was constructed based on experimental and numerical calculations of a

variety of keel shapes and sizes (Figure 54).

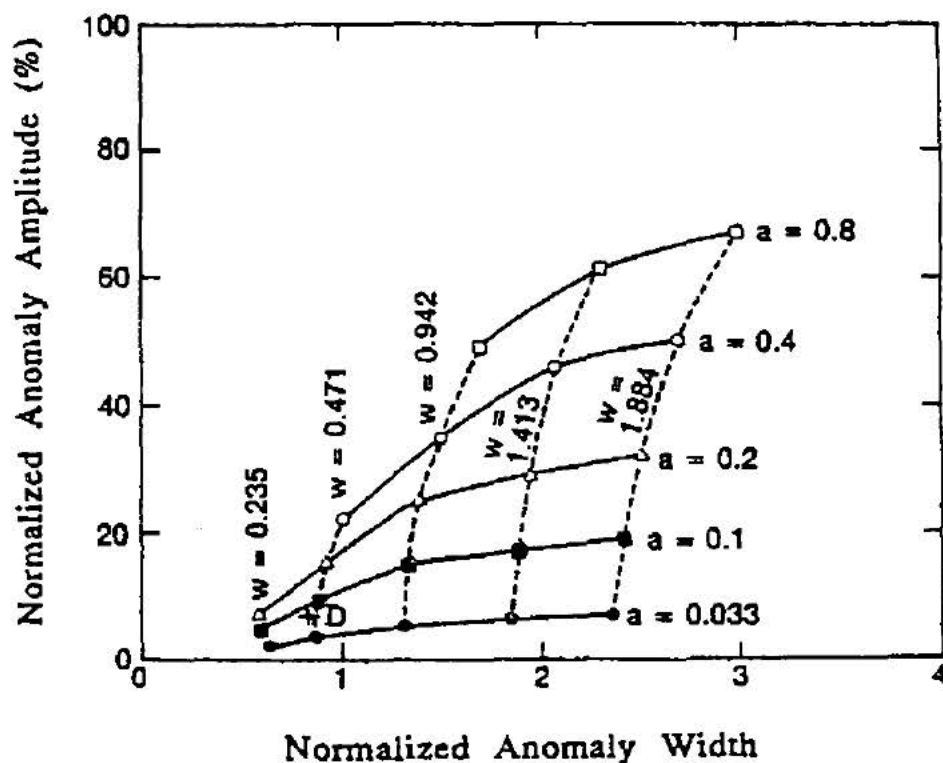


Figure 54: Nomogram Look-Up Table (Liu and Becker, 1990).

This nomogram allows the user to obtain the A and W values from the field EM anomalies. These two values can then be entered into Equation 15 to reconstruct the keel geometry at any location along the line of flight. The nomogram compares the normalized anomaly amplitudes (small a), that is, the EM anomaly amplitude as the system encounters the keel divided by the EM background response expressed as a percentage, to the normalized anomaly width (small w). The nomogram can be used for the in-phase component of the resultant EM wave for frequencies over 2 kHz (Liu and Becker, 1990).

According to AERODAT, the 2-D footprint in the line of flight is approximately 10% of the flight height above the ice. The approach to the footprint size is smaller than the 1-D footprint as the 2-D method incorporates a computational algorithm which considers the rapid forward moving changes in the EM signal responses as the EM field encounters an ice ridge. To date, the footprint's eccentricity (perpendicular line to the line of flight) has not yet been determined. The footprint size in the line of flight for an EM system sampling at 20 hz (actual sampling rate used in the field) travelling at 100 kph at a vertical height of 15 metres would therefore be about 1.5 metres sampled every 1.5 metres of travel (Scott Holladay, personal communication 1992).

Analysis was performed on the EM anomalies of the 2.5 kHz transmitter data. A few problems were encountered during the analysis of the data. The first problem, as previously mentioned, was positioning the EM fiducial marks in relation to the ground truth XYZ coordinate system. The second problem was the determination of the speed of the bird as it travelled over the ice. The effect of the bird speed influences the width calculation of the keel feature. A fast bird speed would yield anomaly data as a sharp spike, whereas, the same keel measured by a slower moving bird would yield a broader anomaly data curve. If the speed is not known, then there is no way of telling the spatial attributes of the data. A thorough investigation of the bird speed produced a speed range of 59.5 - 87 km/hr. These speeds were based on GPS readings and speed averaging of the bird over a number of seconds before, during and after the ridge overflight (the latter carried out by AERODAT). A visual estimate of the bird speed from video records using known ground control points was approximately 78 km/hr. Based on a ground speed of 60 km/hr, the width and maximum draft were estimated by AERODAT to be 35 ± 4 m and 14 ± 3 m respectively. In contrast, a ground speed of 87 km/hr would increase the keel width to 52.5 ± 6 m. This discrepancy of speeds indicates a need for developing an accurate system for measuring ground speed. Using the 60 km/hr speed, a 3-D DTM was generated using Equation 15 multiplied by the width of the swath

(say 15 metres). This DTM (Figure 55) represents the keel geometry as calculated by the 2-D interpretation technique.

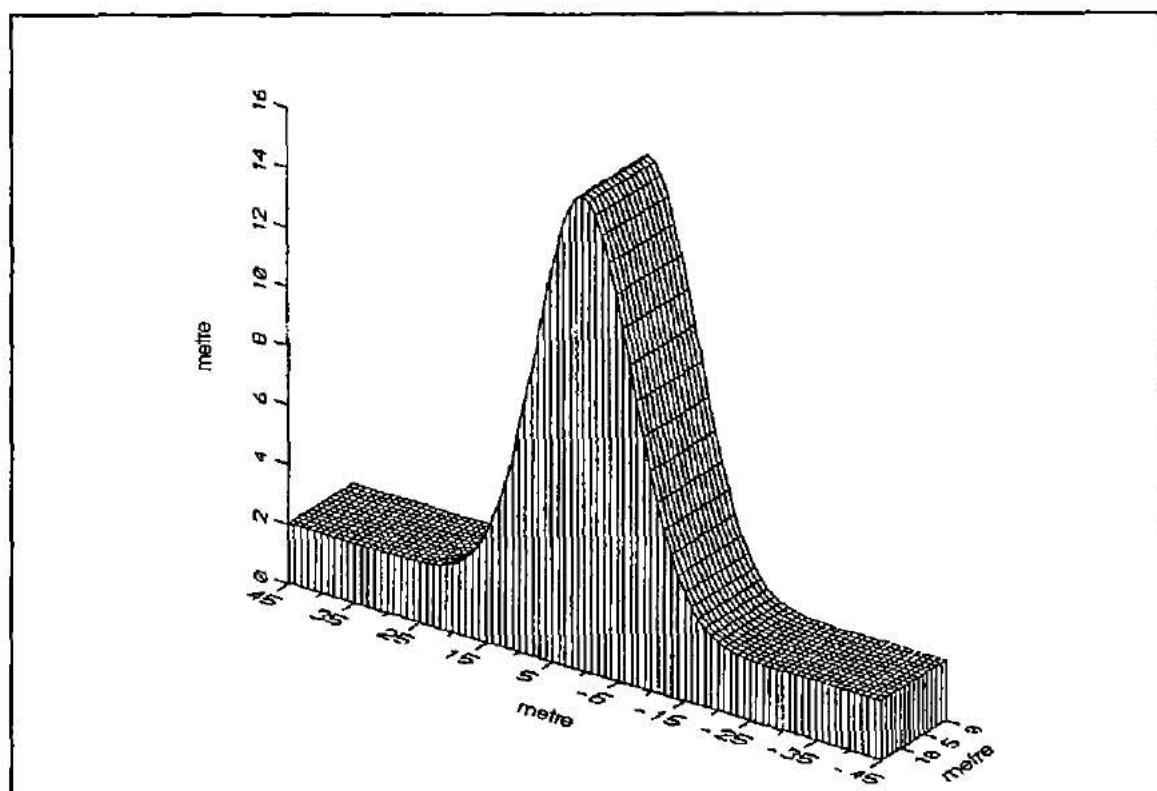


Figure 55: Gaussian Curve of Keel based on 2-D Analysis.

Volume ranges were calculated for keel maximum and minimum drafts of 11 to 17 metres (14 ± 3 m) for, (1) keel widths of 31 to 39 metres (34 ± 5 m); value calculated by AERODAT for a bird speed of 60 kph, and (2) keel widths of 46.5 to 58.5 (52.5 ± 6 m); value calculated by AERODAT for a bird speed of 87 kph. These values are as follows:

2-D EM volume	5411 cubic metres (minimum:width 31m; draft 11m)(60 kph)
2-D EM volume	7971 cubic metres (maximum:width 39m; draft 17m)(60 kph)
2-D EM volume	6766 cubic metres (minimum:width 46.5m; draft 11m)(87 kph)
2-D EM volume	10620 cubic metres (maximum:width 58.5m; draft 17m)(87 kph)

9.0 Discussion

9.1 Evaluation of Airborne EM Thickness Sensor

Visual examination of the ground truth DTM for the EM swath clearly shows a two lobe keel structure. Air photographs taken of the same area suggest that more than one ridge building event occurred generating what appears to be a series of pushes. As a result, a number of sharp narrow ridges were developed creating a challenge to EM keel feature detection and the techniques used to interpret the EM data. The maximum swath draft of the keel measured by the submersible was approximately 15 metres which occurred in the larger of the two lobes. The general feature width was approximately 80 metres.

Comparison of the ground truth DTM with the 1-D DTM illustrates a very poor resemblance. Calculation of the 1-D DTM volume was less than half the volume calculated for the ground truth swath. As can be seen in Figure 50(b) and Figure 51, there is no indication of two distinct lobes. From the ground truth data, the peaks of these two lobes are separated by a significant distance of about 30 metres. It would appear that this technique has very poor spatial resolution as even large coarse features cannot be resolved. Since all 1-D analysis was performed by AERODAT, it is uncertain as to whether the keel estimation is a reflection of the poor ability of the modelling technique or possibly the result of the data treatment (i.e. sub-sampling of the survey data which would render a generalized representation of the feature). Further, the interpreted keel width is only 62% of the ground truth width. This significant underestimation of keel detail and volume concurs well with the findings of other studies using 1-D modelling for irregular ice features (Kovacs and Holladay, 1989).

The comparison of the ground truth DTM with the 2-D DTMs was somewhat more promising than the 1-D comparison. The maximum draft obtained from the 2-D approach was similar to the ground truth draft of 14 metres. It should be noted that

this estimation was made by AERODAT after the keel ground truth geometry was released. In addition AERODAT only used one of the two EM lobes during their determination of the keel dimensions assuming that the second lobe, the larger of the two, was some kind of artifact of drift. The ground truth geometry of both the keel and the sail, however, clearly indicates a two lobes structure. In addition, the smaller lobe selected by AERODAT was only 8 metres thick according to ground truth data. AERODAT, considering this single lobe to be the entire keel, apparently overestimated a feature of approximately 8 metres to be 14 ± 3 metres. This value of 14 ± 3 metres was obtained from the nomogram found in Figure 54 possibly suggesting that adjustments are needed in order to improve the nomogram. Since the nomogram used here was generated from a different coil size and separation (i.e. coil transmitter -- 6 kHz; coil separation 6.5 metres), it would be logical to design a nomogram specific to this coil configuration. Such a nomogram would theoretically be more accurate.

The width of the 2-D DTM was not clear as the speed of the bird was measured by a number of indirect methods. The speed range yielded keel widths of between 35 ± 4 m to 52.5 ± 6 m. The volumes of the corresponding DTMs ranged from 66% to 160% of the volume obtained from the ground truth DTM. If the speed could be accurately determined, the keel volume calculation could be improved. Since the 2-D algorithm seeks only the maximum draft of the encountered keel, this keel could be broken into two separate keels which consider the geometry of the two distinct keel lobes. Unfortunately, since the data were not made available, this step could not be performed.

During the airborne survey, neither the 1-D or 2-D interpretive methods were able to output ice thickness estimates in real time. Postprocessing of data was time consuming and as a result the raw data from the field project would have been of little value for tactical ice breaker operations requiring immediate navigation routing. Recent modifications since the 1991 field project have resulted in the implementation of a working 1-D method for calculating real time ice thickness. At present, the 2-D

method has not yet been developed for real time thickness output. Experimentation has been focused on the development of neural network techniques which utilize 1 and 2-D inversion techniques (see Appendix F for 1 and 2-D neural networks). This technology is required in order to obtain fast processing of EM response patterns, in flight instrument calibration, instrument drift corrections and pitch and roll resolving of raw field data (Holladay et al., 1992). The training and architecture of these neural networks are described in detail in Holladay et al. (1992).

Although both 1 and 2-D interpretation techniques did not estimate keel geometry very well, the raw EM strip chart recordings of the evaluation overflight appear to resemble the keel geometry very well. A number of cross sections were sliced through the ground truth DTM at the EM swath area. Figure 56 illustrates the irregular geometry of the keel at this location showing DTM grid lines located at the 253, 255 and 257 metre mark.

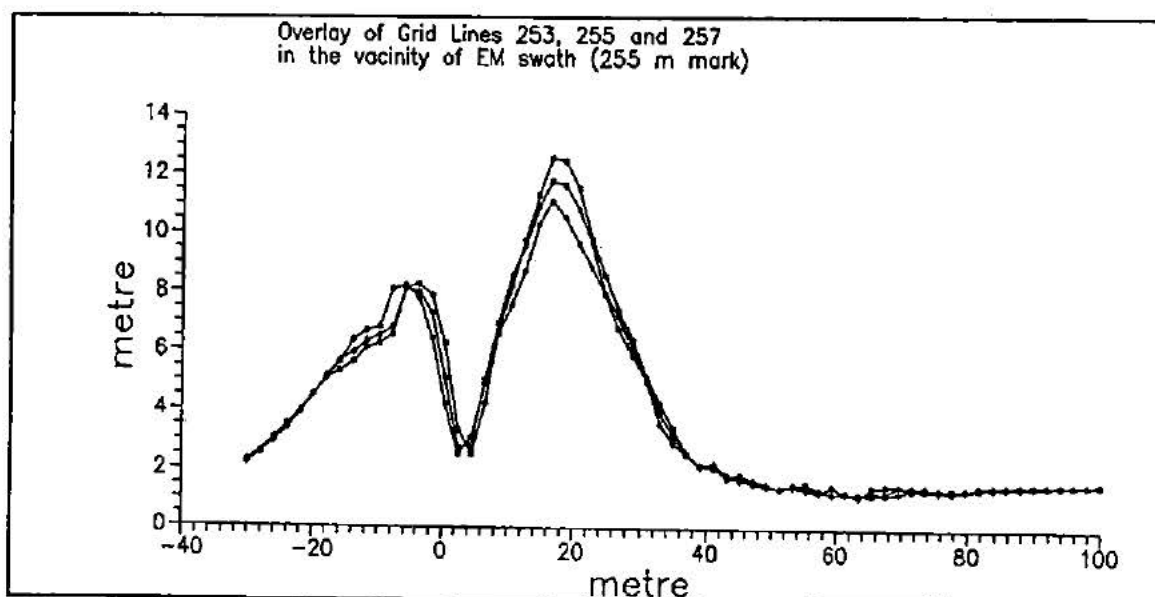


Figure 56: Ground Truth Grid Cross-Sections of EM Swath.

Comparing these cross sections with the raw data of the EM anomalies at the same location indicated that the airborne system's ability to detect the irregular geometry of the keel was remarkably good. The fluctuations in the 2.5 kHz EM in-phase response to the keel is very similar to the shape of the keel geometry (Figure 57). Just as the ground truth data indicated a two lobe structure, it is clear from the EM in-phase response that detected EM anomalies were consistent with a similar two lobe structure (Figure 57). Since neither the vertical metre equivalent or horizontal scale of the in-phase anomalies were accurately known, the EM signal was stretched (but not warped) in both axes to fit the gridded data. The fit is very close.

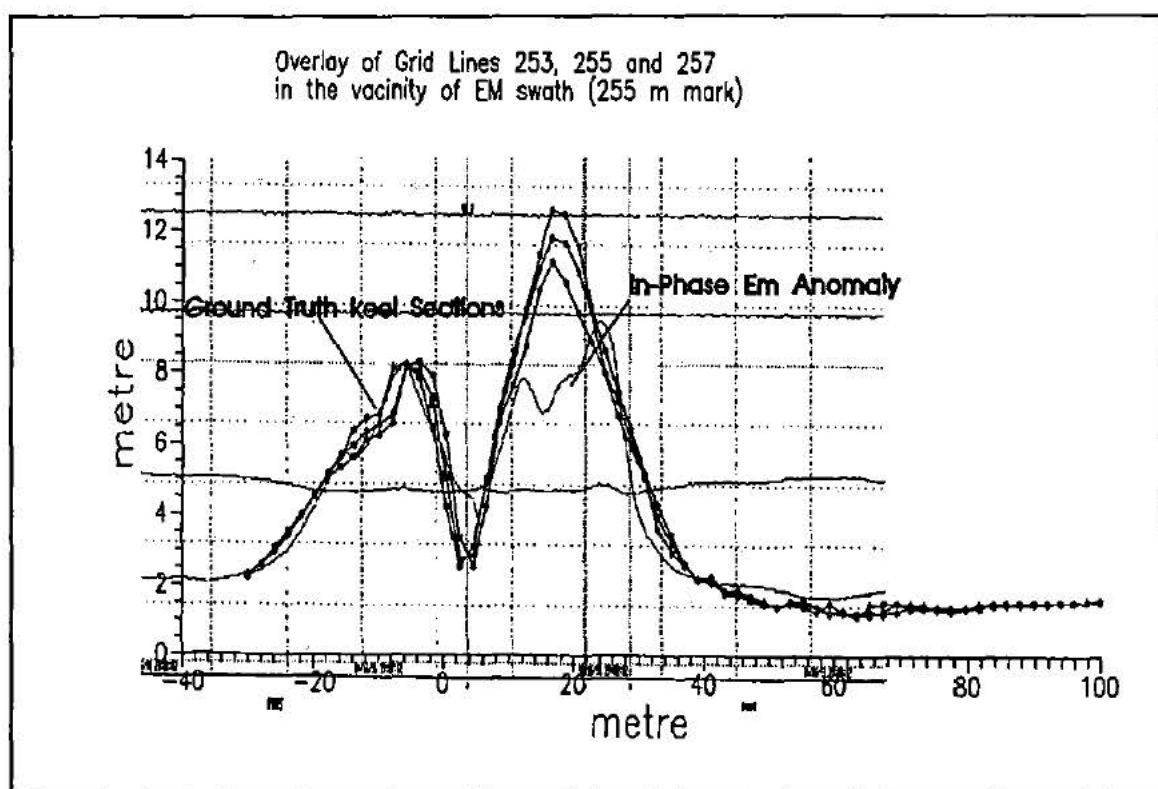


Figure 57: Comparison of EM Anomalies with Grid Cross-Sections.

Although it is not appropriate to scale the EM anomaly without correcting for altitude variations, pitch, roll and ice conductivity, there is sufficient evidence to suggest that the EM instrumentation is much more sensitive than the two interpretation techniques indicate. From this comparison, it would appear that the spatial resolution in the

horizontal plane is of the same order as the gridded data (i.e. 1-2 metres). Comparing the vertical component of the EM anomaly with the keel relief is somewhat more subjective. The EM anomaly for the larger of the two lobes deviates from the gridded data. It is possible that at this depth the keel consisted of an unconsolidated block structure containing large voids of sea water. The large volume of sea water would influence the EM field resulting in an anomaly indicative of a shallower keel.

As noted earlier, there were a number of hardware problems encountered during the 1991 field season. Since the 1991 field season the system has been modified eradicating hardware problems encountered during the 1991 field program (Scott Holladay of AERODAT, personal communication, 1992). There were, in addition to these system malfunctions, some deficiencies in the actual working design the most important of which was the need for a better method of determining the location of the bird above the ice. This is especially important when the ice is moving as is often the case in the Arctic Ocean. Without some sort of tie down system, it is very difficult to associate the bird location with the ice geometry. The GPS readings measured from the helicopter were only accurate to within 25 metres in the horizontal plan. The resolved bird speed range of 60-87 km/hr was far too sloppy making it difficult to interpret the spatial component of the EM anomalies.

From an operational point of view; the flying of the airborne system was challenging to the pilot. Having never towed a bird before, the pilot needed to carry out a number of practice flights using an oil drum to simulate the towing conditions. The relative horizontal and vertical motions of the bird to the helicopter, coupled with low altitude flying required uninterrupted concentration as well as good flying conditions. Since the bird was towed, the pilot could not see where the bird was and, therefore, had to rely heavily on the onboard altimeter and bird laser altimeter. The targeted height for the airborne surveys of approximately 15 metres proved to be extremely difficult due to the changing air currents, accelerations/decelerations of the bird relative to the helicopter and the fluctuating bird to helicopter distance.

9.3 Ridge Geometry Attributes

Volumetric calculations of the generated DTMs were made in order to compare the two different interpolation techniques. Subjectively, the appearance of the sail DTMs generated from both a stochastic and a triangulation interpolation technique were remarkably similar. The volumes, although calculated differently (Stochastic method: Simpson's, Simpson's 3/8 and trapezoidal rules; Triangulation: cross sectional end area calculation) gave similar results. Sail volumes were 12437 m³ for the kriging interpolation DTM and 11035 m³ for the triangulation interpolation DTM for ice accumulations above and including 0.22 metres. This Z value of 0.22 metres was chosen as this was only slightly above the approximate 0.2 metre freeboard of the level ice (ice above water level in level ice). By choosing this elevation, the regular grid data outside of the sail feature was discarded. This comparison of the two DTMs is therefore of the ice accumulation within the sail feature only. A similar comparison was made for the keel DTMs. The level ice draft to the water level measured at the TARS entry hole was approximately 1.8 metres. The volumes of ice accumulation below the level ice draft were 116226 m³ and 107157 m³ for the kriging and triangulation DTMs respectively.

The percentages of the sail and keel ice volumes for the respective interpolation technique are as follows (Table 8):

Table 8: Percent of Ice Contained within the Sail and Keel portions of the Ridged

Percent of Accumulated Ridged Ice above and Below Level Ice		
Interpolation Technique	Sail Ice	Keel Ice
Kriging	10.7%	89.3%
Triangulation	10.3%	89.7%

Comparing these volumes from either of the interpolation techniques suggests that of the total accumulation of ridged ice, approximately 10-11% was contained within the

sail (above the level ice) and 89-90% was contained within the keel (below the level ice) assuming equal porosity of sail and keel rubble. These percentages compare well with the expected isostatic balance of approximately 90% below water level and 10% above (Sanderson, 1988). During the ridge building event(s) the ice was not, however, 2 metres thick. Block thicknesses measured from the sail were of the order of 0.4 metres indicating a much thinner level ice thickness during the ridge formation. As a result, the actual volume of the keel ice would, therefore, be somewhat larger. Sublimation of exposed sail ice, accumulation of snow on and in the voids of the sail, consolidation of the keel and the melting of the keel ice due to the relatively warm sea water would all contribute to the aging of the ridge over time. The vertical growth of ice adjacent to the ridge since the ridge formation has hidden the true keel perimeter making it virtually impossible to assess the true volume of the keel ice. Figure 58, taken from the underwater video coverage of the keel, shows how the vertical growth of the level ice has enveloped the broken block structure of the keel near its edges. The surface area of the ridge above and below level ice was also calculated but only for the stochastic DTM. The sail area was calculated to be 7879 square metres and the keel area was 40441 square metres. In other words, the keel surface area was approximately 5 times the sail surface area. In addition 22 cross-sections were sliced through the ridge in order to generate aspect ratios of ridge geometry. These cross-sections can be found in Appendix G.

Measurements taken off of these cross-sections yielded the following information:

Sail to Keel Depth 4.03 (\pm 0.77):1

Sail to Keel Width 2.8 (\pm 1.4):1

The depth aspect ratios were generally very consistent, however, the width statistics were highly variable. Both of these statistics agree well with those found in the literature (see Figure 8a). Upon examination of the cross-sections it became apparent that classical cross-sections (i.e. those found in the literature) are only valid when the ridge geometry is consistently linear over tens of metres. This is especially true when viewing the keel geometry. As mentioned earlier, where there are abrupt bends in the ridge formation, ice accumulations are distributed quite differently.

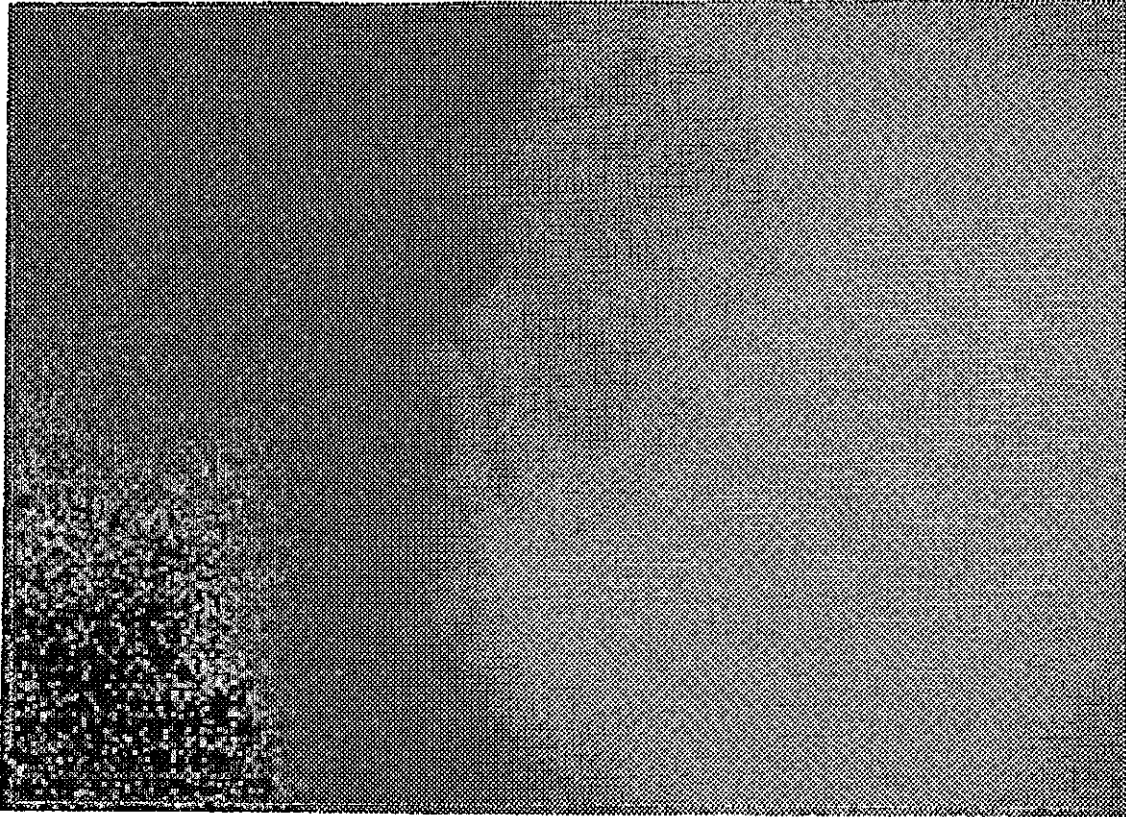


Figure 58: Upward Looking Underwater Video Image of Enveloped Keel Rubble.

The keel widths at these locations are much wider than those obtained from strictly linear ridged areas and often contain additional lobes of ice with no associated surface feature (see cross-sections 110, 120, 240, 260 metres marks--Appendix G). This is possibly an ice management problem where large volumes of ice have failed and been crowded into confined boundary situations. Cross-sections at the 160, 170 and 220 metre marks (Appendix G) show significant offsets of sail and keel features. This offset of ice features was also noted by Melling et al. (1993). In view of the air photographs taken directly over this area, there appears to be surface features departing from the ridge at 90° and 45° angles. These smaller ridge offshoots correspond with the sail/keel offsets and may be related to rafting events and/or areas where cracks in the compressive contact interface propagated due to stress concentration at the contact zone. Either one of these scenarios could be used to explain a bulldozing effect of the sail feature with respect to the keel.

It should be noted that both of the softwares used to generate the DTMs had positive and negative features. The stochastic software clearly produced superior visual representations to that of the triangulation program and had a input data limit almost three times that of the triangulation program. This comparison is true only of the software and not the techniques. The most significant problem encountered with the stochastic techniques were their lack of flexibility in responding to the varying data densities throughout the generated DTMs. The rectangular grid generated nodes in areas where there was no data present. The stochastic techniques did not use the input data in the output DTM. This resulted in the loss of the integrity of the original data as revealed by the residuals. Since the data showed great fluctuations in the Z component, the stochastic process of fitting a surface to the data made it difficult to restrain the DTM from producing fictitious artifacts in sparse data regions. This was overcome by adding restraining points at strategic locations in the data set. The stochastic techniques also smoothed out the roughness of the ice feature. The large jagged ice blocks that were observed both in the submersible data and the underwater video coverage of the keel were rounded out by the statistical derivations required to generate grid nodes at regularly spaced locations. Although the triangulation software was filled with limitations, the technique appeared to be much better suited for this type of application.

10.0 Conclusions and Recommendations

Extensive ground truth surveys were performed in order to evaluate the performance of the state-of-the-art airborne remote sensing system. Unfortunately, only one of the seven airborne survey flights could be used for this comparison.

Ground truth data for the study site were resolved yielding large amounts of data. Digital terrain models were generated from this data based on two different interpolation techniques. These techniques produced similar models and volumetric results. The geometry of the ridge varied in shape at a number of locations. Linear portions of the ridge tended towards the classical triangular sail and keel shapes found in the literature; however, nonlinear portions of the ridge exhibited more complex geometry.

Sub-sampling of the ground truth data was performed in order to generate an additional DTM of the area of the remote sensing swath. Volume calculations of this DTM were made in order to assess the interpretation of the EM data. During the course of this study, numerous conversations with Scott Holladay of AERODAT proved beneficial as raw field data were not released due to the proprietary nature of the project. As a result, much of the EM interpretation was performed by AERODAT. One and two dimensional analyses were performed on the EM anomalies and from this analysis, 3-D models were generated for volume comparisons with the ground truth DTM. As was expected, the 1-D interpretation of the EM anomalies was very poor when compared to the ground truth data. The calculated 1-D volume was less than one half of the calculated ground truth volume. This significant under-estimation of the keel feature is attributed to the assumed flat plane averaging effect of the EM footprint. The 2-D interpretation of the EM anomalies yielded better volumetric results, however, there was no accounting for the two lobes structure observed in the ground truth data. AERODAT performed a 2-D analysis on the smaller of the two lobes considering this single lobe to be the entire keel.

The overestimation of the keel draft of the smaller lobe suggests that there is a need to develop a new 2-D nomogram which is tailored to the specific coil configuration and frequency of the EM system used here.

It should be noted that the spatial component of both 1-D and 2-D methods could not be resolved accurately due to the relative motion of the bird to the moving ice. The helicopter GPS was only accurate to 25 metres and since the ice was moving, GPS coordinate values could not be used to associate the bird location with the moving ice. In future, it is recommended that a number of GPS ground stations be used in conjunction with the inflight GPS. By using the differential mode of the GPS, accuracies of ± 1.5 metres could be obtained.

Comparison of the raw EM anomaly data was made with the ground truth DTM for the EM swath. This comparison suggests that the EM instrumentation measures the keel geometry far better than the EM anomaly interpretation methods would indicate. The shape of both the gridded ground truth cross-sections and the EM anomaly is very similar. The EM anomaly clearly shows the two lobe structure found in the ground truth data. There is some question as to where the EM fields detect the ice water interface due to the water voids, consolidation interface and footprint effects. The EM anomaly for the deeper of the two lobes does not follow the geometry of the gridded ground truth cross-sections. The EM anomaly may be detecting a change in the ice characteristics at depth suggesting that the deeper part of this lobe is highly porous containing more of the conductive sea water than the less conductive ice. The EM instrumentation may prove to be an effective method for determining the depth of rubble consolidation within rubble ice. Given that consolidation begins just after ridge building events, the EM anomaly for a newly formed ridge would probably differ from that of a more consolidated ridge two or three months old. EM surveys of a newly formed ridge may suggest a relatively thin ridge feature due to the large portions of sea water entrapped within the keel. The same ridge surveyed months later may yield EM anomalies suggesting a much deeper keel.

Future research using neural networks is being focused on the development of both 1-D and 2-D interpretive techniques for real time ice thickness. These techniques do not, however, represent the resolution that appears to be apparent from the raw EM data. For this reason, it is recommended that further analysis be carried out on existing data in order to determine a more accurate method for resolving keel geometry. Effort should be placed on trying to recover the two other useable EM overflights in order to determine the spatial resolution of the EM component of the airborne system.

From an operational perspective, the bird prototype required the continuous concentration of the helicopter pilot. In order to obtain useable data, the bird had to be flown in level flight at a height of approximately 15 metres above the ice. This was complicated by the relative horizontal and vertical motions of the bird with respect to the helicopter. For these reasons, it is recommended that pilots using this system, practice low level flying with a ballasted non-instrumented bird. Such practice would greatly improve the data sets obtained from airborne surveys.

Given the nature of the irregularity of ice keel surfaces, the task of remotely sensing the geometry of ice keels is formidable. Further testing of the airborne system and supporting ground truth measurements over ridges of varying geometry and other irregular features, coupled with further development efforts to improve the interpretation software, are clearly indicated.

REFERENCES

- Allyn, N. and B.R. Wasilewski, 1979. Some Influences of Ice Rubble Field Formations Around Artificial Islands in Deep Water. POAC-79, Trondheim, Norway.
- Best, M.E. and J.B. Boniwell, 1989. A Geophysical Handbook for Geologists. The Canadian Institute of Mining and Metallurgy, Vol. 41.
- Blatt, F.J., 1983. Principles of Physics. Allyn and Bacon, Inc., Boston, pp.1-813
- Brooks, L.D., 1983. Statistical Analyses of Pressure Ridge Keel Definitions and Distributions. Proc. of 7th International Con. POAC-83 Technical Research Centre Finland, Espoo, pp 69-78.
- Butt, K.A. and J.B. Gamberg, 1979. Technology of an Airborne Impulse Radar for Sounding Sea Ice. Proc. International Workshop on the Remote Estimation of Sea Ice Thickness, St.John's, pp.385-412.
- Cammaert, A.B. and D.B. Muggerridge, 1988. Ice Interaction with Offshore Structures. Van Nortrand Reinhold, New York, pp. 1-432
- Croasdale, K.R. and R.W. Marcellus, 1981. Ice Forces on Large Marine Structures. Proc. IAHR Symposium on Ice, Quebec, Vol.2, pp. 755-765.
- Flato, G.M. and W.D. Hibler(III), 1991. An Initial Numerical Investigation of the Extent of Sea-Ice Ridging. Proc. Symposium on Ice-Ocean Dynamics and Mechanics, Hanover, Annals of Glaciology, Vol 15, pp. 31-36.
- Gold, L.W., 1981. Designing Ice Bridges and Ice Platforms. Proc. IAHR Quebec, 1981, Vol. 2, pp. 685-701.
- Gow, A.J. and W.B. Tucker (III), 1990. Sea Ice in the Polar Regions. Chapter 2 of Polar Oceanography: Part A: Physical Science, ed Walker O. Smith Jr., Academic Press Inc., San Diego, pp. 47-122.
- Hall, D. and J. Martinec, 1985. Remote Sensing of Ice and Snow. University Press, Cambridge, pp. 1-189.
- Hibler, W.D. III, Mock, S.J. and W. B. Tucker III, 1974. Classification and Variation of Sea Ice Ridging in the Western Arctic Basin. Jour. Geophysical Research, Vol. 79, No. 18, pp. 2735-2743.

Hibler, W.D. III, Weeks, W.F. and S.J. Mock, 1972. Statistical Aspects of Sea-Ice Ridge Distribution. *Journal of Geophysical Research* Vol. 77, No. 30, pp. 5954-5970.

Hibler, W.D. III, 1989. Arctic Ice-Ocean Dynamics. Chapter 2 of *The Arctic Sea*, ed Yvonne Herman, Van Nostrand Reinhold Company, New York, pp. 47-92.

Holladay, J.S., St. John, I.R., Schoeggl, V., Lee, J., Rossiter, J.R. and L. Lalumiere, 1992. Airborne EM Ice Measurement Sensor Phases 1-2. Transport Canada Publication No. TP11282E, Montreal, pp. 1-67.

Holladay, J.S., Rossiter, J.R. and A. Kovacs, 1990. Airborne Measurement of Sea Ice Thickness Using Electromagnetic Induction Sounding. *Proc. 9th International Conf. Offshore Mechanics and Arctic Engineering*, pp. 309-315.

Huijbergts, C. and G. Matheron, 1970. Universal Kriging: An Optimal Method for Estimating and Contouring in trend surface analysis. *Can. Inst. Mining Metall*, Vol.12, pp. 159-169.

Kerr, A.D., 1975. The Bearing Capacity of Floating Ice Plates Subjected to Static or Quasi-Static Load--A Critical Survey. Cold Regions Research and Engineering Laboratory (CRREL), Hanover, N.H., Research Report 333.

Kovacs A. and S.J. Holladay, 1990. Sea-Ice Thickness Measurement using a small Airborne Electromagnetic Sounding System. *Geophysics*, Vol. 55, No. 10, pp. 1327-1337.

Kovacs, A., 1972. On Pressured Sea Ice. *Proc. Sea Ice International Conference Reykjavik*, pp. 276-295.

Kovacs, A. and S. Holladay, 1989. Development of an Airborne Sea Ice Thickness Measurement system and Field Test Results. *CRREL Report 89-19*, pp. 1-47.

Kovacs, A., Morey, R.M. and G.F.N. Cox, 1987. Modelling the Electromagnetic Properties Trends in Sea Ice, Part 1. *Cold Regions Science and Technology*, Vol 14, pp. 207-235.

Kreider, J.R. and M.E. Thro, 1981. Statistical Techniques for the Analysis of Sea Ice Pressure Ridge Distribution. *Proc. POAC-83*, Vol. 2, pp. 789-798.

Kry, P.R., 1977. Ice Rubble Fields in the Vicinity of Artificial Islands. *POAC-77*, St. John Newfoundland, pp. 200-211.

- Lange, M.A. and H. Eicken, 1991. Texture characteristics of Sea Ice and the Major Mechanisms of Ice Growth in the Weddel Sea. *Annals of Glaciology, Proc. Symposium Ice-Ocean Dynamics and Mechanisms, Hanover, Vol.15, pp. 210-215.*
- Lavrov, V.V., 1969. Deformation and Strength of Ice. *Gidrometeoizdat, Leningrad. Isreal Program for Scientific Translations, Jerusalem.*
- Lintz, J. and D. Simonett, 1976. *Remote Sensing of Environment. Addison-Wesley Publishing Co., Massachusetts, pp. 1-694.*
- Liu, G. and A. Becker, 1990. Two-Dimensional mapping of Sea-Ice Keels with Airborne Electromagnetics. *Geophysics, Vol.55, No.2, pp. 239-248.*
- Lorrain, P., Corson, D. and F. Lorrain, 1989. *Electromagnetic Fields and Waves; Including Electric Circuits. W.H. Freeman and Company, New York, pp. 1-754.*
- Massom, R.A., 1991. *Satellite Remote Sensing of Polar Regions: Applications, Limitations and Data Availability. Belhaven Press, London, pp. 1-307.*
- McCullagh, M.J., 1988. *Terrain and Surface Modelling Systems: Theory and Practice. Photogrammetric Record, Vol.12, No.72, pp. 747-778.*
- McNiell, D. and P. Hoekstra, 1973. In-situ Measurements on the Conductivity and Surface Impedance of Sea Ice at VLF. *Radio Sciences, Vol.8, pp. 23-30.*
- Melling, H., Topham, D.R. and D. Riedel, 1993. *Observations of the Topography of the Upper and Lower Surfaces of 10 Hectares of Deformed Sea Ice. Cold Regions Science and Technology (in press).*
- Menke, W., 1984. *Geophysical Data Analysis: Discrete Inverse Theory. Academic Press, Inc., Orlando Florida, pp. 1-260.*
- Michel, B. and R. Ramseier, 1971. *Classification of River and Lake Ice. Canadian Geotechnical Journal, Vol. 8, No.1, pp. 36-45.*
- Michel, B. and L. Gagnon, 1978. *Time-Dependant Deflection of an Ice Plate. Proc. Workshop on Bearing Capacity of Ice Covers, Assoc. Committee, Geotech. Res., National Research Council of Canada, Technical Memo 123, pp. 80-97.*
- Milsom, J., 1989. *Field Geophysics. Open University Press, England, pp. 1-182.*
- Morey, R.M., Kovac, A. and G.F.N. Cox, 1984. *Electromagnetic Properties of Sea Ice. Cold Regions Science and Technology, Vol. 9, pp. 53-75.*

- Nakawo, M. and N.K. Sinha, 1981. Growth Rate and Salinity Profile of First-year Ice in the High Arctic. *Journal of Glaciology*, Vol.27, No.96, pp. 315-330.
- Nautronix Acoustic Tracking System ATS-S04 manual, 1989. Zaknich, A. and P. Doolan (editors), Fremantle Western Australia, pp. 1-20.
- Nevel, D.E., 1976. Pressure Ridge Forces. Seventh International POAC, Technical Research Centre Finland, Helsinki, pp. 219-228.
- Olea, R.A., 1975. Optimal Mapping Techniques using Regionalised Variable Theory. Series on Spatial Analysis, Kansas Geological Survey, University of Kansas, Vol.2. pp. 1-137.
- Parasnis, D.S., 1975. Mining Geophysics. Elsevier Scientific Publishing Co. Amsterdam, pp. 1-395.
- Pounder, E.M., 1965. The Physics of Ice. Pergamon Press, Oxford, pp. 1-151.
- Prinsenbergh, S.J., Holladay, J.S., Rossiter, J.R. and L.A. Lalumiere, 1992. 1991 Beaufort Sea EM/Radar Ice and Snow Sounding Project. Can. Tech. Report of Hydrography and Ocean Sciences, No. 139, pp. 1-61.
- Riedel, D., 1990. Remote Acoustic Profiling of Ice Keels in the Beaufort Sea. U.Vic. Physics Co-op Workterm Report, pp. 1-51.
- Rigby, F.A. and A. Hanson, 1976. Evolution of a Large Arctic Pressure Ridge. AIDJEX Bulletin No.34, pp. 43-71.
- Rossiter, J.R., and L.A. Lalumiere, 1988. Evaluation of Sea Ice Thickness Sensors. CanPolar Project Number 1027 (for Transport Canada), pp. 1-58.
- Rossiter, J.R., 1979. Review of Impulse Radar Sounding of Sea Ice. Proc. International Workshop on the Remote Estimation of Sea Ice Thickness, St.John's, pp. 77-107.
- Roth, D.R. and R.W.W. Marcellus, 1986. Bearing Capacity of Broken Ice Zones. Public Works Canada Technical Report AES/SAG 1-2:86-15, pp. 1-36.
- Rothrock, D.A., 1986. Ice Thickness Distribution - Measurement and Theory. In *The Geophysics of Sea Ice*. Ed N. Untersteiner, Plenum Press, New York, pp. 551-575.
- Sanderson, T.J.O., 1988. *Ice Mechanics: Risks to Offshore Structures*. Graham and Trotman, London, pp. 1-253.
- Sayed, M. and R.M.W. Frederking, 1991. Ridge Sail Statistics at the Shear Edge of

- Lancaster Sound, March 1984. Proc. Symposium on Ice-Ocean Dynamics and Mechanics, Hanover, Annals of Glaciology, Vol.15, pp. 271-275.
- Sayed, M. and R.M.W. Frederking, 1989. Measurements of Ridge Sails in the Beaufort Sea. Canadian Journal of Civil Engineering, Vol. 16, No.1, pp. 16-21.
- Sayed, M., 1988. Transmission of Loads Through Grounded Rubble. Proc. 9th International Symposium on Ice, Sapporo, Japan, IAHR, Vol. 1, pp. 310-326.
- Serway, R.A., 1990. Physics for Scientists and Engineers, with Modern Physics. Saunders College Pub., Philadelphia, pp. 1-1444.
- Shuchman, R.A. and R.G. Onstott, 1990. Chapter:3 Remote Sensing of the Polar Oceans. Ed. Walker O. Smith, Jr., Academic Press, Inc., San Diego, pp. 123-169.
- Sinha, N.K., Timco, G.W. and R. Frederking, 1987. Recent Advances in Ice Mechanics in Canada. International Symposium on Offshore Mechanics and Arctic Engineering (OMAE), Houston, pp. 1214-1231.
- Sinha, N.K., 1978. Rheology of Columnar-grained Ice. Experimental Mechanics, Vol. 18, No. 12, pp. 464-470.
- Timco, G.W. and L.E. Goodrich, 1988. Ice Rubble Consolidation. Proc. 9th International Symposium on Ice, Sapporo, Japan, IAHR, Vol. 1, pp. 427-438.
- Tucker, W.B. III and V.H. Westhall, 1973. Arctic Sea Ice Ridge Frequency Distributions Derived from Laser Profiles. AIDJEX Bull. 21, pp. 171-180.
- Tucker, W.B. III and J.W. Govoni, 1981. Morphological Investigations of First-Year Sea Ice Pressure Ridge Sails. Cold Regions Science and Technology Vol. 5, pp. 1-12.
- Tucker, W.B., Weeks, W.F. and M. Frank, 1979. Sea Ice Ridging Over the Alaskan Continental Shelf. Jour. Geophysical Research, Vol. 84, pp. 4885-4897.
- Vaudrey, K.D., 1983. Characterization of Offshore and Coastal Ice Conditions. ASCE State-of-the-Practice Report, New York, pp. 3-16.
- Vaudrey, K.D. and M.G. Katona, 1977. Viscoelastic Finite Element Analysis of Sea Ice Sheets. Proc. IAHR international Symposium on Ice Problems, Hanover, N.H., pp. 515-543.
- Vivatrat, V. and T.R. Kreider, 1981. Ice Force Prediction Using a Limited Driving Force Approach. Proc. OTC, Houston, Vol.3, pp. 471-485.

Vozoff, K. and D.L.B. Jupp, 1975. Joint Inversion of Geophysical Data. *Geophys. J. R. Astr. Soc.*, Vol 42, pp. 977-991.

Wadhams, P., 1976. Sea Ice Topography in the Beaufort Sea and its Effect on Oil Containment. *AIDJEX Bulletin No. 33*, pp. 1-52.

Wadhams, P., 1981. Sea-Ice topography of the Arctic in the region 70°W to 25°E. *Philos. Trans. R. Soc. London*, Vol.302, pp. 45-85.

Wadhams, P. and R.T. Lowry, 1977. A Joint Topside - Bottomside Remote Sensing Experiment on Arctic Sea Ice. 4th Canadian Symposium on Remote Sensing, Quebec City, pp. 407-423.

Wadhams, P. and T. Davy, 1986. On the Spacing and Draft Distributions for Pressure Ridge Keels. *Journal of Geophysical Research*, Vol. 91, pp. 10697-10708.

Weeks, W.F., 1976. *Sea Ice Properties and Geometry*. University of Washington, *AIDJEX Bulletin No. 34*, pp. 137-172.

Weeks, W.F., Kovacs, A. and W.D. Hibler III, 1971. Pressure Ridge Characteristics in the Arctic Coastal Environment. *Proc. 1st International Conference POAC-71*, Vol.1, pp. 152-183.

Weeks, W.F. and Assur, 1967. *The Mechanical Properties of Sea Ice*. CRREL, Hanover, N.H., Monograph II-C3.

Wright, B.D., Hnatiuk, J., and A. Kovacs, 1978. Sea Ice Pressure Ridges in the Beaufort Sea. *Proc. IAHR Symposium Ice Problems, Lulea*, Vol.1, pp. 249-272.

Wright, B.D. and D. McGonigal, 1980. Features of First and Multiyear Ridges. *Proc. of Workshop on Sea Ice Ridges and Pile-up*, Calgary, Oct 22-24, NRC Tech. Memo No. 134, Jan 1982, pp. 2-8.

APPENDIX A
Field Log

- April 8/91 Departure from Victoria. Overnight in Edmonton.
- April 9/91 Departure from Edmonton. Arrival at Polar Continental Shelf Project base camp in Tuktoyaktuk at 5:30 pm. Set up theodolite and EDM, charged batteries. Unpacked equipment. Equipment checks.
- April 10/91 Field preparations of equipment. Discussion of field strategies. Adjustments made to EDM. Final software adjustments and briefing.
- April 11/91 Ridge site selection from Twin Otter. Suitable site selected with good level ice field for easy landing. Drilled holes adjacent to the ridge to locate level non-rafted ice for the submersible entry hole. Set-up theodolite and EDM and surveyed ridge geometry in immediate area to drilled holes. Set-up survey baseline coordinate system on the south side of the long axis of the ridge. Field sketches noting block dimensions and ridge characteristics.
- April 12/91 Bad weather, Ice fog, no flying. Converted survey data angles into XYZ coordinates and produced an XY plot of the ridge thus far. Submersible prepared for field deployment.
- April 13/91 Day #2 on the ice. The control tent was erected and submersible control systems set up. A large ring hot water hole melter was used to create submersible entry hole #1. Submersible deployed. The navigational coordinate system used by the submersible was aligned with the topside coordinate system. Two radiating tracks were surveyed under the keel. A problem developed with the navigational system which required the removal of the submersible. Marker bags were placed on the ice and surveyed in. These markers were used later as tie down control points for air photo analysis. Numerous survey shots were taken from the theodolite stations set up on the baseline. A series of overlapping photographs were taken along the ridge. Repairs were carried out on the submersible navigational system back at base camp.
- April 14/91 Day #3 on the ice. Air photos taken this day by NRC. Deployment of submersible from hole #1. Fourteen successful survey tracks under the keel. Theodolite station moved to the top of the ridge onto a large flat block. A series of shots were taken backsitings the baseline for referencing. An along the crest survey was performed as well as a number of cross sectional profiles. As a result of strong winds, an open lead appeared only 2-3 kilometres south of

the ridge. This lead was not visible during the morning flight. By the end of the day, the lead was 100s of metres wide and more than double the width in length.

- April 15/91 Day #4 on the ice. The baseline was extended. Theodolite station #3 was set up approximately 200 metres east of the original baseline station of day #1. A second hole was melted creating submersible entry hole #2. Again the navigational system of the submersible was aligned with the topside coordinate system. Three large male Polar bears interrupted work as they approached within 500 metres of the work area. Sixteen tracks of the keel were logged. Extensive survey coverage of the topside geometry was performed as well as a number of field sketches and observations made of ice block orientations.
- April 16/91 Day #5 on the ice. Freezing rain (-2°C). Flight delayed. Numerous block dimensions were measured from the ridge sail. Many blocks were vertically oriented. Generally a cardhouse structure. Navigational checks were performed on the ATS positioning system. The airborne system was flown over the study site (only the EM and laser altimeter).
- April 17/91 Began packing up. Duplicates of all data files made. Radar mounted into airborne bird. Ground and air tested.
- April 18/91 IOS crew return to Victoria. Bad weather grounded airborne system.
- April 19/91 Bad weather grounded airborne system.
- April 20/91 EM/Radar/Laser altimeter all working and packaged in airborne bird. Overflight of study site. Seven overflights in total. Some difficulties with non-linear drift as well as stable bird altitude and attitude.

APPENDIX B
Multi-Line Header (MLH) Format.

***HEADER INFORMATION VERSION 1.2**

***COMMENTS**

70 Number of Records following section

Times within the ATS, TARS, and MESOTECH are in Mountain Daylight Savings Time (MDT).

The study site was located at the GPS measured coordinates of 70 28.574'N and 133 54.780'W. The first year ridge selected was in the order of 300 metres long and varied in width from 15 to 40 metres. Two TARS deployment holes were bored through the level ice adjacent to the ridge for keel surveys. A baseline adjacent to the longest axis of the ridge was surveyed and a coordinate system established. This coordinate system as common to both the sail and keel surveys.

The baseline ran roughly parallel to the long axis of the ridge with 0 degrees being perpendicular to the baseline pointing directly towards the ridge. Reference angles increased clockwise from this 0 reference.

Three data streams were recorded from the TARS:

These are:

- (1) Mesotech (sonar)
- (2) TARS (pressure transducer)
- (3) ATS (acoustic tracking system)

Each of these incoming data streams were initially time stamped with a computer time. Encoded in the first 15 seconds of each data record are 5 synchronizing time stamps at 3 second intervals. These time stamps are used to associate data during post processing.

This data set refers to TARS data

Equipment description:

The information associated with the TARS data files contains important operational information about the submersible behaviour as it travels under the ice. TARS data were transmitted in 5 groups of 32 byte hexadecimal strings. Contained within this string are 5 channels of information which are as follows:

- * Transducer pressure in PSI
- * Sine of heading
- * Cosine of heading
- * Pitch of submersible
- * Roll of submersible

The sampling rate for these data files was 1 hertz.

OUTPUT of data

Naming convention for raw field data files TARSHO_//HOLE#//.//RUN#//

This first day of TARS surveys was April 13 - day#2 of the field work. The TARS was deployed and three survey tracks radiated out from this first entry hole. Some problems were encountered on these first few runs. The screen display of the ATS master control unit did not function properly and in fact blanked out on the last run of the day. The TARS depth for the surveys was set at a fixed 20 metre depth for all keel survey tracks for both holes.

Processing information:

STEP 1

The raw TARS data files were initially processed by the program TARS1.FOR. This program converted the hexadecimal strings into 7 data channels. These channels are as follows:

Channel 1 -----	Time in seconds
Channel 2 -----	Transducer pressure in PSI
Channel 3 -----	Depth of TARS in metres
Channel 4 -----	Sine of heading
Channel 5 -----	Cosine of heading
Channel 6 -----	Pitch of TARS
Channel 7 -----	Roll of TARS

Starting time for this record is 49988.95 seconds April 13, 1991

Editing Information: VIEW: 92/ 2/24 16:43:20.43

Summary of Changes by VIEW:

Channel # : 2 3 4

No of Changes: 78 100 5

*IDENTIFICATION INFORMATION

8 Number of Records following section

'IMP91' 'PROJECT'

'HOLE_1' 'STATION NUMBER'

'MDT' 'TIME ZONE'

'BEAUFORT SEA' 'GEOGRAPHICAL DESCRIPTION'

70.00000 28.57400 0.0000000E+00 'N'

'DECIMAL(LAT): DEGREES,MINUTES,SECONDS; N/S IN QUOTES'

133.0000 54.78000 0.0000000E+00 'W'

'DECIMAL(LONG): DEGREES,MINUTES,SECONDS; E/W IN QUOTES'

'8378' 'INSTRUMENT SERIAL NUMBER'

'MESOTECH 808 SONAR' 'TYPE OF INSTRUMENT'

*PROGRAM INFORMATION

3 Number of Records following section

2 '# OF PROGRAM NAMES FOLLOW (# OF PROGRAMS DATA PROCESSED THROUGH)'

'VIEW YY/MM/DD HH:MM:SS 92/ 2/24 16:43:20.43'

'CALIBRATION version 3.50 YY/MM/DD HH:MM:SS 92/ 6/ 4 14:57:52.41'

*CALIBRATION INFORMATION

14 Number of Records following section

1991	4	11	14	35
------	---	----	----	----

'START TIME Y M D H M S'

0	0	1	172
---	---	---	-----

'TIME INCREMENT H M S MS'

7 'NUMBER OF CHANNELS IN RAW DATA'

'EACH CHANNEL : DESCRIPTION, UNITS, EQUATION #, # OF COEFF., & COEFFICIENTS'

'TIME' 'SEC'	10	2	0.0000000E+00	1.000000
'PRESSURE' 'PSI'	10	2	0.0000000E+00	1.000000
'DEPTH' 'METRES'	10	2	0.2676000	0.9727000
'SINE' 'DEGREES'	10	2	0.0000000E+00	1.000000
'COSINE' 'DEGREES'	10	2	0.0000000E+00	1.000000
'PITCH' 'DEGREES'	10	2	0.0000000E+00	1.000000
'ROLL' 'DEGREES'	10	2	0.0000000E+00	1.000000

0 'NUMBER OF CALCULATED PARAMETERS'

10 'NUMBER OF RECORDING BITS'

99999 'NUMBER OF RECORDS IN RAW DATA'

*FILE INFORMATION

12 Number of Records following section

974 'NUMBER OF DATA RECORDS IN THIS FILE'

7 'NUMBER OF PARAMETERS IN EACH RECORD'

'TIME' 'J.D.'

'PRESSURE' 'PSI'

'DEPTH' 'METRES'

'SINE' 'SIN OF HEADING (Degrees)'

'COSINE' 'COSINE OF HEADING (Degrees)'

'PITCH' 'PITCH OF TARS (Degrees)'

'ROLL' 'ROLL OF TARS (Degrees)'

T 'IF TRUE DATA FILE FORMATTED'

'(1P, 7(E14.6))' 'FORMAT OR RECORD TYPE OF FILE'

'SEQUENTIAL' 'FILE ACCESS MODE'

*END OF HEADER

APPENDIX C
Computer Programs Developed for Thesis Analysis.

```

C*****
C          PROGRAM ATS3.FOR
C
C  This program processes raw ATS field data.  The processed
C  data is presented as an array of seven columns of data:
C
C      Column 1 ----- Time
C      Column 2 ----- X coordinate of TARS
C      Column 3 ----- Y coordinate of TARS
C      Column 4 ----- Z coordinate of TARS
C      Column 5 ----- Heading of TARS
C      Column 6 ----- Pitch of TARS
C      Column 7 ----- Roll of TARS
C
C
C  VERSION 1.0   September 10,1991
C  Written by R. Bowen
C*****
C          FIRST VARIABLE DECLARATIONS
C=====C
C      character*110 INFILE,OUTFILE      ! Input and Output file
C      character*2 RUN                    ! Run number 1-16
C      character*1 Hole                   ! Hole number 1 or 2
C      character*110 DLINE                 ! Individual lines of input
C      character*6 XLOC                    ! X coordinate of TARS
C      character*6 YLOC                    ! Y coordinate of TARS
C      character*6 ZLOC                    ! Z coordinate of TARS
C      character*6 HEADING                 ! Heading of TARS
C      character*4 PITCH                   ! Pitch of TARS
C      character*4 ROLL                     ! Roll of TARS
C
C      integer ROW                          ! number lines data output
C      integer Iter,Col                      ! Loop variables
C
C      real CORTIME                          ! Time in time channel
C      real TIME_CH (100000)                 ! Time array
C      real TIME                             ! Time of data sampled
C      real HOUR                             ! Number of hours
C      real MIN                              ! minutes
C      real SEC                              ! seconds
C      real ATSCLOCK                         ! ATS clock

```

```

real TSTAMP           ! Computer time stamp
real OFFSET          ! Offset ATS&computer
character*1 Junk     ! dummy
character*19 NDAT    !
character*5 MLHDAT(100000,6) ! Array for output
logical error

```

```

=====
C

```

```

Write (6,*)
Write (6,*) 'Initialising array 7 columns wide... '
Do 556 ROW = 1,100000

```

```

C   TIME_CH(ROW) = 0.0
    Do 555 Col = 1,6
        MLHDAT(ROW,Col) = '0'

```

```

555   continue

```

```

556   continue
Write (6,*) 'done.'
Write (6,*)

```

```

C
=====
C

```

```

TO BE PROCESSED

```

```

=====
C

```

```

Write (6,*) 'Please Enter the Filename: '

```

```

Read (5,50) INFILE

```

```

50  Format (A110)

```

```

Write (6,*) INFILE

```

```

Hole = INFILE(8:8)

```

```

RUN = INFILE(11:12)

```

```

WRITE(6,*)Hole,RUN

```

```

Open (8, file = INFILE,STATUS = 'OLD')

```

```

Goto 150

```

```

C
=====
C

```

```

AND ARRAY CREATED

```

```

=====
C

```

```

150  Continue

```

```

C
=====
C

```

```

TIME OF DATA TO SYSTEM

```

```

C   TIME. THIS IS USED TO SYNCHRONIZE THE

```

```

C   VARIOUS DATA STREAM FROM DIFFERENT INSTRUMENTS

```

```

=====
C

```

```

Do 15 Number = 1,10

```

```

Read(8,200,err=900,end=1080)DLINE

```

```

If (INDEX(DLINE, 'I') .NE. 0) Then

```

ENTERING DATA FILE

DATA FILE OPENED

ALIGNING START

```

Count = Count + 1
If (Count .EQ. 5) Then
  CALL SET_SEPARATORS(' :!',3)
  STAT = -1
  Local = 11
  CALL Scan_F4(DLINE,TSTAMP,8,Local,STAT)
  local = 30
  CALL Scan_F4(DLINE,HOUR,2,Local,STAT)
  local = 33
  CALL Scan_F4(DLINE,MIN,2,Local,STAT)
  local = 36
  CALL Scan_F4(DLINE,SEC,2,Local,STAT)
  ATSCl = HOUR*3600+MIN*60+SEC
  Write(6,*)'Computer Time Stamp is',TSTAMP
  Write(6,*)'ATS Clock Time is',ATSCl
  OFFSET = ATSCl-TSTAMP
  WRITE(6,*)'Time offset',OFFSET
  goto 16
end if
end if
15 Continue
16 Continue
ROW = 1
TIME = ATSCl- OFFSET
CORTIME = TIME-TSTAMP
TIME_CH(ROW) = CORTIME
XLOC = DLINE(INDEX(DLINE,'X:')+2:(INDEX(DLINE,'X:')+8))
MLHDAT(ROW,1) = XLOC
YLOC = DLINE(INDEX(DLINE,'Y:')+2:(INDEX(DLINE,'Y:')+8))
MLHDAT(ROW,2) = YLOC
ZLOC = DLINE(INDEX(DLINE,'D:')+2:(INDEX(DLINE,'D:')+8))
MLHDAT(ROW,3) = ZLOC
HEADING = DLINE(INDEX(DLINE,'H:')+2:(INDEX(DLINE,'H:')+8))
MLHDAT(ROW,4) = HEADING
PITCH = DLINE(INDEX(DLINE,'P:')+2:(INDEX(DLINE,'P:')+6))
MLHDAT(ROW,5) = PITCH
ROLL = DLINE(INDEX(DLINE,'R:')+2:(INDEX(DLINE,'R:')+6))
MLHDAT(ROW,6) = ROLL
Write(6,*)CORTIME,XLOC,YLOC,ZLOC,HEADING,PITCH,ROLL
ROW = 2

```

C

C=====

C MAIN DATA HANDLING

C=====

```

C
Do While (IOSTAT .GE. 0)
  Read (8,200,err=900,end=1080)DLINE
200  Format(A110)
  CALL SET_SEPARATORS(' ',2)
  STAT = -1
  Local = 11
  CALL Scan_F4(DLINE,HOUR,2,Local,STAT)
  Local = 14
  CALL Scan_F4(DLINE,MIN,2,Local,STAT)
  Local = 17
  CALL Scan_F4(DLINE,SEC,2,Local,STAT)
  TIME = (HOUR*3600+MIN*60+SEC)- OFFSET
  CORTIME = TIME -TSTAMP
  TIME_CH(ROW) = CORTIME
  XLOC = DLINE(INDEX(DLINE,'X:')+2:(INDEX(DLINE,'X:')+8))
  MLHDAT(ROW,1) = XLOC
  YLOC = DLINE(INDEX(DLINE,'Y:')+2:(INDEX(DLINE,'Y:')+8))
  MLHDAT(ROW,2) = YLOC
  ZLOC = DLINE(INDEX(DLINE,'D:')+2:(INDEX(DLINE,'D:')+8))
  MLHDAT(ROW,3) = ZLOC
  HEADING=DLINE(INDEX(DLINE,'H:')+2:(INDEX(DLINE,'H:')+8))
  MLHDAT(ROW,4) = HEADING
  PITCH = DLINE(INDEX(DLINE,'P:')+2:(INDEX(DLINE,'P:')+6))
  MLHDAT(ROW,5) = PITCH
  ROLL = DLINE(INDEX(DLINE,'R:')+2:(INDEX(DLINE,'R:')+6))
  MLHDAT(ROW,6) = ROLL
  ROW = ROW + 1
End do
1080  CLOSE (8)
  ROW = ROW - 1
C
C=====
C      OUTPUT FILE CREATION
C=====
C
  OUTFILE = '[BOWEN.TUK91.ATS]ATS_ '//Hole//'_ '//RUN//' .data'
  Write(6,*)OUTFILE
  OPEN(9,file=OUTFILE, STATUS='NEW')
  Write(9,*)'There are',ROW,'record in this file'
  Write(9,*)'The starting time for this file is',TSTAMP
  Write(9,*)'Offset between computer and ATS clocks is',OFFSET
  Write(9,300)(TIME_CH(Iter),(MLHDAT(Iter,Col),Col=1,6),Iter=1,ROW)
300  Format(F8.2,6a7)

```

```

      Close (9)
      goto 350
C-----
C      ERROR MESSAGES
C-----
C
900  Write(6,*)'ERROR READING PROGRAM TERMINATED'
350  end

C*****
C      PROGRAM TIMCO.FOR
C
C      Program calculates the average difference between
C      ATS records.
C
C      Written by R. BOWEN
C      MARCH 30,1992
C*****
C=====
C      VARIABLE DECLARATION
C=====
C
      character*100 INFILE ! input file name
      character*50 STUFF1   ! header information
      character*50 STUFF2   ! header information
C
      real TIME,TIME1,TIME2 ! data record times
      real DIF              ! time difference between records
      real AVE              ! average time for non-gapped records
      real Count            ! number of non-gap records
C
      integer Total         ! total number records
      integer LOW,HIGH      ! tolerance widow range
      logical error
C*****
      Write (6,*)'Enter ATS file: '
      Read (5,45,err=900,end=910)INFILE
      Write (6,*)INFILE
45  Format(a25)
      Write(6,*)'Enter lowest time tolerance: '
      Read(5,46,err=900,end=910)LOW
      Write(6,*)LOW

```

```

Write(6,*)'Enter highest time tolerance: '
Read(5,46,err=900,end=910)HIGH
Write(6,*)HIGH
46  Format(i2)
   Open(8,file=INFILE,status='OLD')
   Read(8,*,err=900,end=910)
   Read(8,*,err=900,end=910)
   Read(8,47,err=900,end=910)TIME1
   Write(6,*)TIME1
47  Format(f8.2)
   TIME = 0.0
   Count = 0.0
   Do while (IOSTAT .GE. 0)
     Read(8,47,err=900,end=910)TIME2
     DIF = TIME2 - TIME1
     Total = Total + 1
     If (DIF .GE. LOW .and. DIF .LE. HIGH)then
       TIME = TIME + DIF
       Count = Count + 1.0
     Endif
     TIME1 = TIME2
   End do
910  Close(8)
   Write(6,*)TIME
   Write(6,*)'There are',Count,'good intervals'
   Write(6,*)'There are',Total,'records in the file'
   AVE = TIME/Count
   Write(6,*)'The Average time interval is',AVE,'seconds'
   goto 350
900  Write(6,*)'ERROR READING DATA'
350  end

```

```

C*****
C          PROGRAM TIME.FOR
C
C          Program calculates the time differences between
C          ATS data records and fills gaps.
C
C          Written by R. Bowen
C          Jan 23, 1992
C*****
C          VARIABLE DECLARATIONS
C=====
C
C          character*100 INFILE,OUTFILE      ! Input Output file names
C          character*100 HEADER              ! Header file to be inserted to MLH
C          character*3 RUN                   ! Run number 1-16
C          character*2 HOLE                  ! Hole number 1 or 2
C          character*13 STUFF1
C          character*23 STUFF2              ! Header information
C
C          real DATA(10000,3)              ! Array
C          real TIME                         ! Time record
C          real TIME1                       !
C          real TIME2                       !
C          real T1                          !
C          real T2                          !
C          real DIF                         ! Time difference
C          real FLAG                         ! Flag detects irregular time interval
C          real SUM                          ! Sum to calculate ave time interval
C          real TOTAL                       !
C          real AVE                         ! Average time interval
C          real X,Y,X1,X2,Y1,Y2             ! X and Y record in metres
C          real XDIF                        ! Difference in X records
C          real YDIF                        ! Difference in Y records
C          real XNEW                         !
C          real YNEW                         !
C          real MISS                        ! Number of records missed
C          real PERCENT                     ! Percent filled records added to file
C          real RGAPS                       ! Real gaps used to calculate %
C          real SPACING                     !
C          real RROW                        ! Real count used to calculate %
C
C          integer INTERVAL                 !
C          integer GAPS                    ! Number of gaps in data
C          integer MISSED                   !

```

```

integer REM                !
integer ROW                !
integer JUMP              ! Measure of the largest time gap
integer NUMBER            ! Reference number for largest time gap
integer SKIP              !
integer COUNT             !
integer Iter,Col          !
integer DIFF              !
logical error             !
C*****
C
WRITE (6,*)
WRITE (6,*)
DO 15 ROW = 1,10000
  DO 14 Col=1,3
    DATA(ROW,Col) = 0
14  Continue
15  Continue
    Write (6,*) 'Done'
    Write (6,*)
C*****
C      ARRAY CREATED                *
C*****
    Write (6,*)'Enter ATS file: '
    Read (5,45, err=900,end=910)INFILE
    Write(6,*)INFILE
45  Format(a25)
    HOLE = INFILE(4:4)
    RUN = INFILE(6:8)
    Write (6,*)'Enter time interval: '
    Read (5,*,err=900,end=910)SPACING
    OPEN(8,file=INFILE,status='OLD')
    Read(8,55,err=900,end=910)STUFF1
    Read(8,56,err=900,end=910)STUFF2
55  Format(a13)
56  Format(a23)
    Write(6,*)STUFF1
    Write(6,*)STUFF2
C*****
C      FILE READ IN                *
C      ENTERING MAIN BODY OF PROGRAM      *
C*****
    Read(8,60,err=900,end=910)TIME1,X,Y
60  Format(3f8.2)

```

```

Write(6,*)TIME1,X,Y
ROW = 1
NUM = 0
JUMP = 0
SUM = 0.0
GAPS = 0
TOTAL = 0.0
SKIP = 0
DATA(ROW,1) = TIME1
DATA(ROW,2) = X
DATA(ROW,3) = Y
ROW = ROW + 1
Do while (IOSTAT .GE. 0)
  Read(8,60,err=900,end=910)TIME2,X1,Y1
  t1 = TIME1
  t2 = TIME2
  DIF = t2 - t1
  IF (DIF .GT. NUM) then
    NUM = DIF
  Endif
  XDIF = X1 - X
  YDIF = Y1 - Y
  FLAG = DIF - SPACING
  IF (FLAG .GE. -1.0 .AND. FLAG .LE. 1.0) then
    DATA(ROW,1) = TIME2
    DATA(ROW,2) = X1
    DATA(ROW,3) = Y1
    SUM = SUM + DIF
    TOTAL = TOTAL + 1.0
  ELSE
    MISS = DIF/SPACING
    XNEW = XDIF/MISS
    YNEW = YDIF/MISS
    MISSED = INT(MISS)
    DIFF = INT(DIF)
    INTERVAL = INT(SPACING)
    REM = MOD(DIFF,INTERVAL)
    DATA(ROW,1) = TIME1
    DATA(ROW,2) = X
    DATA(ROW,3) = Y
    IF ( REM .EQ. 0) then
      Do 11 Number =1,MISSED
        TIME = TIME1 + INTERVAL
        X2 = X1 + XNEW

```

```
Y2 = Y1 + YNEW
DATA(ROW,1) = TIME
DATA(ROW,2) = X2
DATA(ROW,3) = Y2
TIME1 = TIME
ROW = ROW + 1
X1 = X2
Y1 = Y2
GAPS = GAPS + 1
11 Continue
TIME1 = TIME2
ROW = ROW - 1
Else
Do 12 Number = 1,MISSED
TIME = TIME1 + INTERVAL
X2 = X1 + XNEW
Y2 = Y1 + YNEW
DATA(ROW,1) = TIME
DATA(ROW,2) = X2
DATA(ROW,3) = Y2
TIME1 = TIME
ROW = ROW + 1
X1 = X2
Y1 = Y2
GAPS = GAPS + 1
12 Continue
TIME1 = TIME2
ROW = ROW - 1
Endif
SKIP = SKIP+1
ENDIF
TIME1 = TIME2
X = X1
Y = Y1
ROW = ROW + 1
end do
910 CLOSE(8)
ROW = ROW - 1
```

```

C*****
C          OUTPUT
C*****
C
  OUTFILE = '[Bowen.tuk91.ats]ATS'//Hole//'_ '//Run//'.DATA_EDIT'
  HEADER = '[Bowen.tuk91.ats]HEADER'//Hole//'_ '//Run//'.DAT'
  Write(6,*)OUTFILE
  Write(6,*)HEADER
  Write(6,*)SUM
  Write(6,*)TOTAL
  AVE = SUM/TOTAL
  Write(6,*)'Average time interval',AVE,'seconds'
  OPEN(9,file=OUTFILE, STATUS ='NEW')
  OPEN(10,file=HEADER, STATUS ='NEW')
  Write(6,*)GAPS
  Write(6,*)ROW
  RGAPS = REAL(GAPS)
  RROW = REAL(ROW)
  Percent = (RGAPS/RROW) * 100
  Write(9,55)STUFF1
  Write(9,56)STUFF2
  Write(10,*)'There are',ROW,'records'
  Write(10,*)'The average ATS time interval was',AVE,'seconds'
  Write(10,*)'The number of irregular time intervals',SKIP,'total'
  Write(10,*)'There were',gaps,'gaps that were filled in the record'
  Write(10,*)'The largest gap in the record was',NUM,'seconds'
  Write(10,*)'Number of good intervals are',TOTAL,'TOTAL'
  Write(10,*)'Percentage of filled data in record',percent,'total'
  Write(9,300)((DATA(Iter,Col),Col=1,3),Iter=1,ROW)
300 Format(3f8.2)
  Close(9)
  Close(10)
  goto 350
C*****
C          ERRORS
C*****
900 Write(6,*)'ERROR READING DATA, PROGRAM TERMINATED'
350 End

```

```

C*****
C          PROCESS_RAW_MES.FOR
C
C    A program to take field MESOTECH data and prepare it for
C    further editing...
C    The program takes MES 2-way times and converts them to
C    equivalent depths.
C    The output has a time column (beginning at 0.0 seconds and
C    going up by steps of 1/16 th of a second) and a MES depth
C    column. In addition, a stamp is placed at the top of the
C    file stating the date and time of the data collection.
C
C    The output has the naming convention:
C
C    MES_H_RR.DATA
C
C    where H is the hole number (1 or 2)
C    RR is the run number (0-18)
C
C    Written by D. Riedel/ R. Bowen July 1991
C
C*****
C
C Variables...
C
C    character*80 INFILE,OUTFILE      ! Input and Output file names
C    character*1  Hole                ! Hole number
C    character*2  Run                 ! Run number
C    character*10 none                ! junk buffer
C    character*16 Date                ! Date stamp
C    character*30 TSTAMP              ! String of time info
C    character*80 DLINE               ! Data line
C
C    real MES                        ! 2-way time (MESOTECH)
C    real DAT(40000,2)              ! Array of output data
C
C    integer Count1                  ! Number used for time stamp
C    integer Count                   ! Number of records in file
C    integer Iter,Col                ! Loop variables
C
C    logical ERROR                   ! Boolean variable(=T bad record)
C
C***** Get filename from user... *****
C    write(6,*)'Please enter the filename: '

```

```

read (5,50)INFILE
50  FORMAT(A80)
WRITE(6,*)INFILE
Hole=INFILE(8:9)
Run=INFILE(INDEX(INFILE,')'+2:INDEX(INFILE,')'+3)
if (Hole .eq. '1') then
  if (Run .le. '10') then
    Date = 'April 13, 1991'
  else
    Date = 'April 14, 1991'
  end if
else
  if (Run .le. '15') then
    Date = 'April 15, 1991'
  else
    Date = 'April 16, 1991'
  end if
end if
C
C-----
C
open (8,file=INFILE,status='old')
read (8,60)none
60  format(A10)
Count1 = 0
Do 15 Number = 1,750
  Read(8,65,err=9000,end=250)DLINE
  if (INDEX(DLINE,'!') .NE. 0) Then
    Count1 = Count1 + 1
    if (Count1 .EQ. 5) Then
      TSTAMP=DLINE(INDEX(DLINE,'!')+10:(INDEX(DLINE,'!')+17))
      Write(6,*)'Computer time stamp is',TSTAMP
      goto 23
    end if
  end if
15  continue
23  continue
65  Format(A30)
C
C***** Set up variables and begin looping through data...
C
DAT(Count,1)=0.0
CALL SET SEPARATORS(' :!',3)
DAT(Count,2)=(MES*11.3932*1436.7)/2000000

```

```

Time=0.0
write(6,*)'Reading...'
DO while (IOSTAT .GE. 0)
  ERROR=.FALSE.
  read (8,*,err=9000,end=250)MES
100   Count=Count+1
      if (Count .eq. 1) then
          DAT(Count,1)=0.0
          goto 200
      end if
      DAT(Count,1) = DAT(Count-1,1) + 0.0625
200   if (ERROR .NE. .TRUE.) then
          DAT(Count,2)=(MES*11.3932*1436.7)/2000000
      else
          DAT(Count,2)=DAT(Count-1,2)
      end if
  end do
250  close(8)
      OUTFILE='[BOWEN.MES]MES_//Hole//'_//Run//'.DATA'
      open (9,file=OUTFILE,status='NEW')
      write(9,*)'The starting time of this file is',TSTAMP
      write(9,*)'There are ',Count,' records in this file'
      write(9,300)((DAT(Iter,Col), Col=1,2), Iter=1,Count)
300  format(2F10.4)
      close(9)
      write(6,*)
      write(6,*) 'Conversion complete.'
      goto 9999
C
C*****Error messages...*****
C
9000 write(6,*)'Found a bad record ',Count,' (skipping)...'
      ERROR=.TRUE.
      goto 100
9999 end

```

```

C*****
C          PROGRAM IMES1.FOR
C
C      This program subsamples mesotech raw data.  The time
C      interval between samples is 0.5 Sec as is the other
C      ATS and TARS data files.
C
C      Processing of the original raw data files skipped the
C      first data point.  This program corrects for this
C      oversight by adding an initial data point of zero.
C      This added point realigns the data for subsampling
C
C      Input files have the following name convention:
C          MES91_hole_run.data
C      Output files have the following name convention:
C          MEShole_run.data_raw
C*****
C          VARIABLE DECLARATION
C=====
C      real DATA(100000,2)      ! Array for output
C      real TIME                 ! Mesotech sample time
C      real DEPTH                ! Calculated Mes depth(m)
C      real Tdepth
C
C      integer Iter              ! Loop variable
C      integer Count            ! Counter for subsampling
C      integer ROW,COL          ! No.lines & columns
C      integer Number           ! Counter for Do loop
C
C      character*60 INFILE,OUTFILE ! Input, Output file names
C      character*1 HOLE         ! Hole number of file
C      character*2 RUN          ! Run number of file
C-----
C      Write(6,*)
C      Write(6,*)'Initializing....'
C      Do 15 ROW = 1,10000
C          Do 14 COL = 1,2
C              DATA(ROW,COL) = 0.0
14      Continue
15      Continue
C      Write(6,*)'Done'
C      Write(6,*)
C      Write(6,*)'Enter data file to be Interpolated:'
C      Read(5,16,err=900,end=910)INFILE

```

```

16  Format(a60)
    HOLE = INFILE(7:7)
    RUN = INFILE(9:10)
    Open(8,file=INFILE,STATUS='OLD')
    Read(8,*,err=900,end=910)
    Read(8,*,err=900,end=910)
20  Format(2f10.4)
    Count = 0
    ROW = 1
    Do while (IOSTAT .GE. 0)
        Read(8,20,err=900,end=910)TIME,DEPTH
        if (mod(Count,8) .eq. 0) then
            DATA(ROW,1)=TIME
            DATA(ROW,2)=Tdepth
            ROW =ROW + 1
        end if
        Count = Count + 1
        Tdepth = DEPTH
    End do
910  Close(8)
    ROW = ROW - 1
    OUTFILE ='[bowen.tuk91.mes]MES'//HOLE//'_0'//RUN//'.DATA_RAW'
    Write(6,*)OUTFILE
    Open(9,file=OUTFILE,STATUS='NEW')
    Write(9,*)'There are',ROW,'records in this file'
    Write(9,300)((DATA(Iter,COL), COL=1,2), Iter=1,ROW)
300  Format(2f10.4)
    Close(9)
    goto 999

C
C-----
C
900  Write(6,*)'Error Reading program terminated'
999  end

```

```

C*****
C          TARS3.FOR
C
C    Copyright 1989 Government of Canada,
C    Department of Fisheries & Oceans,
C    Institute of Ocean Sciences, Sidney B.C.
C
C Version: 1.0      Date: August 20, 1991
C
C Purpose:  To convert '91 TARS field data to raw format...
C           Also included are various conversions for
C           future convenience.
C
C           The processed data is presented as an array of
C           seven columns of data
C
C           Column 1----- Time in seconds
C           Column 2----- Transducer pressure in PSI
C           Column 3----- Depth of TARS in meters
C           Column 4----- Sine of heading
C           Column 5----- Cosine of heading
C           Column 6----- Pitch of TARS
C           Column 7----- Roll of TARS
C
C Written by: D. Riedel   Date: Aug, 1991
C Revised by: R. Bowen   Date: Sept,1991
C
C *****
C
C PARAMETERS
C =====
C
C   real PSI2Pa          ! Conversion factor: P.S.I.to Pascals
C   real GRAV            ! Acceleration due to gravity
C   real VSOUND          ! Velocity of sound in water:S=31.85
C                       ! T=-1.74 and P=20 dbars
C   real PSCALE          ! Scale factor for transducer to PSI
C   real YINT            ! Offset of least-squares-fit ofabove
C
C   parameter (PSI2Pa = 6.895)
C   parameter (GRAV = 9.81)
C   parameter (RATE = 7.2337962E-7) ! Sample rate for MES data
C   parameter (VSOUND = 1436.7)
C   parameter (PSCALE = 7.6740)

```

parameter (YINT = 0.854365389)

C

C VARIABLE DECLARATIONS

C

C

```
integer*4 ROW           ! Number of lines of data
integer*4 Iter          ! DO loop variable
integer Col             ! as above
integer NEG             ! Flag (=-1 number is negative)
integer START(3)       ! Array of start positions of HYD fields
integer count           ! Number leading spaces in HYD field
integer Count1         ! Count for computer time stamps
```

C

```
real*8 MLHDAT(100000,7) ! Output array
real MDEPTH             ! Depth in metres
real DAY                ! Standard day as read from input
real MONTH              ! " month" " " " "
real YEAR               ! " year " " " "
real SEC                ! " secs " " " "
real MIN                ! " mins " " " "
real HOUR               ! " hrs " " " "
real*8 JDAYS            ! Julian Date
real*8 TOFDAY           ! Time of day of reading
real OFFSET(3)         ! Correction for HYD times
```

C

```
character*9 TSTAMP      ! System time to sync data sets
character*80 INFILE,OUTFILE ! Name of input and output files
character*3 FTYPE       ! Input file type (HYD,TAR,MES)
character*60 DLINE      ! Individual line of input file data
character*8 DATE        ! Standard date
character*8 TIME        ! Standard time
character*3 PDEPTH      ! Depth (in terms of lbs/sq. inch)
character*2 DIRSIN      ! Sine component of heading
character*2 DIRCOS      ! Cosine component of heading
character*2 PITCH       ! Pitch of TARS
character*2 ROLL        ! Roll " "
character*80 CHECK      ! First line of input to check FTYPE
character*80 PLUS       ! Junk buffer
character*7 CHAN        ! Forward, starboard and vertical posn.
character*1 Hole        ! Hole number
character*2 Run         ! Run number
```

C

C

C MAIN PROGRAM

```

C =====
C
  write(6,*)
  write(6,*) 'Initialising...'
  DO 996 ROW = 1,100000    ! Initialise arrays
    DO 995 ICOL = 1,7
      MLHDAT(ROW,ICOL) = 0.0
995   continue
996   continue
      DO 998 Loop = 1,3
        START(Loop) = 0
998   continue
      write(6,*) 'Done.'
      write(6,*)
C
999  write(6,*) 'Enter Data File Name: (Please use caps lock) '
      read(5,1000,err=900,end=910)INFILE
1000 format(A80)
      write(6,*)INFILE
      Hole = INFILE(8:8)
      Run = INFILE(11:12)
      open(8,file=INFILE,READONLY,STATUS='OLD',ERR=899)
      goto 3000
C
C
C TARS DATA HANDLER
C -----
C
3000 read(8,3010,err=900,end=910)
      Count1 = 0
      DO 15 Number = 1,20
        Read(8,3010,err=900,end=3018)DLINE
        if (INDEX(DLINE, 'I') .NE. 0) Then
          Count1 = Count1 + 1
          if (Count1 .EQ. 5) Then
            TSTAMP=DLINE(INDEX(DLINE,'I')+10:(INDEX(DLINE,'I')+17))
            Write(6,*)'Computer time stamp is',TSTAMP
            goto 23
          end if
        end if
15   continue
23   continue
      ROW = 1
      do while (IOSTAT .GE. 0)

```

```

    read(8,3010,err=900,end=3018)DLINE
3010  format(A60)
    MLHDAT(ROW,1) = (ROW-1)
    PDEPTH = DLINE(7:9)
    call UNHEX (PDEPTH,MDEPTH)
C
C **NOTE: The depth is converted to PSI using a least-squares-fit C calibration
C      scaling done for the TARS pressure transducer in lab at C IOS 23/05/90.
C
    MDEPTH = (MDEPTH/PSCALE) + YINT
    MLHDAT(ROW,2) = MDEPTH
    MDEPTH = ((MDEPTH*PSI2Pa)/(GRAV))
    MLHDAT(ROW,3) = MDEPTH
    DIRSIN = DLINE(11:12)
    call UNHEX (DIRSIN,MLHDAT(ROW,4))
    MLHDAT(ROW,4) = (MLHDAT(ROW,4)/255)*2 - 1
    DIRCOS = DLINE(13:14)
    call UNHEX (DIRCOS,MLHDAT(ROW,5))
    MLHDAT(ROW,5) = (MLHDAT(ROW,5)/255)*2 - 1
    PITCH = DLINE(21:22)
    call UNHEX (PITCH,MLHDAT(ROW,6))
    MLHDAT(ROW,6) = (MLHDAT(ROW,6)/256)*90 - 45
    ROLL = DLINE(23:24)
    call UNHEX (ROLL,MLHDAT(ROW,7))
    MLHDAT(ROW,7) = (MLHDAT(ROW,7)/256)*90 - 45
    ROW = ROW + 1
end do
3018 close(8)
    ROW = ROW - 1
    OUTFILE = '[BOWEN.TUK91.TAR]TARS_ '//Hole//'_ '//Run//' .data'
    write(6,*)OUTFILE
    OPEN(9,file=OUTFILE,STATUS='NEW')
    write(9,*)'The system time at the start of data is',TSTAMP
    write(9,*)'There are ',ROW,'records in this file'
    write(9,3025)((MLHDAT(Iter,Col), Col=1,7), Iter=1,ROW)
3025 format(1X,F6.1,6F10.4)
    close(9)
    write(6,*) 'NUMBER OF RECORDS: ',ROW
    write(6,*)
    write(6,*) 'Conversion complete.'
    goto 920
C
C
C ERROR MESSAGES

```

```

C=====
C
899  write(6,*) 'Error opening file. Please reenter info.'
      goto 999
900  write(6,*) 'Error reading... Program terminated. '
910  write(6,*) 'Unexpected end of data... Program terminated. ' C
920  end

```

```

C
C
C SUBROUTINES

```

```

C=====
C
  SUBROUTINE UNHEX (string, number)
C Routine to convert a random length hexadecimal string to a
C decimal real.
C
C Variables
  character*(*) string
  real digit,number
  integer Loop
  integer posn
C
  digit = 0.0
  number = 0.0
  do 100 Loop = 0, LEN(string) - 1
    posn = LEN(string) - Loop
    if (ICHAR(string(posn:posn)) .GT. 57) then
      digit = ICHAR(string(posn:posn)) - 55
    else
      digit = ICHAR(string(posn:posn)) - 48
    end if
    number = number + digit*(16**Loop)
  100 continue
  end

```

```

C
C
C-----
  real FUNCTION UNCHAR(word)
C Routine to convert a character string to a decimal real.
C
C variables
  character*(*) word      ! String to be converted
  integer qq              ! Loop variable
  integer dec             ! Position after the decimal point

```

real ascii	! ASCII code for given character
integer point	! Position of the decimal point
logical frac	! Boolean flag (.TRUE. if past decimal)
logical noni	! Boolean flag (.TRUE. if decimal in #)

C

```

UNCHAR = 0.0
dec = 1
point = 0
ascii = 0.0
noni = .FALSE.
frac = .FALSE.
if (INDEX(word, '.') .NE. 0) then
  noni = .TRUE.
  point = INDEX(word, '.')
end if
DO 4900 qq = 1, LEN(word)
  ascii = ICHAR(word(qq:qq))
  if (((ascii .LT. 48) .OR. (ascii .GT. 57))
&    .AND. (ascii .NE. 46)) then
    UNCHAR = 99999
    goto 4910
  end if
  if (ascii .EQ. 46) then
    frac = .TRUE.
    goto 4900
  end if
  if (frac) then
    UNCHAR = UNCHAR + (ascii - 48)/(10**dec)
    dec = dec + 1
  else
    if (noni) then
      UNCHAR = UNCHAR + (ascii-48)*(10**(point-qq-1))
    else
      UNCHAR = UNCHAR + (ascii-48)*(10**(LEN(word)-qq))
    end if
  end if
4900 continue
4910 end

```

C*****

C PROGRAM RUN_AVERAGE.FOR

C

C This programs takes ATS data that has
 C been processed by the program TIMER.FOR and smooths
 C the data by using a running average with a user
 C specified window. This window refers to the number
 C of points used in the averaging process.

C

C In order to maintain the multiline header format, the
 C the data output file is stamped with the two identifying
 C MLH codes that associate the data with the appropriate
 C header file.

C

C INPUT NAMING CONVENTION:
 C ATS/hole#_/run#/.DATA_EDIT

C

C OUTPUT NAMING CONVENTION:
 C ATS/hole#_/run#/.DATA_AVE

C

C Written by R. Bowen
 C April 3, 1992

C*****

C VARIABLE DECLARATIONS

C=====

C

character*100 INFILE,OUTFILE
 character*23 STUFF1,STUFF2
 character*3 RUN
 character*2 HOLE

C

real DIF
 real DATA(10000,3)
 real EDIT(10000,3)
 real AV
 real AVE
 real SUM
 real HAFWIN
 real TIME
 real TIME1,TIME2
 real BASE

C

integer TOTAL
 integer COUNTER

```

integer NEAREND
integer INCREMENT
integer WINDOW
integer NUMREC
integer ROW
integer COL
integer POINT
integer HALFW
logical error

```

```
C*****
```

```
C
```

```
Write (6,*)' Initializing...'
```

```
Do 37 ROW = 1,10000
```

```
  Do 36 COL = 1,3
```

```
    EDIT(ROW,COL) = 0.0
```

```
36   Continue
```

```
37   Continue
```

```
Write (6,*)'Done'
```

```
Write (6,*)'Enter ATS file: '
```

```
Read (5,45,err=900,end=910)INFILE
```

```
45   Format(a25)
```

```
Write (6,*)INFILE
```

```
HOLE = INFILE(4:4)
```

```
RUN = INFILE(6:8)
```

```
Write (6,*)'Enter Averaging Window(odd number only): '
```

```
Read (5,47,err=900,end=910)WINDOW
```

```
47   Format(i3)
```

```
Write (6,*)WINDOW
```

```
OPEN(8,file=INFILE,status='OLD')
```

```
Read(8,55,err=900,end=910)STUFF1
```

```
Read(8,55,err=900,end=910)STUFF2
```

```
55   Format(a23)
```

```
Write(6,*)STUFF1
```

```
Write(6,*)STUFF2
```

```
ROW = 1
```

```
C*****
```

```
Do while (IOSTAT .GE. 0)
```

```
  Read (8,56,err=900,end=950)(DATA(ROW,COL),COL=1,3)
```

```
  ROW = ROW + 1
```

```
56   Format(3F8.2)
```

```
End do
```

```
950 NUMREC = ROW - 1
```

```
Write(6,*)NUMREC
```

```
C*****
```

```

COUNT = 1
ROW = 1
Do while (COUNT .LE. NUMREC)
  SUM = 0
  DO 27 NUMBER = COUNT,COUNT+WINDOW-1
    SUM = SUM + DATA(NUMBER,1)
27  Continue
  AVE = SUM/WINDOW
  HALFW = WINDOW/2
  HALWIN =HALFW + 0.5
  HALFW = INT(HALWIN)
  POINT = COUNT+HALFW
  NEAREND = NUMREC - COUNT
  IF(COUNT .EQ. 1)Then
    DO 17 NUMBER = 1,POINT
      EDIT(NUMBER,1) = DATA(NUMBER,1)
      EDIT(NUMBER,2) = DATA(NUMBER,2)
      EDIT(NUMBER,3) = DATA(NUMBER,3)
17  Continue
    Endif
  IF(NEAREND .EQ. WINDOW)Then
    DO 54 NUMBER = POINT+1,NUMREC
      EDIT(NUMBER,1) = DATA(NUMBER,1)
      EDIT(NUMBER,2) = DATA(NUMBER,2)
      EDIT(NUMBER,3) = DATA(NUMBER,3)
54  Continue
    EDIT(POINT,1) = DATA(POINT,1)
    EDIT(POINT,2) = DATA(POINT,2)
    EDIT(POINT,3) = DATA(POINT,3)
    goto 910
  Endif
  EDIT(POINT,1) = AVE
  EDIT(POINT,2) = DATA(POINT,2)
  EDIT(POINT,3) = DATA(POINT,3)
  COUNT = COUNT + 1
end do
910 CLOSE(8)
C*****
C          OUTPUT                      *
C*****
C
OUTFILE = '[BOWEN.TUK91.ATS]AT'//HOLE//'_'//RUN//'.DATA_AVE'
Write(6,*)OUTFILE
OPEN(9,file=OUTFILE,STATUS = 'NEW')

```

```

C   Write(9,45)STUFF1
C   Write(9,45)STUFF2
   Write(9,300)((EDIT(Iter,Col),Col=1,3),Iter=1,NUMREC)
300  Format(3F8.2)
     goto 350
C*****
900  Write(6,*)'Error reading data'
350  end

```

```

C*****

```

```

C           PROGRAM COMBINE.FOR

```

```

C           This program combines ATS, TARS, and MES processed
C           data files into one large array 12 columns wide.
C           The data is arranged in the following order:

```

```

C           Column 1-----ATS X Coordinate
C           Column 2-----ATS Y Coordinate
C           Column 3-----TARS Depth
C           Column 4-----MESOTECH (distance to ice)
C           Column 5-----TARS Sin of Heading
C           Column 6-----TARS Cos of Heading
C           Column 7-----TARS Pitch
C           Column 8-----TARS Roll
C           Column 9-----TIME (reference)

```

```

C           The data has been synchronized using the computer time
C           stamp imbedded in the raw field data files. The sequence
C           of the initial data firing was ATS, MES, TARS. The gaps
C           between data file time stamps is calculated and data is
C           arranged starting at the last time stamp of the TARS data

```

```

C*****

```

```

C           VARIABLE DECLARATIONS

```

```

C-----

```

```

C

```

```

C   character*80 OUTFILE           !
C   character*80 DATA1           ! Data file ATS
C   character*80 DATA2           ! Data file MES
C   character*80 DATA3           ! Data file TARS
C   character*60 Junk

```

```

character*1 HOLE
character*2 RUN
C
integer ROW, COL
integer Number
C
real DATA(10000,9)
real TV1,TV2
real QT1,QT2
real Offset,Offset1
real Ttars,Tmes,Tats
real T1,X1,Y1,Z1,H1,P1,R1
real T2,D2
real T3,PSI,SH,CH,P,R
C
C=====
C
Do 15 ROW = 1,10000
    Do 14 COL = 1,9
14      Continue
15      Continue
      ROW = 1
      Write(6,*)'Done'
      Write(6,*)'First data set(ATS): '
      Read(5,30,err=900,end=920)DATA1
30      format(A80)
      HOLE = DATA1 (9:9)
      RUN = DATA1 (12:13)
      Write(6,*)'Second data set(MES): '
      Read(5,30,err=900,end=920)DATA2
      Write(6,*)'Third data set(TARS): '
      Read(5,30,err=900,end=920)DATA3
      OPEN(8,file=DATA1,STATUS='OLD')
      OPEN(9,file=DATA2,STATUS='OLD')
      OPEN(10,file=DATA3,STATUS='OLD')
      Write(6,*)'Data files opened...'
      Write(6,*)'Start time of ATS data: '
      Read(5,22,err=900,end=920)Tats
      Write(6,*)'Start time of MES data: '
      Read(5,22,err=900,end=920)Tmes
      Write(6,*)'Start time of TARS data: '
      Read(5,22,err=900,end=920)Ttars
22      Format(f8.2)
      TV1 = Ttars-Tats

```

```

QT1 = TV1-INT(TV1)
if (QT1 .LT. .25) Then
  Offset = INT(TV1)
  Goto 215
endif
if (QT1 .GE. 0.25 .AND. QT1 .LT. 0.75) Then
  Offset = INT(TV1) + 0.5
  Goto 215
endif
if (QT1 .GE. .75) Then
  Offset = INT(TV1) + 1.0
  Goto 215
endif
215 Continue
write(6,*)Offset
Read(8,11,err=900,end=910)Junk
Read(8,11,err=900,end=910)Junk
11 Format(a30)
Do 25 Number=1,100
  Read(8,35,err=900,end=910)T1,X1,Y1
35 Format(3F8.2)
  if (T1 .EQ. Offset) Then
    DATA(ROW,1) = X1
    DATA(ROW,2) = Y1
    Goto 26
  endif
25 Continue
26 Continue
TV2 = Ttars-Tmes
QT2 = TV2 - INT(TV2)
if (QT2 .LT. .25) Then
  Offset1 = INT(TV2)
  Goto 216
endif
if (QT2 .GE. 0.25 .AND. QT2 .LT. 0.75) Then
  Offset1 = INT(TV2) + 0.5
  Goto 216
endif
if (QT2 .GE. .75) Then
  Offset1 = INT(TV2) + 1.0
  Goto 216
endif
216 Continue
Write(6,*)Offset1

```

```

Read(9,11,err=900,end=911)JUNK
Read(9,11,err=900,end=911)JUNK
Do 36 Number = 1,500
  Read(9,38,err=900,end=911)T2,D2
38  Format(2F10.4)
    if (T2 .EQ. Offset1) Then
      DATA(ROW,4) = D2
      write (6,*)T2
      write (6,*)D2
      write(6,*)Number
      Goto 37
    endif
36  Continue
37  Continue
Read(10,11,err=900,end=912)Junk
Read(10,11,err=900,end=912)Junk
Read(10,39,err=900,end=912)T3,PSI,DEPTH,SH,CH,P,R
39  Format(1P,7(E14.6))
    DATA(ROW,9)=T3
    DATA(ROW,3)=DEPTH
    DATA(ROW,5)=SH
    DATA(ROW,6)=CH
    DATA(ROW,7)=P
    DATA(ROW,8)=R
    write(6,*)T1,X1,Y1,T2,D2,T3,PSI,DEPTH,SH,CH,P,R
    ROW = ROW + 1
    Do while (IOSTAT .GE. 0)
      Read(8,35,err=900,end=910)T1,X1,Y1
      DATA(ROW,1) = X1
      DATA(ROW,2) = Y1
      Read(9,38,err=900,end=911)T2,D2
      DATA(ROW,4) = D2
      Read(10,39,err=900,end=912)T3,PSI,DEPTH,SH,CH,P,R
      DATA(ROW,9)=T3
      DATA(ROW,3)=DEPTH
      DATA(ROW,5)=SH
      DATA(ROW,6)=CH
      DATA(ROW,7)=P
      DATA(ROW,8)=R
      ROW = ROW + 1
    end do
910  Close(8)
911  Close(9)
912  Close(10)

```

```

ROW = ROW + 1
OUTFILE = 'SCRATCH$PHYSICS:[BOWEN]ICE_ '//HOLE//'_ '//RUN//' .dat'
Write(6,*)OUTFILE
Open(11,file=OUTFILE,STATUS='NEW')
Write(11,*)'The time interval between ats and TARS:',Offset
Write(11,*)'The time interval between MES and TARS:',Offset1
Write(11,1212)((DATA(Iter,COL), COL=1,9), Iter=1,ROW)
1212 Format(9F8.2)
Close(11)
Write(6,*)'The number of records in this file is: ',ROW

```

```

C=====
C      ERROR MESSAGES
C=====
C

```

```

900 Write(6,*)'Error reading...Program terminated. '
920 end

```

```

'*****'

```

```

'FIT_RES.BAS      Version 1.0

```

```

',
',
',   This program takes track segment data from the KEEL91 survey data set
',   and corrects the geometry of the data for pitch and roll of the TARS
',   vehicle. It is assumed that the TARS follows the direction of travel.
',

```

```

',   The input file to this program must be a sequential file with the
',   following format:

```

```

',       Channel 1:   X position (normal displacement)
',                   2:   Y position (orthogonal displacement)
',                   3:   TARS depth (below sea level)
',                   4:   MESOTECH distance (to ice)
',                   5:   Sine of TARS heading      unused
',                   6:   Cosine of TARS heading    unused
',                   7:   Pitch of TARS
',                   8:   Roll of TARS
',                   9:   Time (reference)          unused
',
',

```

```

',   In addition, the file must contain a header with the following
',   information(X and Y):

```

```

',       Line 1: An integer giving the number of lines to follow in
',               the header (i.e. number of coefficients)
',

```



```

DIM DelX, DelY AS SINGLE      ' Offset direction indicators
DIM XCOEFFS(XDEGREE) AS SINGLE      ' Array of polynomial coefs from time vs X
DIM YCOEFFS(YDEGREE) AS SINGLE      ' Array of polynomial coefs from time vs Y
DIM KEEL(1500, 9) AS SINGLE      ' Array of input file data (one line)
DIM HDG AS SINGLE              ' Direction of TARS
DIM TanTheta AS SINGLE      ' Tangent of projected roll (actual)
DIM TanPhi AS SINGLE          ' " " " " pitch "

```

```

Path = "C:\ROB\SPLIT"          ' Set default directory
BACKHAUL = "F"

```

```

'***MAIN

```

```

PROGRAM*****

```

```

CLS                                ' Get input file
PRINT "FIT_RES  VER. 1.0"          ' from user, open
PRINT "-----  -----"          ' it and the output
PRINT
PRINT
PRINT "The file directory is currently: "; Path
INPUT "Do you wish to change this ? (<CR> = No) ", Change
IF (Change = "Y" OR Change = "y") THEN INPUT "Enter the new path ", Path
PRINT
INPUT "Is there a list of files to be processed "; Change
IF Change = "N" OR Change = "n" THEN GOTO 100
INPUT "What is the name of the list file [****.LST] "; FLIST
FLIST = Path + FLIST
OPEN FLIST FOR INPUT ACCESS READ AS #3
INPUT #3, INUM
FOR L = 1 TO INUM
    INPUT #3, NOM(L)
NEXT L
CLOSE #3
GOTO 200
100 INPUT "Please enter the name of the input file ", infile
GOTO 300
200 FOR M = 1 TO INUM
    infile = NOM(M)
300 outfile = Path + "_TRCK" + MID$(infile, 6, 14)
IF (UCASE$(MID$(infile, INSTR(infile, ".") - 1, 1)) = "H") THEN BACKHAUL = "T"
infile = Path + infile
OPEN infile FOR INPUT ACCESS READ AS #1
OPEN outfile FOR OUTPUT AS #2
INPUT #1, XDEGREE

```

```

REDIM XCOEFFS(XDEGREE) AS SINGLE

FOR I = 1 TO XDEGREE
    INPUT #1, XCOEFFS(I)
NEXT I
Derivative XDEGREE, XCOEFFS()
INPUT #1, YDEGREE
REDIM YCOEFFS(YDEGREE) AS SINGLE
FOR I = 1 TO YDEGREE
    INPUT #1, YCOEFFS(I)
NEXT I
Derivative YDEGREE, YCOEFFS()
COUNT = 1
PRINT
'LOCATE 15, 1, 0
PRINT "Reading "; infile
WHILE NOT EOF(1)
    FOR J = 1 TO 9
        INPUT #1, KEEL(COUNT, J)
    NEXT J
    COUNT = COUNT + 1
WEND

PRINT
POSI = "F"
IF (KEEL(COUNT - 1, 1) - KEEL(1, 1)) > 0! THEN POSI = "T"
'LOCATE 17, 1, 0
PRINT "Writing "; outfile
FOR K = 1 TO COUNT - 1
    'LOCATE 19, 30, 0
    INPUT a$
    PRINT "Record #: "; K
    Heading XCOEFFS(), YCOEFFS(), KEEL(K, 9), POSI, HDG, XDEGREE, YDEGREE,
BACKHAUL
    'PRINT "Heading= "; HDG
    DelX = 1!
    DelY = 1!
    KEEL(K, 7) = DegToRad(KEEL(K, 7))
    KEEL(K, 8) = DegToRad(KEEL(K, 8))
    'PRINT KEEL(K, 7), KEEL(K, 8)
    IF KEEL(K, 7) > 0! THEN DelY = -1!
    IF KEEL(K, 8) < 0! THEN DelX = -1!
    'PRINT DelY, DelX
    TanTheta = Roll(KEEL(K, 7), KEEL(K, 8))

```

' Read coefficients
' of polynomial

' Read coefficients
' of polynomial

' Step through file
' reading the data

' Step through and
' resolve data

'Find actual roll

```

TanPhi = TAN(KEEL(K, 7))
FindOffsets TanTheta, TanPhi, DelX, DelY, KEEL(K, 4) 'Find deltas
YawCorrection DelX, DelY, HDG
'PRINT "Initial X and Y: "; KEEL(K, 1), KEEL(K, 2)
KEEL(K, 1) = KEEL(K, 1) + DelX
KEEL(K, 2) = KEEL(K, 2) + DelY
'PRINT "Final X and Y: "; KEEL(K, 1), KEEL(K, 2)
IF K <> 1 THEN
    FOR L = 1 TO 9
        PRINT #2, KEEL(K, L); ' Write the new data
    NEXT L
PRINT #2,
END IF
NEXT K
IF Change = "N" OR Change = "n" THEN GOTO 400
CLOSE #1
CLOSE #2
NEXT M
400 END

FUNCTION DegToRad! (Angle)

PI = 3.1415927#

DegToRad = (Angle / 180!) * PI

END FUNCTION

'***Determine the derivative of the polynomial*****
SUB Derivative (DEG%, Coef()) STATIC

FOR J = 1 TO DEG%
'    PRINT Coef(J);
    Coef(J) = Coef(J) * (J - 1)
'    PRINT "    "; Coef(J)
NEXT J
PRINT

END SUB

'***Subroutine to determine position change due to pitch and roll*****
SUB FindOffsets (TanT, TanP, DelX, DelY, MES)

```

```

'PRINT "DelY: "; DelY, "DelX: "; DelX
DelX = DelX * MES * SQR(1 / (1 + TanP ^ 2)) * SQR(TanT ^ 2 / (1 + TanT ^ 2))
DelY = DelY * MES * SQR(TanP ^ 2 / (1 + TanP ^ 2))
MES = MES * SQR(1 / (1 + TanP ^ 2)) * SQR(1 / (1 + TanT ^ 2))
'PRINT "New offsets... (dx,dy,z) ", "("; DelX; ","; DelY; ","; MES; ")"
END SUB

```

```

****Determine angular heading of TARS based on polynomial fit to track*****
SUB Heading (XCoef(), YCoef(), t, POSIS$, HDG, XDEG%, YDEG%, BACKS$) STATIC

```

```

PI = 3.14159
DIM XSLOPE AS SINGLE
DIM YSLOPE AS SINGLE

```

```

XSLOPE = 0!
FOR K = 2 TO XDEG%
    XSLOPE = XSLOPE + XCoef(K) * t ^ (K - 2)    ' Find slope
NEXT K

```

```

YSLOPE = 0!
FOR K = 2 TO YDEG%
    YSLOPE = YSLOPE + YCoef(K) * t ^ (K - 2)    ' Find slope
NEXT K

```

```

IF (XSLOPE = 0) THEN
    IF (YSLOPE > 0) THEN
        HDG = PI / 2
    ELSE
        HDG = -(PI / 2)
    END IF
    GOTO 220

```

```

END IF
HDG = ATN(YSLOPE / XSLOPE)    ' Adjust for quadrant
'PRINT "SLOPE "; SLOPE, "HEADING= "; HDG
IF (POSI$ <> "T") THEN HDG = PI + HDG
'The following line adjusts the heading for the reverse orientation of the
'TARS (i.e. backwards) - if necessary
IF (BACKS$ = "T") THEN HDG = HDG - PI
IF HDG < 0! THEN HDG = HDG + 2 * PI    'QUADRANT FOUR
220 'HDG extremes ( +or- PI/2)
LOCATE 19, 5
PRINT "HDG= "; HDG
'INPUT a$
END SUB

```

```
****Determine the actual roll angle*****
```

```
FUNCTION Roll (PhiPR, ThetaPR)
```

```
Roll = TAN(ThetaPR) * COS(PhiPR)
```

```
END FUNCTION
```

```
****Correct x and y positions for yaw (TARS bearing)*****
```

```
SUB YawCorrection (DelX, DelY, HDG)
```

```
PI = 3.1415927#
```

```
DIM Xtemp AS SINGLE
```

```
DIM Ytemp AS SINGLE
```

```
Xtemp = DelX
```

```
Ytemp = DelY
```

```
DelY = Ytemp * SIN(HDG) - Xtemp * COS(HDG)
```

```
DelX = Ytemp * COS(HDG) + Xtemp * SIN(HDG)
```

```
'PRINT "Final X and Y offsets: ", DelX, DelY
```

```
END SUB
```

```
*****
```

```
'THIN2.BAS (vers 2.01)
```

```
,
```

```
'A program to reduce the density of the track data collected by the TARS.
```

```
'The method used is such that any point within a user specified distance
```

```
'from the previous point is discarded.
```

```
'*nb: The final output has only X45, Y45 and Feature-Depth.
```

```
,
```

```
'Dave Riedel, July 1991
```

```
,
```

```
'Revised by D. Riedel, June 1992: Code altered to skip records until window
```

```
,
```

```
size is met...
```

```
,
```

```
June 8, 1992: Altered to meet Rob Bowen's criteria
```

```
,
```

```
*****
```

```
DEFINT I-L                   ' Loop variables
```

```
***VARIABLES*****
```

```
*
```

```

DIM infile(50) AS STRING      ' Name of input file
DIM outfile AS STRING        ' Name of output file
DIM FLIST AS STRING          ' Name of input list file
DIM NOM(40) AS STRING        ' An array of files to be processed
DIM Path AS STRING           ' Location of files
DIM JUNK AS STRING           ' String to hold header info
DIM Change AS STRING * 1     ' Response to path change inquiry

DIM COUNT AS INTEGER        ' Number of lines in data file

DIM KEEL(9) AS SINGLE        ' Array of input file data (one line)
DIM PITCH AS SINGLE          ' Pitch of TARS
DIM ROLL AS SINGLE           ' Roll of TARS
DIM MINDIST AS SINGLE        ' The minimum space between output pts
DIM DIST AS SINGLE          ' The distance between the last two points

```

```
Path = "C:\ROB\ " ' Set default directory
```

```
'***MAIN
```

```
PROGRAM*****
```

```

CLS                                ' Get input file
PRINT "THIN  VER. 2.01"             ' from user, open
PRINT "----  -----"             ' it and the output
PRINT
PRINT
PRINT "The file directory is currently: "; Path
INPUT "Do you wish to change this ? (<CR> = No) ", Change
IF (Change = "Y" OR Change = "y") THEN INPUT "Enter the new path ", Path
PRINT
INPUT "Is there a list of files to be processed "; Change
INPUT "What is the minimum distance between points ? ", MINDIST
INPUT "What is the maximum Pitch cutoff ? ", PITCH
INPUT "What is the Maximum Roll cutoff ? ", ROLL
IF Change = "N" OR Change = "n" THEN GOTO 100
INPUT "What is the name of the list file [****.LST] "; FLIST
FLIST = Path + FLIST
OPEN FLIST FOR INPUT ACCESS READ AS #3
INPUT #3, INUM
FOR L = 1 TO INUM
    INPUT #3, infile(L)
NEXT L
CLOSE #3
GOTO 200

```

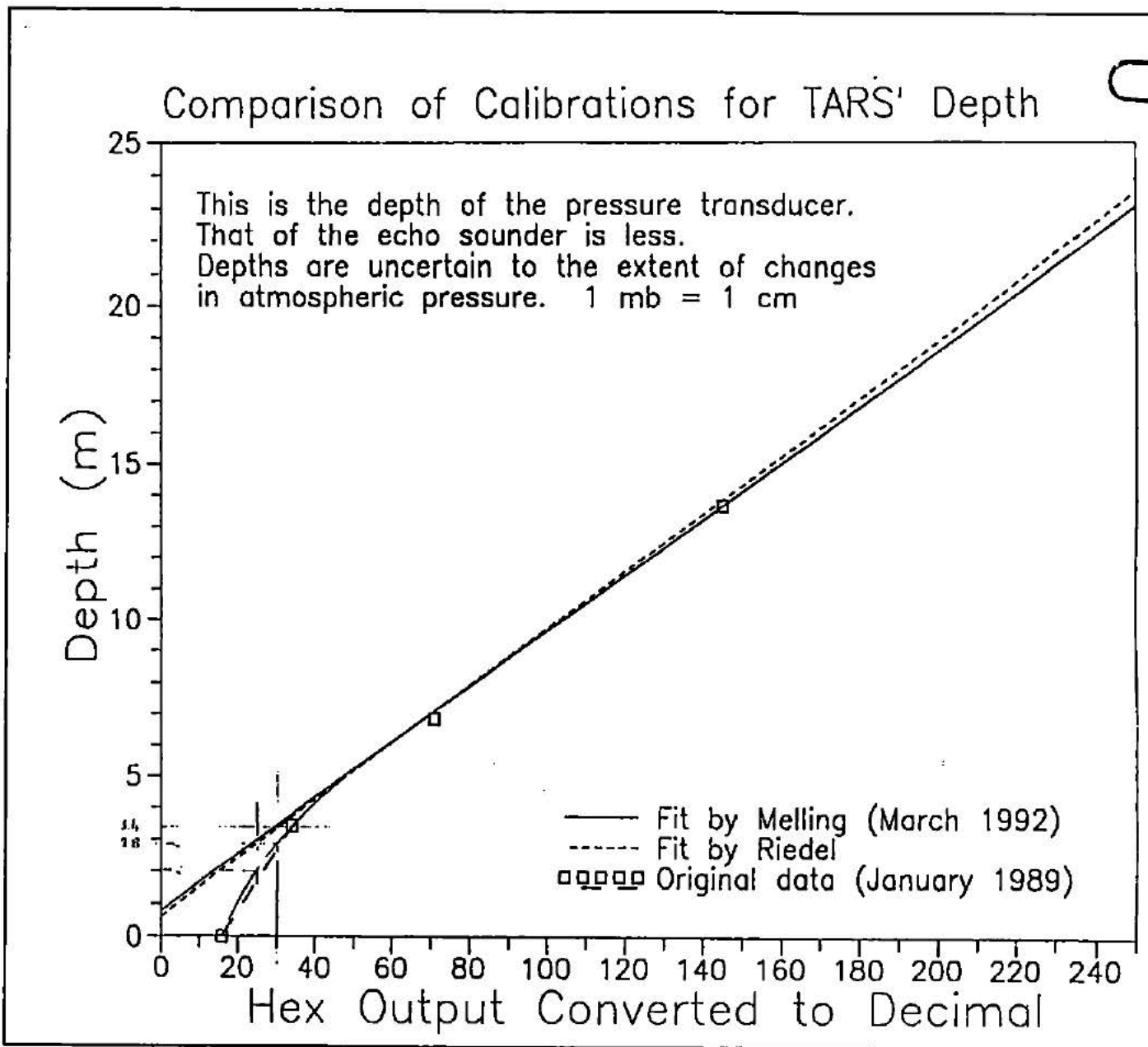
```

100 INPUT "Please enter the name of the input file ", infile(0)
GOTO 300
200 FOR M = 1 TO INUM
infile(M) = "TH" + infile(M) + ".DAT"
300 outfile = Path + LEFT$(infile(M), 7) + "T.DAT"
infile(M) = Path + infile(M)
OPEN infile(M) FOR INPUT ACCESS READ AS #1
OPEN outfile FOR OUTPUT AS #2
COUNT = 1
PRINT
LOCATE 15, 1, 0
PRINT "Thinning "; infile(M)
FOR K = 1 TO 3: INPUT #1, JUNK: NEXT K
DO
  INPUT #1, KEEL(1), KEEL(2), KEEL(3), KEEL(4), KEEL(5), KEEL(6), KEEL(7),
  KEEL(8), KEEL(9)
LOOP UNTIL (KEEL(3) > 5)
'PRINT #2, KEEL(1), KEEL(2), KEEL(3), KEEL(4), KEEL(5), KEEL(6), KEEL(7),
KEEL(8), KEEL(9)
X0 = KEEL(1)
Y0 = KEEL(2)
TotDist! = 0!
WHILE NOT EOF(1)
  DO
  FOR J = 1 TO 9
    INPUT #1, KEEL(J)
  NEXT J
  DIST = SQR((KEEL(1) - X0) ^ 2 + (KEEL(2) - Y0) ^ 2)
  LOOP UNTIL ((DIST >= MINDIST) OR EOF(1))
  DRAFT! = KEEL(3) - KEEL(4)
  IF ((DRAFT! >= 1!) AND (KEEL(3) > 5)) THEN
    IF (KEEL(7) <= PITCH AND KEEL(7) >= -(PITCH)) THEN
      IF (KEEL(8) <= ROLL AND KEEL(8) >= -(ROLL)) THEN
        PRINT #2, KEEL(1), KEEL(2), KEEL(7), KEEL(8); DRAFT!, KEEL(9)' Write
the new data
          TotDist! = TotDist! + DIST
          LOCATE 1, 74
          PRINT COUNT
          COUNT = COUNT + 1
          X0 = KEEL(1)
          Y0 = KEEL(2)
        END IF
      END IF
    END IF
  END IF
END IF

```

```
390 WEND
PRINT
LOCATE 17, 1, 0
PRINT "The file now contains "; COUNT; " records"
PRINT "Average distance between points: "; TotDist! / COUNT
CLOSE #1
CLOSE #2
IF Change = "N" OR Change = "n" THEN GOTO 400
NEXT M
400 END
```

Calibration Curve for TAR'S Pressure Transducer.



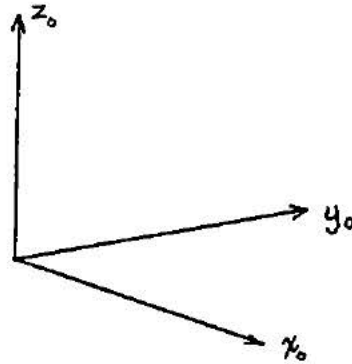
APPENDIX D
Calibration Curve of Pressure Transducer.

APPENDIX E

Resolving Pitch and Roll Transformations for TARS (David Topham's Notes)

Calculation of the orientation of the TARS amount MESOTECH acoustic beam relative to earth coordinates.

Define the earth fixed coordinates as the HR set s_o, y_o, z_o



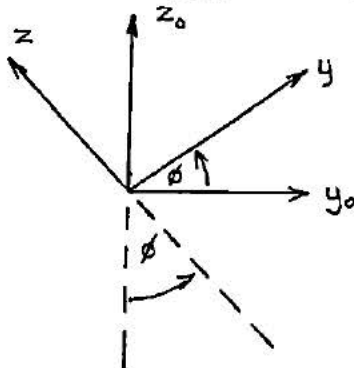
Centred on the centre of rotation of the vehicle, with the y_o -axis along the vehicle ϕ , +ve in the forward direction with both roll and pitch zero.

Define vehicle centred coordinates as the RH set x, y, x , with zero pitch and roll x_o, y_o, z_o and x, y, z , coincide.

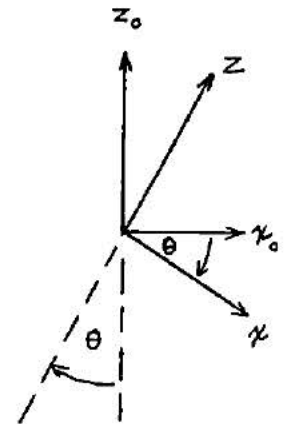
The roll angle is defined to be +ve with clockwise rotation when looking in the + direction of the y -axis (R.H. down).

The pitch angle is defined to be +ve with clockwise rotation when looking along the +ve direction of the x -axis (H are up).

Here we choose to apply roll first, followed by pitch.



Pitch



Roll

Pitch and roll are measured by pendulum sensors fixed in the y, z and z, x planes of the vehicle.

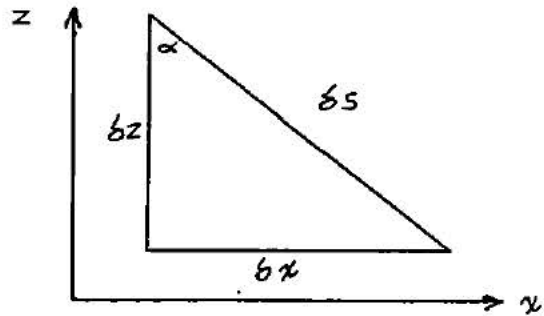
When subjected to pitch and roll combined, in general the sensor readouts denoted ϕ' and θ'

respectively do not equal the rotations ϕ and θ defined above. Since angular rotations in 3-D space do not commute, the ultimate position of the z-axis relative to earth coordinates can be achieved by two distinct pairs of angles ϕ, θ , depending upon whether pitch is applied first, followed by roll or vice versa.

The problem has two parts, the relation between the measured quantities ϕ^*, θ^* and the angles ϕ, θ followed by the relationships between ϕ, θ and the coordinate system x_0, y_0, z_0 .

The response of the roll sensor in the x, z plane

The pendulum will seek the point of lowest gravitational potential, or equivalently seek the path of steepest descent.



Consider a function $f = f(x, z)$ and its derivative along the direction δs making an angle α with the z-axis.

$$\delta f = \frac{\partial f}{\partial x} \delta x + \frac{\partial f}{\partial z} \delta z$$

from the diagram

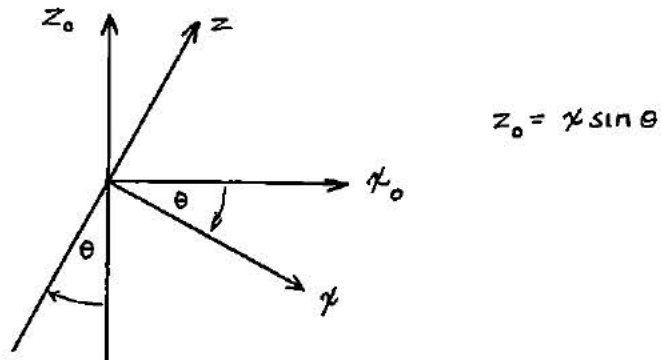
$$\delta x = \delta s \sin \alpha \text{ and } \delta z = - \delta s \cos \alpha$$

hence

$$\frac{df}{ds} = \frac{\partial f}{\partial x} \sin \alpha - \frac{\partial f}{\partial z} \cos \alpha$$

To find the angle of the pendulum we associate f with the gravitational potential and relate its functional dependence on x and y to the successive application of the rotations θ and ϕ , taken in that order, i.e. roll followed by pitch.

Simple example, roll angle θ , pitch angle zero



$$f = gz_0, \quad \frac{\partial f}{\partial s} = -g \sin \theta, \quad \frac{\partial f}{\partial z} = g \cos \theta$$

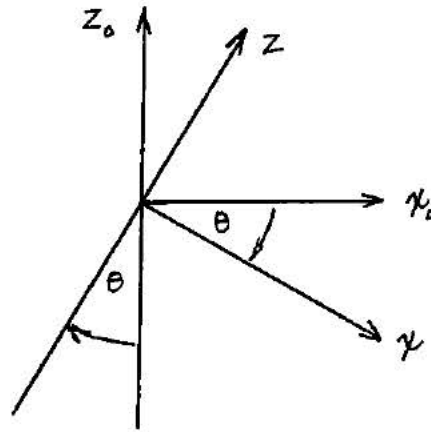
Hence

$$\frac{\partial f}{\partial s} = -g [\sin \theta \sin \alpha + \cos \theta \cos \alpha]$$

$$\frac{df}{ds} = -g \cos (\theta - \alpha)$$

This has a maximum at $\alpha = \theta$, i.e. when the pendulum hangs along the z_0 direction, which is as expected for this simple case.

Combined roll and pitch, applied in that order.



Consider that a roll θ has been applied, and consider a rotation ϕ about the x -axis; lines parallel to the x -axis will remain parallel to it as ϕ increases, and the rate of change in gravitational potential with x remains the same, i.e.

$$\frac{\partial f}{\partial x} = -g \sin \theta$$

Changes in gravitational potential along the z direction on the other hand are decreased, i.e. a unit vector along the z axis has a projection $\cos \phi$ on the x_0, z_0 plane, thus

$$\frac{\partial f}{\partial z} = g \cos \theta \cos \phi$$

Hence
$$\frac{\partial f}{\partial s} = -g [\sin \theta \sin \alpha + \cos \theta \cos \phi \cos \alpha]$$

which can be re-written in the form

$$\frac{df}{ds} = -g [\sin^2 \theta + \cos^2 \theta \cos^2 \phi]^{1/2} \cos(\lambda - \alpha)$$

with

$$\tan \lambda = \frac{\sin \theta}{\cos \theta \cos \phi} = \frac{\tan \theta}{\cos \phi}$$

$\frac{df}{ds}$ is therefore a maximum when $\alpha = \lambda$.

As the angles have been defined, $\alpha \equiv \theta'$, the angle indicated by the roll sensor.

Hence

$$\tan \theta' = \frac{\tan \theta}{\cos \phi}$$

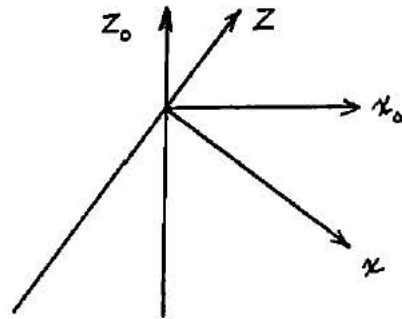
If $\phi = 0$, i.e. no pitch $\tan \theta' = \tan \theta$ as expected

If $\phi = \frac{\pi}{2}$ $\tan \theta' = \infty$, $\theta = \frac{\pi}{2}$

Response of the pitch sensor to combined roll and pitch applied in that order

Under the action of roll only, the reading of the pitch sensor remains at zero, rotation about the x-axis (pitch) then merely rotates the y,z plane in the y,z plane, the pendulum directly records this rotation, i.e.

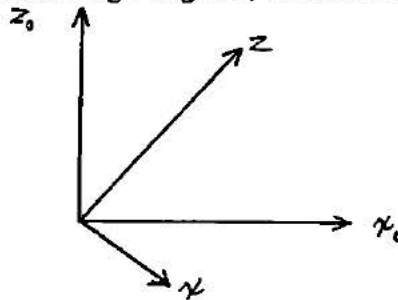
$$\phi' = \phi$$



Note: By applying roll first, θ is actually a rotation about the y_0 -axis, but ϕ is about the x-axis, hence the asymmetry and the non-commutality.

The relationship of the z-axis (Mesotech beam) to the z_0 -axis (gravitational vertical).

Consider first the application of roll through angle θ , a rotation about the y_0 -axis.

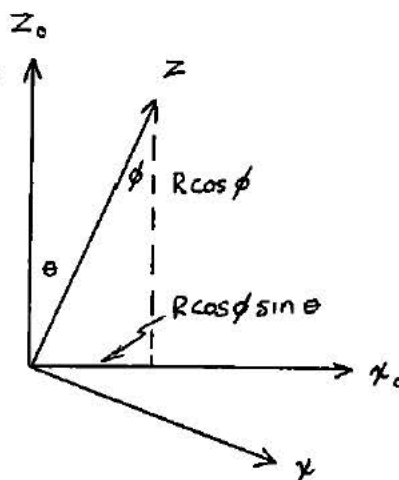


The projection of the Mesotech large R on the z_0 -axis is $R \cos \phi$. The application of pitch, a rotation about the x-axis of an angle θ results in a further projection giving $R \cos \phi \cos \theta$ as the final projection on the z_0 -axis.

The projection of the ray R onto the y_0 -axis is thus $R \sin \phi$, since rotation about this axis leaves the projection onto it unchanged.

The projection onto the x_0 -axis become $R \cos \phi \sin \theta$.

Projection of R onto the z_0, x_0 plane



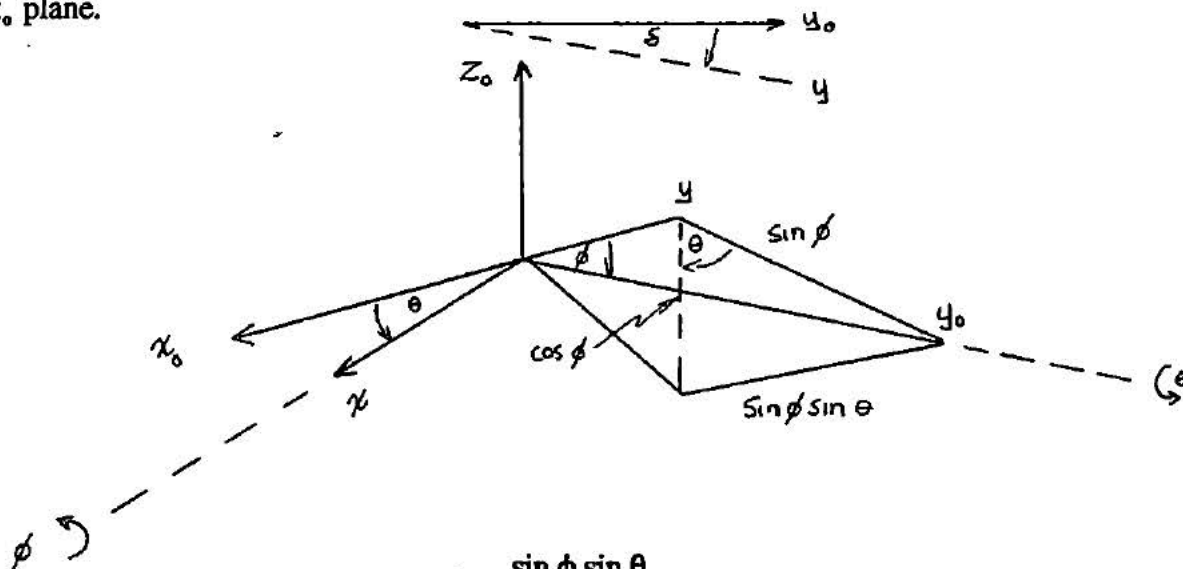
check

$$R^2 \cos^2 \phi \cos^2 \theta + R^2 \sin^2 \phi + R^2 \cos^2 \phi \sin^2 \theta = R^2 \cos^2 \phi (\cos^2 \theta + \sin^2 \theta) + R^2 \sin^2 \phi = R^2 \cos^2 \phi + R^2 \sin^2 \phi = R^2$$

= R as expected.

The heading correction, gimballed compass

With a gimballed instrument, the compass will output the projection of the y-axis onto the y_0-x_0 plane.



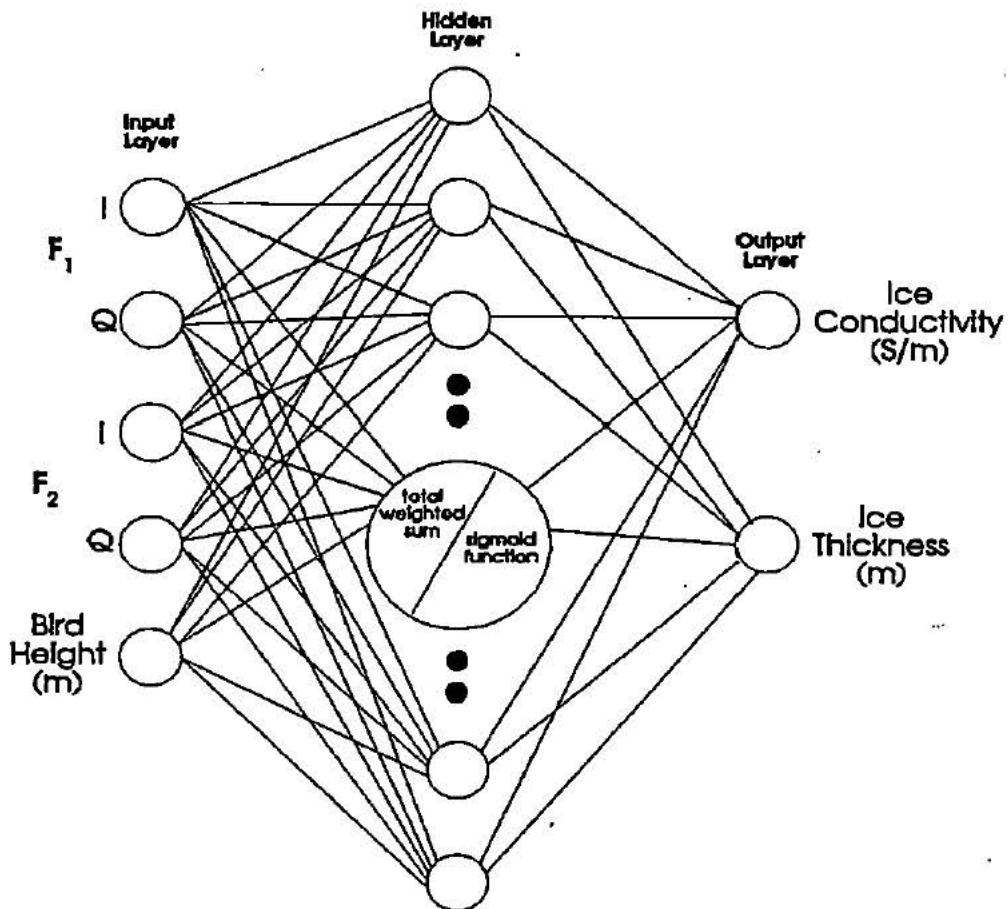
$$\tan \delta = \frac{\sin \phi \sin \theta}{\cos \phi}$$

$$\tan \delta = \tan \phi \sin \theta$$

if $\theta = 0, \delta = 0, \text{ if } \theta = \frac{\pi}{2}, \delta = \phi$

APPENDIX F
Neural Networks

1-D Neural Network with Ice Conductivity



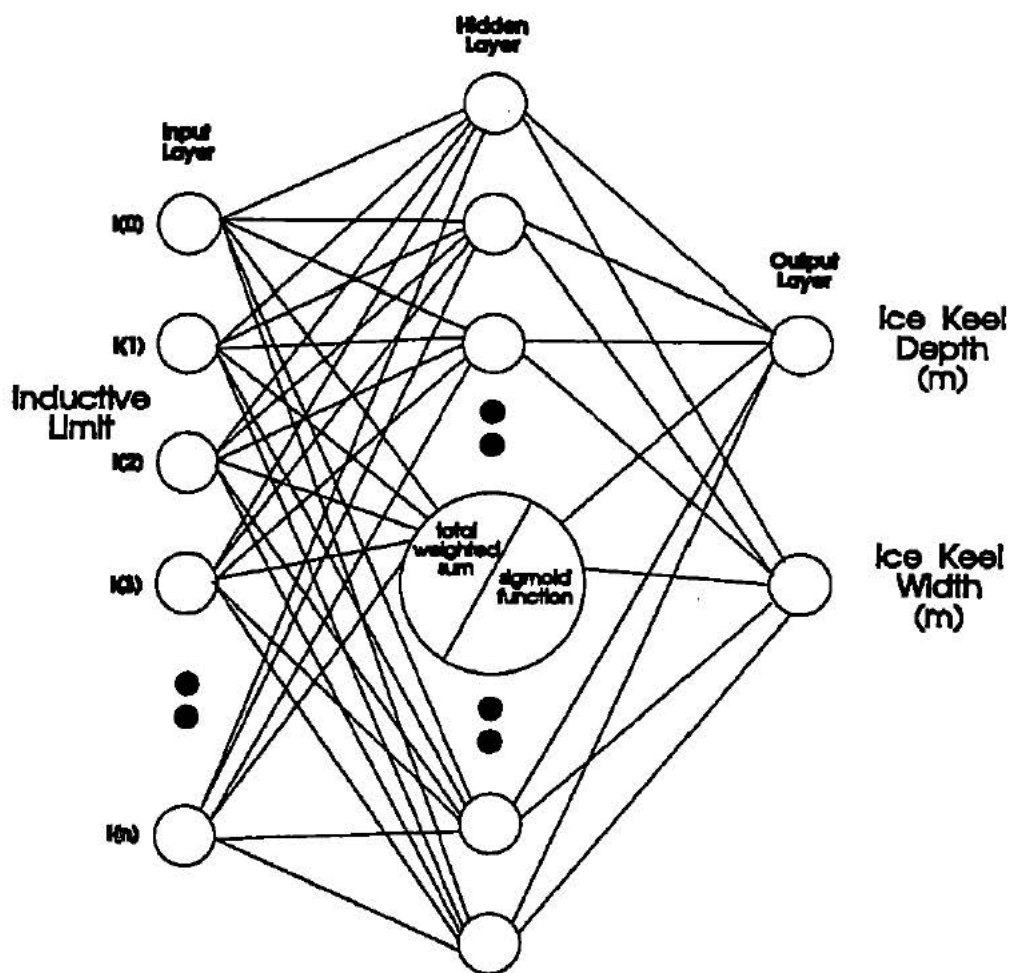
Frequencies: F1 - 2500 Hz
F2 - 94000 Hz

Altitude: Random from 10 m to 30 m
Ice thickness: Random from 0 m to 15 m
Ice Conductivity: Random from 0.003 S/m to 0.3 S/m

Coil separation - 3 m
Sea water conductivity - 2.5 S/m

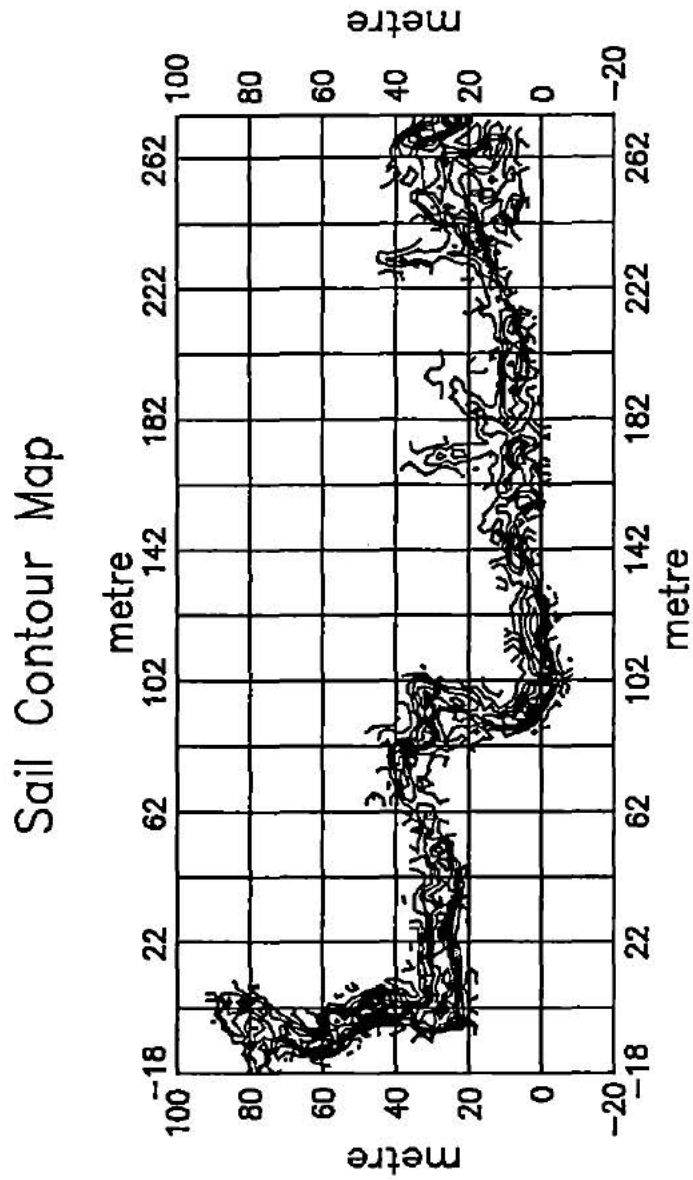
1-D Neural Network for EM Interpretation (Holladay et al., 1992).

Neural Network for 2-D Inversion of Ice Keels



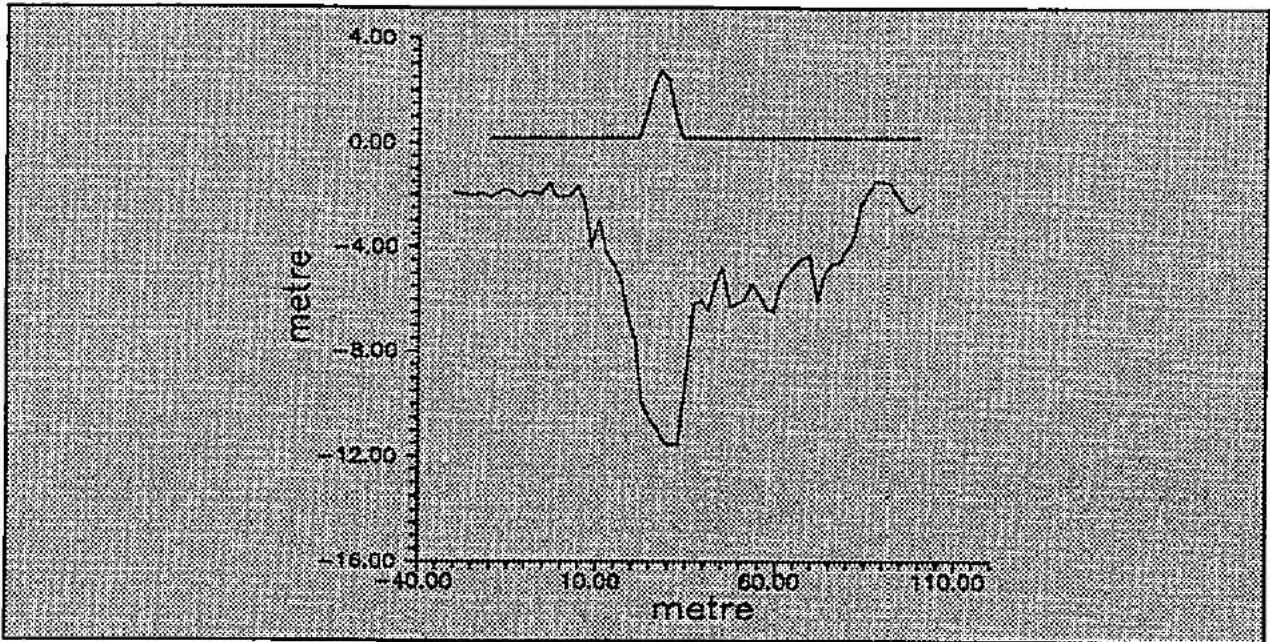
Altitude: 20 m
 Keel Width: Random from 10 m to 30 m
 Keel Depth: Random from 5 m to 20 m
 Coil separation - 3 m
 Input points: from -100 m to 100 m over ice keel
 Keel Shape = $D e^{-4 \ln 2 \left(\frac{N}{W}\right)^2}$

APPENDIX G
Ice Ridge Cross Sections

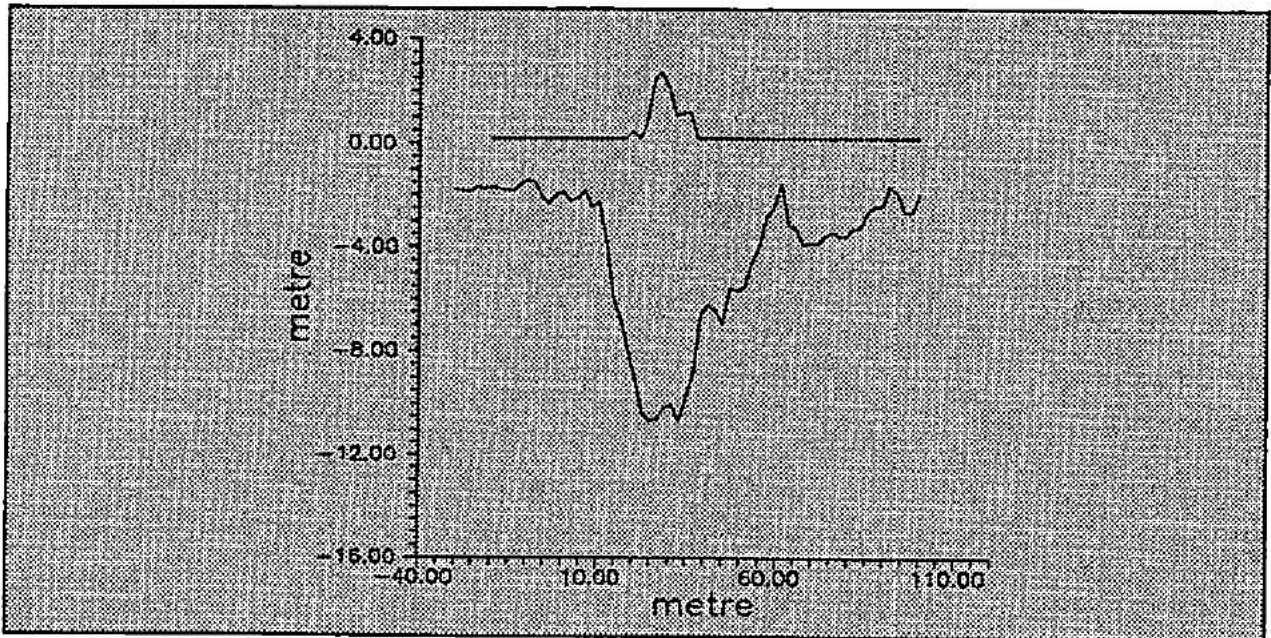


The following cross sections are slices taken through the short axis at locations along the long axis.

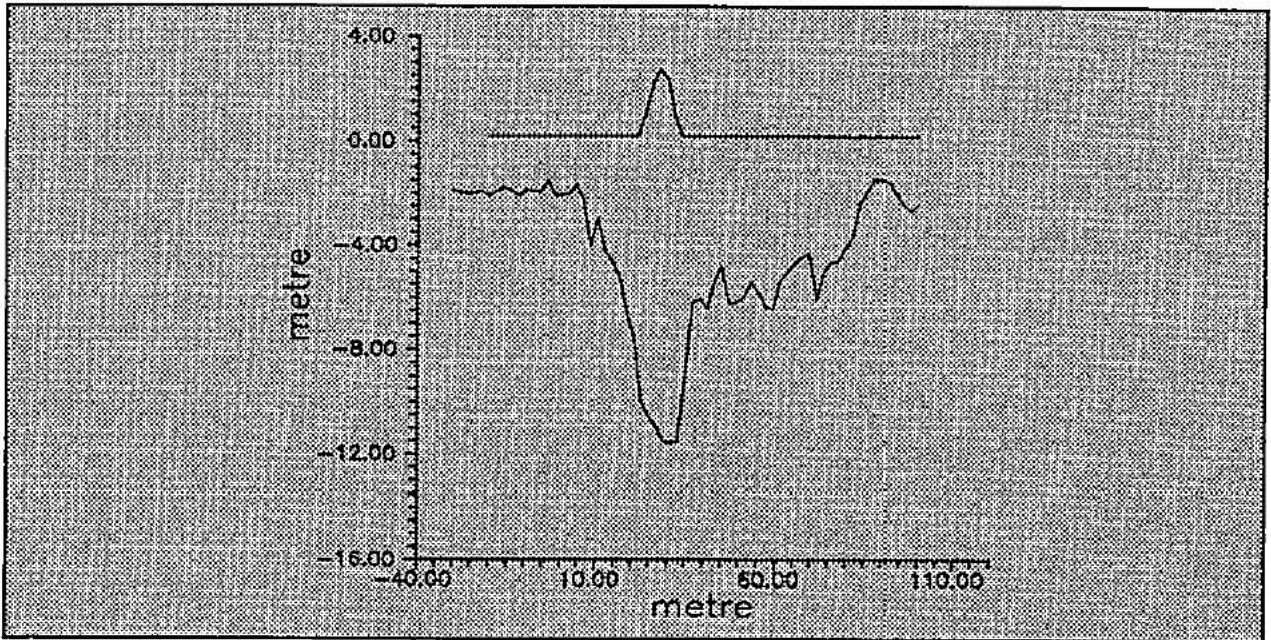
CROSS SECTION OF ICE RIDGE AT THE 20 METRE MARK



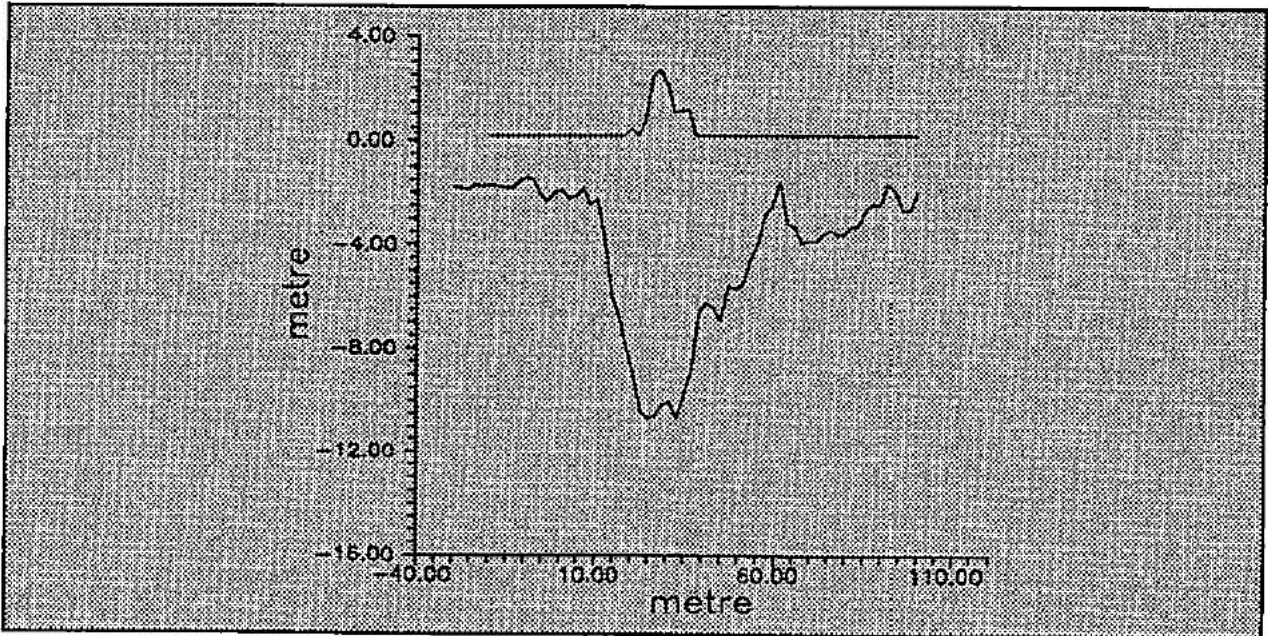
CROSS SECTION OF ICE RIDGE AT THE 30 METRE MARK



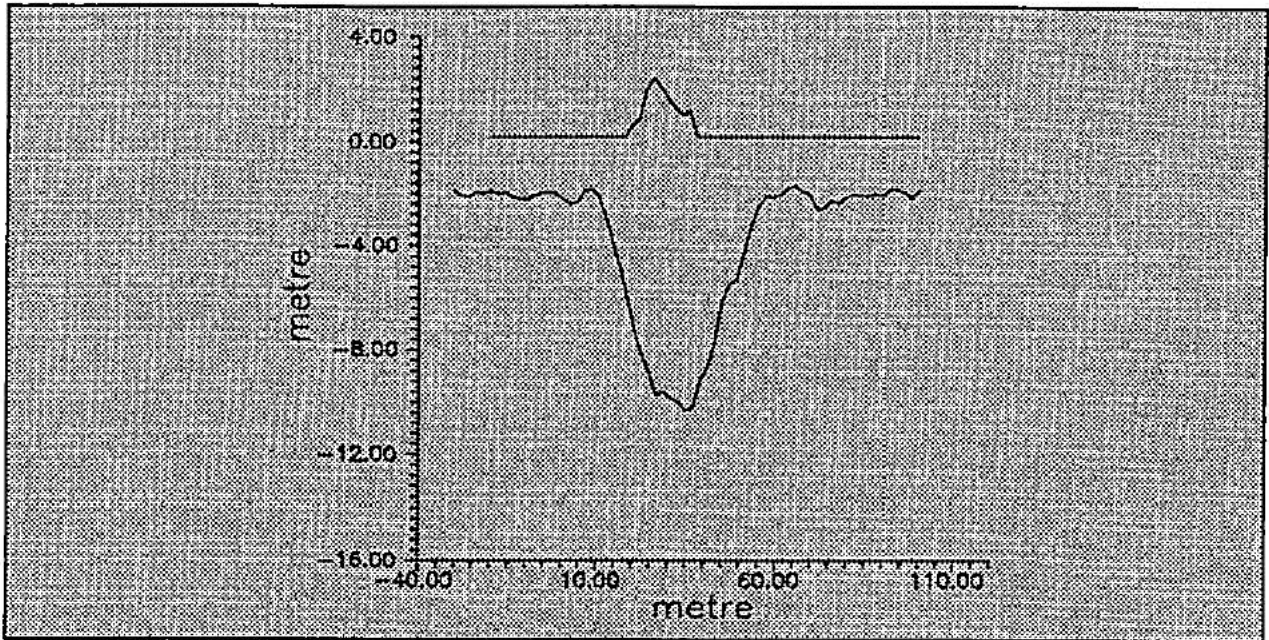
CROSS SECTION OF ICE RIDGE AT THE 40 METRE MARK



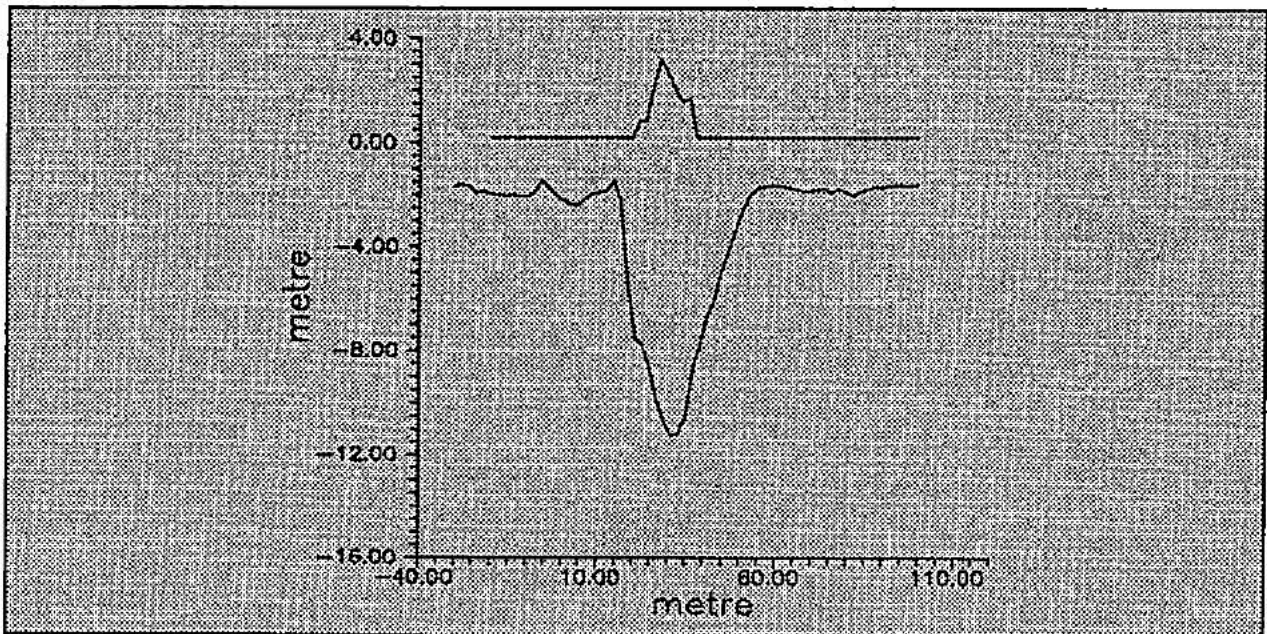
CROSS SECTION OF ICE RIDGE AT THE 50 METRE MARK



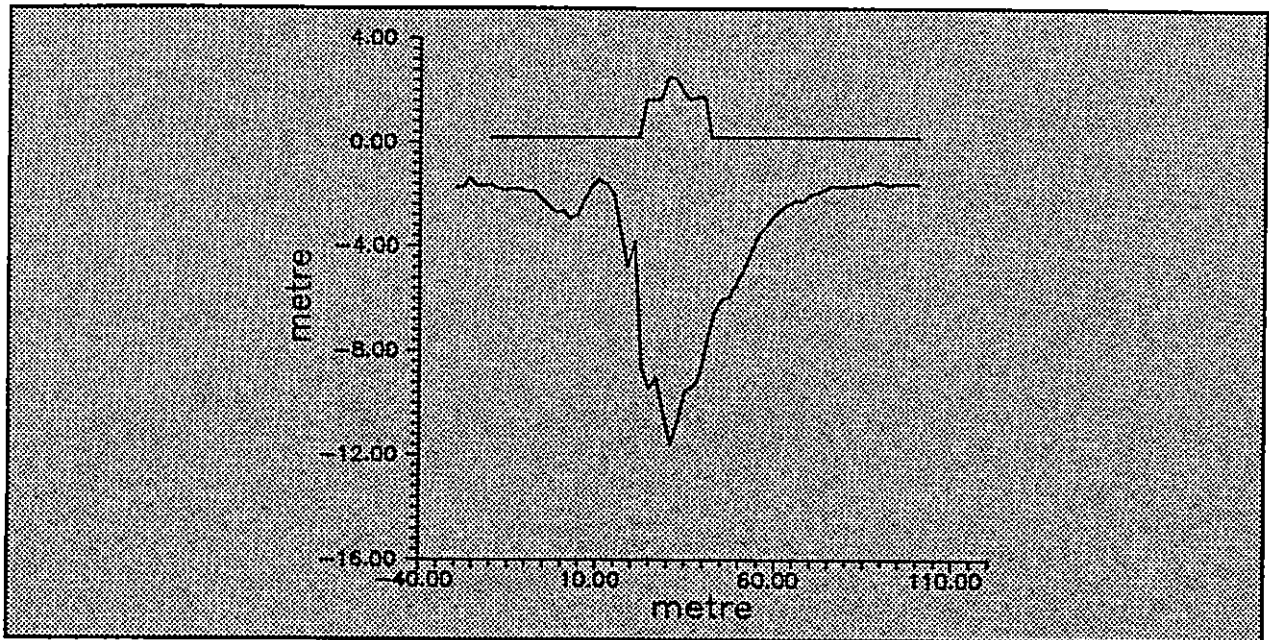
CROSS SECTION OF ICE RIDGE AT THE 60 METRE MARK



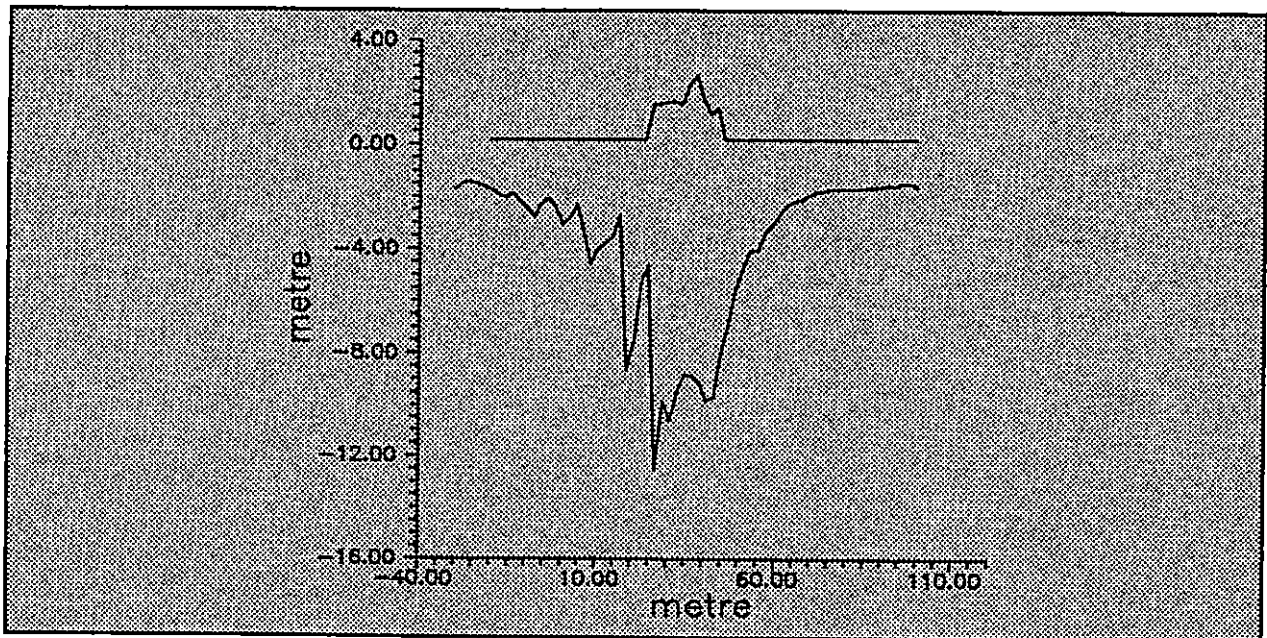
CROSS SECTION OF ICE RIDGE AT THE 70 METRE MARK



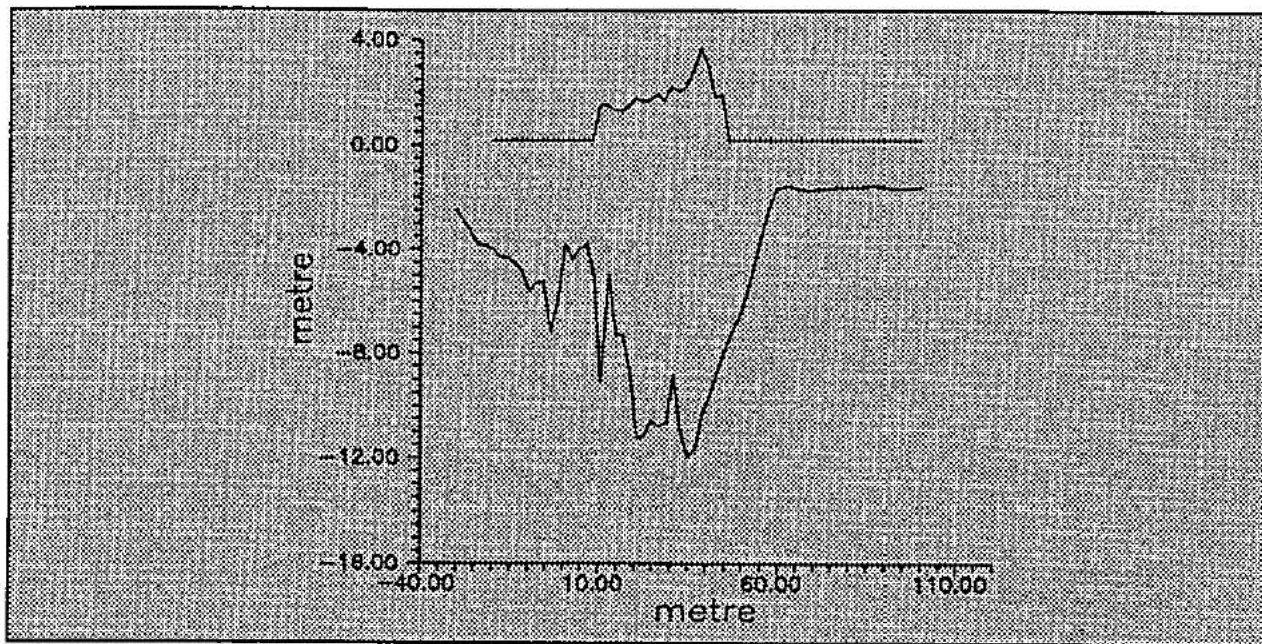
CROSS SECTION OF ICE RIDGE AT THE 80 METRE MARK



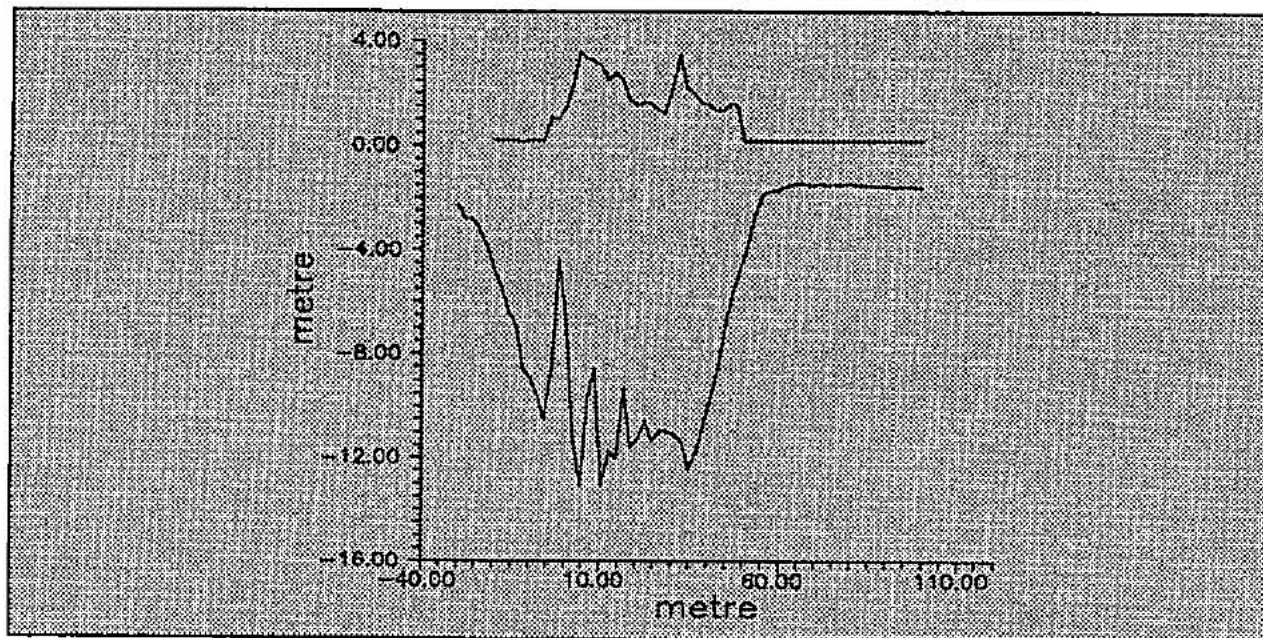
CROSS SECTION OF ICE RIDGE AT THE 90 METRE MARK



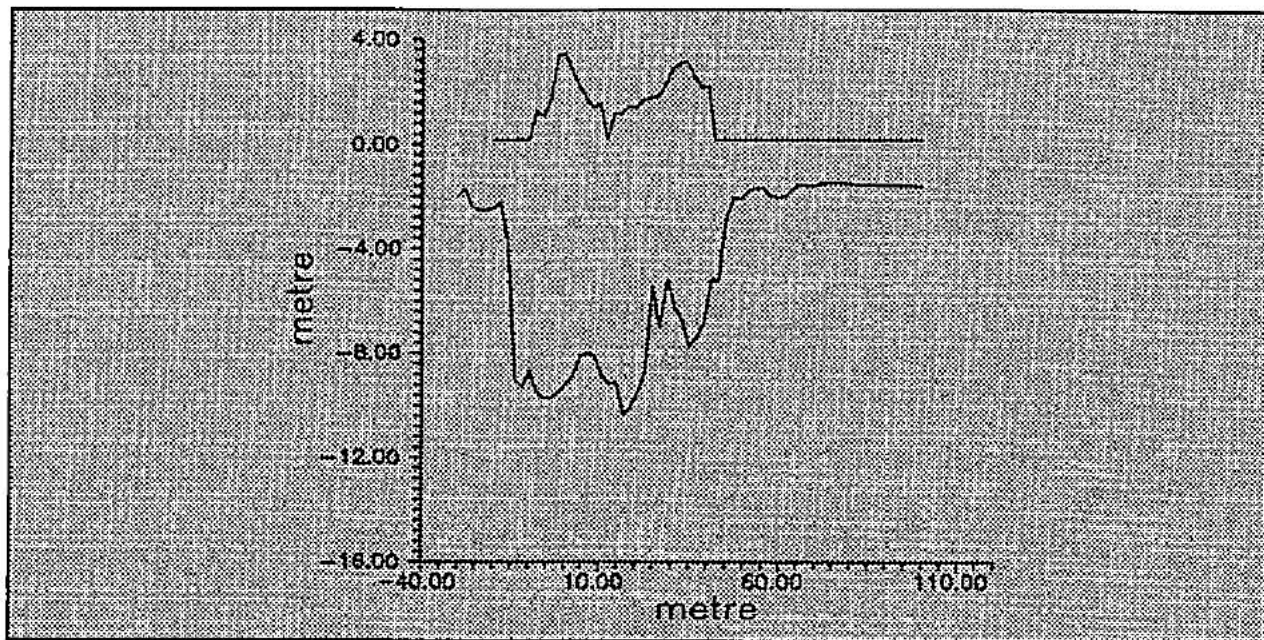
CROSS SECTION OF ICE RIDGE AT THE 100 METRE MARK



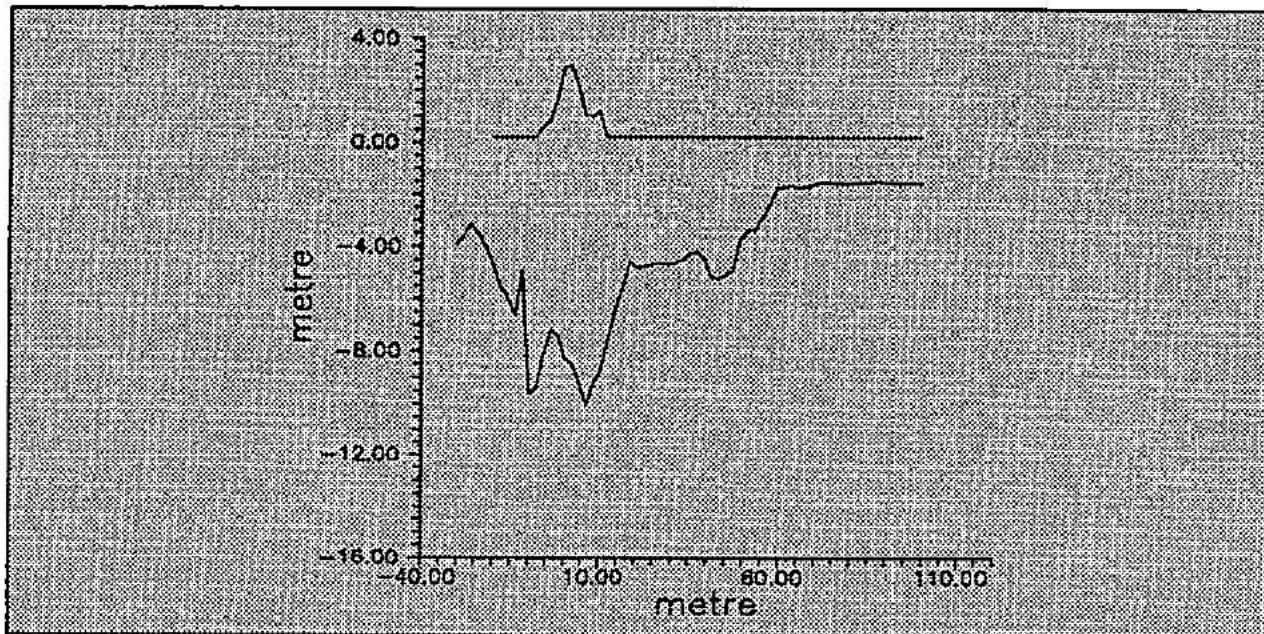
CROSS SECTION OF ICE RIDGE AT THE 110 METRE MARK



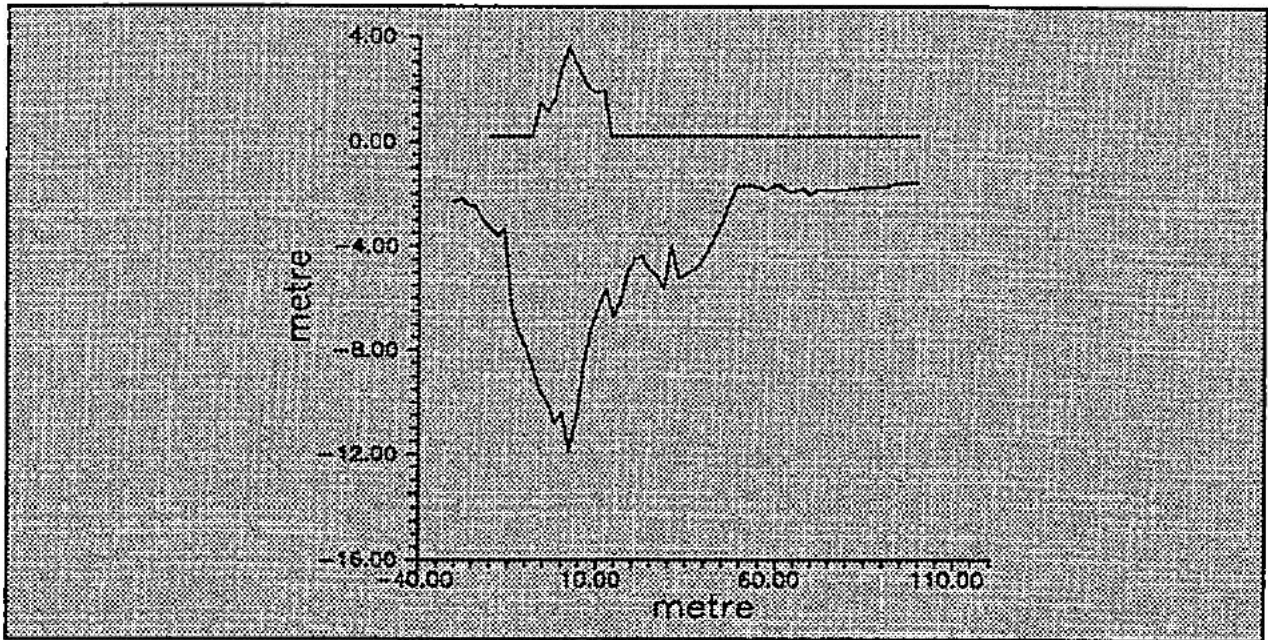
CROSS SECTION OF ICE RIDGE AT THE 120 METRE MARK



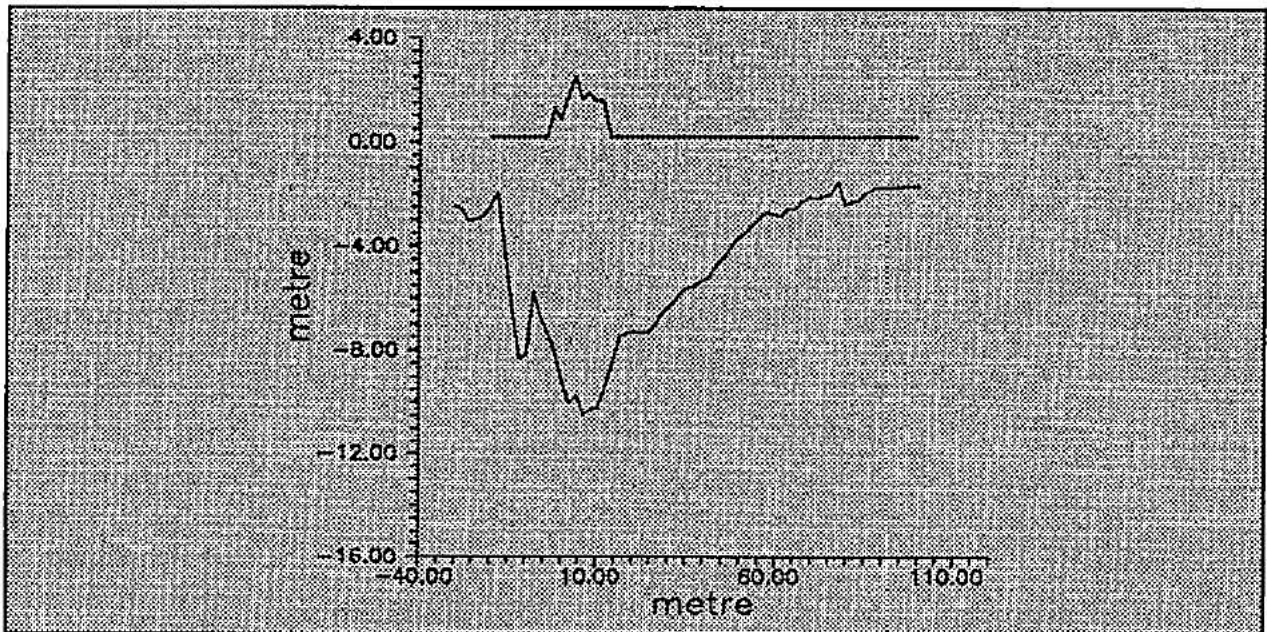
CROSS SECTION OF ICE RIDGE AT THE 130 METRE MARK



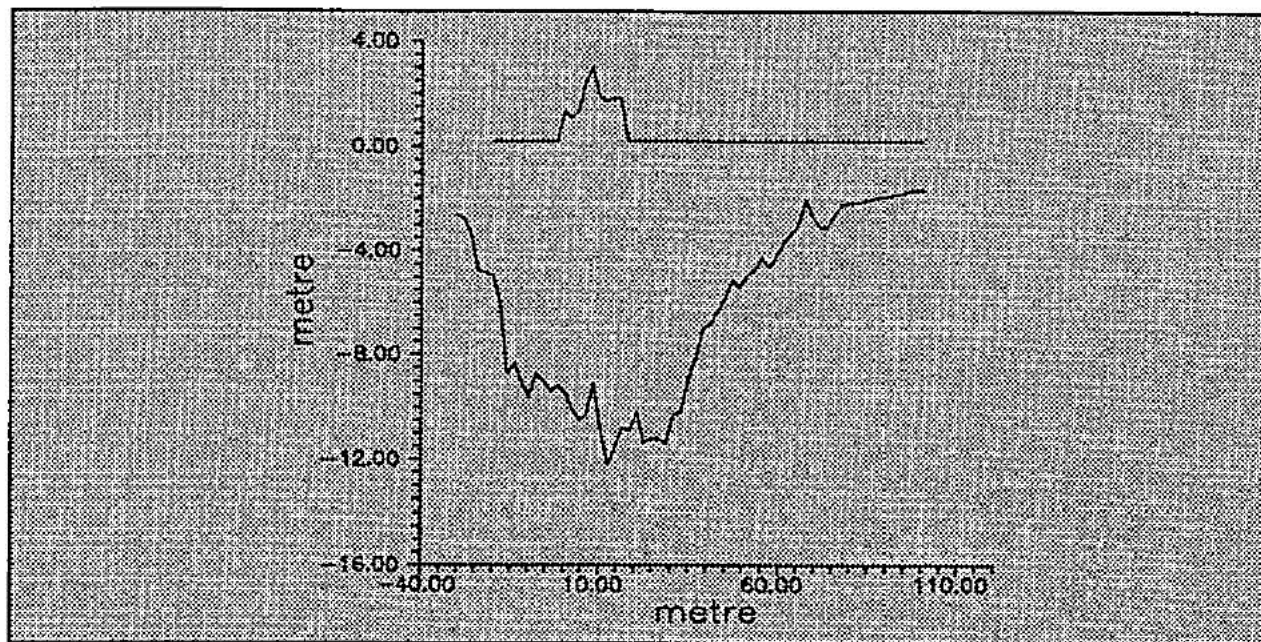
CROSS SECTION OF ICE RIDGE AT THE 140 METRE MARK



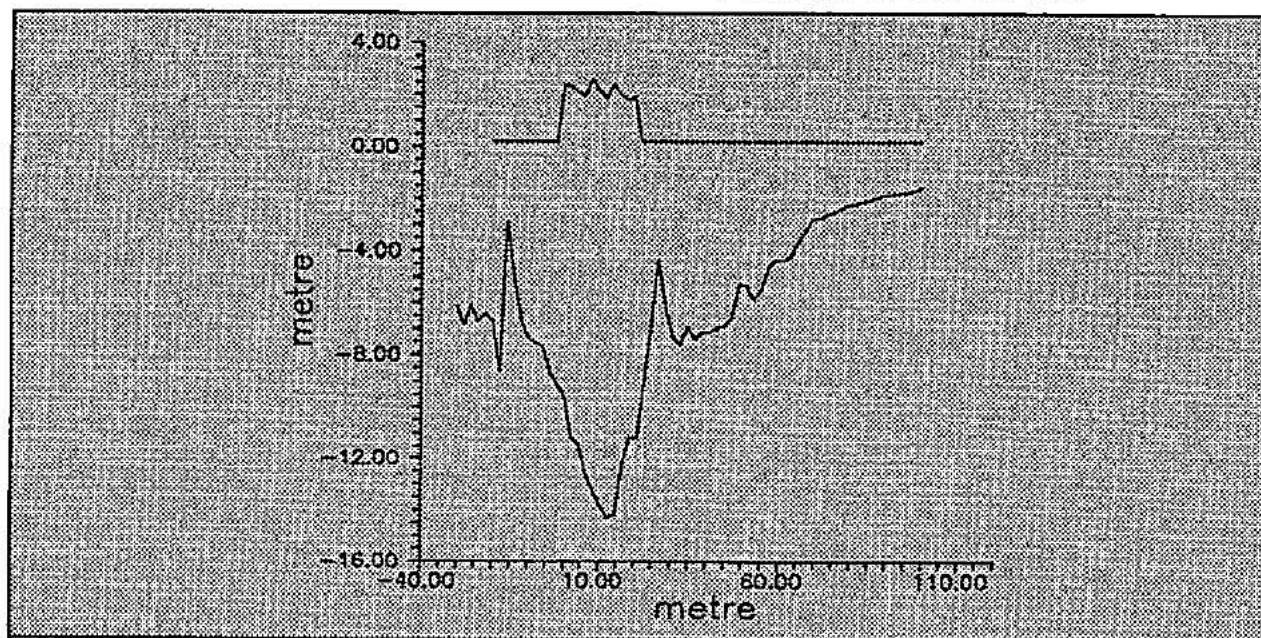
CROSS SECTION OF ICE RIDGE AT THE 150 METRE MARK



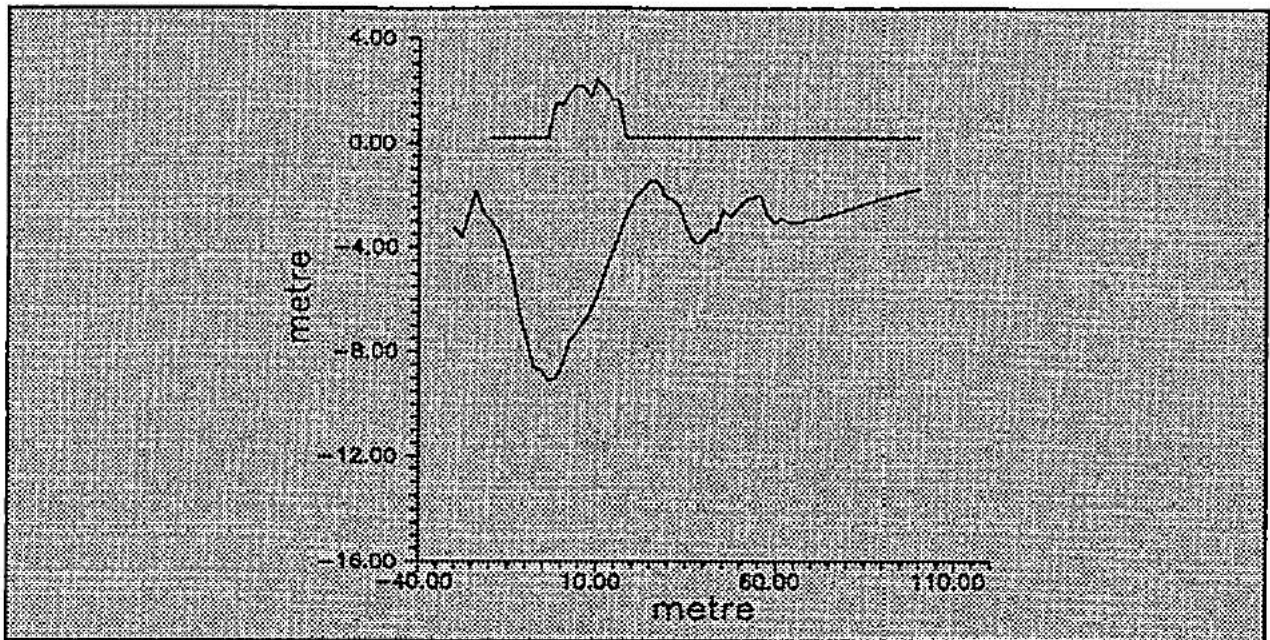
CROSS SECTION OF ICE RIDGE AT THE 160 METRE MARK



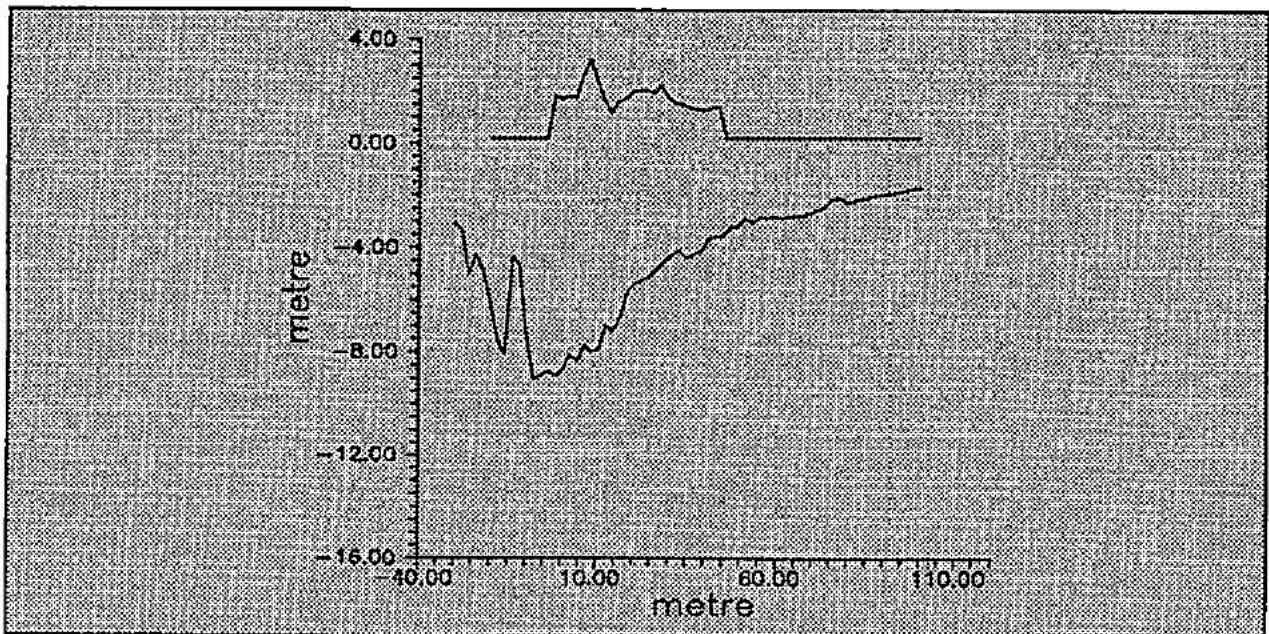
CROSS SECTION OF ICE RIDGE AT THE 170 METRE MARK



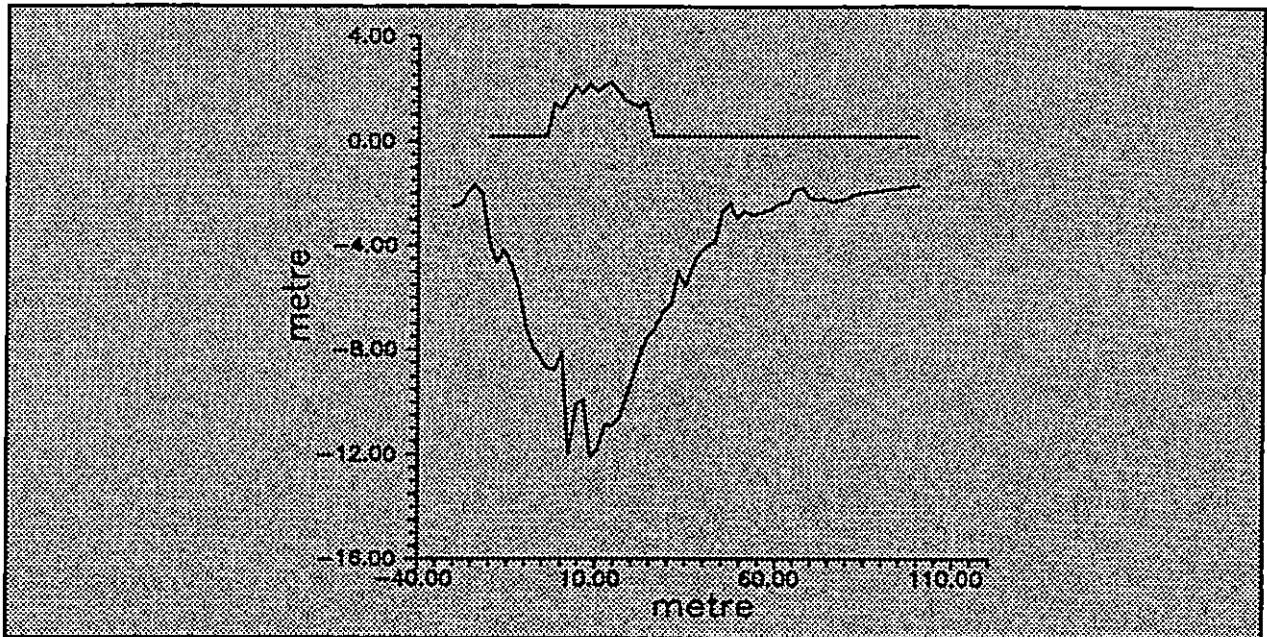
CROSS SECTION OF ICE RIDGE AT THE 180 METRE MARK



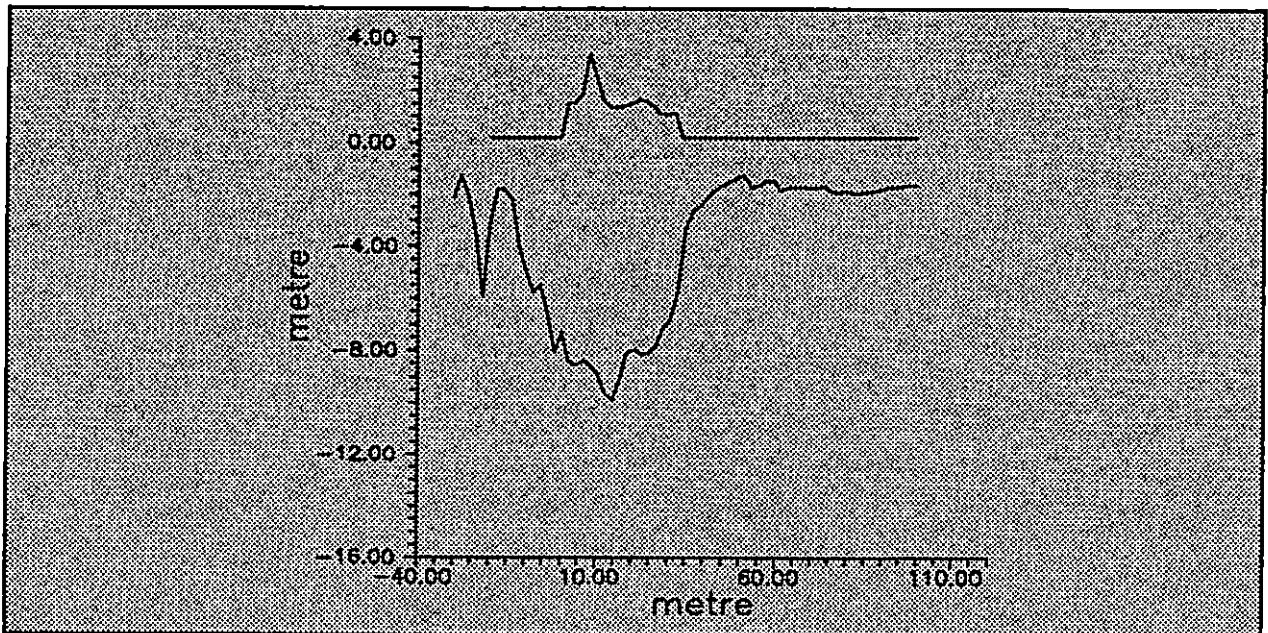
CROSS SECTION OF ICE RIDGE AT THE 190 METRE MARK



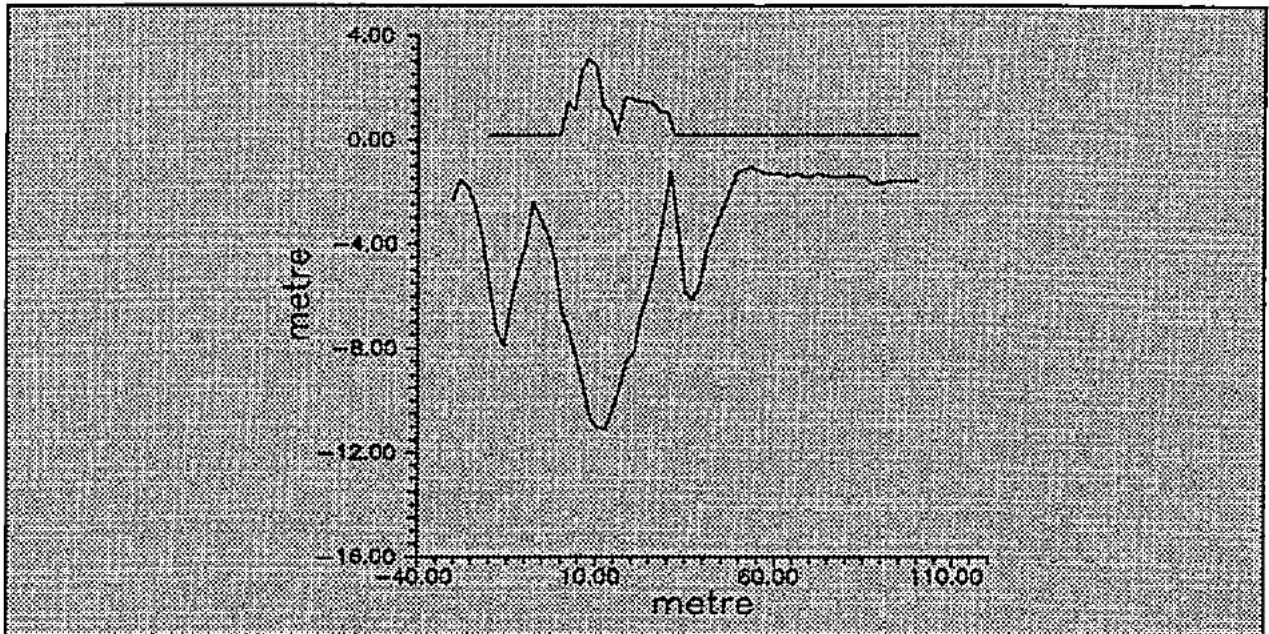
CROSS SECTION OF ICE RIDGE AT THE 200 METRE MARK



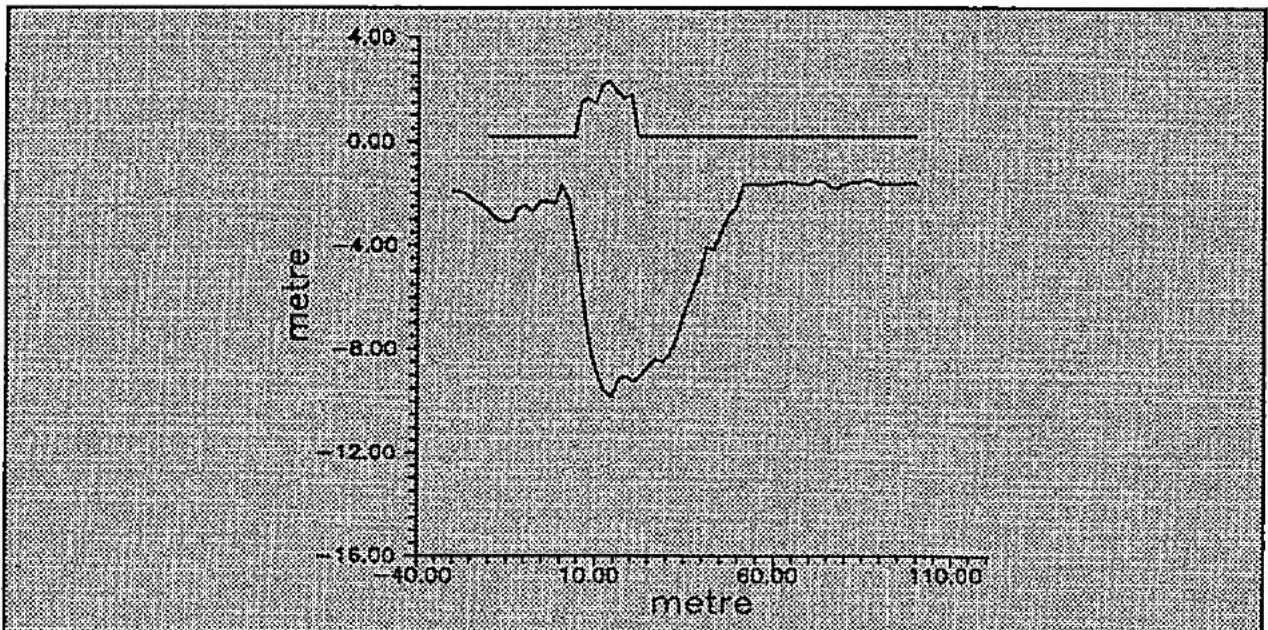
CROSS SECTION OF ICE RIDGE AT THE 220 METRE MARK



CROSS SECTION OF ICE RIDGE AT THE 240 METRE MARK



CROSS SECTION OF ICE RIDGE AT THE 260 METRE MARK



VITA

Surname: BOWEN Given Names: ROBERT

Place of Birth: VANCOUVER, BC. Date of Birth: MAY 29, 1960

Educational Institutions Attended:

Trent University	1979 to 1982
Carleton University	1986 to 1988
Trent University	1987 to 1988
University of Victoria	1990 to 1993

Degrees Awarded:

BSc	Trent University	1982
BSc (Honours)	Trent University	1988

Publications:

Bowen, R.G., 1993. Field Testing of a State of the Art Airborne Remote Sensing System on a first Year Sea Ice Ridge. Muskox, pp.12, in press.

Timco, G.W., Goodrich, L.E., Bowen, R.G. and J.C. Plunkett, 1987. Experiments on the Freezing of Ice Rubble. Division of Mechanical Engineering/National Research Council Technical Report 28288, pp. 55.

PARTIAL COPYRIGHT LICENSE

I hereby grant the right to lend my thesis to users of the University of Victoria Library, and to make single copies only for such users or in response to a request from the library of any other university, or similar institution, on its behalf or for one of its users. I further agree that permission for extensive copying of this thesis for scholarly purposes may be granted by me or a member of the university designated by me. It is understood that copying or publication of this thesis for financial gain shall not be allowed without my written permission.

Title of Thesis:

An Evaluation of an Airborne Remote Sensing System used to Determine Ice Thickness and Geometry of a First Year Sea Ice Ridge Located in the Beaufort Sea.

Author


(Signature)

Robert G. Bowen
(Name in Block Letters)

March 3/93
(Date)